N° d'ordre : 42241

UNIVERSITE DE LILLE1- SCIENCES ET TECHNOLOGIES

ECOLE DOCTORALE SCIENCES POUR L'INGENIEUR UNIVERSITE LILLE NORD-DE-FRANCE

THESE

Présentée en vue d'obtenir le grade de

DOCTEUR

Spécialité : Micro et Nanotechnologies, acoustique et télécommunications

Par

Boubakeur AYACHI

Towards full sputtering deposition process for CIGS solar cell fabrication: from single thin film deposition up to device characterization

Thèse soutenue le 15 Décembre 2016 devant le jury d'examen composé de:

Président	Marie-Paule Besland, Directrice de recherche CNRS, IMN, Nantes.
Rapporteur	Frédérique Ducroquet, Chargée de recherche, HDR, IMEP-LAHC, Grenoble INP, Grenoble.
Rapporteur	Denis Mencaraglia, Directeur de recherche CNRS, GeePs, Gif sur Yvette.
Examinateur	Marie-Paule Besland, Directrice de recherche CNRS, IMN, Nantes.
Examinateur	Patrice Miska, Maitre de conférences, HDR, IJL, Université de Lorraine, Vandoeuvre les Nancy.
Examinateur	Philippe Torchio, Maitre de conférences, HDR, IM2NP, Université d'Aix-Marseille, Marseille.
Invité	Pierre-Yves Thoulon, Directeur Technique et Fondateur, CROSSLUX, Rousset.
Directeur de thèse	Jean-Pierre Vilcot, Directeur de recherche CNRS, IEMN, Villeneuve d'Ascq.

Acknowledgements

The work of this PhD thesis has been done at the IEMN (Institut d'Electronique, de Microélectronique et de Nanotechnologie), with a financial support from Université de Lille1.

First of all, I would like to thank, Dr. Jean-Pierre Vilcot, for having accepted me as a PhD student under his supervision, for his guidance and continuous encouragement and finally for carefully correcting this work.

I would also like to thank all members of the Optoelectronic group. Thanks to Thomas for being my tutorial during my first days in the clean room. One advice for him: slow down, slowly but surely and better late than never!!

Thanks to Marc, Guillaume, David and the pseudo-Japanese Etienne for their technical help.

Special thanks to Mr. Patrick Chapon from HORIBA Jobin-Yvon group for the GDOES analyses, without which our cells would have never transformed the light of the day!!! Without forgetting to thank Dr. Pascal Roussel, Dr. Dominique Vignaud and Dr. David Troadec for the XRD, Raman and FIB analyses, respectively.

Finally, I would like to thank the committee members Dr. Denis Mencaraglia, Dr. Frédérique Ducroquet, Dr. Marie-Paule Besland, Dr. Patrice Miska, Dr. Phillipe Torchio, for having accepted to review this work.

Thanks to all of those who have helped and contributed, directly or indirectly, to this work.

Contents

General introduction

Motivation

At research level, the copper-indium-gallium-selenium (CIGS) thin film technology exhibits a now record efficiency of 22.3% to be compared to bulk silicon technology which is at 25% and 25.6% for monocrystalline and heterojunction with intrinsic thin-layer (HIT) structures, respectively (non-concentrator illumination) (Figure I.1) [NREL 2016]. The CIGS-based technology has so attracted considerable attention since it can provide high efficiency, more than twice a-Si technology, and less environmental concerns than CdTe technology.

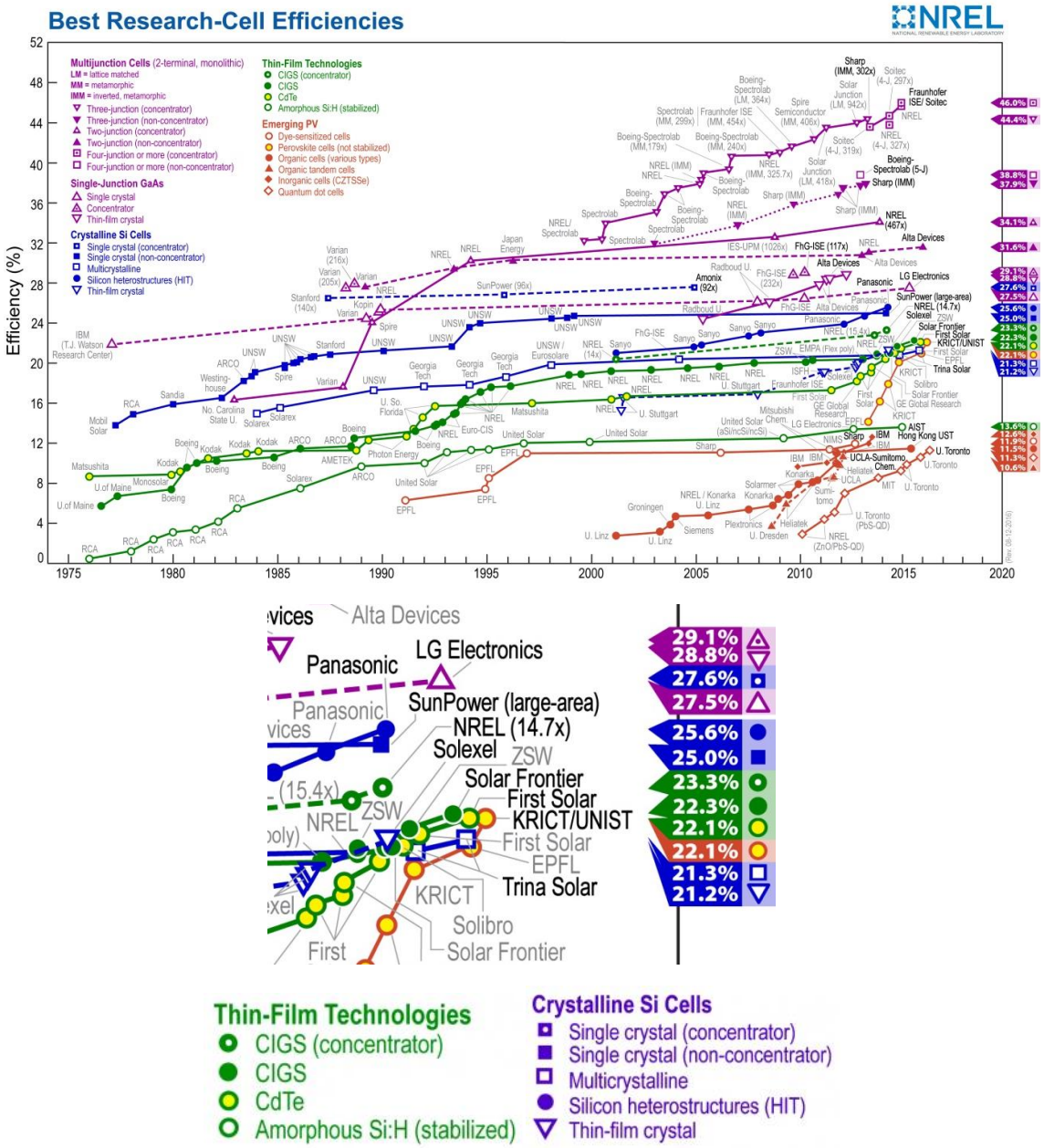

Figure I.1: Best research cell chart [NREL 2016]. (It has to be noticed that higher efficiency values for the CIGS based technology have been recently announced by both ZSW (22.6% certificated)[ZSW] and Solar Frontier (22.8% home measurement) [T. Kato. 2016]).

Nevertheless, thin film technology still faces silicon supremacy even if its raw material consumption is roughly 100 times less and hence thwarts the basic idea that was the seed of its study. However scientific and technical aspects are not solely accountable and geopolitical financial aspects have a major impact on the respective development and deployment of these technologies. We will not enter this debate and we just report factual data on the current and forecast technology deployment [GVR 2016]. Main thin film technologies, CIGS and CdTe, contribute equally to share together 8% of the whole market.

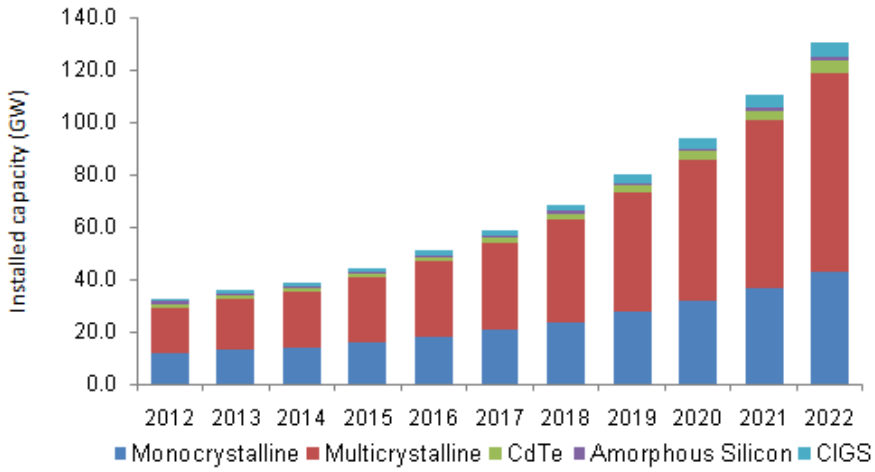

Figure I.2: Germany's market share (actual and forecast) of the main photovoltaic technologies [GVR 2016].

Contrary to bulk silicon technology, thin film solar cell technology is a very promising solution, especially when it is applied to the fabrication of photovoltaic glass for building integrated photovoltaics (BIPV) where the use of crystalline silicon-based technology leads to a rather unpleasant aesthetics with checkerboard visual effect [for example, Himinsun 2016] (Figure I.3a). In such applications, some new designs are based on micro-patterned or laser-machined thin film cells leading to adjustable glass transparency (and consequently power generation) by layout [CROSSLUX 2016].

Figure I.3a: Bulk silicon based BIPV
[Himinsun 2016]

Fig I.3b: Thin film based BIPV
[CROSSLUX 2016]

As can be seen on Figure I.1, thin film technologies have recent challengers that are gathered together under the emerging PV banner. Particularly, the perovskite cell family exhibits a sharp performance increase those last years. Nevertheless, these latter still suffer from up-scaling and lifetime issues that CIGS technology has already proven to comply with. This is reflected by Figure I.2 where no deployment, and so related industrial development, of such technologies are forecast in the following years.

One of the key steps in the fabrication of CIGS-based solar cells is the choice of the absorber deposition technique, to which, cells performance is strongly dependent. Furthermore, the choice of the nature and the deposition technique of the buffer layer is another crucial step for achieving high performance solar cells.

At the industrial level, several companies working in this field have developed their appropriate process. In table I.1, we present the used process and the achieved efficiency by the two pioneer manufacturers of CIGS thin film photovoltaic solar panels.

Company		Solar Frontier [Solar Frontier]	AVANCIS [AVANCIS]
Back contact		Sputtered molybdenum layer	
CIGS deposition process		Two steps process: material sputtering/selenization	
Buffer layer: process/nature		CBD/ZnS_xO_{1-x}	Evaporation/In_xS_y
Window layer		i-ZnO/IIIA-doped ZnO	
Sub-module efficiency %		17.5	17.9
Advantages of using sputtering process for CIGS layer deposition		High deposition rate Good uniformity over large surfaces Low cost High yield	
Drawbacks	CIGS process	The need for a selenization step is still pointed out as a real issue	
	Buffer layer nature/process	Waste recycling of ZnOS solution	High-cost

Table I.1: Followed process by the pioneer manufacturers of CIGS thin film photovoltaic solar panels: advantages and drawbacks. (It has to be noticed that efficiency values are here different from the ones shown in Figure I.1 that refer to elementary cell data).

Thin film cell technology development and in a broader term photovoltaic research activity started at IEMN in 2009 by the PhD of Thomas Aviles in the frame of a "Délégation Générale à l'Armement" support. The goal was to investigate an energy harvesting technology able to be integrated with other electronic functions onto the same chip. Photovoltaic technology was

then focused on since it allows furnishing larger energy amount that other alternatives such as piezo- or thermo-electricity at this scale. Co-integration led us to thin film technology and our core trade to physical vapor deposition. At that time, such an approach was quite innovative, moreover taking into account the different guidelines we self-imposed. Main were: i) use of single target for absorbing layer, ii) removal of hazardous gas or process and iii) decrease of thermal budget. This PhD work is so in continuation of the previous PhD work of Thomas Aviles It has been carried out in close collaboration with the new startup ‘’CROSSLUX’’ which works on the development of photovoltaic glass for building integrated photovoltaics (BIPV) (see Figure I.3b) Thomas Aviles is additionally involved in. Our ultimate goal is then developing a full sputtering deposition process. Furthermore, reaching a reduced environmental footprint drove us removing both selenization step and cadmium material from the fabrication process.

Scientific approach

The outcome of these 3 years of PhD work is structured in five chapters. Chapters 1 to 4 are composed of two parts: a first part in which the state of the art is given, while in the second part we present our scientific contributions. CIGS cells being studied from a while, we thought it was important to make a clear situational analysis before describing our work.

The first chapter will be devoted to understand the role of molybdenum layer as a back contact, to understand, explain and develop an innovative solution for the commonly reported substrate bending issue which can be of real concern in the BIPV application targeted by CROSSLUX (up to 2m x 4m window glass size, in fine).

In the second chapter, after a very detailed overview on the already obtained results, an original deposition process for the absorber layer will be presented. It gathers the three main guidelines reported above, i.e. the use of a single quaternary target, no use of Se based process and limited thermal budget.

The purpose of the third chapter will be to develop a standard (CBD-CdS) and an alternative (room temperature sputtered zinc oxysulfide (ZnS_xO_{1-x})) buffer layers. Basically, only zinc oxysulfide approach by sputtering was studied. However, the chemical bath deposition technique for a usual CdS layer was developed in order to separate absorbing and buffer layer contribution in cell performance as well as to compare more easily with literature results.

Our contribution in the development of a sputtering process for the deposition of the window layer will be the subject of chapter 4.

The electrical characterizations and the microstructural analyses of full fabrication stages towards the fabrication of working solar cells will be presented in chapter 5, before ending this manuscript with the conclusions and a brief outlook.

Chapter 1: Back contact

This chapter is mainly devoted to the development of an innovative solution for the commonly reported substrate bending issue.

In the first part, we will justify the choice of both molybdenum material and sputtering deposition technique for the deposition of the CIGS solar cell back contact. We will also give a quick review on alternative materials for specific application, their advantageous and drawbacks. A special interest will be addressed to the commonly reported substrate bending issue. Finally, since we believe that this substrate bending is, in somehow, related to the stress state of the as-deposited thin films, a detailed review on the origin of different stresses within sputtered thin films will be given.

In the second part, we will first start by proposing a simple model explaining the dependence of substrate bending on the initial stress state of the molybdenum layer. Then, we will show that it is possible to overcome this issue by simply using a reactive sputtering process for the deposition of the molybdenum layer. Finally, we will show that using a bilayer structure Mo/Mo(O) allows a more precise control of the flatness of the annealed samples.

Part A. State of the art

1.1. Why molybdenum (Mo) as a back contact material for CIGS solar cells in standard configuration (substrate configuration with ±2.5 µm thick CIGS absorber layer)?

Over more than four decades of chalcopyrite solar cells development, molybdenum is always used as a reference back contact material ‘’thanks to its low cost and abundance, excellent mechanical and electrical properties, low reactivity with and diffusivity into the CIGS layer, ability to conserve this properties at/after high temperature deposition/annealing process of CIGS, and its ability to form an ohmic contact with the CIGS absorber layer’’.

On the other hand, sputtering deposition technique is commonly used for the deposition of molybdenum back contact of CIGS solar cells. In addition to the reduction in fabrication cost, the use of sputtering offers the possibility to manage the stresses within the molybdenum layer. Furthermore, sputtered molybdenum layer density, which is easily controlled by changing the deposition conditions, is known to play a very important role in controlling the out-diffusion of alkaline elements from the substrate.

All these advantages and others, related to both molybdenum material and sputtering deposition technique, make of the sputtered molybdenum layer a back contact of choice for CIGS solar cells.

In the following, we give some details on the most important points previously highlighted.

1.1.1. Metal-semiconductor contact nature

One very important point that should be taken in consideration while choosing the back contact material is the nature of the metal/semiconductor (CIGS absorber) contact: forming a low resistivity ohmic contact is a mandatory condition for a better carrier collection and lower interface recombination.

The nature of a metal/p-semiconductor contact is commonly expressed using the Schottky model, which shows the hole barrier height (Φ_{bp}) dependence on both the band gap (Eg_{sc}) and electronic affinity (χ_{sc}) of the p-semiconductor, on one side and on the other side, on the work function of the metal:

$$\Phi_{bp} = Eg_{sc} + \chi_{sc} - \Phi_m$$

Taking into consideration that an ohmic contact is only achievable for a low hole barrier height (Φ_{bp}), and both band gap (Eg_{sc}) and electronic affinity (χ_{sc}) of the p-semiconductor are constant (for a given CIGS), therefore it is clear that the use of high work function metal (Φ_m) is mandatory to get an ohmic contact. Theoretical calculations have shown that the barrier height should be less than 0.3 eV, otherwise cell characteristics will be affected. As a consequence, the use of a metal with a work function higher than 5 eV seems to be necessary [A. Simchi. 2014 and references therein].

Consequently, one can expect that a rectifying contact nature should take place in case of using molybdenum due to its low work function (around 4.4 eV); whereas, this expectation is in contradiction with experimental results in which an ohmic contact characteristics is commonly reported [T. Wada. 2001].

In fact, the use of a Schottky model to explain experimental observations might be confusing, since it does not take in consideration neither the surface chemistry of both sides nor their defect densities, which might highly influence the contact type in real conditions [E.H. Rhoderick. 1970]. Furthermore, this model is only valid for abrupt interfaces which is not the case for molybdenum-high temperature deposited/annealed CIGS interface.

A deep investigations of the Mo-CIGS interface have revealed the existence of an interfacial layer ($MoSe_2$), to which the ohmic contact behavior is commonly attributed [T. Wada. 2001] [D. Abou-Ras. 2005]. This $MoSe_2$ layer is, in few words, the result of selenium reaction with molybdenum surface during the high temperature deposition/annealing process (more details will be presented in §2.7).

1.1.2.Effect of sputtering deposition conditions on molybdenum layer properties

It is commonly reported that the kinetic energy of the sputtered Mo atoms arriving at the substrate surface, which is itself dependent of both sputtering power and pressure, is a critical parameter for the resulting layer properties.

From the crystallographic point of view, highly oriented (110) sputtered molybdenum layers are commonly achieved on glass substrates independently of the sputtering conditions and even when (100)-textured molybdenum foils are used as substrates [M. A. Contreras. 2000]; however, an enhancement of the crystalline quality is commonly reported for lower sputtering pressures (higher kinetic energy of the sputtered Mo atoms at the substrate surface) [C. Roger. 2013] [Z.H. Li. 2011]. In parallel to that, is was also found that the resistivity of sputtered molybdenum layers depends on the crystalline quality and therefore on the sputtering deposition conditions: the higher the kinetic energy of the sputtered Mo atoms at the substrate surface, the lower the resistivity is [M. Jubault. 2011] [Z.H. Li. 2011] [C. Roger. 2013].

On the other hand, the induced stresses within the sputtered molybdenum layers are also believed to be dependent on the deposition conditions. As the deposition pressure increases, the stress state changes from highly compressive to highly tensile passing by a zero point (stress free point at low pressure) and then again down to zero (stress free point at high pressure) [H.A. Al-Than. 2001]. In fact, this is a characteristic that is related to the sputtering technique rather than the molybdenum material itself [J.A. Thornton. 1977]. A detailed study of the origins of stresses within the sputtered molybdenum layers will be presented later.

Another very important property of sputtered molybdenum layers is the one related to their adhesion to substrate. It is largely reported that sputtered molybdenum layers obtained at low deposition pressure show a poor adhesion to substrate even if they are obtained at a deposition pressure corresponding to the stress free point, while those obtained at high deposition

pressure show a very good adhesion to substrate [J.H. Scofield. 1995]. It is interesting to note that the adhesion is commonly evaluated using the so called tape test.

To sum up, using sputtered molybdenum layers with a good adhesion and a low resistivity is mandatory for high efficiency CIGS solar cells. However, obtaining a single molybdenum layer with both properties at the same time seems to be difficult, if not impossible, since the first property is achievable at high deposition pressure while the second is achievable at low deposition pressure (opposing conditions).

1.1.3.Multilayer structure

To overcome the adhesion/resistivity issue, Scofield et al. have developed a sputtered molybdenum bilayer back contact which provides a good adhesion to the substrate while maintaining a low resistivity [J.H. Scofield. 1995]. Their bilayer structure is based on the use of a combination of an adhesion bottom layer and a conductive top layer, sputtered at high and low deposition pressure, respectively. It is worth to note that since the publication of their work in 1995, the bilayer structure became a reference structure, used by everyone, for the deposition of sputtered molybdenum back contact of standard CIGS solar cells (substrate configuration).

Furthermore, a trilayer structure was also developed in the last few years. This trilayer structure is based on the addition of a high pressure deposited third layer on the classical bilayer, aiming in controlling the CIGS orientation [D.H. Shin. 2012] [J.H. Yoon. 2014] (more informations will be given in § 2.4.1).

1.1.4.Sodium out-diffusion control

One very important advantage of using sputtered molybdenum layer as a back contact for CIGS solar cells is the possibility of using it as a control valve for sodium out-diffusion (as far as a soda lime glass substrate is used) to the CIGS layer. This sodium out-diffusion is known to be easily controlled by the engineering of the molybdenum layer porosity through the changing of the deposition conditions [J.H. Scofield2. 1995] [P. Bommersbach. 2011] [J.H. Yoon. 2012]. Furthermore, a clear relationship between the amount of the out-diffused sodium and the oxygen concentration within the molybdenum layer (from residual oxygen in the deposition chamber) was also found [J.H. Scofield2. 1995] [P. Bommersbach. 2011]: the higher the oxygen concentration the more important the amount of out-diffused sodium. It is believed that molybdenum oxides at the grain boundaries play an important role in facilitating sodium out-diffusion [M. Bodegard. 1999] [A. Rockett. 1999].

On the other hand, for a better control of the diffused sodium concentration into the CIGS layer and/or to find an alternative sodium source in case of using other substrates than the soda lime glass (flexible substrates: polyimide or metallic foils), sodium doped molybdenum layers as a back contact were recently investigated [J.H. Yun. 2007] [P. Blösch. 2014] [M. Lee. 2015].

1.2. Alternative back contact materials

In parallel to the development of molybdenum back contact layer for CIGS solar cells, alternative materials such as: Au, Ag, Pt, Ni, Al, Cu, W, V, Cr, Mn, Ta and Nb [K. Orgassa. 2003] [R. J. Matson. 1984] [S. Ashour. 1993] as well as some transparent conductive oxides [T. Nakada. 2005] [P.J. Rostan. 2005], have also attracted some attention.

The reason behind the showed interest for alternative back contact materials is mainly due to the development of other CIGS solar cell structures such as reduced CIGS absorber layer thickness cells, bifacial cells and tandem cells, for which the use of the standard molybdenum back contact is not any more suitable because of either its low reflectivity, its low work function or its opacity.

1.2.1.Back contact for reduced CIGS absorber layer thickness

In standard CIGS solar cells, the fact that molybdenum has a very low optical reflection does not create any problem since the entire incident light should be absorbed within the 2 µm thick CIGS layer. However, for reduced CIGS layer thickness cells, only part of the incident photons which energy is larger than the band gap can be absorbed within a single pass through the absorber. In this case the optical reflection on the back contact might highly affect the cell performance and therefore the use of an alternative material with high optical reflection is highly recommended.

For this sake, various materials have been investigated and the obtained results have shown that only few of them (Ag, Au, Al, and Cu) have a high optical reflection [Z.J.L. Kao. 2012]. However, the suitability of Ag, Al, and Cu has been questioned in view of their very low work function which does not meet the ohmic contact requirement. On the other hand, even though Au has shown high optical reflection and high work function, its high diffusivity into the CIGS layer is still considered as a real issue.

To overcome these drawbacks, one should either use a room temperature deposition process in order to prevent the metal-CIGS inter-diffusion, or add a transparent conductive oxide intermediate layer between the CIGS and the low work function metal to ensure an ohmic contact.

In this scope, Z.J.L. Kao et al. have first used a mechanical lift-off technique to peel a CIGS layer, originally grown on molybdenum, from its substrate and transfer it to another substrate using epoxy glue, and then deposited Au metal at room temperature [Z.J.L. Kao. 2012]. This technique allowed them to fabricate reduced CIGS absorber thickness (down to 400nm) solar cells without (almost not) influencing their performance. However, knowing that the main reason behind the development of the reduced CIGS absorber layer thickness technology is lowering the cell fabrication cost, is it worth to use gold as a back contact material?

A combination of high reflectivity metal (Ag) and a transparent conductive oxide (TCO) was also used as a back contact for reduced CIGS layer thickness cells [A. Čampa. 2007]. In this case the TCO has a triple role: (i) in addition to its role as a back contact (see the next section), (ii)

it is also used in order to allow non absorbed photons to pass through and to be reflected at the metal surface, and (iii) to prevent the metal diffusion into the CIGS layer.

1.2.2.Transparent back contact for bifacial and tandem cells

In the framework of bifacial and tandem cell development, several groups have shown some interest in developing alternative back contacts using different TCOs. First results have shown that the use of TCOs as back contact is only possible for low temperature CIGS layer deposition processes; otherwise, a dramatic degradation of cells performance take place due to the increase in resistivity of the TCO layer [T. Nakada. 2005]. This increase in resistivity is commonly attributed to the formation of an intermediate Ga_2O_3 resistive layer in case of using ITO or AZO layer, and to the fluorine depletion in case of using FTO layer [T. Nakada. 2005] [M. Terheggen. 2002].

However, adding a thin molybdenum layer on the top of the TCO before the CIGS absorber layer deposition was found to prevent the formation of the Ga_2O_3 intermediate layer and to transform the rectifying contact to an ohmic contact [T. Nakada. 2004] [P.J. Rostan. 2005]: thanks to the formation of the $MoSe_2$ layer either by a direct selenization of the deposited Mo layer before CIGS deposition [D. Abou-Ras. 2005] or by classical selenization reaction during CIGS deposition [P.J. Rostan. 2005]. Based on this process, comparable efficiencies to those obtained using standard molybdenum back contact were achieved.

1.3. Substrate bending after annealing

High temperature annealing of molybdenum coated soda lime glass substrates is commonly reported leading to substrates bending.

Researchers from Saint-Gobain Glass group have investigated this phenomenon and have concluded that the inhomogeneous temperature distribution over the substrate thickness is the main cause of substrate bending [S. Jost. 2015].

According to them, the observed substrate bending (concave) can be explained as follow: the inhomogeneous temperature distribution leads to a different expansion of the coated side and the uncoated side (since the coated side is heated more than the uncoated side), which results in substrate deformation (convex shape). Then, once reaching the substrate softening point, the substrate bending disappears and the substrate gets back its normal shape (flat), thanks to the mechanical relaxation of stresses due to the viscoelasticity of the substrate. During the cooling down, a greater thermal contraction of the hotter side of the substrate would take place which results in a bended substrate with a concave shape.

However, we have to introduce a somewhat discordant note into their explanation since it excludes the possibility of getting convex substrates at the end of the cooling down and we observed such a behaviour in some of our experiments.

As a solution, they have proposed the use of a both side heating system and the deposition of an ‘’auxiliary‘’ layer on the uncoated side of the substrate in order to ensure a symmetrization of the temperature gradient along the substrate thickness. In other words, this auxiliary layer

is used to counterbalance the stress existing on both sides of the substrate. One important condition that should be taken in consideration while choosing the auxiliary layer is its chemical neutrality otherwise an additional protective layer will be needed [S. Jost. 2015].

Despite the predicted increase in production cost resulting from the use of an additional layer, the suitability of this proposed solution for the development of photovoltaic windows with controlled transparency should be questioned.

A more complete explanation of substrate bending was proposed by C. Broussillou, in which both the temperature distribution throughout the substrate thickness and the tensile stress state of the molybdenum layer (native tensile stresses resulting from the deposition technique and created during the heating up due to the different thermal coefficients) were taken in consideration [C. Broussillou. 2011].

Based on these two explanations, we were able to establish a more generalized model for substrate bending shape dependence, in case of a front side halogen lamps-based heating configuration (RTA furnace), on the stress state within the molybdenum layer (free, tensile or compressive). This model will be presented within the experimental results part.

But before that, we believe that a deep understanding of the origin of the different types of stress, as a first step, is important to get in order to find a simpler solution than the one proposed by Saint-Gobain Glass group to avoid substrate bending after the annealing process.

1.4. Different sources of stress in sputtered thin films

Visually, all sputtered thin films deposited on a given substrate are subjected to mechanical stresses. Grouped under the generic term "residual stresses", they result from the contribution of three types of stresses: thermal, intrinsic and extrinsic (not necessarily all of them at the same time).

The thermal stresses are due to the difference in the thermal expansion coefficients between the thin film and the substrate (some authors consider them as extrinsic stresses).

The intrinsic stresses are the component of stress in the thin film caused by the deposition process itself, known to be easily managed through the control of the deposition process parameters.

The extrinsic stresses result from the interaction of the thin film with its surrounding atmosphere (environment) after deposition.

1.4.1.Thermal stresses

When a film coated substrate is at a different temperature from the one used during the film deposition, a thermal stress will occur as a result of the difference in the film and substrate thermal expansion coefficients.

The film thicknesses are generally less than 10^{-4} times the substrate thickness, therefore plastic deformation of the substrate can generally be neglected and the thermal stresses induced in the thin film are given in a one-dimensional approximation [J.A. Thornton. 1989]:

$$\sigma_{th} = E_f (\alpha_f - \alpha_s)(T_s - T_a)$$

Where E_f is Young's modulus, α_f and α_s are the average coefficients of thermal expansion for the thin film and substrate, T_s is the substrate temperature used for the film deposition, and T_a is the temperature of the coated substrate under test.

Consequently, room temperature deposited thin films are thermal stress free; however, as the temperature increases, tensile or compressive stresses will take place within those.

If the thin film has a higher coefficient of thermal expansion (CTE) than the substrate, then it expands more than the substrate does, resulting in compressive stress generation in the thin film while the substrate surface will be put into tensile stress. If the thin film has a lower CTE than the substrate, then it will be put into tensile stress and the substrate surface into compressive stress.

1.4.2.Intrinsic stresses

1.4.2.1. Tensile stresses

Hoffman's "grain boundary relaxation" model is the most frequently cited to explain the origin of tensile stress within polycrystalline thin films [R.W. Hoffman. 1976]. This model is based on the consideration of the inter-atomic attractive forces between the columnar grains, inducing an elastic deformation "relaxation". This tensile stress is inversely proportional to the grains "column" size, while it increases linearly as the distance between grains "columns" increases. The validity/credibility of Hoffman's model was experimentally verified for several materials [J.A. Thornton. 1977], as well as through numerical simulations [M. Andritschky. 1993].

On the other hand, Abermann and his coworkers have shown through several experimental studies that the tensile stresses in thin films are rather related to the crystallite coalescence [R. Abermann. 1985]. To explain these observations, W.D. Nix et al. have established a model which is based on the crystallite coalescence during the initial stages of growth in polycrystalline thin films with island growth morphology. They concluded that as the growing crystallites get in contact each other at their base, the side-walls zipped together until a balance is reached between the energy associated with eliminating surface area, creating a grain boundary and straining the thin film [W.D. Nix. 1999].

It is worth to note that Nix' model is not useful for the interpretation of the induced tensile stress in sputtered molybdenum thin films after annealing process due to the high melting temperature of molybdenum, however it could be helpful for the explanation of the induced tensile stress in annealed CIGS layers (next chapter).

1.4.2.2. Compressive stresses

Intrinsic compressive stress was also observed in sputtered molybdenum thin films. The origin of this type of stress was, in the best of our knowledge, discussed for the first time by

F.M. d'Heurle in 1970 [F.M. d'Heurle. 1970]. He supposed that the origin of the compressive stresses in sputtered thin films could be attributed to the "shot-peening" action of the deposited atoms arriving at the surface of the film with considerable kinetic energy. According to d'Heurle, it is conceivable that atoms might be inserted into small interstices, which if they remained empty could cause tensile stresses, but instead cause compressive stresses.

Based on this explanation, several models quantitatively predicting the stress within the thin films as a function of the sputtered atoms energy were established.

H. Windischmann's model shows a stress dependence on the physical properties of the film ''elastic modulus and molar volume'' and the incident particles energy [H. Windischmann. 1987]. This model is based on the knock-on linear cascade theory proposed by Sigmund [P. Sigmund. 1969], and which is only valid when the following three hypotheses are verified: (i) particle energy is high enough to penetrate the surface and randomly displace atoms from their equilibrium positions through a series of primary and recoil collisions, producing a volumetric distortion, (ii) deposition temperature is low, and therefore mass transport and defect mobility is sufficiently low to freeze the volumetric distortion in place, and (iii) the relative volumetric distortion is proportional to the fractional number of atoms displaced from equilibrium sites. For more details, please refer to H. Windischmann's paper [H. Windischmann. 1987].

In fact, this model shows some limitations: (i) it is not valid if the energetic particles are lighter than the growing thin film atoms, (ii) this model does not predict any limitation for stress as the particles energy increases, while experimental results have shown that there exists a limit energy value, above which the compressive stresses do not increase any more (even decrease) [T. Yamaguchi. 1991].

To overcome these limitations, C.A. Davis has proposed a modified model. While it is still based on the knock-on linear cascade theory, it differs from H. Windischmann's model by taking in consideration the so called thermal spikes effect ''local heating induced by implanted atoms'', leading to a local modification of the microstructure and therefore a stress relaxation [K.H. Muller. 1986] [C.A. Davis. 1993]. This model offers a logical explanation of the observed limit in compressive stresses by taking in consideration the existence of a balance between implantation and relaxation processes.

1.4.3.Extrinsic stresses

Post deposition incorporation of impurities, such as oxygen, hydrogen, water vapor and carbon monoxide, is also reported as a source of stress in thin films. The mechanisms inducing such a stress are different and depend on the nature of the incorporated impurity: oxidation, lowering the grains surface energy… etc.

E.H. Hirsch has found that tensile stresses in magnesium fluoride take place after exposure to water vapor. According to him, they are originated from the electrostatic dipole interactions between the adsorbed water molecules [E.H. Hirsch. 1980].

In contrast to that, R. Abermann et al. have found that the exposure of chromium thin films to H_2O or CO environment gives rise to compressive stresses. They attribute that to the lowering

in surface tension of the metal, owing to saturation of free surface valences at the grain boundary surfaces. On the other hand, they have also found that chromium thin films exposure to H_2, CH_4 and N_2 environment does not affect their stress state, while O_2 exposure gives rise to slight compressive stresses which for extended exposure time change to tensile stresses [R. Abermann. 1984].

It is worth to note that those observations have been made on evaporated thin films; however, since the induced stresses were not attributed to the deposition technique but rather to the exposure environment and the material nature, on one hand and on the other hand, knowing that sputtered thin films show in general more porous microstructure, one can then expect similar effects or even more pronounced in case of sputtered thin films exposure to similar environments.

1.5. Partial conclusion

In the first part, we have done our best in order to give a short but complete overview on sputtered molybdenum thin films as a back contact for CIGS solar cells. The reasons behind choosing such a back contact material and deposition technique were discussed. Then a particular interest have been addressed to the commonly reported substrate bending issue: the proposed explanations and the found solution have been reviewed. Finally, we have concluded this first part by reviewing on the origins of stresses within sputtered thin films, since they are believed to be the main cause of substrate bending.

In the next part, we will mainly show our innovative/original solution for overcoming the substrate bending issue: starting by proposing a model and then presenting the experimental results.

Part B: Experimental results

1.6. Background and problematic

After the fabrication of a first set of samples, using Scofield's bilayer structure [J.H. Scofield. 1995] and checking out the adhesion of the deposited thin films to the substrate (scotch test), mainly two issues have been found: wrinkles at the molybdenum/substrate interface and substrate bending once annealed.

Wrinkles at the interface were found to be originated from particles bombardment of the glass substrate surface either during argon plasma etching (further cleaning of the substrate before molybdenum deposition) or during the first stage of the molybdenum thin film deposition.

Therefore, this issue was simply overcome by both avoiding the use of the plasma etching step and using a low sputtering power for the deposition of the first 20-30nm of the molybdenum thin film (as a protection layer).

In a second time, finding a simple solution for substrate bending was our priority. Therefore and as a first step, molybdenum deposition conditions effect, mainly sputtering power and pressure, was intensively investigated (power and pressure were tuned from very low to very high).

Unfortunately, all our attempts were in vain and in the best cases reduced bending was achieved. ''*We should never give up, failure does not mean impossible'', that is our principle.*

1.7. Proposed model explaining substrate bending

In the following, we will try to explain, through the schematic sketches presented in figure 1.1, the possible scenarios that might occur during and after the annealing of different stress state molybdenum thin films in a front side halogen lamp-based annealing configuration (Rapid Thermal Annealing –RTA- equipment).

- ✓ First of all, one should point out that the initial stress state (σ_i) of the sputtered molybdenum thin films can be different from zero (internal or external stresses can be present) ($\sigma_i > 0$: tensile stress, $\sigma_i < 0$: compressive stress) (1);
- ✓ The inhomogeneous temperature distribution throughout the substrate thickness, resulted from the use of such an annealing configuration should be taken in consideration (2);
- ✓ Because the molybdenum layer has a lower expansion coefficient than the substrate, the substrate surface is within compressive stress while the stress state within the molybdenum layer is changed by adding the contribution of the thermal component (σ_{th}) (2);
- ✓ Up to the softening temperature ($T_{softening}$), the system (substrate and thin film) expansion is, intuitively, expected to be governed by the substrate because that the film thickness is less than 10^{-4} times the substrate thickness (3);

- ✓ One consequence of the inhomogeneity in temperature distribution throughout the substrate thickness is the different expansions of the top and the bottom of the substrate (3);
- ✓ At high temperature, this difference in expansion between the top and the bottom of the substrate is expected to induce a substrate deformation (4);
- ✓ Once reaching the softening temperature, the substrate changes its nature from rigid to viscous fluid-like and therefore the implied forces by molybdenum layer become dominant.
- ✓ At this stage, the molybdenum layer releases its stresses (the initial stresses plus the induced stresses during the heating up ‘’thermal stresses‘’), leading to a substrate deformation (bending);
- ✓ The shape of the induced deformation (bending) depends on both the nature and the intensity of the released stresses (5), (7) & (9);
- ✓ In case that the initial stresses within the molybdenum layer are tensile ($\sigma>0$), then both initial and induced (thermal) stresses will pull on the substrate resulting in highly bended substrate with a concave-shape (5);
- ✓ Similarly, stress free molybdenum layer should results in concave shape bended substrate. In this case, only the thermal component of stress will act and consequently less pronounced bending is expected (7);
- ✓ The greater thermal contraction of the hotter side of the substrate during the cooling down will results in a more pronounced concave shape (6) (8);
- ✓ On the contrary, molybdenum layer with highly compressive initial stresses (higher than the induced thermal component) is expected to result in a more pronounced convex shape bending after stresses relaxation (9);
- ✓ Depends on the initial compressive stresses intensity and the annealing temperature, flat or less pronounced convex samples are achievable once cooling down (10) (11);

As a conclusion, flat substrate after annealing process can be achieved by simply using as-deposited molybdenum thin films in adequate compressive stresses. This conclusion can explain the obtained reduction in substrate bending using high sputtering power at low deposition pressure.

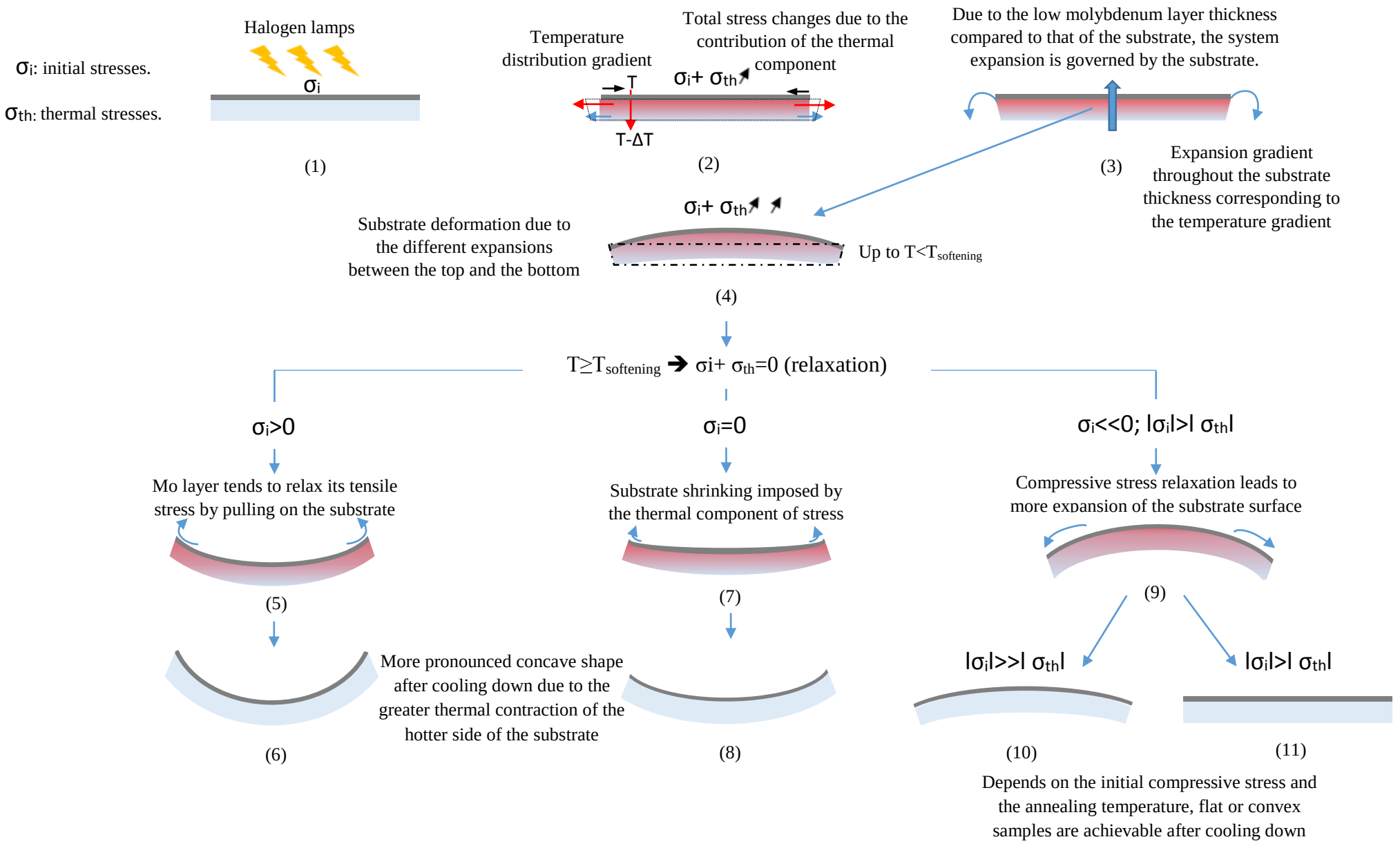

Figure 1.1: Schematic sketches representing the possible scenarios that might occur during and after the annealing of different stress state molybdenum thin films in a front side halogen lamps-based configuration.

1.8. Annealing of air stocked molybdenum thin films

The annealing of air stocked molybdenum thin films for more than six months (they have been used as sacrifice samples) during the recalibration of the annealing furnace has led to a surprising result.

These samples were supposed to have a concave shape once annealed (previously observed on annealed samples from the same fabrication run); however, a convex shape was obtained!!! *At that time, we had no idea about the effect of the surrounding atmosphere on the stress state of the thin films, summarized in section 1.4.3.*

Based on that and as a first reflection, an accelerated aging process (low temperature annealing either under air environment or O_2 gas) was investigated: unfortunately, the obtained results were disappointing.

Possible explanations: either oxygen was not at the origin of the changed properties of the aged molybdenum layers or the accelerated aging process led to the formation of an oxide layer at the surface preventing the diffusion of oxygen into the grain boundaries.

Whatever was the reason, the accelerated aging process did not work.

1.9. Reactively sputtered Mo(O) thin films

Our persistence in finding a solution for the substrate bending issue has conducted us to the investigation of enforced oxygen incorporation into the sputtered molybdenum layer using a reactive process.

The obtained results were more than surprising: we were able to change the bending shape simply by tuning the oxygen flux during the sputtering process. The first obtained set of samples is presented in figure 1.2.

As can be seen, the concave bending radius was found to increase when an oxygen flux of 0.4sccm is used, while an oxygen flux of 0.5sccm was found to be sufficient to change the bending shape from concave to very slightly convex. Furthermore, a more pronounced convex bending was observed for an oxygen flux of 0.6sccm, while higher oxygen flux led to a reduced convex bending.

Unfortunately, the precise control of the oxygen flux in order to achieve a perfect flatness of the substrate was not possible since the minimum tuning step is 0.1 sccm (precision limit of our sputtering equipment).

We should never give up!! An alternative solution to overcome this limitation was found and a perfect flatness of the substrate was achieved. But before presenting this solution, we first present some analyses we have performed to understand the origin of the observed bending changes as a function of oxygen flux.

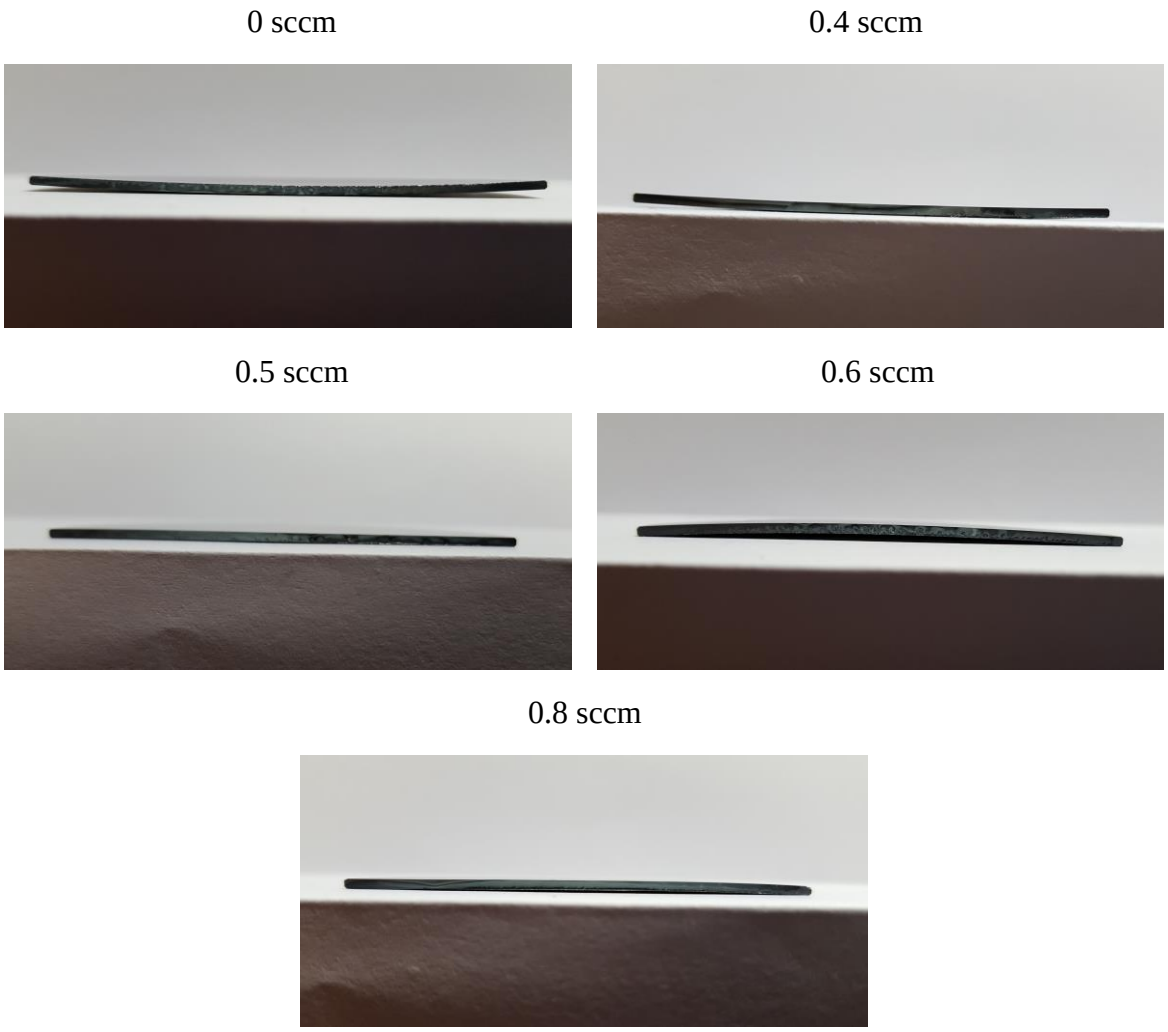

Figure 1.2: Photographs showing the change in bending shape after annealing of reactively sputtered molybdenum thin films on glass substrates as a function of oxygen gas flux.

The SEM surface and the corresponding cross sectional images of the reactively sputtered molybdenum thin films using different oxygen flux are presented in figure 1.3. As can be clearly seen, molybdenum thin films microstructure was found to be highly affected by the presence of oxygen during the deposition process. The thin films morphology was found to gradually change from regular grains surface with well-defined edges (for oxygen-free process) to grinded grains surface (for oxygen flux of 0.6sccm). Correspondingly, the cross sectional feature was found to have a gradual change from clear columnar structure to fibrous structure.

This change in the microstructure can be simply explained by the knock-on linear cascade theory [P. Sigmund. 1969]: high energy particles penetrate the surface and randomly displace atoms from their equilibrium positions through a series of primary and recoil collisions, producing a volumetric distortion.

Consequently, and based on Davies' model, previously reviewed in section 1.4.2.2, the stress state within the as deposited molybdenum layer is expected to change from tensile to highly compressive. Therefore, applying our model for substrate bending shape dependence on the

initial stress state within the molybdenum layer, one can find out the perfect coherence between the observed change in the bending shape and the found change in microstructure.

For higher oxygen flux (0.8sccm), the cross sectional feature and therefore the surface morphology have shown some improvement. This is most likely related to the local heating induced by implanted oxygen atoms (thermal spikes effect), leading to a local modification of the microstructure and therefore balancing, in part, the induced damage. This might explain the reduced compressive stress, and therefore, the increase in bending radius after annealing.

On the other hand, XRD analyses, presented in figure 1.4, reveal a decrease in the (110) peak intensity with a shift towards lower diffraction angles as the oxygen flux increase. These observations evidence the crystalline quality deterioration and the change of the stress state, which is in a good consistent with the previous SEM results.

Furthermore, no crystalline oxide phases such as MoO_2, MoO_3 and Mo_2O_5, were observed; however, that does not mean they are completely absent since they might exist in an amorphous state [T. Yamaguchi. 1991].

Finally, it is of high importance to note that previously reported defects as a consequence of high compressive stresses [J. Tranchant. 2007] were not observed neither before nor after the annealing process.

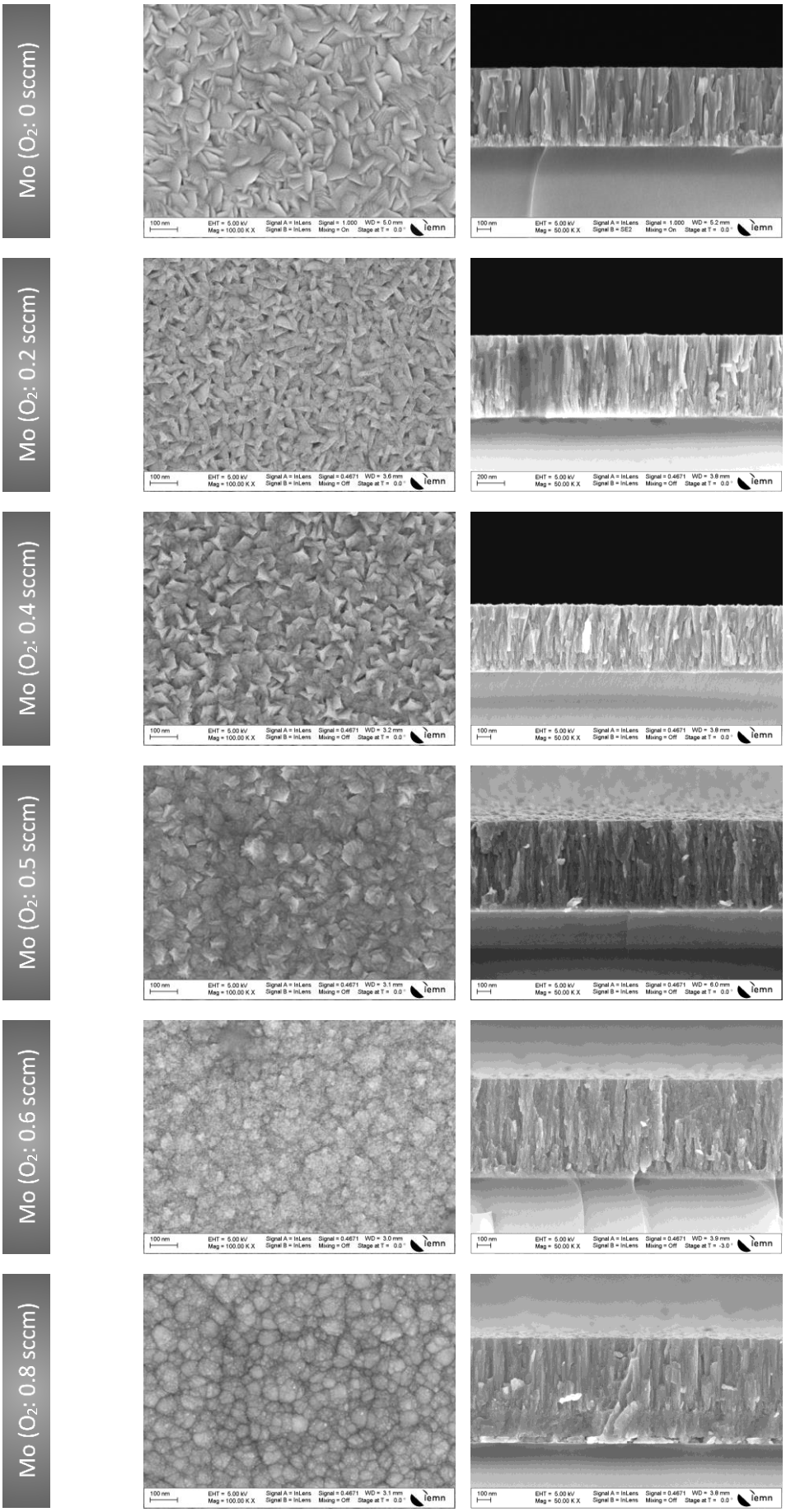

Figure 1.3: SEM surface (on the left) and cross sectional (on the right) images of sputtered molybdenum layer at different oxygen flux and annealed at 540°C under N_2H_2.

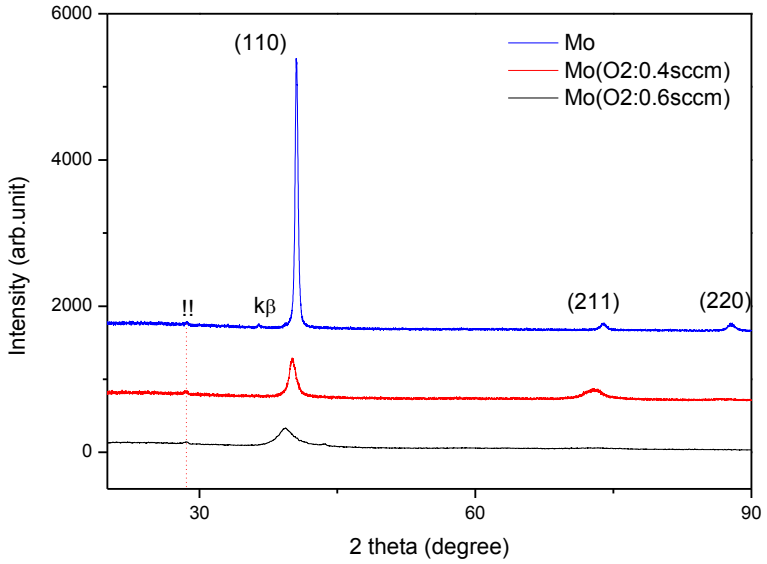

Figure 1.4: XRD patterns of Mo and reactively sputtered Mo(O) thin films after annealing at 540°C under N_2H_2.

1.10. Mo(O)/Mo bilayer structure for a perfect flatness of substrates

Because of the faced difficulty in precisely controlling the oxygen flux, an alternative solution was investigated. This is based on counterbalancing the high intensity compressive stress by the deposition of a tensely stressed top layer. Consequently, the total stress of the structure is easily and more precisely controlled by varying the tensely stressed layer to the compressively stressed layer thickness ratio.

Furthermore, using this bilayer structure for controlling substrate bending has in fact two additional advantages compared to a single Mo(O) layer: (i) avoiding Ga_2O_3 formation at the interface with the CIGS layer, (ii) avoiding any series resistance related issues (once integrated in cell fabrication process) due to the observed increase in resistivity of the Mo(O) thin films, as shown in figure 1.5.

The elemental distribution throughout the bilayer structure depth was investigated and the obtained SIMS profiles are given in figure 1.6. The SIMS depth profile of oxygen in a single molybdenum layer is also shown as a reference background signal. It is important to note that these analyses have been performed on a complete solar cell structure, and therefore, the elemental profiles are obtained after annealing.

As can be seen, the oxygen signal clearly evidences the presence of two layers: Mo and Mo(O). Furthermore, the non-abrupt cut-off in oxygen signal is attributed to the target contamination: the Mo top layer was immediately deposited and no target cleaning was then performed between the Mo(O) and Mo layer deposition steps.

On the other hand, the fact that oxygen signal shows a non-zero level within the top molybdenum layer and a slight increase at the interface Mo/CIGS might indicate the oxygen diffusion from the Mo(O) bottom layer to the Mo top layer due to the annealing process.

Therefore, a deep investigation of the Mo/CIGS interface seems to be necessary in order to check out whether Ga_2O_3 is formed or not. If it is the case, adding a buried oxygen-diffusion barrier within the bilayer structure can be used as a solution.

Finally, the abrupt change in molybdenum signal at the Mo/Mo(O) interface is believed to be related to the different sputtering rates due to the different matrix structures.

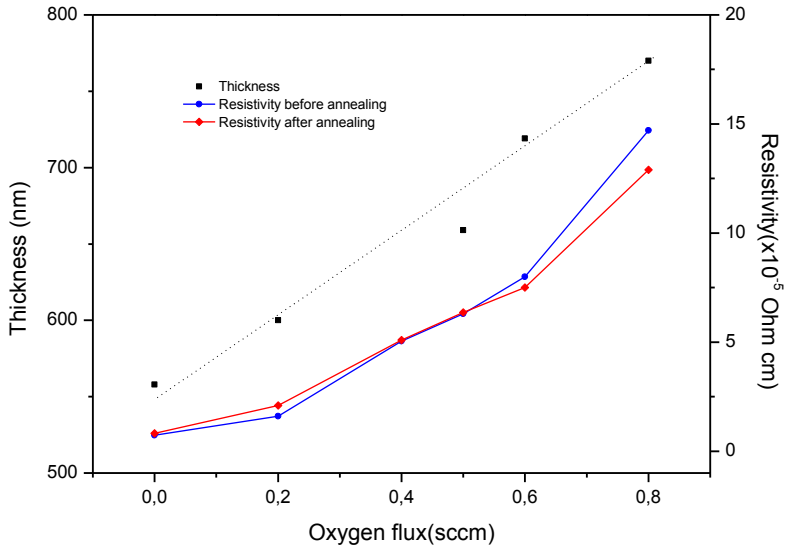

Figure 1.5: Variation of molybdenum thin film thickness and resistivity as a function of oxygen flux.

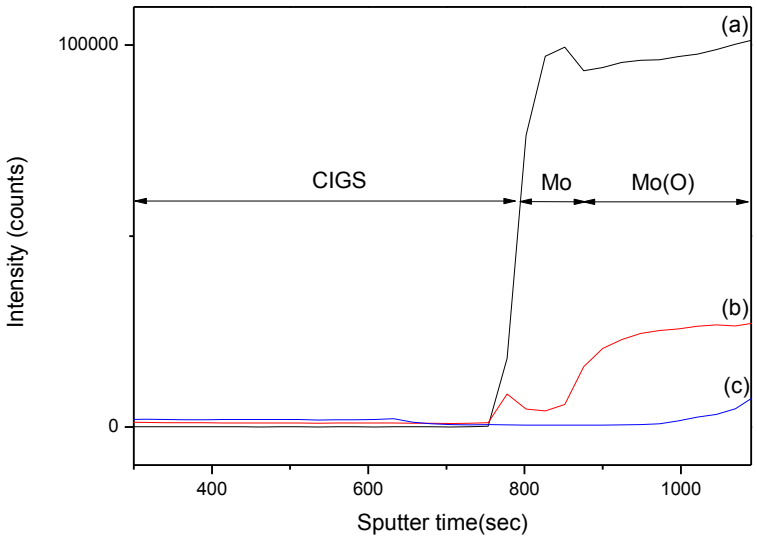

Figure 1.6: (a) and (b) SIMS depth profiles of molybdenum and oxygen in a Mo/Mo(O) bilayer structure. (c) SIMS depth profiles of oxygen in a single molybdenum layer.

1.11. Chapter conclusion

Based on previous explanations of substrate bending proposed by S. Jost and J. Palm, and by C. Broussillou, we have proposed a more generalized model showing the dependence of the substrate bending on the initial stress within the molybdenum layer. We have concluded that flat substrates are achievable by simply adjusting the compressive stresses within the molybdenum thin films.

Experimentally talking, with some chance and a lot of persistence, an original method for substrate bending management was found. Comparing to that previously patented by S. Jost and J. Palm, our proposed process has the superiority of simplicity and low cost since it does not require the deposition of additional layers on the back surface and it is based on the use of one side heating configuration.

The observed change in reactively sputtered molybdenum thin films microstructure and therefore the stress state, on one hand and on the other hand, the corresponding bending shape, were found to be in an excellent coherence with our proposed model for bending dependence on the stress state.

For a better control of the initial stress intensity and in order to avoid any undesirable effect on cell performance, Mo/Mo(O) bilayer structure was investigated. The obtained results have shown that it is easier to control the substrate flatness by tuning the top to the bottom layer thickness ratio than by tuning oxygen flux.

Finally, using this process for substrate bending management is very useful especially for the development of room temperature deposited CIGS thin films followed by an annealing step

where the recrystallization of the CIGS thin films is found to contribute, in part, into the final substrate bending.

Chapter 2: Absorber layer

This chapter is devoted to the development of an original deposition process: low cost, easily up scalable and environmentally friendly.

We will first start by giving a detailed overview on already obtained results, discussing their advantages and drawbacks. We will also try to find a logical correlation between the obtained results from different laboratories and/or give an interpretation for the divergent points of view and the confusing points.

In a second part, we will first start with a quick review on the already obtained results within our group: the solved issues and those still to be resolved. Starting with this, we aim to give a background which justifies our working approaches. Then we will present our contribution and highlight the possible approaches for further improvement.

Part A. State of the art

2.1. CIGS material

Historically, the first chalcopyrite solar cells were based on CIS material. However, the need for higher band gap material, in order to satisfy the modified Shockley-Queisser limit for high efficiency simple p-n junction solar cells [C.H. Henry. 1980], requires the use of a modified chalcopyrite material. It was found that partial replacement of indium in CIS by either gallium or aluminum leads to higher efficiency [S. Marsillac. 2002]; nevertheless, the safety issues related to the use of aluminum makes the use of gallium more favorable [S. Karthikeyan.2014].

In the following, we give a brief presentation of CIGS material properties:

2.1.1.Structural properties

From the crystallographic point of view, the chalcogenide structure, which is the required one for photovoltaic application, is based on two overlapped anion and cation sublattices with face-centered tetragonal structure: the cations (Cu, In, Ga) and the anion (Se) occupy the unit cell sites and half of the tetrahedral sites, respectively. According to L. Ribeaucourt, the chalcogenide structure differs from other possible structures of CIGS material by the regularly ordered distribution of cations within the same xy plane [L. Ribeaucourt. 2011].

Furthermore, it is widely reported that the linear variation of the unit cell parameters as a function of Ga/In ratio is verified (Vegard's low).

On the other hand, the phase diagram highlights the existence of a tight region for single chalcopyrite phase corresponding to a copper concentration around 24%; otherwise, multi-phase material will be obtained [N. H. Quang. 2004].

2.1.2.Optoelectronic properties

As mentioned above, the reason behind alloying Ga to CIS is to obtain an optimum band gap (higher than that of CIS). Other than the increase in band gap value as a function of Ga concentration, it was found that this increase is only related to the shift of the conduction band towards higher energies, while the valence band energy remains constant [S. Sharbati.2014]. The dependence of the band-gap energy on Ga concentration is commonly expressed as follow:

$$Eg = (1 - x)\, Eg^{CIS} + x\, Eg^{CGS} - b x (1 - x)$$

Where Eg^{CIS} is the band gap of CIS ($0.94eV \leq Eg^{CIS} \leq 1.04eV$), Eg^{CGS} is the band gap of CGS ($1.65eV \leq Eg^{CGS} \leq 1.7eV$) and b is the bowing parameter ($0 \leq b \leq 0.3$) (see [F. Pianezzi.t. 2014] and references therein).

Moreover, it was proved that the presence of a minimum concentration of Ga leads to low defect concentrations and therefore reduces recombination losses [G. Hanna.2001].

In parallel to that, it was found that sulfur might also lead to an increase in band gap energy; however, in this case, the conduction band remains constant while the valence band shifts to lower energies as sulfur concentration increases [T. Kobayashi. 2015].

In the same context, it is widely accepted that Cu vacancies are the main origin of the p-type nature while Se vacancies and Ga or In on Cu antisite defects are considered as compensating donors [F. Pianezzi.t. 2014].

Other important properties of CIGS material, as an absorber for thin films solar cells, are its direct band gap nature and its high absorption coefficient (about 10^5 cm^{-1}), which might explain the low thickness needed for light absorption [D. Rudmann.t. 2004].

2.2. Deposition techniques

Knowing that CIGS material for solar cells application is a subject of interest since the seventies, one should not be surprised by the number of developed deposition techniques. In general, they are classified in two categories: vacuum and non-vacuum techniques. Among the non-vacuum techniques, electrodeposition is the one that showed competitive efficiencies, both on laboratory (17%) and industry (14.9%) levels [Nexcis]. Despite the fact that this technique has several advantages such as: low cost, simplicity, ease in upscaling on large surfaces and others, one should worry about the waste recycling and the amount of needed chemical products.

On the other hand, high efficiency solar cells are commonly obtained using the so called vacuum processes. Recently, efficiencies as high as 22.6% [ZSW] and 22.8% [T. Kato. 2016] were obtained using co-evaporation and sputtering processes, respectively.

In the following, we will briefly present the different co-evaporation techniques, while the sputtering techniques will be presented in detail in an independent part.

2.2.1.One stage evaporation process

It consists of the simultaneous evaporation of all elements (Cu, In, Ga and Se) at constant evaporation rates and substrate temperature, throughout the whole process. The evaporation rates should be adjusted in order to get a final composition that is slightly Cu-poor. As far as we know, the highest efficiency achieved using this process is about 16.3% (without anti-reflection layer) [P-M-P. Salomé. 2015].

2.2.2.Two stages evaporation process

The main difference compared to the one stage process is the transition from Cu rich conditions in the first stage to Cu poor in the second, by changing the evaporation rates of metallic elements at the end of the first stage. It has to be noted that the Se evaporation rate is kept constant throughout the whole process while the substrate temperature is changed from 400°C in the first stage to 550°C in the second (for more details, see [D. Rudmann.t. 2004] and references therein).

2.2.3.Three stages evaporation process

In the contrary to the previously described processes, in the three stages process neither evaporation rates nor substrate temperature are constants throughout the whole process.

In the first stage, ln, Ga and Se are simultaneously evaporated at a relatively low substrate temperature (around 350°C). During the second stage, only Cu and Se are evaporated, at higher temperature (around 550°C), until the film becomes slightly Cu rich. Keeping the temperature constant, In, Ga and Se are again evaporated in the third stage to form the slightly Cu poor CIGS layer.

This process offer the possibility of changing the elemental depth profile, which is proved to enhance cells efficiencies (to be discussed in the gap grading section).

Recently, efficiency as high as 22.6% was achieved using this process [ZSW].

2.3. Sputtering process

In contrary to the evaporation technology, sputtering from either alloys or metallic targets is considered as a promising technique, since it leads to good deposits uniformity over large surfaces and high deposition rate, while keeping a low fabrication cost.

Over years, several sputtering processes have been developed. From one process to another the type of targets, the deposition temperature, the post deposition annealing atmosphere ... etc, might change.

In the following, we present an overview on the sputtering processes that have already led to functional solar cells:

2.3.1.Sputtering from multi targets

In this process, separate targets are used as a metallic elements source, while Se (or Se excess) is introduced by different ways:

The so called two steps process which is based on the selenization at high temperature of sputtered CuInGa precursor using H_2Se gas, is known to be the most efficient one. Using this process, researchers from Solar Frontier Company have recently announced a new record of 22.8% on laboratory cells [T. Kato. 2016]. However, other than the use of an additional sulfurization step, no further details on the used process are published!!

On the other hand, J. Schulte et al. have reported on the possibility of using reactive sputtering at high deposition temperature for the formation of CIGS layer in a single step process. To do so, H_2Se was used as a reactive gas. They have proved that good crystalline quality and single chalcopyrite phase are achievable if a sufficiently high H_2Se gas and substrate temperature are used. Using this process, efficiency as high as 14.3% was obtained [J. Schulte. 2015].

In order to find an alternative way for selenization, other than using H_2Se toxic gas, some groups have studied the rapid thermal annealing of a Se layer deposited on the top of a CuInGa precursor sputtered from two targets [Z-H. Li. 2013] [W-T. Lin. 2014]. To the best of our knowledge, the highest efficiency obtained using this process without and with an additional

sulfurization step is about 8.2% [Z-H. Li. 2013] and 12.7% [S-S. Kulkarni. 2009], respectively. Furthermore, X.L. Zhu et al. have reported an efficiency of 13.6% using Se pellet instead of H_2Se gas [X.L. Zhu. 2013]. Unluckily, both techniques have led to relatively low efficiency compared to that obtained using H_2Se gas.

2.3.2.Sputtering from ternary target

It consists of the selenization of CuInGa precursor sputtered from a ternary target. Among the advantages of this process, one might note the simplicity and the high in-plane elemental distribution homogeneity; nevertheless, it is commonly reported that this process suffers from Ga accumulation towards the back contact [H.R. Hsu. 2012] [K.H. Liao. 2013]. According to K.H. Liao et al., this back segregation of Ga is believed to be originated from the difference in the chemical affinities between Se and In and between Se and Ga [K.H. Liao. 2013]. As a consequence, low open circuit voltage is commonly observed.

To the best of our knowledge, the highest efficiency obtained using this process is about 6.3% [H.R. Hsu. 2012].

2.3.3.Sputtering from quaternary target

It is interesting to note that the properties of CIGS thin films sputtered from a quaternary target were first studied in the early 90s [J.L.H. Rojas. 1992] [J.L.H. Rojas. 1993] [T. Yamaguchi. 1992]; however, no solar cells were prepared at that time. In the recent years, a sharp orientation towards the development of solar cells using this process, mainly for industrial reason, has taken place.

Even though the huge number of groups working on this subject, only few of them were able to success in fabricating solar cells. In table 2.1, we summarize all published works reporting on solar cells fabricated using this process.

Following a selenization free process, some groups have showed efficiencies up to 10.6% using RF-sputtered absorbers. Other groups have reported comparable efficiencies using the pulsed-DC mode.

The main reason behind the tendency to the substitution of the RF mode by a pulsed-DC one is believed to be related to the considerable reduction in cost, which is very important from the manufacturing point of view. However, all of them use high temperature deposition process which is considered as a drawback for an in-line processing.

On the other hand, L. Ouyang et al. have reached an efficiency of 16.7% using an additional selenization step [L. Ouyang. 2015] which is, in fact, in contradiction with the main purpose for developing this process (avoiding the use of an additional Se supply).

Target type	Sputtering mode	Deposition temperature		Additional Se source			KCN surface treatment	Buffer layer		Efficiency %	year	Reference
		RT	HT	Selenization		sputtering		CdS	ZnS			
				gas	Se vapor							
Quaternary target	Middle frequency MF	?	?	-	x	-	?	x	-	9.6	2013	[J. Liu. 2013]
		-	x	-	x	-	?	x	-	8.6	2014	[L. Ouyang.2014]
	Radio-frequency RF	-	x	-	-	-	?	-	RF	3.6	2014	[J.XIANG. 2014]
		-	x	-	-	-	?	x	-	8.9	2011	[J.A. Frantz. 2011]
		-	x	-	-	-	?	x	-	9.9	2011	[J.A. Frantz2. 2011]
		-	x	-	-	-	?	x	-	1.2	2014	[G.X. Liang. 2014]
		-	x	-	-	-	-	x	-	10.6	2012 2014	[J.A. Frantz. 2012] [J.D. Myers. 2014]
		?	?	-	x	-	?	x	-	10.8	2013 2012	[X.L. Zhu. 2013] [X. Zhu. 2012]
		x	-	-	x	-	?	x	-	7.9 !!!	2011	[J. H. Shi. 2011]
	DC !!	x	-	x	-	-	?		-	16.7	2015	[L. Ouyang. 2015]
	Pulsed DC	-	x	-	-	-	x	x	-	10.1	2012	[C.H. Chen. 2012]
		-	x	-	-	-	x	x	-	8	2011	[C.H. Chen. 2011]
		-	x	-	-	-	?	x	-	4.4	2013	[Y.S. Su. 2013]
				?	?	?				6.7		
		-	x	-	-	-	x	x	-	8.2	2013	[C.H Chen. 2013]
		-	x	-	-	-	?	x	-	8.9	2011	[Y.S. Su. 2011]
		-	x	-	-	-	x	x	-	5.8	2014	[J.D. Myers. 2014]
		-	x	-	-	x	?	x	-	11	2015	[C.H. Hsu. 2015]
		-	x	-	-	-	?	x	-	11	2015	[C.H. Hsu2. 2015]
		-	x	-	-	x+Ga	?	x	-	12.5	2015	[T.Y. Lin. 2015]
		-	x	-	-	-	x	x	-	3.1	2013	[Y.C. Wang. 2013]
							x+Ar etching	x	-	5.2		

(x): Yes; (-): No; (?): not mentioned

Table 2.1: Overview on CIGS based solar cells achieved by sputtering from single quaternary target.

2.4. CIGS orientation

2.4.1.Origins of preferential orientation

From the energy point of view, first-principles calculations on chalcopyrite structure reveal that the nonpolar (110) surface is more stable than the polar one (112); nevertheless, the introduction of defects, such as Cu vacancies (V_{Cu}) in Cu-poor conditions, and/or Cu-on-In anti-site defects (Cu_{In}) in In-poor conditions, makes the (112) polar plane lower in energy than the nonpolar plane [J.E. Jaffe. 2001].

From the practical side, the deposition parameters, the Na concentration and the Mo surface density have been considered to be the most likely origins of the preferred orientation of the CIGS layer:

* Using the three stage process, S. Chaisitsak et al. [S. Chaisitsak. 2002] have investigated the effects of the deposition parameters on the orientation of the final layer. They have resulted to the following conclusions: (i) the growth of (112)-oriented and (220)-oriented CIGS films are closely related to the (006)-orientation and (300)-orientation of the precursors at the first stage, respectively, (ii) the orientation of the $(InGa)_2Se_3$ precursor itself depends on Se flux

during the deposition, (iii) highly (300)-oriented $(InGa)_2Se_3$ precursor is not necessary, but its existence is required for obtaining CIGS films with (220) preferred orientation, (iv) the increase of the substrate temperature has the same effect as decreasing the Se flux due to the Se sticking coefficient decrease with increasing substrate temperature.

* M.A. Contreras et al. [M.A. Contreras. 2000] have, in an early time, observed a similar relationship between the orientation of the In_2Se_3 precursor and that of the CIS films. Their explanation of this relationship was based on the symmetry between the orientation of the In_2Se_3 and CIS phases. Also, they highlighted the effect of Na concentration on CIS films orientation: the (220) orientation is obtainable for low Na concentration, while higher Na concentration lead to the (112) orientation. They concluded that Na lowers the surface energy of CIS during nucleation and growth, leading to the most stable and favorable (112) preferred orientation.

* In a recent work, D.H. Shin et al. [D-H. Shin. 2012] have found that the orientation of CIGS films depends rather on that of the $MoSe_2$ layer which itself depends on the Mo surface.

* In a more recent work, J.H. Yoon et al. have combined the effect of Na concentration and that of Mo surface density on CIGS layer orientation [J-H. Yoon. 2014]. They have concluded that a highly dense Mo surface does not strongly force the CIGS film to grow with any specific orientation. In this case, a high concentration of Na tends to enhance the development of the (112) orientation, while a lower one leads to a randomly oriented CIGS films. On the other hand, they have found that such a Na effect is negligible in the case of high pressure deposited Mo surface and the ability of the porous Mo surface to force the (220) orientation is much stronger.

It is important to note that all the previous investigations on the origin of the preferential orientation of a CIGS layer were performed using the three stage process. In the case of sputtering from quaternary target at room temperature one might expect similar relationships between the Mo surface density, the Na concentration and the CIGS orientation, to that given by J.H. Yoon et al.: high dependence on the molybdenum surface density, while sodium concentration might only play a decisive role in case of using dense molybdenum surface.

2.4.2.Effect of preferential orientation on cells performance

Many works have shown an enhancement in cells characteristics once the CIGS preferential orientation changes from (112) to (220)/(204). Such an enhancement is commonly attributed to the better p-n junction quality. It was found that Cd atoms, issued from the CdS buffer layer, show higher diffusivity into (220)/(204)-oriented CIGS layers than into the (112)-oriented layers. This is due to the fact that the (220)/(204) planes are characterized with a much more open structure as compared to the (112) planes [D-H. Shin. 2012] [J-H. Yoon. 2014] [S. Chaisitsak. 2002] [M.A. Contreras. 1999].

On the other hand, W. Witte et al. have found that the deposition of a very thin buffer layer (CBD: CdS or ZnOS) on a (112)-oriented CIGS layer results in a sparsely covered surface; whereas, a very dense coverage of a (220)-oriented CIGS layer was observed for the same buffer layer thickness [W. Witte. 2013].

2.5. Impurities effect

2.5.1.Metallic elements effect

It was largely reported that metallic impurities incorporated in the CIGS layer affect in a negative way the functionality of the solar cells. Because of the high purity of evaporated elements, it was thought that these impurities might be incorporated in the absorber layer by diffusion, either from the bottom layer (the Mo layer and/or the substrate which is the most likely source) or from the top layer (the buffer layer: during deposition or after heat treatment).

As the early developments of CIGS solar cells have been carried out using SLG substrates, such a problem was not addressed until the day researchers started developing solar cells on stainless steel foils. Among the elements composing the stainless steel foils one can note Fe, Cr and Ni.

F. Pianezzi et al. have reported on the effects of both Cr and Ni on cells characteristics. They showed a decrease in cells efficiency from 17.2% to 9.8% when only 0.4 at% of Cr is incorporated in the CIGS layer. They also reported on a dramatic decrease in efficiency (from 17.2% to 2.6%) when almost the same quantity of Ni, as compared to that of Cr (0.4at %), was incorporated [F. Pianezzi. 2015]. The same group has previously reported on the effect of Fe impurity, and a decrease in efficiency from 13.4% to 9.0 % was observed [F. Pianezzi. 2012].

The relationship between the incorporated Fe concentration and the cells efficiency was studied by at least two groups: T. Eisenbarth et al [T. Eisenbarth. 2012] and R. Wuerz et al [R. Wuerz. 2014]. Both of them have shown that even a small concentration of Fe, in the range a few hundred of ppm, might dramatically affect the efficiency of the solar cells.

Using the admittance spectroscopy, F. Pianezzi et al. have attributed the degradation of cells characteristics to the introduction of deep defect levels in the absorber: the Cr impurities show a deep defect level with an activation energy E_A above 500 meV, the Ni impurities show two defect levels with E_A *at* 310 meV and 500 meV, while a deep defect level at around 320 meV was observed for the Fe impurities [F. Pianezzi. 2015] [F. Pianezzi. 2012].

2.5.2.Sodium effect

It is well known that Na might affect structural properties of CIGS layers, both grain size and orientation; nevertheless, the way it affects is still a subject of debate (rather, a confusing subject) since one might find inconsistent results.

Several groups have reported an increase in CIGS grains size in case that sodium is either out diffused from the SLG substrate or incorporated from alternative Na sources [K. Granath. 2000] [Q. Guo. 2013] [M. B. Ard. 2000] [J. Eid. 2015]. In conjunction to that, other groups have observed a decrease in grains size as far as Na is present during the CIGS layer growth [D. Rudmann. 2003] [D. Rudmann. 2004] [J. H. Yun. 2007] [S. Ishizuka. 2009] [V. Izquierdo-Roca. 2011].

That leads to the conclusion that the effect of Na on grains size is rather, in somehow, related to the growth conditions. It was also reported that Na during the layer growth limits metals inter-diffusion which leads to a strange GGI (Ga/Ga+In) profile [D. Rudmann. 2003].

In contrast to the ambiguous effect of Na on the grains size, everyone agrees with its effect in improving CIGS electrical properties, regardless of its incorporation process: before, during or after the CIGS layer growth. It is largely reported that Na plays an important role in improving cells efficiency through the passivation of defects at the CIGS grain boundaries: (i) elimination of compensating In_{Cu} donor defects, (ii) formation of acceptor-like Na_{In} defects, and (iii) neutralization of Se vacancies and In dangling bonds donor defects [D. Rudmann.t. 2004] [S. Ishizuka. 2009].

Finally, it is interesting to note the stimulating effect of Na on the formation of $MoSe_2$ interfacial layer, which might directly influence the nature of the electrical contact between the CIGS absorber layer and the Mo back contact layer [P.J. Rostan. 2005].

2.5.3.Potassium effect

By the end of 2008, CIGS based solar cells have already reached a record efficiency of almost 20% [I. Repins. 2008]. Since that time and over more than five years, scientific community has faced some difficulties to further improve cells efficiency. In the recent years, a remarkable leap in cells efficiency has taken place: thanks to the introduction of potassium element.

Perusing in previously published papers, one might find out that the effect of potassium on CIGS solar cells characteristics was already studied in an earlier time: Contreras et al. have replaced the naturally out diffused potassium from the soda lime glass substrate using a thin KF layer on the top of the Mo layer. They concluded that potassium plays the same role as sodium does in passivating defects but not at the same level because of the lower potassium diffusivity in CIGS (larger atomic radius) [M.A. Contreras. 1997].

In a more recent work, researchers have confirmed that the incorporation of potassium directly in the CIGS bulk during the layer growth leads, in the best case, to a similar efficiency compared to that of the reference cell [F. Pianezzi. 2013], even though the GGI profile is stronger due to the effect of potassium on the metals inter-diffusion [A. Laemmle. 2015].

In fact, the novelty is rather in the way that potassium is incorporated and in the way it reacts with the CIGS layer. For the first time, Chirila et al. have found that a post deposition of few nanometers of KF (15 nm) on the top of CIGS layer results in copper and gallium depletion, limited to the near surface (about 30 nm below the surface), while a considerable amount of potassium is incorporated. Copper depletion is thought to be a consequence of an electrochemically induced migration towards the bulk, while potassium incorporation is believed to be a result of partial ion exchange of Na with K within the CIGS layer. Using this post deposition treatment, they were able to reach, for the first time, an efficiency of 20.4%: even though a thinner CdS buffer layer was used, a better p-n junction quality was obtained. They attributed that to the surface modification which facilitates Cd diffusion in the Cu depleted surface [A. Chirila. 2013].

From the same group, F. Pianezzi et al. have showed that the improvement in cells characteristics should not be attributed only to the increase in holes concentration resulted from potassium passivation of defects at the grain boundaries [F. Pianezzi. 2014]. Calculating the activation energies, they concluded that the recombination at the interface CdS/CIGS is not

any more possible in K-PDT (post-deposition treatment) devices even if a thin CdS layer is used which is not the case in K-PDT free devices. According to the authors, a strong electronic inversion of the CIGS surface (from p to n type), due to the high density of Cd_{Cu} shallow donner defects, is highly believed to be at the origin of the suppression of recombination at the interface.

As another consequence of the copper depletion, a lowering in the valence band energy by about 0.4eV, was observed by Pistor et al., leading to an increase of the open circuit voltage of 60–70mV compared to the untreated absorber [P. Pistor. 2014].

T. Lepetit et al. have investigated the effect of K-PDT on two types of CIGS layers. They found out that the presence of the OVC (ordered vacancy compound) layer is mandatory to ensure a beneficial effect of K-PDT, otherwise a detrimental effect will be obtained due to the formation of $Cu_{2-x}Se$ phase. Based on a deep investigation of the CIGS surface before and after K-PDT, a hypothetical model explaining what happens was proposed. They suppose that during K-PDT, a consumption of the OVC takes place resulting, at the end of the treatment, in the formation of $KInSe_2$ new layer accompanied by a gallium fluoride phase. During the CBD-CdS buffer layer deposition, they suppose that the $KInSe_2$ layer transforms to a $CdIn(S,Se,OH)_4$ layer while the gallium fluoride phase dissolves in the bath. Experimentally, they confirmed the formation of a 5 nm-thick $CdIn(S,Se,OH)_4$ thin layer in between the stoichiometric CIGS layer and the CdS buffer layer. This new layer is believed to form a buried p-n junction with a low distance between the Fermi level and the conduction band at the interface, which prevents interface recombinations [T. Lepetit. 2015].

2.6. The role of the band gap engineering

Two types of band gap grading were investigated by the CIGS community: simple and double grading. The simple band gap grading is characterized by an increase of the GGI ratio towards the back surface, while an increase of the GGI ratio both towards the back and front surfaces, leading to its minimum in between, are the characteristics of the double graded band gap.

2.6.1. Simple graded band gap

T. Dullweber et al. have reported on the effect of the band gap grading towards the back on cells performance. Their experimental and simulation results have led to the conclusion that the band gap grading contributes to the enhancement of cells characteristics through the reduction of back surface recombination [T. Dullweber. 2001]: thanks to the additional force at the back interface, resulting from the change in the band gap over some distance x related to the Ga-grading, that drives the photoelectrons away from this interface.

However, due to the increase in band gap, a trade-off between carrier collection enhancement and low energy photons generation shall be found.

2.6.2. Double graded band gap

As was said by T. Dullweber et al.: ‘’the key objective is to design a larger band gap for lower recombination and a lower band gap for better absorption’’ [T. Dullweber.2. 2001].

For better understanding the mechanisms behind the improvement of both current and voltage, one prefers dividing the GGI profile in three zones:

* The grading towards the back surface zone: an increase of the band gap towards the back surface creates a back surface field which is believed to increase the collection efficiency by reducing the recombination velocity at the back contact.

* The minimum band gap zone: it is mainly designed for better absorption of the long wavelength light, and therefore enhancement of the short circuit current J_{sc}.

* The grading towards the font surface zone: as it includes the space charge region, one might expect the high dependence of the V_{oc} on the band gap grading within this zone. A higher band gap is expected to result in a higher V_{oc}, while the decrease towards the notch should enhance the absorption within the space charge region.

2.6.3. Double grading profile and its effect

Simulation results from S.Y. Kuo et al. have shown the dependence of cells performance on the grading profile and the depth of the so called notch/valley (minimum band gap). Despite the increase in absorption resulted from a deep valley, a strong increase towards the front surface might create a high barrier for electrons. As a solution, they have shown that a highly graded band gap towards the back is necessary to provide the electrons more energy to overpass this barrier; otherwise, recombinations will take place in the valley [S.Y. Kuo. 2014].

From the experimental side: efficiency as high as 21.7% have recently obtained by P. Jackson et al. [P. Jackson. 2015]. They showed that a strong GGI grading including a high GGI at both the front and the back with a low minimum in between, leads to a gain in the short current density, due to the better absorption in the longer wavelength region, without a significant loss in the open circuit voltage or fill factor. One should mention that their samples have undergone a K-PDT, which is a key step for reaching such a high efficiency.

2.7. $MoSe_2$ interfacial layer

2.7.1. Formation conditions

It is commonly observed that $MoSe_2$ interfacial layer takes place during the growth of co-evaporated CIGS films or the selenization of metallic precursors (regardless of the deposition method: sputtering, electrodeposition...). In both cases, this layer resulted from the reaction of the Mo surface with Se, leading to a conversion of the dense cubic Mo surface into a layered hexagonal $MoSe_2$ layer [T. Wada. 2001] [D. Abou-Ras. 2005] [S. Nishiwaki. 1998].

A deep investigation performed by D. Abou-Ras et al. shows that this Mo surface conversion to $MoSe_2$ layer is both temperature and duration dependent: the higher the temperature and duration, the thicker the $MoSe_2$ layer is [D. Abou-Ras. 2005]. They have also reported on the effect of temperature on the orientation of $MoSe_2$ layer: the $MoSe_2$ c-axis changes its orientation from normal to parallel as the substrate temperature increases. Furthermore, the orientation dependence of this layer on Mo surface density was also investigated: c-axis parallel and random orientations are obtained on low and high Mo surface density, respectively [D.H. Shin.

2012]. In parallel to that, P.J. Rostan et al, have proved that sodium is indispensable as a catalyst for Mo selenization during CIGS growth [P.J. Rostan. 2005].

2.7.2.Effect on CIGS adhesion and metal-semiconductor contact type

For a good adhesion of the CIGS layer, it is largely reported that the c-axis of the hexagonal $MoSe_2$ layer should be parallel to the Mo surface; otherwise the CIGS layer peels off easily [D. Abou-Ras. 2005] [S. Nishiwaki. 1998] [T. Wada. 2001]. According to D. Abou-Ras et al., the poor adhesion is related to the Se-Mo bonding type: along the c-axis, Se–Mo–Se is of van-der-Waals type, while Se–Mo–Se normal to the c-axis is of covalent type.

On the other hand, because of the low work function of molybdenum material, one can expect holes blocking attitude at an abrupt back interface (CIGS/Mo), resulting from the high Mo Φ_{bh} which leads to a Schottky contact. Thanks to the $MoSe_2$ wide band gap p-type semiconductor interfacial layer, an ohmic contact instead of a Schottky contact, resulting from the creation of a back surface field, was reported by T. Wada et al [T. Wada. 2001].

Furthermore, J-H. Yoon et al. have reported on the change of the contact resistance as a function of the orientation of the $MoSe_2$ layer: a twofold reduction in CIGS/Mo contact resistance due to the change of the orientation of the $MoSe_2$ layer from c-axis normal to parallel was obtained [J-H. Yoon.2. 2014].

Finally, due to the high reactivity between Mo and Se, it is interesting to note that selenization of metallic precursors for long time might lead to the formation of a too thick $MoSe_2$ layer. As a consequence of a thick $MoSe_2$ layer, X. Zhu et al. have obtained a high series resistance and therefore low cells performance [X. Zhu. 2012]. To limit the thickness of the formed $MoSe_2$ layer, researchers from NEXCIS have introduced a buried molybdenum nitride layer, at about 50 nm from the surface. This layer acts as barrier for Se diffusion, and therefore limits the $MoSe_2$ thickness [S. Angle. 2014].

2.8. Partial conclusion

In this first part, we have tried to give a clear overview on what is already achieved by summarizing all important findings and conclusions. More attention has been payed to the sputtering based processes since it is the one used in this work. Points of view and explanations from different schools have been taken in consideration, and interpretations of the confusing subjects have been proposed.

It is worth to note that some results from literature were discussed even though no related experiences will be presented within the following experimental part (such as the effect of band gap engineering and potassium impurity). By doing that, we aim leaving a complete paper/review for the one who will take over!!

In the next part, we will present an original absorber deposition process which is based on magnetron pulsed-DC sputtering at room temperature from a single quaternary CIGS target using argon plasma without any additional selenium supply, followed by annealing under inert atmosphere. One thing to keep in mind is that all annealing processes, if not mentioned, were performed using a halogen lamp-based RTA system.

Part B. Experimental results

The results presented in this part are, in fact, the continuity of a previously started study made in our group by Thomas Aviles. Therefore, by the time I took over, mainly two points were already overcome: the target composition and the CIGS thin films delamination.

(i) The target composition

The exact composition of the target was already determined after the fabrication of a first set of samples by comparing the compositions of the obtained films and of the stoichiometric target used for these first tests. Therefore, it is worth to note that all CIGS thin films that will be presented in the following were prepared from a single non-stoichiometric quaternary CIGSe target which composition has been slightly enriched with Se and slightly depleted in Cu, with respect to the stoichiometric composition, in order the adequate film composition to be obtained once annealed. This adequate composition was targeted to be Cu/(In+Ga) ≈ 0.9, Ga/(In+Ga) ≈ 0.3 and Se/(Cu+In+Ga) ≈ 1.1. The elemental composition and the calculated ratios of the as deposited and annealed CIGS thin films are summarized in figure 2.1.

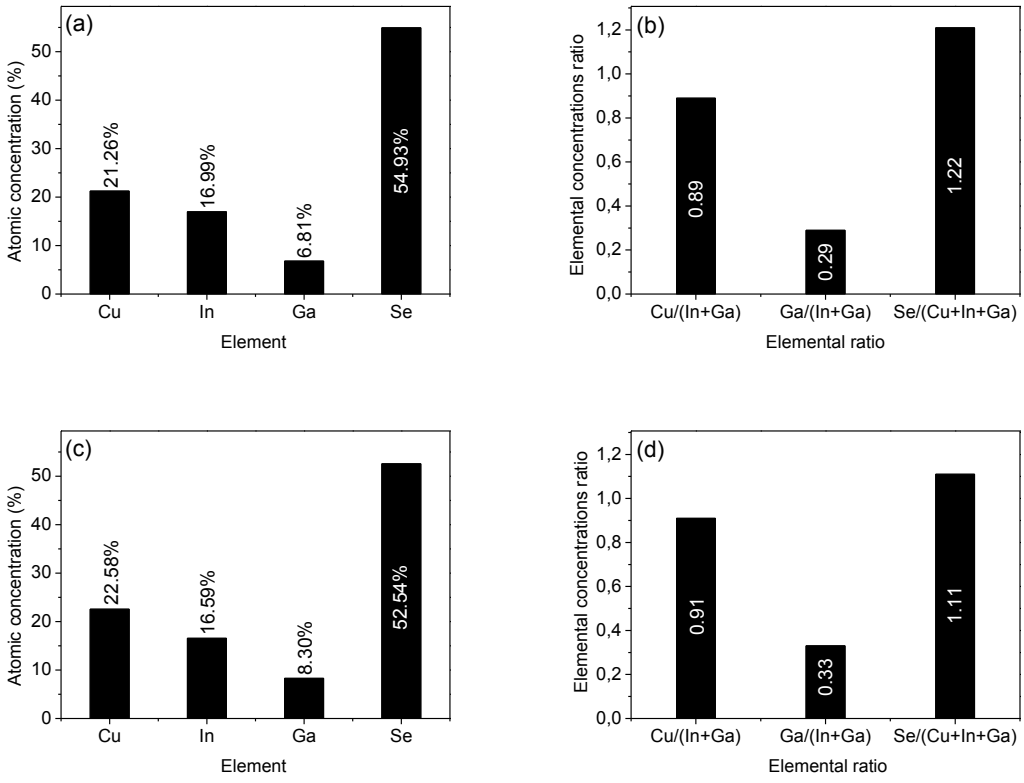

Figure 2.1: Measured elemental composition of as deposited (a) and annealed (c) pulsed-DC sputtered CIGS thin films using EDX. Calculated elemental composition ratios before (b) and after annealing (d).

(ii) CIGS thin films adhesion to Mo back contact (delamination issue) and argon outgassing

Intuitively, a low pressure condition has first been used for the deposition of the first set of CIGS thin films. This choice was made aiming to achieve high crystalline microstructure. However, two dramatic consequences were observed once the CIGS thin films went through the recrystallization annealing process.

The first is related to the peeling off of the CIGS thin films, as can be seen in figures 2.2(a) and (b) (even though the used low pressure process condition corresponds to the stress free point), while the second is related to the out diffusion of incorporated argon[1] due to the peening effect (argon outgassing), creating micrometric holes (crater-like shape), as clearly shown in figure 2.2(c).

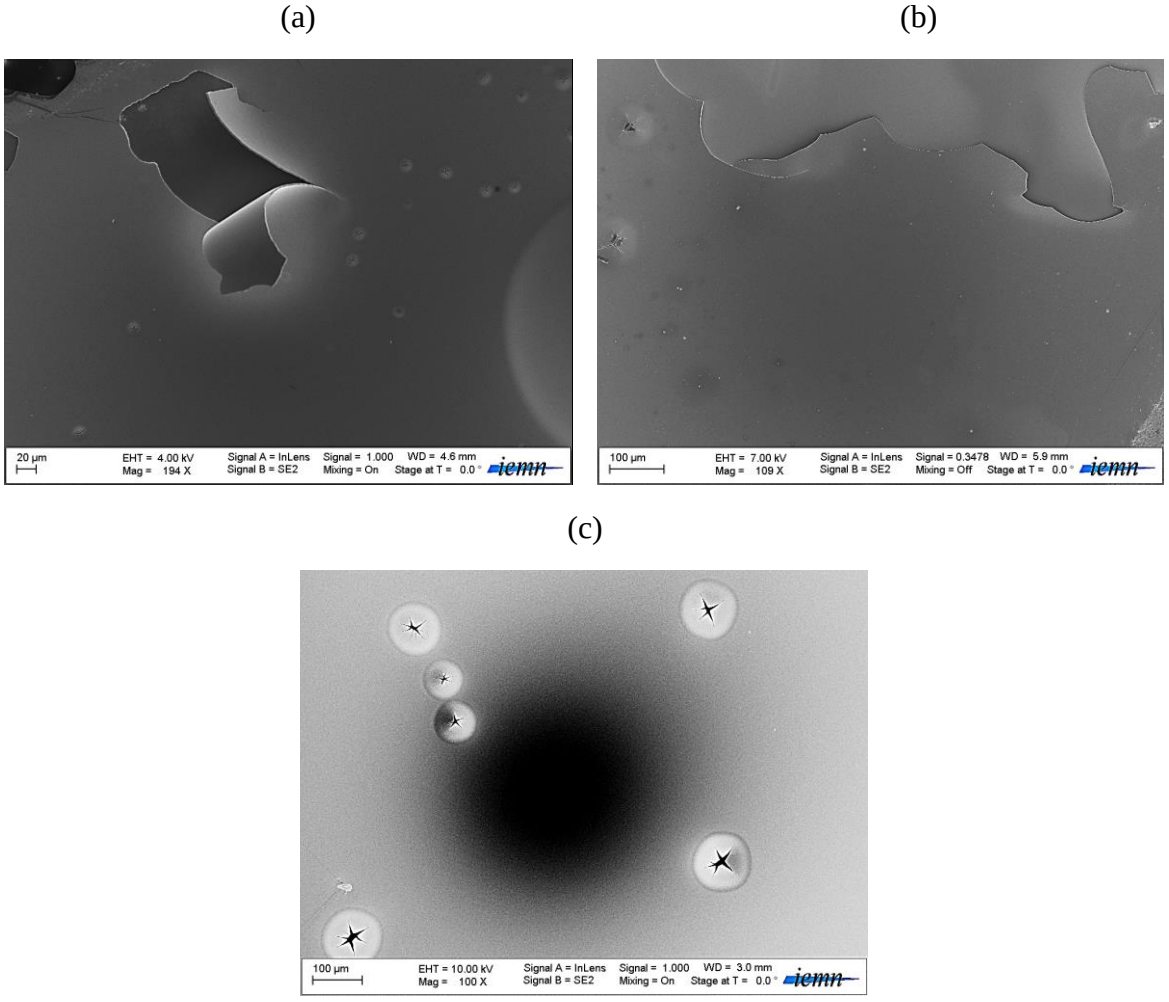

Figure 2.2: SEM surface images of low pressure deposited CIGS thin films. (a) and (b) Show the CIGS thin film peeling off. (c) Shows the induced crater-like defects from argon outgassing.

[1] One has to keep in mind that our sputtering process is only based on inert gas, Ar.

Proposed solution for better adhesion: Bilayer structure

As a first step, the adhesion problem was overcome by imitating Scofield's bilayer structure for well adhered molybdenum back contact layer: a high pressure (HP) deposited CIGS thin layer (100-300nm) followed by a low pressure (LP) deposited thick layer (2µm). The cross sectional image of the annealed CIGS bilayer structure is presented in figure 2.3.

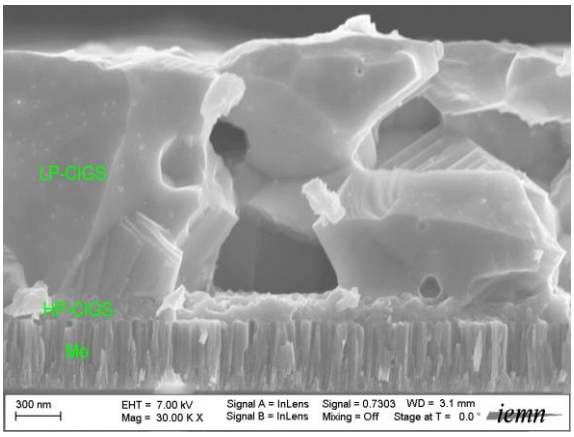

Figure 2.3: SEM cross sectional image of the annealed CIGS bilayer structure.

By using this bilayer structure, the CIGS thin film peeling off was not anymore observed; however, the effect of argon outgassing was still observed.

2.9. Stack of reduced thickness CIGS bilayers for argon outgassing management

To overcome the argon outgassing issue, reduced thickness CIGS bilayers stacking was investigated.

This was expected to play a double role: (i) by reducing CIGS bilayer thickness, we aimed facilitate the argon outgassing and therefore limiting the induced damage, (ii) covering the induced crater-like defects, if any, by alternating their positions and therefore avoiding short circuit paths once this layer is used for solar cells fabrication.

The effect of the adhesion layer thickness, the annealing time and temperature were investigated, and the following conclusions were obtained:

- ✓ Using the bilayer structure for each stack was found to be a key point for keeping a good adhesion;
- ✓ Reducing the adhesion layer thickness of the first bilayer was found to have dramatic consequence (peeling off);
- ✓ Deposition and annealing of an adhesion layer (of 100nm-thick) as a seed layer, as shown in figure 2.4(a), allowed reducing the thickness of the adhesion layer of the following bilayers (down to 10nm). The SEM cross sectional image of the annealed stack (5 bilayers) is shown in figure 2.4(b);
- ✓ Final annealing longer than 30min at the same temperature (550°C) was found to result in slightly improved inter-diffusion of the different interfaces, as can be concluded from comparing figures 2.4(b), (c), (d), (e) and (f);

- ✓ Annealing at higher temperatures was found to lead to an improved interfaces inter-diffusion, as can be deduced from comparing figures 2.5(a), (b) and (c)/(d);
- ✓ Independently of the annealing time and temperature, argon outgassing induced surface defects (crater-like) were not anymore observed;
- ✓ The observed holes, especially at the interface between the first bilayer and the adhesion layer, are real and are not a sort of grains displacement related to the preparation of samples for SEM cross sectional imaging (cleavage). This was confirmed using a FIB-SEM imaging, as shown in figure 2.6.

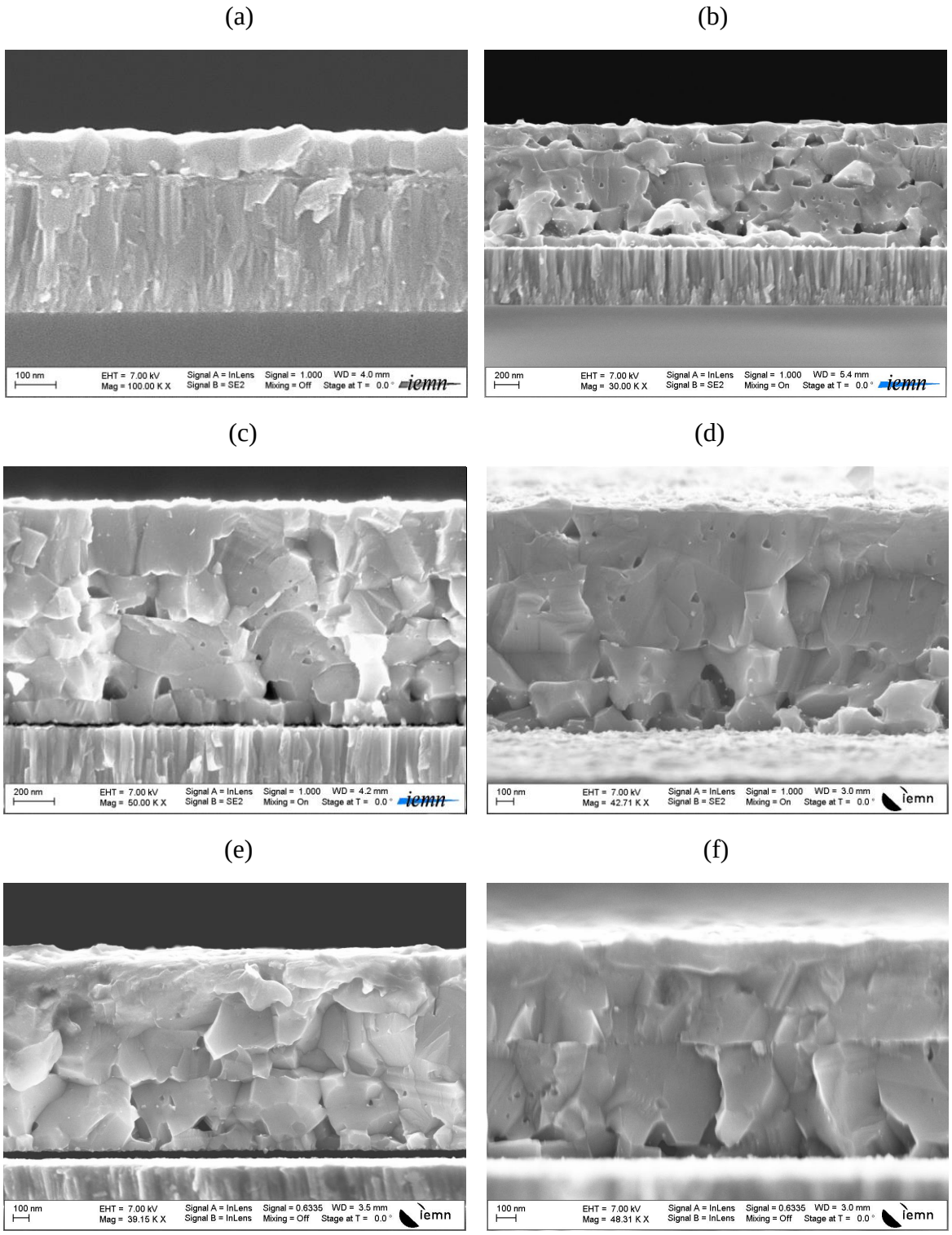

Figure 2.4: SEM cross sectional images of (a) 100nm-thick adhesion layer annealed for 5min. (b) to (f) a stack of 5 bilayers (10/150nm) on 100nm-thick adhesion layer subjected to a final annealed for different times: (b) 5min. (c) 15min. (d) 30min. (e) 45min. (f) 60min. All samples have been annealed at 550°C under N_2H_2 atmosphere.

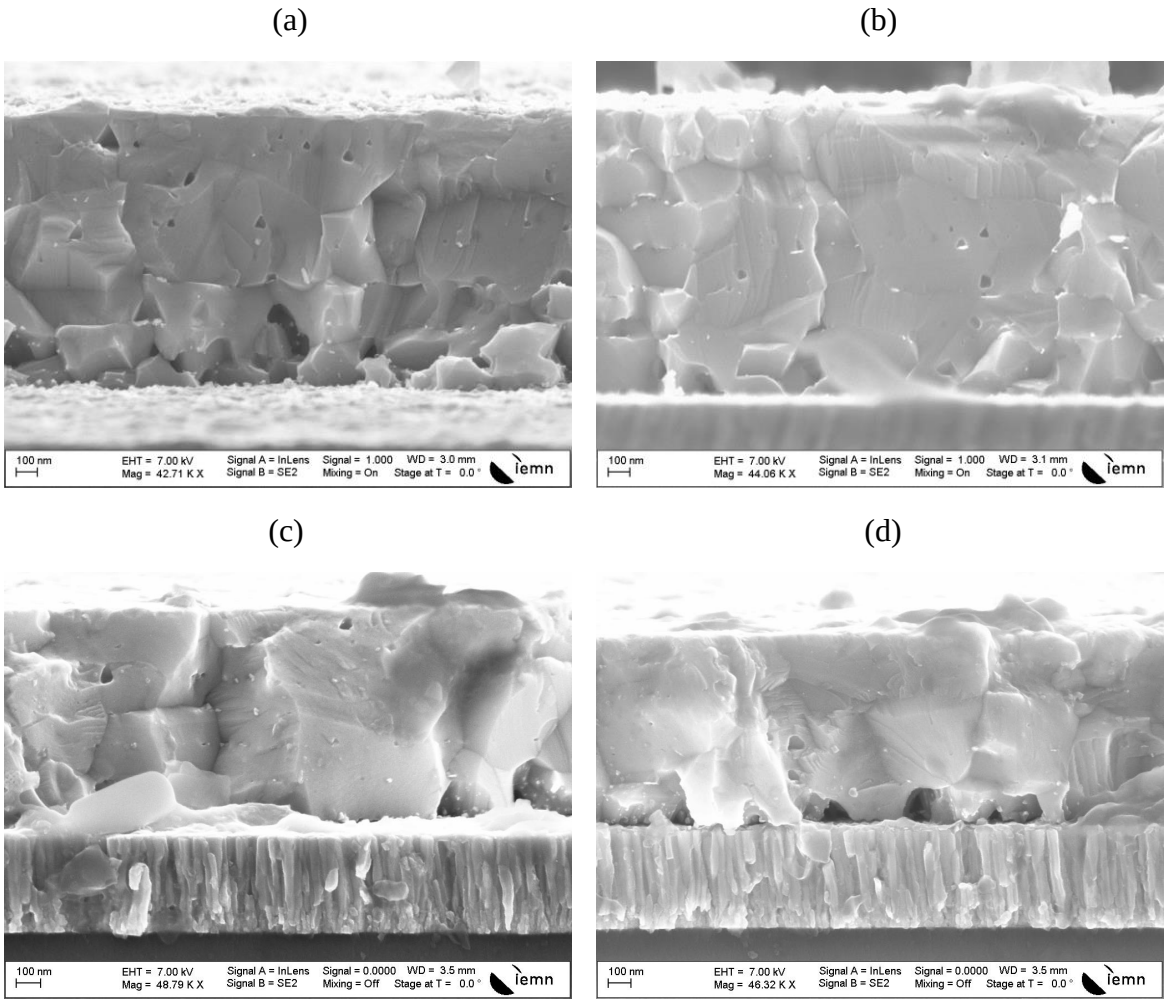

Figure 2.5: SEM cross sectional images of a stack of 5 bilayers (10/150nm), on a 100nm-thick adhesion layer, annealed for 30 min at different temperatures: (a) 550ºC. (b) 570ºC. (c) and (d) 580ºC.

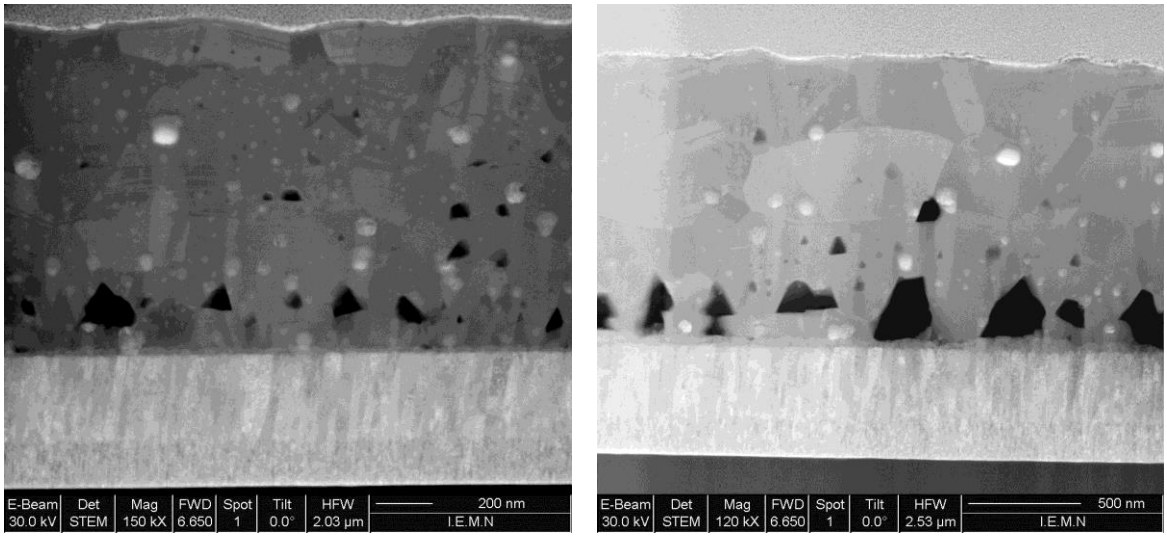

Figure 2.6: FIB-SEM cross sectional images of a 5bilayers stack CIGS film annealed at 580ºC for 30 min.

On the other hand, XRD analyses, have shown that, independently of the used bilayer thickness, annealing temperature and time, highly oriented (112) single chalcopyrite structure is obtained for all samples. In addition, a slight progressive improvement of the crystallinity as the annealing time increases can be deduced by comparing the XRD patterns in figures 2.7 (a) to (d). Finally, slightly better crystallinity was observed in case of annealing at higher temperature, as shown in figure 2.7(e). This results are in good agreement with the SEM observations.

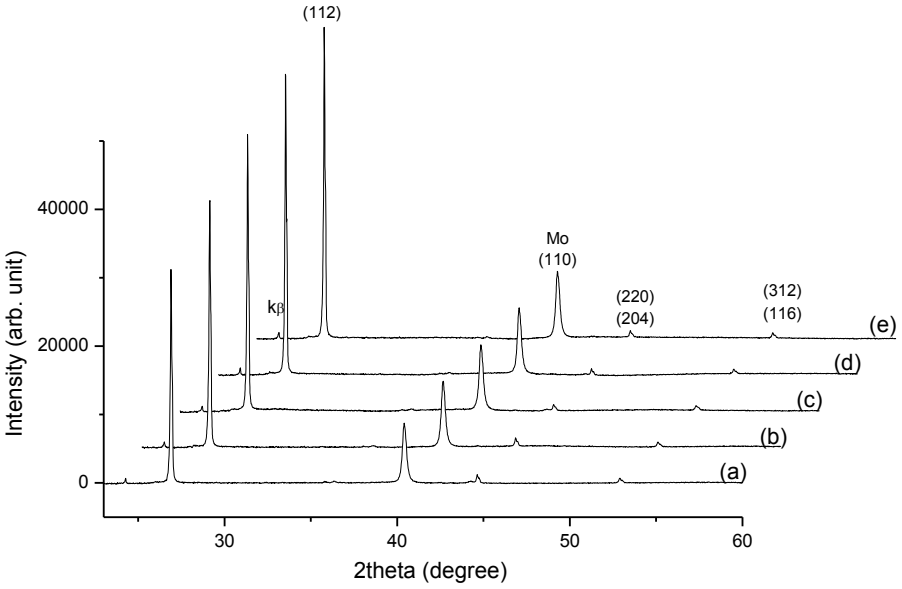

Figure 2.7: XRD patterns of 5-bilayers stack CIGS films obtained after different annealings. (a) to (d) final annealing at 550°C for different periods: (a) 15min, (b) 30min, (c) 45min, (d) 60min. (e) final annealing at 570°C for 30 min

However, changes in elemental concentration with the final annealing time and therefore deviations from optimal composition were observed, as can be seen in figure 2.8(a) and (b). An increase in both selenium and indium concentration was observed for longer annealing time. In fact, this rather reflects the depletion in copper and gallium (which is still not clear for us) since neither additional supply of selenium nor of indium were used. Furthermore, this does not mean that there were no selenium loss but rather that copper and gallium losses were more important!!!

On the other hand, higher annealing temperature was found to have almost no harmful effect on elemental composition (calculated composition ratios are still acceptable).

Finally, as shown in the inset of figure 2.8(a), argon concentration within all samples prepared using this stack process is in the range of 0.07% to 0.1%, which is in fact the same order of the measurement error.

NB: For better accuracy, means over 10 measurements on the same point were calculated.

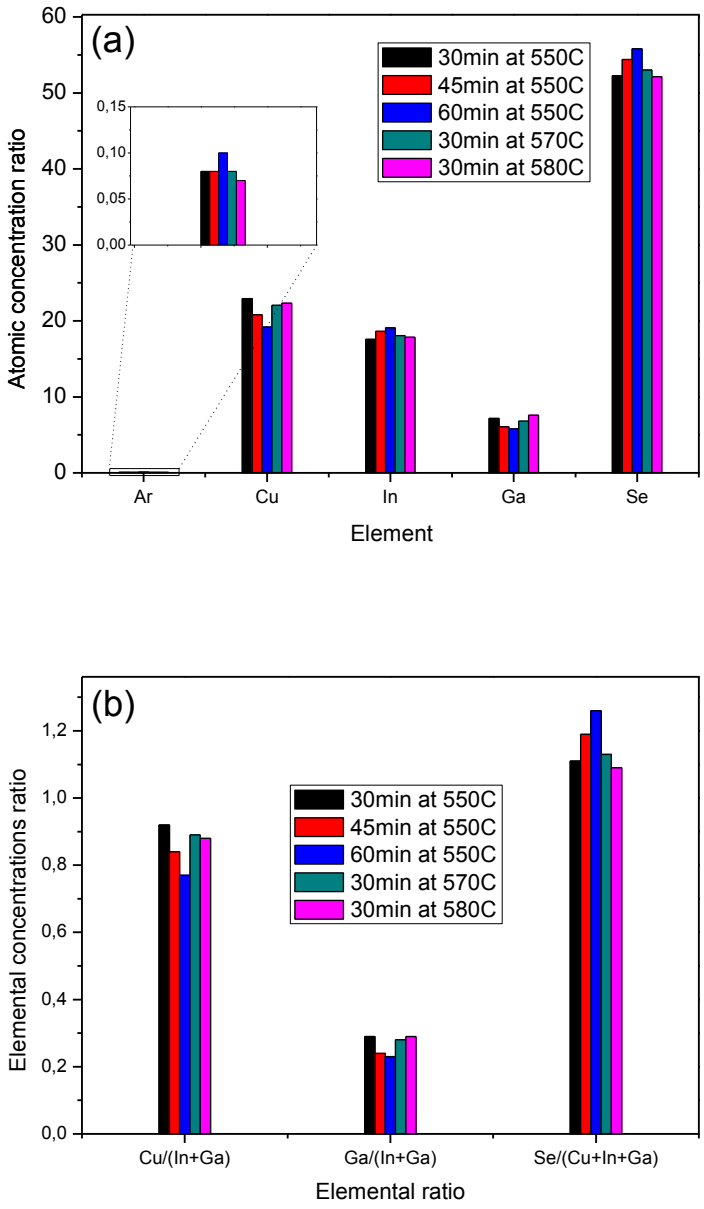

Figure 2.8: Variation of the elemental concentration (a) and the corresponding elemental ratios (b) in a 5-bilayers stack CIGS film as a function of annealing time and temperature (EDX measurements).

Partial conclusion: ‘’Limits of this process’’

Talking about microstructural quality, it was found that it is quite hard, if it is not impossible, to get defect-free CIGS layer. Annealed samples at low temperature and for short time have shown clear interfaces between the bilayers. Improved microstructure was obtained by either increasing annealing time or temperature; however, in the first case composition deviation from optimal one was found while in the second large holes were observed.

From the industrial point of view, one should admit that this process leads to a considerable waste in both time and energy, and therefore finding an alternative solution for argon outgassing management would be highly appreciated.

2.10. Third developed process: high pressure process

After the Scofield-inspired CIGS bilayer structure and the stack of reduced thickness CIGS bilayer processes, a third process was investigated.

Our previous efforts were not in vain since this third process is in fact inspired from the examination of the obtained SEM cross sectional images of the annealed 100nm-thick adhesion layer (deposited at high pressure) shown in figure 2.4(a): ***so why not trying the deposition of the entire CIGS layer at high pressure!!***. The obtained results were surprising!!

Despite the reduced argon peening effect at high deposition pressure (due to the low particle energy), the porous structure facilitates the outgassing of argon and limits, if not eradicates, the induced damage.

In the following we present, in detail, the properties of the obtained CIGS thin films using such a process.

Figure 2.9 shows the cross-sectional SEM images of the as deposited and annealed CIGS thin films. As can be seen in figure 2.9(a), the as deposited thin film shows a clear columnar/fibrous microstructure, which is in a good consistency with Thornton's model [J.A. Thornton. 1974]. Such a structural feature is characteristic of low temperature deposited thin films due to the low surface mobility of deposited particles, resulting in a tendency of the initial nuclei to grow in the direction of available coating flux [J.A. Thornton. 1974].

After post-annealing, coalescence process and large grains are observed. The resulting thin film microstructural properties are then similar to those obtained when using usual co-evaporation or sputtering-selenization techniques: grain size larger than 2 micrometers and good adhesion to the Mo back contact, as can be seen in figure 2.9(b).

Furthermore, small holes within the thin film volume are observed. This is believed to be originated from the tensile stress relaxation resulted from the arrangement and shrinkage of the disordered material [J.A. Thornton. 1989].

On the other hand, the EDX quantitative analysis was performed on as deposited and annealed thin films in order to assess the changes in chemical composition after annealing ''*For better accuracy, means over 10 measurements on the same point were calculated''*. The obtained results confirm that the annealed thin film is still slightly Se-rich (Se/Cu+In+Ga=1.13), and slightly copper poor (Cu/ In+Ga= 0.9), while the ratio Ga/Ga+In is equal to 0.3.

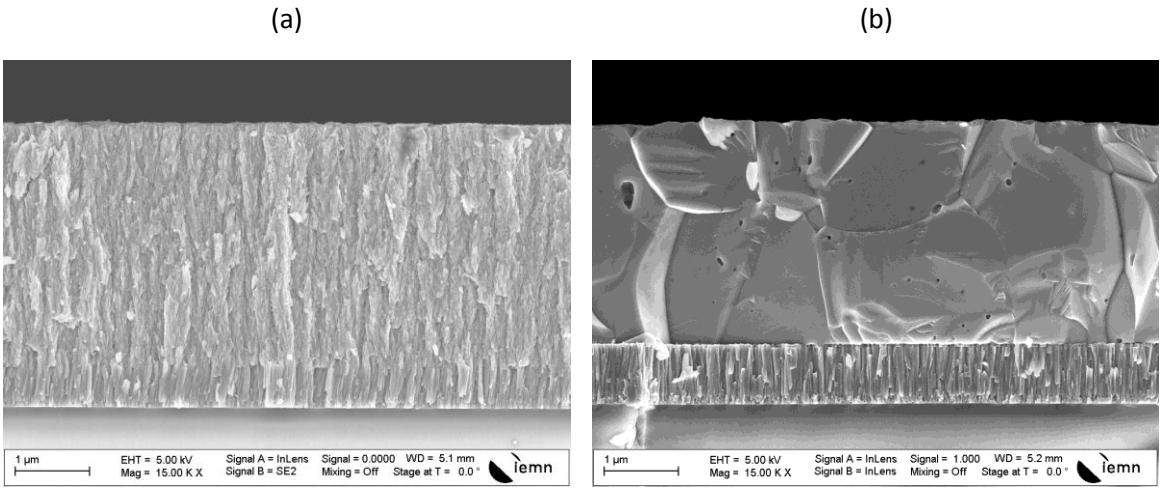

Figure 2.9: Cross-sectional SEM images of high pressure deposited CIGS thin films: (a) as-deposited film, (b) annealed film at 540°C for 30min.

However, one may wonder about other possible negative consequences of using high pressure deposition process such as phase decomposition. For this reason, X-ray diffraction data of the as deposited and annealed thin films were recorded and the XRD patterns are presented in figure 2.10. As can be seen, both thin films reveal a chalcopyrite polycrystalline structure with a (112) preferred orientation. The relatively weak and large peaks of the as deposited thin film are attributed to its limited crystalline quality, while the very intense and narrow peaks obtained after annealing clearly express the high crystalline quality, which is consistent with the previous cross-sectional SEM images.

Furthermore, the origin of the (112) preferred orientation was previously explained in details in §2.4.1: either due to the low (112) plan energy of the Cu-poor chalcopyrite structure compared to that of the (110) [J.E. Jaffe. 2001], or to the effect of molybdenum surface density [D.H. Shin. 2012] [J.H. Yoon. 2014].

Also, it is interesting to note that no extra peaks corresponding to metallic or other compound phases, such as In_2Se_3, $Cu_{11}In_9$, Cu_9Ga_4, $CuInSe_2$, $CuGaSe_2$, were detected. However, knowing that the characteristic XRD-peaks of the CIGS chalcopyrite phase and those of the Cu_2Se secondary phase have almost the same position, one cannot confirm the absence of this secondary phase just by analysing the XRD spectra. To remove this ambiguity, Raman measurement seems to be useful for further investigation before confirming whether such a secondary phase exists or not.

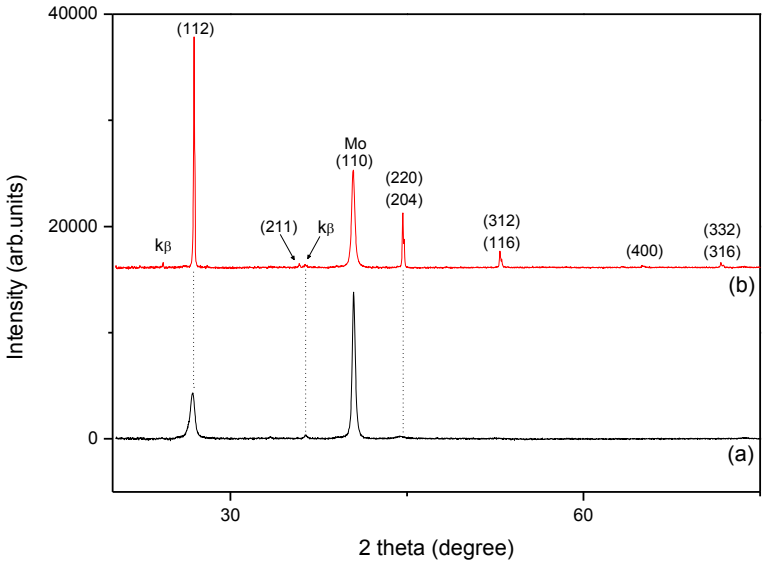

Figure 2.10: XRD patterns of high pressure deposited CIGS thin films. (a) as-deposited thin film, (b) annealed thin film at 540°C for 30min.

As can be seen on the Raman spectrum in figure 2.11, the annealed thin film shows an intense and sharp peak at 175 cm^{-1} related to the A_1 vibrational mode, and a weak and broad peak at 217 cm^{-1} which corresponds to the B_2/E vibrational modes. Both of them are characteristics of the chalcopyrite structure [J. Xiang. 2014] [L. Ouyang. 2015] [L. Ouyang. 2014].

The high intensity and sharpness of the A_1 mode is largely reported as a sign of the high crystalline quality of the chalcopyrite phase [J.H. Shi. 2011] [L. Ouyang. 2015] [H. Kong. 2014], which is in a good consistency with the SEM and XRD analyses.

On the other hand, no peak in the range 258-263cm^{-1}, which is characteristic of the $Cu_{2-x}Se$ secondary phase vibrational mode [J. Xiang. 2014] [J.H. Shi. 2011] [L. Ouyang. 2014], was detected; this demonstrates the single phase chalcopyrite structure.

Moreover, no peak at 156 cm^{-1}, corresponding to the vibrational mode of the ordered vacancy compound (OVC) [L. Ouyang. 2015], was observed.

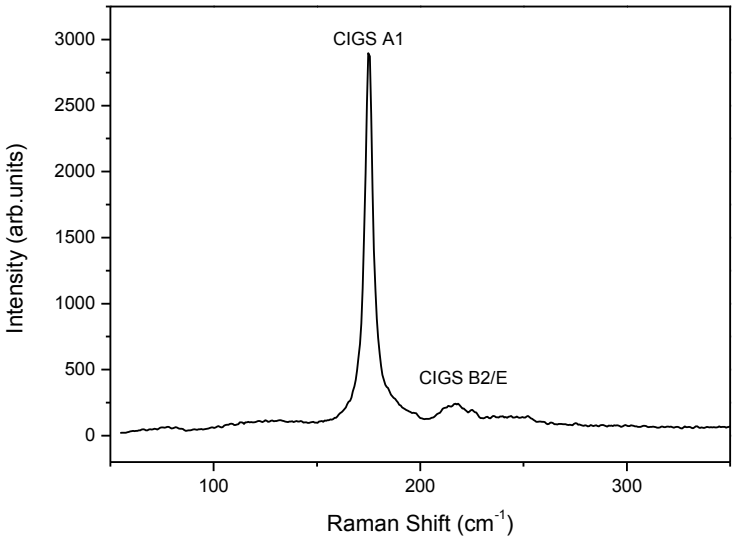

Figure 2.11: Raman spectrum of a high pressure deposited CIGS thin film annealed at 540°C for 30min.

Finally, the SIMS depth profiles of the constituent elements of the annealed CIGS thin film are presented in figure 2.12(a). As can be seen, all elements show a homogeneous composition distribution along the CIGS thin film depth, evidencing a uniform and single-phase CIGS thin film which supports our previous conclusions.

On the other hand, it is interesting to note that Ga accumulation toward the back contact, widely observed in CIGS thin films prepared by the two-stage process [H.R. Hsu. 2012] [K.H. Liao. 2013] [A. Rockett. 2000], was not observed.

It was suggested that such a Ga accumulation in selenized thin films, leading in general to a reduction in Voc [H.R. Hsu. 2012] [K.H. Liao. 2013], is due to the difference in the chemical affinity between Se and In compared to that between Se and Ga, resulting in In and Ga migration toward the surface and back contact, respectively [K.H. Liao. 2013]. On the contrary, because of the already bonded Ga and In to Se in the sputtered thin film from a quaternary target, such a migration of elements is suppressed.

Furthermore, it is particularly interesting to note that Se signal exhibits a peak at the CIGS-Mo interface, as shown in Figure 2.12(b), which might be attributed to the formation of $MoSe_2$ interfacial layer.

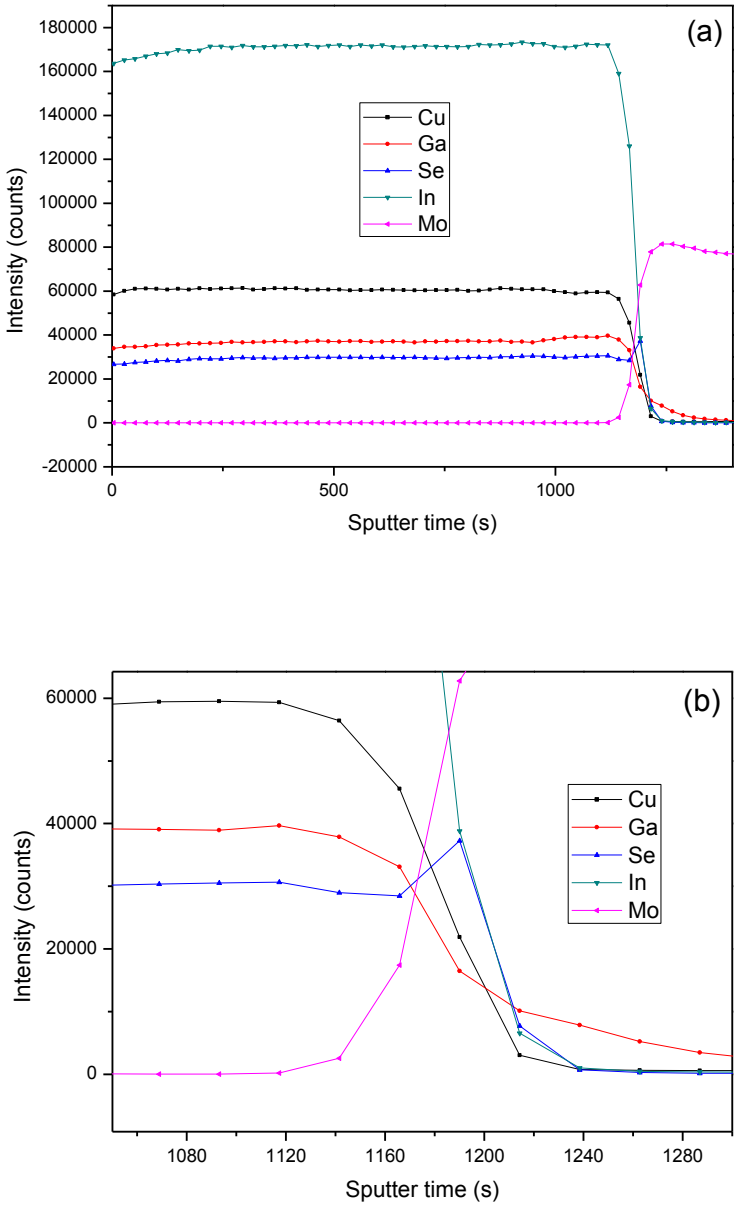

Figure 2.12: (a) SIMS depth profiles of the constituent elements of a high pressure deposited CIGS thin film annealed at 540°C for 30min. (b) Zoom in SIMS profiles.

2.11. Short annealing time process "10 min"

The effect of reducing the annealing time, while keeping the same temperature, on the microstructural properties of high pressure deposited CIGS thin films has also been investigated. The cross-sectional SEM image and the XRD analysis of the obtained film, shown in figures 2.13 and 2.14, respectively, reveal a clear similarity to that obtained after 30min of annealing: (i) grain size larger than 2 micrometers and good adhesion to the Mo back contact; (ii) highly oriented (112) single chalcopyrite phase.

From the technological point of view, annealing time is not a matter of interest, however, this become of high importance once transferring the process from laboratory to industry.

In the light of this observations and purely for industrial sake, shorter annealing time process, down to 1min, is planned to be investigated in the future.

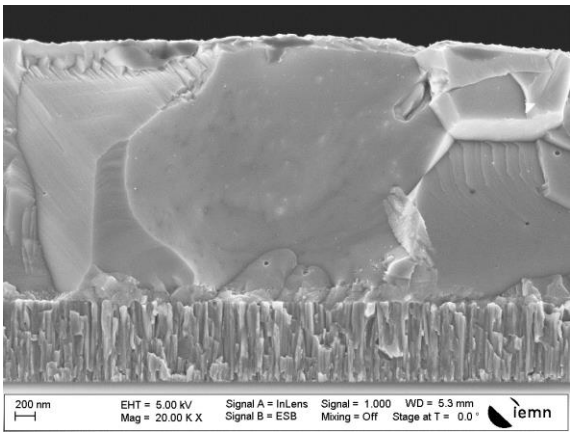

Figure 2.13: Cross-sectional SEM image of a high pressure deposited CIGS thin film and annealed at 540°C for only 10min.

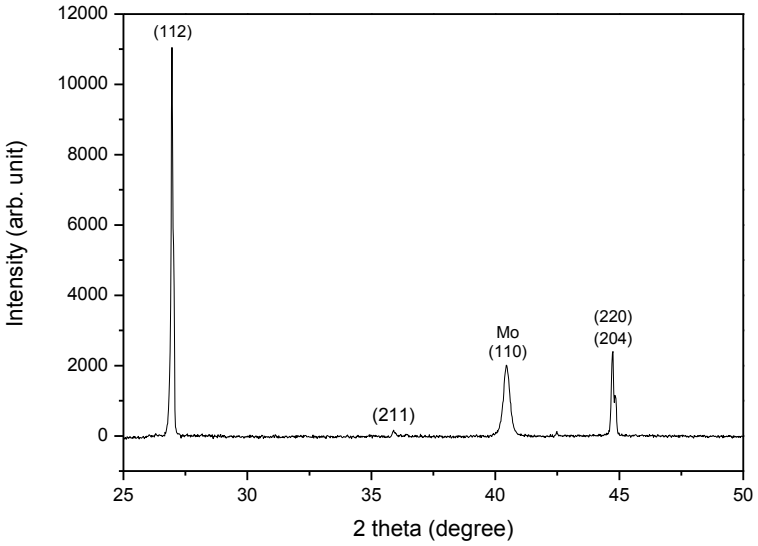

Figure 2.14: XRD pattern of high pressure deposited CIGS thin film and annealed at 540°C for 10min.

2.12. Induced cracks in molybdenum after CIGS recrystallization

Unfortunately, the recrystallization annealing process of high pressure deposited CIGS thin films was found to induce cracks in the molybdenum layer:

The SEM imaging of the CIGS surface has revealed the presence of some kind of "white line" patches, as shown in figure 2.15(a), while no changes in the GIGS features could be deduced by zooming in, as shown in figure 2.15(b).

However, the FIB-SEM imaging, with a tilt of 52^{o}, has shown a clear valley-like feature corresponding to such a "white line", as shown in figure 2.15(c). For deeper understanding, a FIB-SEM cross sectional imaging was then performed and the obtained image is shown in figure 2.15(d).

The cross sectional FIB-SEM image shows a clear crack within the molybdenum layer. We are quite sure that the observed cracks in the molybdenum layer are related, in somehow, to the use of high pressure deposition of the CIGS thin film. This conclusion is based on two observations:

* Similar annealing process of only the molybdenum layer (deposited in the same conditions) was found to have no effect (no cracks were observed)

** During the development of the CIGS stack process with reduced thickness bilayers structure, no molybdenum cracks were observed in case of using 10nm adhesion layer.

On the other hand, the fact that the cracks are found to be filled suggests that the GIGS thin film becomes quasi-liquid at high temperature. Furthermore, the different contrast observed between the bulk CIGS thin film and the filled crack might reflect a difference in composition (deeper investigation is needed for confirmation).

One more important question is: do these ‘’cracks-defects’’ have an effect on solar cells performance? To answer this question, complete solar cells structure should first be prepared!!

Developed solution:

The use of 300nm Al_2O_3 sodium barrier layer was found to prevent molybdenum layer cracking. One possible explanation is that this barrier layer offers a certain flexibility at the interface with molybdenum and therefore prevents crack formation. Nevertheless, further investigation is needed for deeper understanding.

Furthermore, it is very important to note that higher annealing temperature was found to be necessary to get similar crystalline microstructure to that obtained when no Al_2O_3 barrier layer is used, otherwise very poor crystalline microstructure will be obtained, as shown in figures 2.16(a) and (b). This is believed to be originated from the lack of sodium [K. Granath. 2000] [Q. Guo. 2013] [M. B. Ard. 2000] [J. Eid. 2015] which is known to play an important role in lowering the crystallization energy.

It is important to note that by adding this barrier layer, a sodium post deposition treatment (Na-PDT) will be necessary for cell fabrication. Anyway, this sodium post deposition

treatment is highly suggested for a better control of sodium concentration and therefore high CIGS solar cells performance.

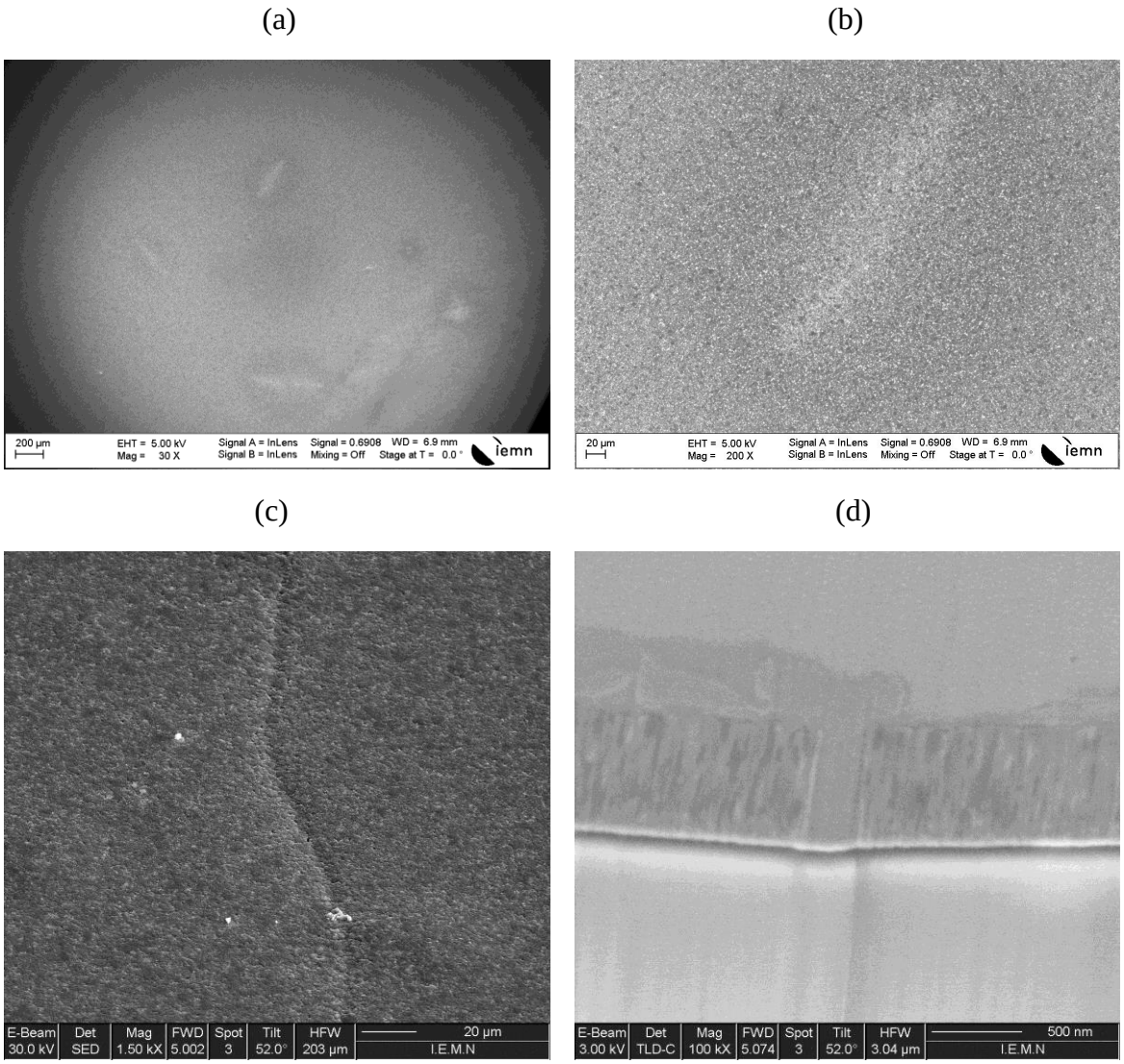

Figure 2.15: (a) and (b) SEM surface images of a high pressure deposited CIGS thin film and annealed at 540˚C. (c) FIB-SEM surface image with a tilt of 52^{o}. (d) Cross sectional FIB-SEM image of the valley-like line.

(a) (b)

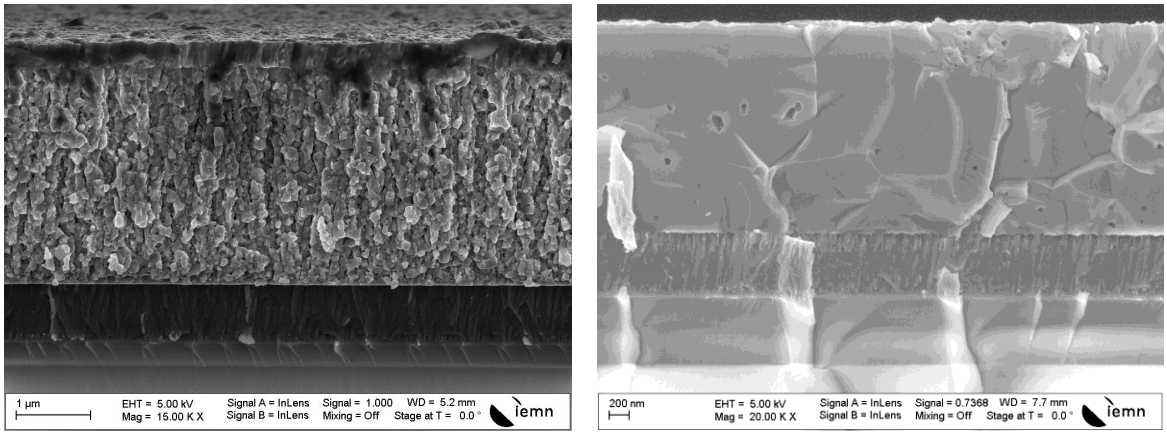

Figure 2.16: Cross sectional SEM images of a high pressure deposited CIGS thin films and annealed at different temperatures: (a) 540˚C. (b) 560˚C. In both cases, Al_2O_3 barrier layer coated SLG substrates were used.

NB: Please note that figure (a) presents a complete CIGS solar cell structure (CdS/i-ZnO/ Al-ZnO on the top).

2.13. CIGS thin film orientation control

Having in hidden agenda the reported enhancement in solar cell efficiency using (220)/(204) oriented CIGS absorbers, as previously presented in paragraph 2.4.2, the effects of molybdenum layer density as well as of the film side exposed to heating were investigated.

2.13.1. Effect of molybdenum density

The effect of using lower molybdenum density (deposited at $1.5x10^{-2}$mbar) on the CIGS layer microstructure is presented in figure 2.17.

Using lower molybdenum density, it was found that the previously optimized annealing process (540°C) leads to a very poor crystalline microstructure quality, as shown in figure 2.17(a).

Furthermore, higher annealing temperature (560°C) was found to lead to a clear improvement (even if it is not as good as that previously obtained), as shown in figure 2.17(b). In parallel to that, continuous cracks were, unfortunately, observed, as shown in figure 2.17(c).

These cracks were found to be larger (compared to those observed in case of high pressure CIGS thin film deposited on high density molybdenum without Al_2O_3 barrier layer and annealed at 540°C, see figure 2.15) and to extend up to the CIGS layer surface (the cracks are not filled).

Based on our previous results, one can expected that further increase in temperature and the use of an Al_2O_3 barrier layer might be, again, the right way to overcome these issues.

More important, the annealed CIGS thin film at 560°C is not anymore (112) preferentially oriented but rather (220)/(204), as shown in figure 2.17(d). The ratio of the integrated

intensities of the (220) reflection to the (112) reflection is about 2, which is the optimum one for high efficiency solar cells as previously reported by S. Chaisitsak et al. [S. Chaisitsak. 2002].

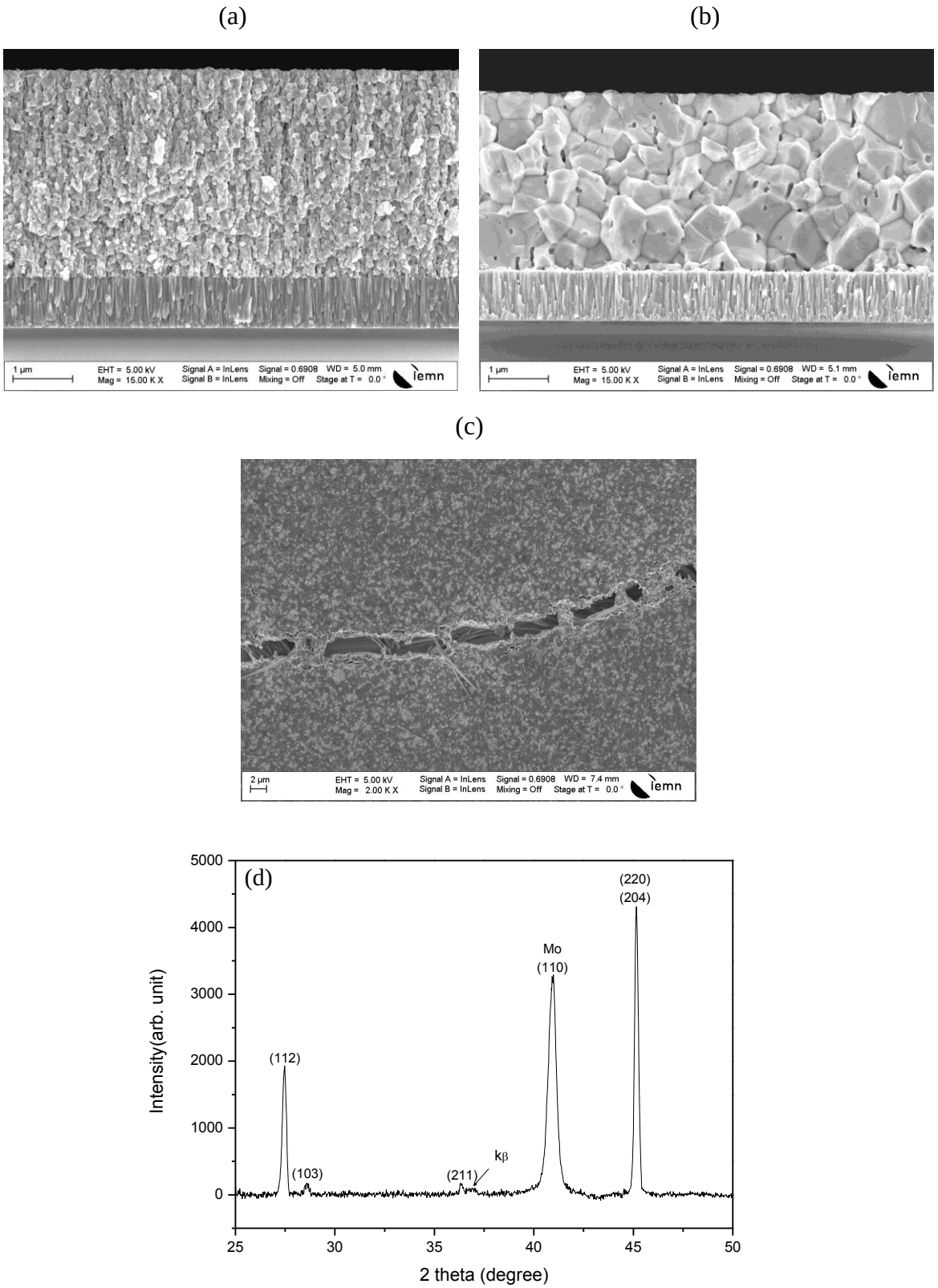

Figure 2.17: Cross sectional SEM images of high pressure deposited CIGS thin films on high pressure deposited molybdenum and annealed at different temperatures: (a) 540˚C. (b) 560˚C. (c) surface SEM image of CIGS thin film annealed at 560ºC. (d) XRD pattern of CIGS thin film annealed at 560ºC.

2.13.2. In-situ annealing: Back side heating effect

Despite the obtained high quality microstructure, as shown in figure 2.18, back-side resistance-based heating/annealing process was found to play a decisive role in the determination of the CIGS thin films crystalline orientation.

As can be seen in figure 2.19, using a back-side resistance-based heating/annealing process, a different CIGS orientation was obtained compared to that previously obtained using a front-side halogen lamp-based heating process (§ 2.10): CIGS thin films are not anymore (112) highly oriented but rather (220) with an integrated intensity ratio of almost 3.

It is very important to note that the used molybdenum layers in both cases have the same density, therefore the effect of molybdenum layer discussed in section 2.13.1 should not be at the origin of the observed change in orientation.

One possible explanation is the following:

In case of back-side resistance-based heating process, the recrystallization starts at the CIGS-molybdenum interface and then the recrystallization moves towards the surface. Therefore, the CIGS orientation is highly affected by the molybdenum surface density, at least near to this interface while the (112) orientation might only dominate, due to its low surface energy, far from this interface.

On the contrary, using a front-side halogen lamp-based heating process (which is our usual annealing process in RTA furnace), no progressing recrystallization front towards surface should be expected since more homogenous heat distribution within the CIGS layer is guaranteed, and therefore, we can imagine a competition between the (112) and the (220) orientations: (112) far from the CIGS-molybdenum interface and enforced (220) at the molybdenum surface. In this configuration, only very low density molybdenum surface might lead to slightly (220) orientation, as shown in §2.13.1.

NB: The aim of presenting the effect of back-side resistance-based heating on CIGS thin films orientation is not to propose this annealing configuration as a solution for achieving the (220) orientation, since the use of such a configuration is out of the question from the industrial point of view, but rather to show that molybdenum surface density and sodium concentration are not the only parameters controlling the orientation of CIGS thin films and that the front-side halogen lamp-based annealing configuration plays an important role in favoring the (112) crystalline orientation.

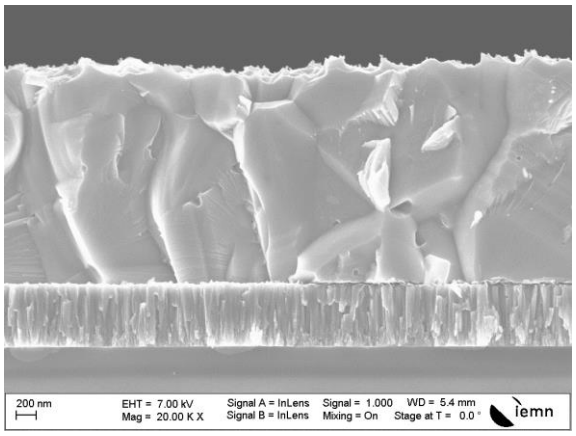

Figure 2.18: Cross sectional SEM images of a high pressure deposited CIGS thin film and annealed using a back-side resistance-based heating configuration.

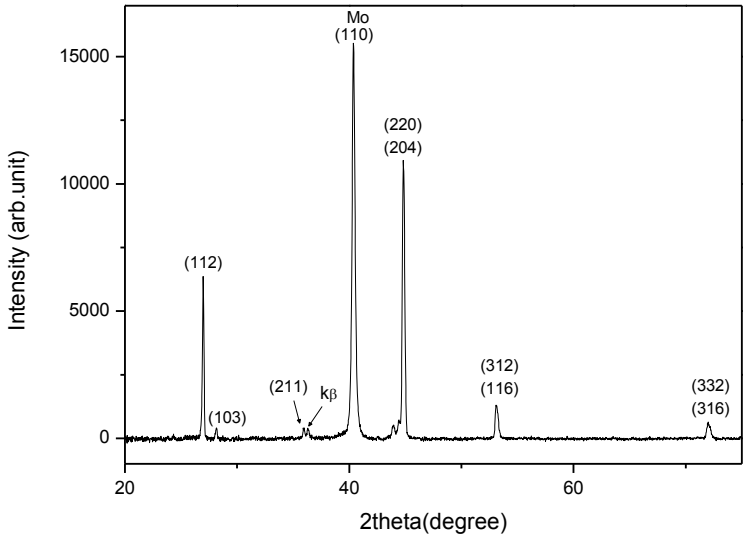

Figure 2.19: XRD patterns of high pressure deposited CIGS thin film and annealed using a back-side resistance-based heating configuration.

2.14. Chapter conclusion

Aiming to find a solution for argon outgassing induced crater-like defects, a CIGS stack of several bilayer structures was investigated. Unfortunately, it was found that it is quite difficult to get inter-diffused bilayer interfaces at an annealing temperature of 550^{o}C. Improved microstructure was obtained by either increasing annealing time or temperature; however, in the first case composition deviation from optimal was found while in the second large holes were observed.

In a second time, high pressure deposited CIGS thin films process was investigated. Despite getting rid of the argon outgassing induced crater-like defects on the surface, the cross sectional SEM image showed a micrometric-grains microstructure with high similarity to that

commonly obtained using the co-evaporation technique. On the other hand, the XRD and Raman analyses have evidenced the presence of a single chalcopyrite phase and the absence of the $Cu_{2-x}Se$ secondary phase at the CIGS surface, respectively. Furthermore, SIMS analysis have revealed the elemental distribution homogeneity throughout the whole thin film thickness while no evidence of Ga back accumulation or phase segregation.

However, such a process was found to suffer from molybdenum cracks. One found solution to overcome such an issue is the addition of an Al_2O_3 barrier layer and the increase of the annealing temperature (up to 560^{o}C).

Moreover, promising results for shorter annealing time process were obtained which opens the door to further annealing time shortening.

Finally, the effect of the molybdenum density as well as the annealing configuration on the CIGS thin film crystalline orientation was investigated. On one hand, we have shown that improved (220) orientation is achievable for lower molybdenum density. On the other hand, we have proved that the annealing configuration has a strong impact in favouring one orientation or another.

Chapter 3: Buffer layer

The purpose of this chapter is to present our contribution in the development of a chemical bath (CBD) process for the deposition of cadmium sulfide (CdS) thin films and of a room temperature sputtering process for the deposition of zinc oxysulfide (ZnS_xO_{1-x}) thin films as an environmentally friendly alternative. CdS material will be used in order to decorrelate absorber and buffer layer contributions in the overall cell performance. Ultimately, ZnS_xO_{1-x} films will be used.

The first part of this chapter is devoted to a state of the art review, in which the role of the buffer layer is discussed. The advantages and drawbacks of commonly used buffer layers as well as the reason behind choosing sputtered ZnS_xO_{1-x} will also be presented.

The second part presents our work on CdS and ZnS_xO_{1-x} thin films properties as materials for a buffer layer of CIGS solar cells. Concerning ZnS_xO_{1-x} thin films, we more deeply focus on the effect of the used deposition technique and the relationship between thickness and composition.

Part A. State of the art

3.1. Buffer layer roles

Intuitively, the fundamental role of the buffer layer is expected to be the formation of the p-n junction; nevertheless, rummaging in related published works, several additional roles of the buffer layer are commonly reported and some of them are generalized and are, over time, accepted as postulates. Such a generalization should not have place, since most of them are related to the nature and/or to the deposition technique of the buffer layer.

For more clarification, we summarize the confusing roles in the following:

* reducing recombinations at the p-n junction interface due to the epitaxial growth of the buffer layer: only true using both CdS material (good lattice matching to CIGS) and CBD deposition technique (even PVD-CdS layer does not show epitaxial growth [D. Abou-Ras2. 2005]);

* CIGS surface cleaning (deoxidation of the surface): mainly related to the use of ammonium-based CBD technique [J. Kessler. 1993];

* CIGS surface protection against damage during window layer deposition: only possible using soft deposition techniques (such as CBD, ALD …). Moreover, it was also reported that the omission of the buffer layer does not show a harmful effect (see §3.2.5 buffer layer free process);

* lowering shunt paths due to the optimal covering of the CIGS surface: which is highly dependent on both the thickness and the used deposition technique (with a superiority of the chemical bath technique) [M. Buffiere. 2011] [R.S. Araoz. 2004].

In parallel to that, there exists other roles that are independent of the buffer layer nature and deposition technique:

* Homo-junction formation through conductive type inversion: largely accepted that it leads to a low interface recombination [R. Klenk. 2001] by moving the electrical junction away from the physical one. This is known to be a consequence of CIGS surface doping through metallic elements diffusion, either during the buffer layer deposition (Cd) [T. Nakada. 1999] [C.S. Jiang.2003] or after the post deposition treatment (Zn) [T. Nakada. 2000].

* Conduction band alignment: the reference paper dealing with this subject is the one published by T. Minemoto et al. [T. Minemoto. 2001]. In this work, they have used a simple model, with an abrupt p-n junction between the buffer layer and the absorber layer (neglecting the formation of a buried junction), to understand the effect of the conduction band alignment at buffer/absorber interface on cells performance. They showed that only devices exhibiting a positive offset (a spike) in the range of 0 to 0.4eV in conduction band positions might show high efficiency, otherwise a dramatic decrease will take place due to the recombination between majority carriers via defects at the interface.

3.2. CBD-CdS buffer layer and its alternatives

3.2.1.CBD-CdS advantages

Over more than four decades, chemically deposited CdS buffer layer was considered as a reference one, since it commonly leads to high efficiency CIS/CIGS solar cells. The reason behind its superiority, compared to other buffer layers, is believed to be related to both CdS material and CBD process: CBD technique ensures surface cleaning, surface protection from damage and good covering; while CdS material guarantees the formation of the buried junction and a good conduction band alignment and therefore low recombination level; whereas both of them (CdS and CBD) are needed for an epitaxial growth.

Despite all these advantages, there are several drawbacks associated with the use of CdS as buffer layer material and CBD as deposition technique:

3.2.2.CBD-CdS drawbacks

* CdS has relatively small band-gap energy (2.4-2.5 eV); as a consequence, even for thin CdS layers, part of light is absorbed before reaching the CIGS layer. It is interesting to note that the absorption in CdS does not contribute to the photocurrent, because of the small diffusion length of minority carriers in CdS, which leads to a high recombination rate [D. Rudmann.t. 2004];

* From the environmental point of view, using Cd, which is highly carcinogenic element, is a real issue especially when it comes to waste recycling at the industrial scale;

* From the manufacturing point of view, the chemical deposition process has two drawbacks: (i) it leads to an increase in the production cost resulting from the need for waste recycling; (ii) the non-compatibility of the CBD technique to an in-line vacuum process leads to a time loss (as it is said: time is money).

Based on that, the substitution of the CBD-CdS buffer layer by a another one that features better in-line-processing compatibility and less harmful impact on the environment is highly desired

3.2.3.Essential criteria of the optimal alternative buffer layer

* For better collection of short and long wavelength photons, replacing CdS by a larger band gap and more transparent material is highly desired;

* Good crystal matching is essential for low defect density at the buffer/CIGS interface;

* Optimal conduction band alignment should be taken into consideration;

* Optimal n doping (higher (absolute value) than that of the absorber) is needed, in order to confine the space charge region on the absorber side;

* Chosen deposition technique should guarantee an optimal surface covering without introducing interfacial defects;

* Finally, stability over time and cheapness of the chosen material and the in-line compatibility of the chosen deposition technique are other important criteria from the manufacturing point of view.

3.2.4.Alternative buffer layers

Several groups have worked on the development of alternative buffer layers, taking into consideration some or most of the above mentioned criteria. In table 3.1 we give a quick overview on recent researches and record cells based on alternative buffer layers. As a reference value, the latest obtained record (June 2016) using CdS buffer layer is also given.

It is important to note that the list of alternative buffer layers presented in table 3.1 is not an exhaustive one, since only those that led to high efficiency ($\eta \geq 18\%$) are reported. Several other alternative buffer layers, such as ZnSe, ZnInSe, InSe, ZnCdSe …etc, have also been explored; however, relatively low performance was obtained. For a deeper insight, the main four reviews on alternative buffer layers (S. Siebentritt [S. Siebentritt. 2004], D. Hariskos et al. [D. Hariskos. 2005], N. Naghavi et al. [N. Naghavi. 2010] and W. Witte et al. [W. Witte. 2014]) are highly suggested.

Reference	Buffer material	Deposition technique	Obtained efficiency		Advantageous	Drawbacks	Remarks
			Alternative	Reference with CdS			
[ZSW]	CdS	CBD	-	22.6	Have a look on the previous paragraphs: CBD-CdS buffer layer/drawbacks		Despite the use of 3-stage process, no more details are available
[P. Eraerds. 2016]	In_2S_3	PVD	17.9	n.a.	-Both material and process are environmentally friendly; -Deposition process compatible for in-line vacuum process	An increase in the production cost is expected due to the use of a rare material (indium)	-SAS process was used for CIGS; -Results achieved on mini-module; -No result on lab cells is published
[J. Lindahl. 2013]	ZnSnO	ALD	18.2	18.5		The use of ALD technique at the CIGS industrial scale is not developed yet.	Single stage process was used for preparing CIGS
[A. Hultqvist. 2010]	ZnMgO	ALD	18.1	16.4			No i-ZnO was used
[T. Kato. 2016]	ZnOS	CBD	22.8	n.a.	-Environmentally friendly material; -Low cost technique	Waste recycling and non-compatibility for an in-line vacuum process	Despite the use of selenization and sulfurization process, no more details are available
[T. Kobayashi. 2016]		CBD	19.0	18.4	Detailed review on ZnOS buffer layer will be presented in the next section		
		ALD	19.7				
[R. Klenk. 2014]		Sputtering	18.3	failed			

Table 3.1: Overview on recent researches and record cells based on alternative buffer layers.

Even though high efficiencies have been achieved using these alternative buffer layers, there is no doubt about the superiority, in terms of cost, of using Zn based buffer layers, since the scarcity of indium is a limiting factor for low manufacturing cost.

On the other hand, a direct comparison between the obtained results, related to the performance of ZnOS, ZnSnO and ZnMgO buffer layers, is, in fact, not so viable since they were not obtained using the same cell fabrication process (absorber quality, deposition method…etc); however, the latest obtained record using ZnOS buffer layer [T. Kato. 2016] might confirm its superiority. That is why we will devote more importance to this buffer layer, and a detailed status will be presented.

But before that, we would like to give a quick status about an alternative way that allowed obtaining a p-n junction and therefore working solar cells without any need for any buffer layer.

3.2.5.Buffer layer free process (p-n buried junction by diffusion)

Back to the early seventies, P.W. Yu et al. have for the first time confirmed the possibility of forming a p-n homo-junction, by changing the conductivity type of CIS from p to n, through Cd diffusion [P.W. Yu.1975]; however no solar cells were presented.

Based on this background, a buffer free process for CIGS solar cells was first developed by the NREL. It was based on the intentional doping of the CIGS surface using a heat-treatment of the absorber either in Cd or Zn- containing solutions [K. Ramanathan. 1998]. As far as we know, the best results obtained using such a process are 15.7% and 14.2% for Cd and Zn doping, respectively [K. Ramanathan. 2002]. This process was mainly developed for environmental reasons: (i) reducing the production waste resulting from using the chemical deposition bath technique and (ii) finding alternative to Cd.

This approach has also opened the door for further prospects: the development of one step absorber-buffer process. T. Sugiyama et al. and S. Nishiwaki et al. have succeeded in preparing buffer layer free cells by either evaporating Zn during the last step of CIGS deposition or right at the end of it [T. Sugiyama. 2000], [S. Nishiwaki. 2003]. They were able to reach 14.8% of efficiency (which is slightly higher than that of their reference cell) [S. Nishiwaki. 2003].

3.3. Zinc oxy-sulfide (ZnOS) layer: properties and deposition techniques

3.3.1.Optoelectronic and structural properties

From the optoelectronic point of view, one important property of zinc oxy-sulfide material is its ability to adopt different band energy levels as a function of oxygen to sulfur ratio [C. Persson. 2006] [S. Sharbati. 2014], which is key property to satisfy Minemoto's condition for high efficiency solar cells [T. Minemoto. 2001]. Theoretical calculations supported by experimental results have revealed that, as the S/S+O ratio increases, the conduction band offset at the interface CIGS (GGI~0.3)/buffer layer changes from a negative one (a cliff ~ -0.3 eV for a pure ZnO) to a positive one (a spike ≥+1eV for a pure ZnS) [S. Sharbati. 2014] [C. Platzer-Björkmana. 2006] [T. Minemoto. 2011] [D. Kieven. 2012].

Furthermore, the conduction band offset changes are known to be accompanied by a variation in the band gap value: starting from ZnO material, as the S/S+O increases, the gap value decreases until reaching a minimum value at S/S+O= 0.5, then it increases for higher ratios. This variation in the gap value reflects the increase and the stability of the valence band (VB) and the conduction band (CB) energy levels for S/S+O in the range 0 to 0.5, respectively; while an increase and a stability of the CB and the VB energy levels, respectively, are the bands characteristics for S/S+O changes in the range 0.5 to 1 [C. Persson. 2006].

One explication for these phenomena is proposed by C. Persson et al. (only valid for 0<S/S+O<0.5): the local ZnS-like bonds in the ZnO host matrix would form a ZnS-like VB defect states and thereby increase the VB energy level [C. Persson. 2006]. For S/S+O in the range 0.5 to 1, one can imagine a similar explanation: local ZnO-like bonds in the ZnS host matrix that form a ZnO-like CB defect states and thereby decrease the CB energy level.

Another consequence of S to O ratio increase, especially in the range 0.5<S/S+O<1, is the increase in resistivity due to the divergence between the conduction band and the Fermi level.

Another very important point that should be highlighted is the dependence of the band gap variation and therefore its minimum value at S/S+O=0.5 on the crystalline structure. X.F. Fan et al. have revealed, through theoretical calculations, that zinc oxy-sulfide material with a wurtzite structure might show a sharper band gap variation (larger bowing parameter), with a lower minimum value of about 2.5eV, compared to the material crystallized in zinc blende structure (minimum value of about 2.9eV) [X.F. Fan. 2009].

Talking about the crystalline structure, one known challenge is getting single phase zinc oxy-sulfide material over the entire composition range. In thermal equilibrium conditions, theoretical calculations predict that single phase is achievable over only a very narrow composition range at relatively low temperature, while a complete solubility is reachable at very high temperature [X.F. Fan. 2009].

Thanks to non-equilibrium environments offered by most of the used techniques for ZnOS thin layer deposition, it is experimentally proved that getting a single phase material is possible over an extended range. C.P. Björkman et al. have reported on single phase ALD deposited thin films for S/Zn in the range 0 to 0.28 and 0.84 to 1, and an amorphous phase in between [C. Platzer-Björkmana. 2006]. Using PLD technique, single phase over a narrower region (S/S+O in the range 0 to 0.23 and 0.94 to 1) was reported bay Y. He et al [Y. He. 2012]. For sputtering technique, one might quote H.L. Pan's work, in which single phase thin films were obtained for S/S+O composition in the range 0 to 0.23 and 0.77 to 1 [H.L. Pan. 2010].

Finally, one important point to highlight is the fact that the effect of ZnOS layer crystalline quality on cells performance is still not so clear, since even using amorphous layers leads to comparable cell efficiencies [C. Platzer-Björkmana. 2006].

3.3.2.Deposition techniques for CIGS solar cells

In table 3.2, we summarized the principle characteristics of the main three techniques used for depositing ZnOS buffer layers (only those that have led to get high efficiency solar cells are reported). Once again, a direct comparison between these results might not be the right thing to do since the used absorber quality is not the same, on one hand and on the other hand, the window layer and/or the post-deposition/final treatment were not identical.

Moreover, an accurate evaluation of R.Klenk's results is not possible at the moment since the efficiency of the reference cell was not published; nevertheless, analyzing their older results obtained using a lower absorber quality (14.5% against 14.9% for the reference cell) [A. Grimm. 2012] might give us an approximate idea about how good their results using sputtered buffer layer are.

On the other hand, it would be fairer to take in consideration, while comparing these results, the fact that the number of groups working on sputtered ZnOS buffer layer might be counted using one hand fingers, and that R.Klenk's results were obtained in a relatively short development time: certainly there is room for further improvement !!.

<table>
<tr><th colspan="2" rowspan="2">Deposition technique</th><th colspan="2">Best reported efficiency (± 0.5cm²)</th><th rowspan="2">Reference</th><th colspan="2" rowspan="2">Advantageous</th><th colspan="2" rowspan="2">Drawbacks</th></tr>
<tr><th>ZnOS</th><th>Ref CdS</th></tr>
<tr><td colspan="2" rowspan="2">CBD</td><td>22.8</td><td>n.a.</td><td>[T. Kato. 2016]</td><td colspan="2" rowspan="2">-Low cost technique;
-Excellent coverage even of very rough surfaces [R.S. Araoz. 2004];
-Surface protective technique;
-High homogeneity over large surfaces
-Surface cleaning before buffer layer deposition [J. Kessler. 1992].</td><td colspan="2" rowspan="2">-Waste recycling (production cost increase);
-Non-compatibility to an in-line vacuum process (time loss);
-Additional rinsing in ammonia is needed to remove the top zinc hydroxide layer[M. Izaki. 2015];
-Very low growth rate, and several baths are needed for a thick layer;
-Difficulty to control oxygen concentration.</td></tr>
<tr><td>19.0</td><td rowspan="2">18.4</td><td rowspan="2">[T. Kobayashi. 2016]</td></tr>
<tr><td colspan="2">ALD</td><td>19.7</td><td rowspan="4">-Compatibility to an in-line vacuum process;
-Ease in controlling O to S ratio</td><td colspan="2">-</td><td colspan="2">-Low growth rate (time loss);
-Substrate heating (energy loss);
-Safety issues related to the use of H_2S gas.</td></tr>
<tr><td rowspan="4">Sputtering</td><td>Reactive sputtering</td><td>13.7</td><td>17.8</td><td>[A. Grimm. 2011]</td><td rowspan="4">-Low cost technique;
-High deposition rate;
-No need for surface rinsing in ammonia;
-Safe technique</td><td rowspan="4">-Low temperature process</td><td rowspan="4">-Possible surface damage induced by energetic particles.</td><td>- Losses in time and energy related to the relatively high deposition temperature (200-300C), a deep diffusion of Zn might result in a detrimental effect [T. Nakada. 2000].</td></tr>
<tr><td rowspan="2">Co-sputtering</td><td>8.0</td><td>14.7</td><td>[M. Buffiere. 2011]</td><td>-Classical co-sputtering: elemental distribution inhomogeneity [M. Buffiere. 2011].</td></tr>
<tr><td>11.1</td><td>12.2</td><td>[T. Minemoto. 2011]</td><td>-ALD-inspired co-sputtering: material and time losses.</td></tr>
<tr><td>Ternary target</td><td>18.3</td><td>n.a.</td><td>[R. Klenk. 2014]</td><td>-Hill like S to O ratio distribution with high S concentration at the center (most likely related to the distribution of sputtered elements inside the plasma!!) [R. Klenk. 2014].</td></tr>
</table>

Table 3.2: Overview on most efficient techniques for ZnOS buffer layer deposition.

3.4. ZnOS buffer layer thickness

In the contrary to the largely accepted thickness of the CdS buffer layer (±50nm) as a reference value for high efficiency solar cells, several ZnOS buffer layer thicknesses ranging from very thin (some nanometers) to relatively thick (more than 100nm) are reported. One point that should be highlighted is the dependence of the upper layer (window layer) nature, thickness and deposition technique on the chosen thickness of the ZnOS buffer layer.

3.4.1.Ultra-thin (≤5nm)

The most impressing work based on the use of an ultra-thin ZnOS buffer layer is that published by C. Platzer-Björkman et al. They have shown that it is possible to reach 16.4% of efficiency using only few nm-thick ALD-deposited ZnOS buffer layer (1-2nm) with S to Zn ratio in the range 0.8-0.9 (vs 15.8% for the reference cell) [C. Platzer-Björkman. 2006]. In their work, the sputtered i-ZnO layer was replaced by an ALD-deposited one.

It is also interesting to note that Solar Frontier process, for their previous world record cell (22.3%), is also based on the use of an ultra-thin ZnOS buffer layer (~5nm-thick, presented within the 2016 EMRS conference). However, no more details were given.

3.4.2.Thin (10-30nm)

In a recent work, T. Kobayashi et al. have shown efficiency as high as 19.0% using 10-20nm-thick CBD-ZnOS buffer layer (vs 18.4% for the reference cell). Surprisingly, such a high efficiency was obtained without an additional i-ZnO or ZnOMg layer. Most likely, the good coverage related to the CBD technique and the high resistivity of the ZnOS layer are the key parameters limiting shunt paths. To the best of our knowledge, this is the highest efficiency obtained using a buffer layer thickness within this range [T.Kobayashi. 2016]. In table 3.3, we summarize the best reported works using 10-30nm-thick ZnOS buffer layer.

Reference	[T.Kobayashi. 2016]	[W. Witte2. 2013]	[C. Platzer-Björkman. 2006]	[K. Ramanathan. 2012]	[D. Hariskos. 2009]
Thickness	10-20	20-30	30	20-30	20-30
Efficiency%	19.0	16.5	16.4	18.5	18
Ref. cell	18.4	16.6	15.8	-	-
Dep. tech	CBD	CBD	ALD	CBD	CBD
S/(S+O)	0.6-0.7	0.7	-	0.4	-
Remarks	No i-ZnO MOCVD ZnO:B HLS, 0.5cm^2, ARC	Sputt ZnOMg Sputt ZnO:Al 0.5cm^2, No ARC	Sputt ZnO/ Sputt ZnO:Al No ARC	No i-ZnO ZnO:X ARC	ZnOMg Sputt ZnO:Al ARC

Table 3.3: Best reported works using 10 to 30nm-thick ZnOS buffer layer.

3.4.3.Medium thickness (50-60nm)

For this range of thicknesses, some groups were also able to overpass the 18% threshold using different deposition techniques, as shown in table 3.4.

T. Kobayashi et al. have also reported on high efficiency cells using either ALD (19.7%) [T. Kobayashi. 2016] or CBD (18.8%) [T. Kobayashi. 2014] techniques. Another interesting result [R. Klenk. 2014] is that related to the use of sputtered buffer layer for achieving 18.3% of efficiency.

Reference	[T. Kobayashi. 2016]	[T. Kobayashi. 2014]	[R. Klenk. 2014]
Thickness	50	50	60
Efficiency%	19.78	18.8	18.3
Ref. cell	18.4	-	-
Dep. tech	ALD	CBD	RF-Sputtering
S/(S+O)	0.33	0.6	0.19-0.22
Remarks	100nm- i-ZnO (ALD) MOCVD ZnO:B ARC, HLS, 0.5cm^2	No i-ZnO MOCVD ZnO:B ARC, HLS, 0.5cm^2	No i-ZnO/ Sputt ZnO:Al ARC, 0.5cm^2

Table 3.4: Best reported works using 50 to 60nm-thick ZnOS buffer layer.

3.4.4.Relatively thick (≥100nm)

Finally, a very thick buffer layer was also used, and it has yielded in cells efficiency of around 18%: 18.1% [T. Nakada. 2002], 18.5% [R. N. Bhattacharya. 2004] and 18.6% [M.A. Contreras. 2003], all of them were obtained using CBD process and no highly resistive i-ZnO upper layer was needed.

3.5. Buffer layer annealing

Regardless of the buffer layer nature and deposition technique, air annealing just after its deposition was found to be a critical step for high efficiency solar cells. The physical phenomena behind that will be summarized in the following: some of them are common to all buffer layers, others are not.

3.5.1.CdS layer

In case of using a CdS buffer layer, the post deposition annealing was found not to have an effect on the CdS buffer layer itself (despite the slight increase in transmittance reported by Y.D Chung et al. [Y.D Chung. 2011]), but rather on the surface of the CIGS layer.

Other than the inversion type at the absorber surface originated from thermal induced Cd diffusion, changes in defects density at the CIGS surface were also observed.

In an early time, D. Cahen et al. have attributed the enhancement in cells performance, resulted from air or O_2 annealing, to the O-induced neutralization of donor states (Se vacancies and In_{Cu} anti-sites) at the grain surface and boundaries, and therefore eliminating recombination centers and increasing the effective doping level. This explanation was supported by previous observations: (i) a degradation in cells efficiency in case of H_2 annealing; (ii) no effect of air annealing on already selenized samples. It was also found that annealing time and temperature are grain size dependent: lower temperature and shorter time for larger grain CIGS layer (for more details, please have a look on [D. Cahen. 1988] and references therein).

Combining the admittance spectroscopy and the deep level transient spectroscopy techniques, a deep investigation on the effect of annealing was carried out by R. Herberholz et al. They have confirmed the previous presumptions by showing the progressive attenuation over annealing time of the peak correspond to the shallow holes traps, while the one related to the bulk holes traps remains unaffected [R. Herberholz. 1997].

Finally, one should note that the optimal annealing time and temperature, commonly reported for high efficiency CdS based solar cells, are in the ranges of 1 to 2min and 180 to 200°C, respectively [I. Repins. 2008] [A. Chirila. 2013].

3.5.2.ZnOS layer

In case of ZnOS buffer layer, multi effects of the post deposition annealing were reported. In addition to the inversion type and passivation of the CIGS surface (same effect as in the case of using a CdS buffer layer) [W. Witte2. 2013], [T. Nakada. 2000], the effect of the post deposition annealing on the enhancement of the CBD-buffer layer stoichiometry and therefore the adjustment of the band alignment have also been reported [W. Witte2. 2013].

Furthermore, a longer annealing time is commonly reported (about 10 min) and it is justified by the low diffusivity of Zn (compared to Cd) in CIGS; whereas, the annealing at higher temperature (higher than 200°C) is reported to be a cell performance killer (due to the excess diffusion of Zn into CIGS) [T. Nakada. 2000].

3.6. Partial conclusion

In this first part, we have summarized the commonly reported roles of the buffer layer. The origins of the superiority of commonly used CdS buffer layer were clarified, and the main criteria of the suitable alternative were given. We have also presented a non-exhaustive list of already developed alternatives, their advantages and drawbacks.

More effort was devoted in summarizing the most important properties of ZnS_xO_{1-x} buffer layer (only those might help in improving CIGS solar cells), as well as the advantages and drawbacks of commonly used deposition techniques.

More important, classifying previously reported works on high performance cells as a function of the used ZnS_xO_{1-x} buffer layer thickness (independently of the deposition technique), allowed us to extract the following conclusion: ‘’high efficiency solar cells are

achievable whatever the ZnS_xO_{1-x} buffer layer composition is; however, the higher the x composition is, the lower the thickness should be''.

In the next part, we will show our contribution in the development of both CBD-CdS and room temperature sputtered ZnS_xO_{1-x} buffer layers.

Part B. Experimental results

3.7. Chemical bath deposition of CdS layer

3.7.1.Deposition protocol

On figure 3.1 is reported the flow chart of the developed CBD process for CdS layer.

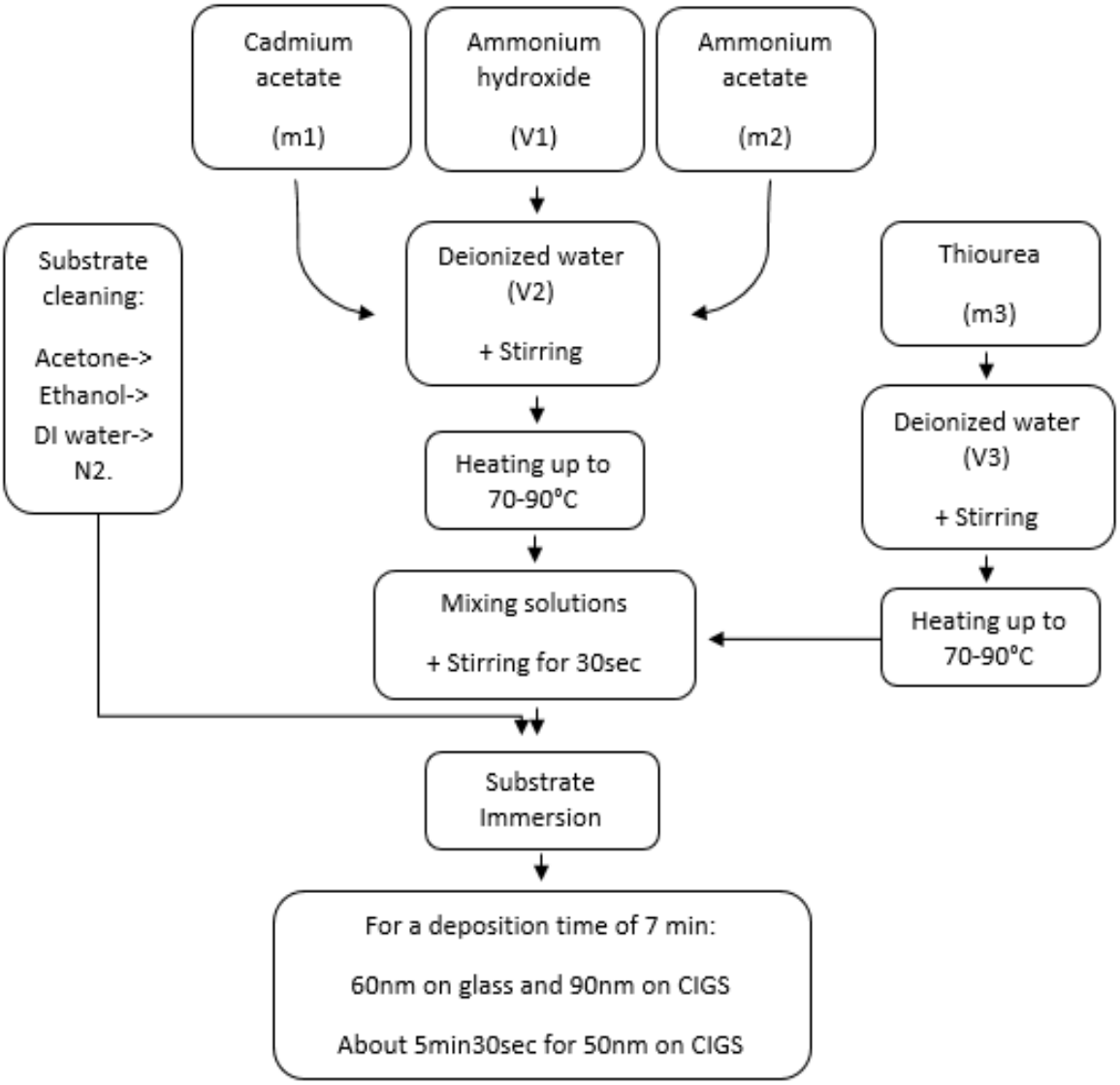

Figure 3.1: Typical experimental protocol for CBD-CdS buffer layer.

It is worth to note that using the above described protocol, immediate rinsing in deionized water after CdS deposition was found to be necessary in order to remove loose CdS particles from the surface.

Another very important point ''based on our experience'' to highlight is the fact that following a modified protocol e.g. changing the temperature of solutions mixing and/or the time/temperature of substrate immersion might lead to dramatic consequences!!

For example, mixing the two solutions at room temperature and then heating up was found to lead to the appearance of a cotton-like very thick film (few mm) on the substrate as long as this later is kept inside the bath. This cotton-like film was found to disappear once the substrate is removed from the bath; however, no CdS film remained on the substrate (only fibrous-like wastes were observed on the surface).

3.7.2.Growth and coverage

CdS uniform coverage of the CIGS surface is known as a corner stone for high efficiency solar cells due to its role as a protection layer from high energy sputtered particles, on one hand and on the other hand, as a limiting shunt paths layer. Consequently, we have paid a special attention to the optimization of the deposition conditions of this layer in order to ensure a good coverage for a standard thickness (50nm).

To do so, the influence of ammonium hydroxide concentration on surface coverage was investigated, and the obtained results are shown in figure 3.2. It was found that the high ammonium hydroxide concentration deposited layer shows a poor coverage with nanocrystallite sizes in the range of 100 to 150nm, while an optimum ammonium hydroxide concentration leads to a better coverage uniformity and a more uniform nanocrystallite size distribution (around 50nm) were achieved. It is worth to note that in both conditions, a CdS layer thickness of 50nm was achieved by tuning the deposition time.

The very poor coverage observed in case of using high ammonium hydroxide concentration deposition solution is most probably originated from the domination of the homogenous reaction which is more preferable in such a condition [I.O. Oladeji. 1997].

In addition to the improved surface coverage using low ammonium hydroxide concentration bath, this deposition condition would also be beneficial for CIGS solar cells fabrication since previous studies have shown that ammonium hydroxide might react with CIGS surface leading to a preferential etching of indium and gallium and therefore the formation of a thin Cu_2Se layer might take place [C.L. Perkins. 2005].

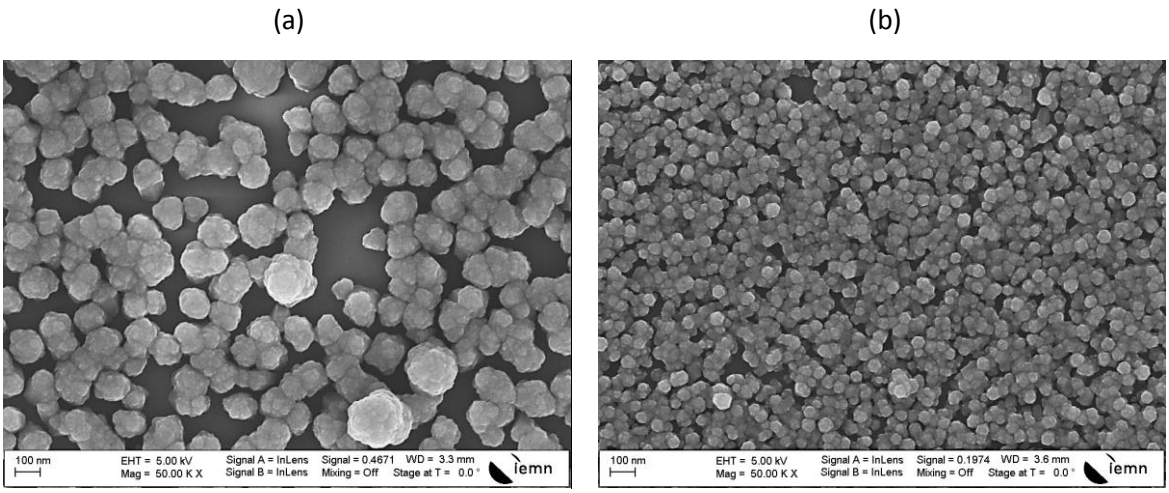

Figure 3.2: SEM images of 50 (±5) nm-thick CBD CdS layers on glass substrate at a bath temperature of 70°C. (a) Using ammonium hydroxide concentration of M. (b) Using ammonium hydroxide concentration of M/2.

Even though optimized ammonium hydroxide concentration has resulted in an improved surface coverage, some poorly covered small zones were observed.

Further improvement of the surface coverage was possible by increasing the deposition bath temperature, as can be seen in figure 3.3. Once again, the deposition time was tuned in order to get almost the same thickness for all samples (50±5nm).

An optimum coverage was achieved at 80°C, while further increase in temperature (90°C) was found to have almost no effect. Furthermore, the nanocrystallite size was found to be unchanged as the deposition temperature increases (around 55nm). However, the growth rate was found to be temperature dependent: the higher the temperature, the higher the growth rate. The measured growth rates for deposition bath temperatures of 70°C, 80°C and 90°C are about 3.33nm/min, 9.16nm/min and 10nm/min, respectively. Similar growth rate and nanocrystallite size dependences on deposition bath temperature were previously observed by H. Moualkia et al. [H. Moualkia. 2009]. Finally, it is worth to highlight that the close growth rates for bath temperatures of 80°C and 90°C might be at the origin of the observed coverage similarity.

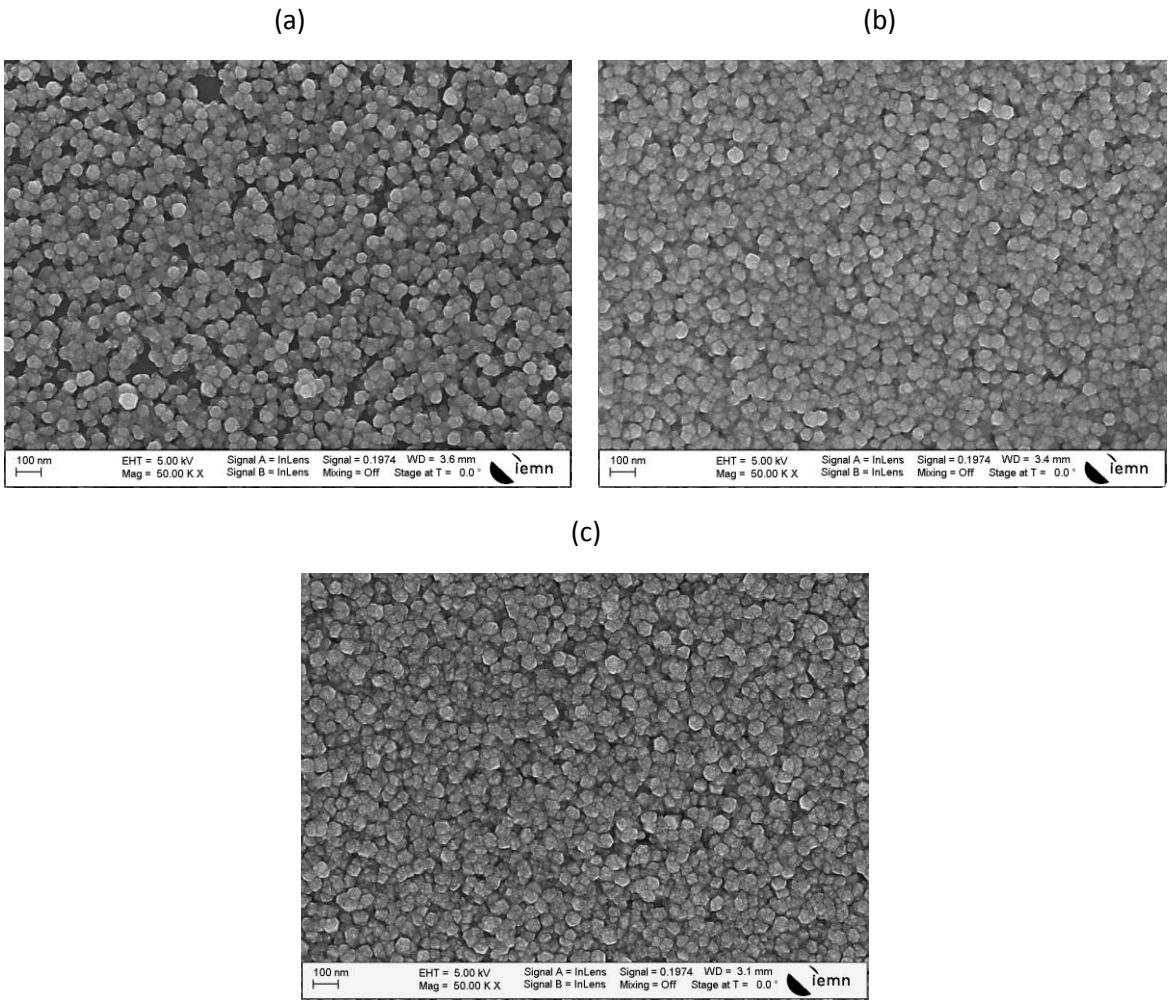

Figure 3.3: SEM images of 50 (±5) nm-thick CBD CdS thin films on glass substrate obtained at different bath temperatures. (a) 70ºC. (b) 80ºC. (c) 90ºC.

Furthermore, the coverage dependence on the deposited thickness was also investigated and the obtained SEM images are presented in figure 3.4. The measured thicknesses after deposition times of 6min, 11min and 15min were 50nm, 80nm and 90nm, respectively.

First point to highlight is the changes in deposition rate along the deposition process. This is known as a characteristic of the CBD process during which the growing layer might go through three phases: (i) incubation or latent period, (ii) high growth rate phase (heterogeneous reaction) and (iii) saturation phase (homogeneous reaction).

Furthermore, it was found that the hail-like nanocrystallites become bigger and the surface coverage denser as the layer thickness increases from 50nm to 80nm. Further improvement in surface density was observed for 90nm-thick layer; however, the nanocrystallites were found to have lower size (note that the SEM image C was taken at magnification of 10^5).

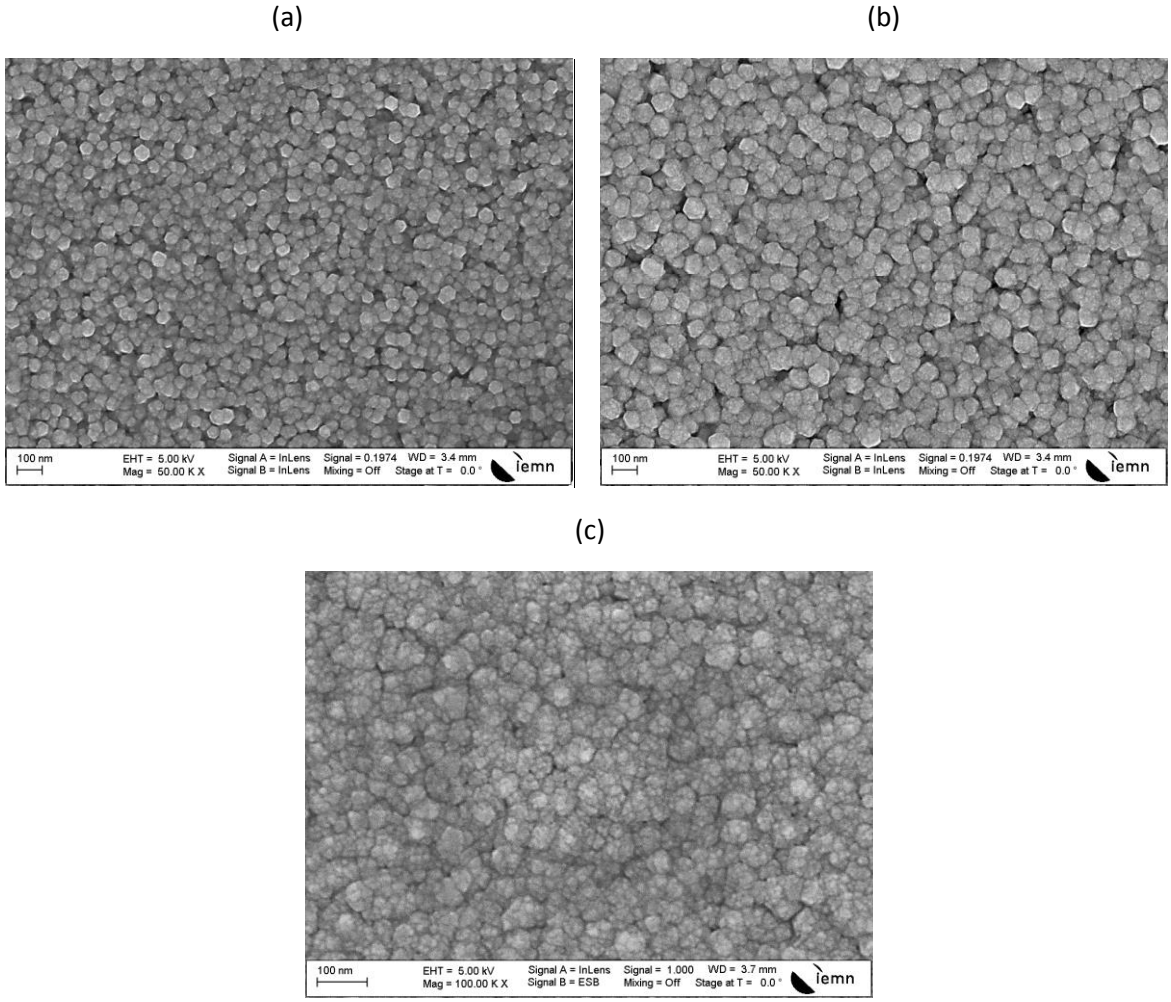

Figure 3.4: SEM images of CB-deposited CdS thin films at 80°C for different deposition times. (a) 6min. (b) 11min. (c) 15min.

Finally, one very interesting point to highlight is the observed change in CBD-CdS thin film thickness in case of deposition on CIGS-covered substrate. Using a recipe that is supposed to result in 50nm-thick CdS layer (already proved on glass substrate), a thickness of almost 90nm was measured on CIGS-covered substrate, as can be seen in figure 3.5 (a) and (b). However, by adjusting the deposition time, a 50 (±5) nm-thick CBD-CdS layer was successfully deposited on CIGS-covered substrate, as can be seen in figure 3.5 (c).

On the other hand, the SEM cross sectional images of deposited CdS thin films on both glass and CIGS-covered substrates have revealed the excellent surface coverage using standard 50nm-thick CdS layer, as shown in figures 3.5 (a) and (c).

N.B: please note that the SEM cross sectional images were taken at different magnifications either for more clarification or due to the very low film thickness and therefore the difficulty we faced to get clear and non-distorted SEM scan at high magnification.

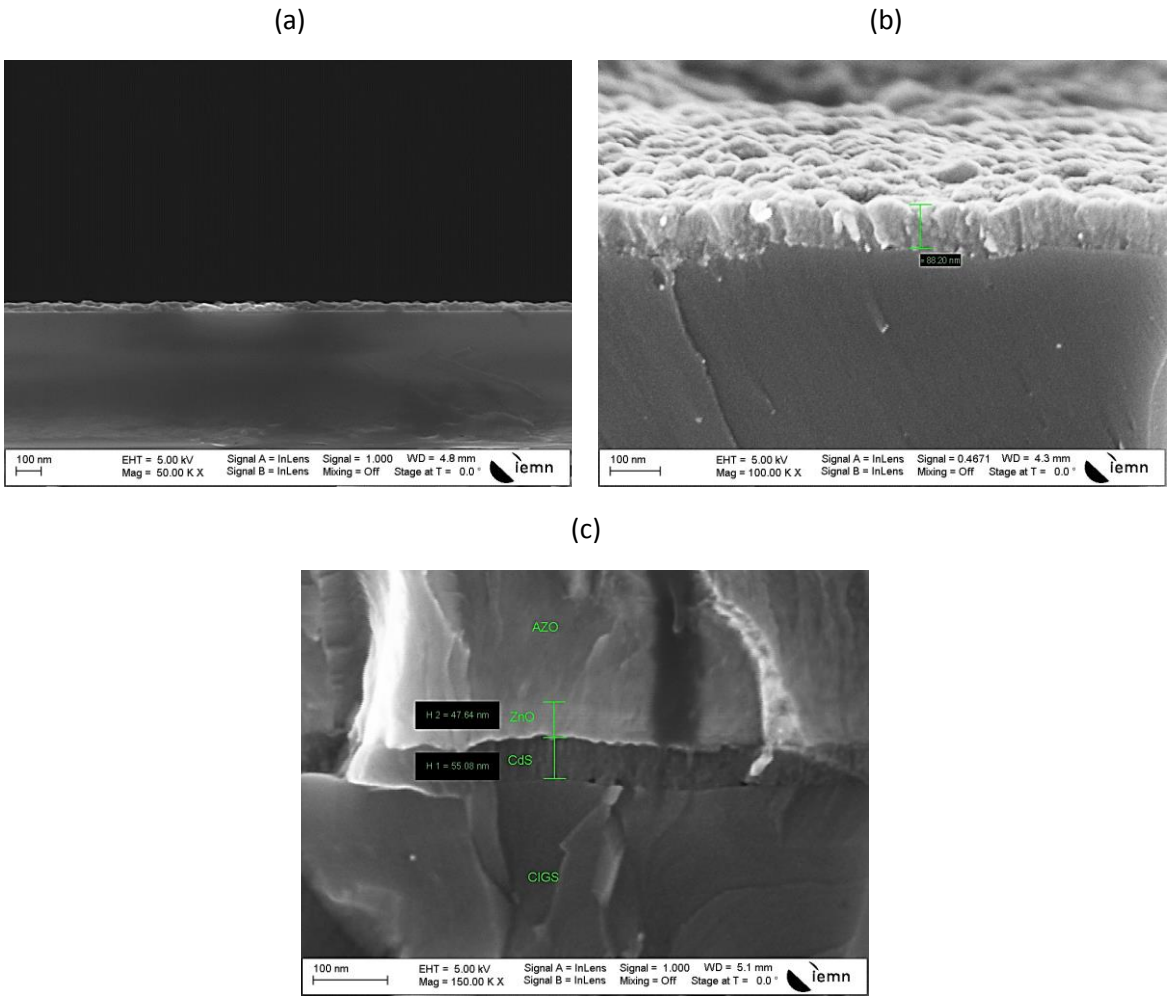

Figure 3.5: Cross sectional SEM images of CBD CdS thin films on different substrates. (a) On glass substrate (50 nm). (b) On CIGS-covered substrate (90 nm, same deposition time as in (a)). (c) CIGS solar cell stack with a zoom on the 50nm-thick CdS film (adjusted deposition time compared to (b) in order to get 50 nm thickness).

3.7.3.Structural and optical properties

In order to evaluate our deposition process, structural and optical properties of the obtained 50nm-thick CdS layer deposited at 80°C (on glass substrate) were investigated.

As can be seen in figure 3.6, the XRD analysis of our deposited CdS thin film reveals a strong preferred orientation along either the (002) of the hexagonal structure or the (111) of the cubic structure, confirming the polycrystalline nature of the thin film.

Furthermore, neither other diffraction peaks characteristic of the CdS phase nor those characteristic of other phases, such as cadmium oxides, were detected; however, the non-detection of diffraction peaks corresponding to cadmium oxide phases does not exclude their presence since they might exist in an amorphous state.

From literature, similar results have been previously obtained by T.L. Chu et al [T.L. Chu.1992]. They have attributed the observed preferred orientation to the controlled nucleation process associated with the low growth rate. On the other hand, I.O. Oladeji et al. have reported that

CBD-CdS thin films deposited on glass substrate rather has a zinc-blende (cubic) structure [I.O. Oladeji. 2000].

However, the orientation of CdS thin film deposited on CIGS cannot be guessed based on the obtained one on glass substrates since several previous results have shown a sort of dependence between the orientation of the CdS layer and that of the CIGS layer [M.J. Furlong. 1998] [T. Nakada. 1999] [D. Abou-Ras2. 2005].

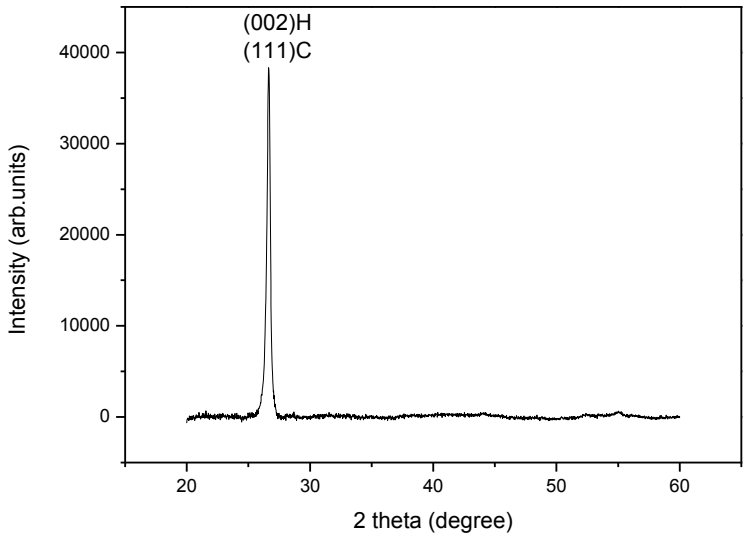

Figure 3.6: XRD patterns of 50nm-thick CB-deposited CdS thin film on glass substrate at 80°C.

Concerning the optical properties, transmittance measurements have been performed and a typical obtained spectrum is displayed in figure 3.7. It was found that optical transmittance decreases continuously from 87 % at 900nm down to about 69% at around 540nm with almost a constant slope. At this wavelength, a sharp decrease in transmittance (down to 51%) was observed, which corresponds to the band gap of the CdS thin film. The measured band gap value using Tauc's method is about 2.25eV, as shown in the inset of figure 3.7. At lower wavelengths, the optical transmittance was found to keep decreasing with almost the same slope observed in high wavelength region. Finally, the cut-off in transmittance at short wavelength is attributed to the absorption of the substrate.

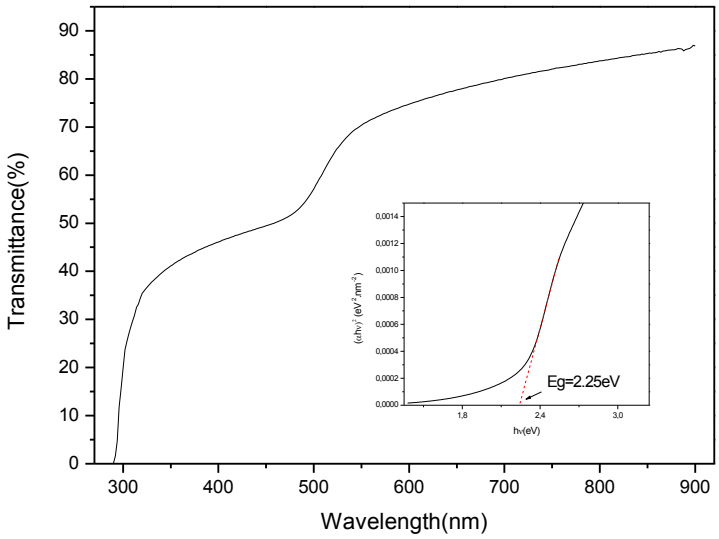

Figure 3.7: Optical transmittance spectra of 50nm-thick CB-deposited CdS thin film on glass substrate at 80°C. The inset shows the extracted band gap value.

3.8. Sputtered ZnOS layer

3.8.1.Reactive sputtering process

Based on some already published works dealing with zinc oxysulfide thin films deposition [B.K. Meyer. 2004] [H.L. Pan. 2010] [H. Xu. 2013] [A. Grimm. 2011], supposed zinc oxysulfide thin films have been reactively sputtered from a pure zinc sulfide target. The only difference compared to those works is that a room temperature deposition process was used.

Since the use of high temperature deposition process does not meet the requirements for simple in line processing, on one hand and on the other hand, might have a harmful effect on the CIGS solar cell, we have checked out whether a room temperature reactive sputtering deposition process leads to similar results or not.

Unfortunately, the obtained results were disappointing. Previous theoretical and experimental results have shown that the band gap variation of zinc oxysulfide thin films as a function of sulfur to oxygen ratio shows a valley-like curve with a minimum value at a ratio of 0.5 [X.F. Fan. 2009] [B.K. Meyer. 2004] [A. Grimm. 2011].

In contrast, our room temperature reactively sputtered thin films have shown completely different characteristics. The optical transmittance was found to increase as the oxygen to argon ratio increases (as displayed in figure 3.8), accompanied with a slight shift of the cut-off in transmittance towards lower wavelength (blue shift) and therefore a slight increase in the optical band gap value, as shown in figure 3.9.

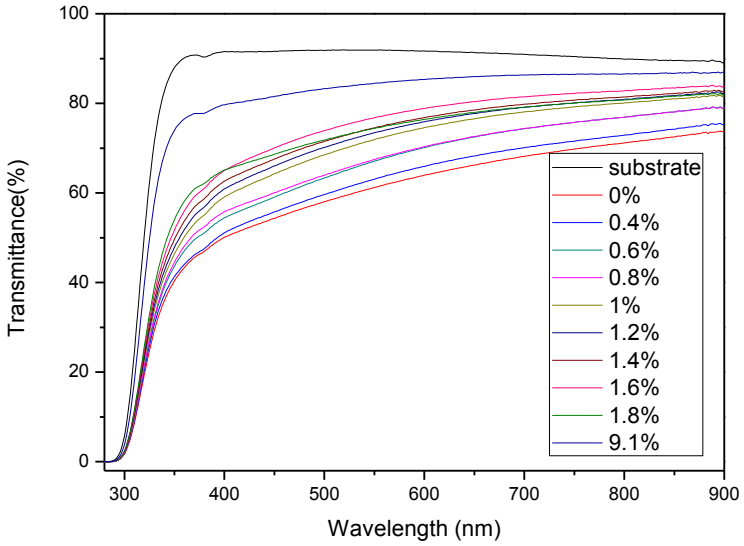

Figure 3.8: Optical transmittance spectra of 50nm-thick reactively sputtered thin films from a pure ZnS target, using different oxygen to argon gas ratios.

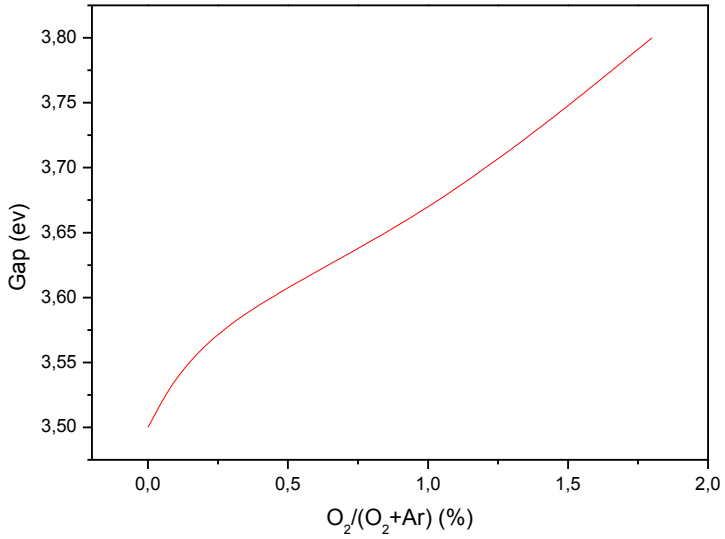

Figure 3.9: Optical band gap variation of 50nm-thick reactively sputtered thin films from a pure ZnS target, as a function of oxygen to argon gas ratio.

One possible explanation is that the high energy bombardment of oxygen atoms which hereby implies a degraded crystalline quality, as clearly shown in figure 3.10, might be counterbalanced in case of using high temperature deposition process. Consequently, high temperature deposition is a key parameter for reactively sputtered zinc oxysulfide thin films. However, high temperature deposition process was not our driving parameter and an alternative solution was then looked for.

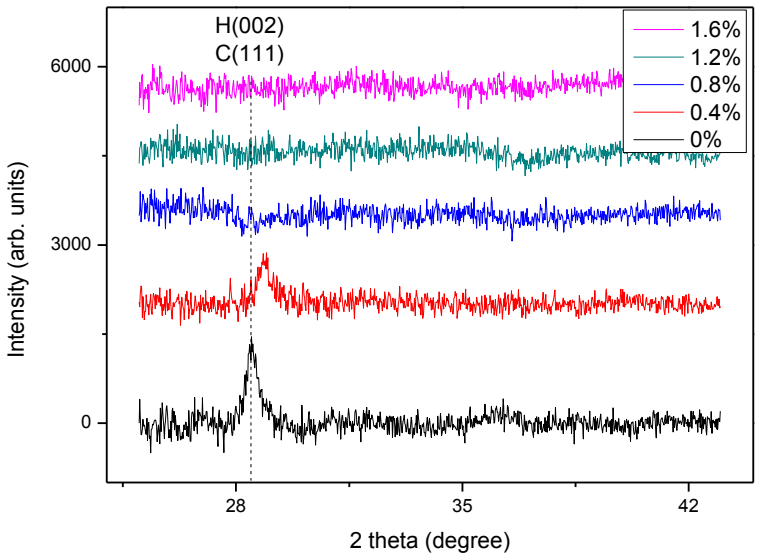

Figure 3.10: XRD spectra of 50nm-thick reactively sputtered thin films from a pure ZnS target, as a function of oxygen to argon gas ratio.

3.8.2.ALD-inspired sputtering process

For scientific/intellectual honesty, it is worth to note that such a process was used for the first time by T. Minemoto's group for the deposition of zinc oxysulfide thin films (they have even previously used it for studying magnesium-doped zinc oxide thin films) [T. Minemoto. 2011] [A. Okamoto. 2011].

3.8.2.1. Deposition protocol

Two targets, ZnO and ZnS, have alternatively been sputtered using a continuous rotation of the substrate holder[1]. Depending on the applied power (and pulsed-DC duty cycle) to each target, it was possible to deposit 100nm-thick ZnS_xO_{1-x} films in which the composition, x, can be tuned between 0 and 1. The adjusted applied sputtering power to each target (for a given composition) and deposition time (for 100nm-thick thin films) are summarized in figure 3.11.

Furthermore, it is important to note that the mentioned composition was not directly measured but rather empirically calculated. To do so, thin films were considered to have the same density, which is not completely true because of the thin films density dependence on sputtering power; however, the error is believed not to be so large, therefore the indicated composition values are approximate and not exact.

On the other hand, we would highlight that the multilayer structure, that one can have as a first reflection for the overall film structure using such a deposition technique, should not be obtained due to (i) the low deposited thickness each time the substrate passes under one target

[1] Due to the deposition chamber configuration/limitations, ZnO and ZnS targets could not be deposited the same way: one has been deposited in RF mode(ZnS) and the second one in pulsed-DC mode (ZnO).

(less than 2.3nm for the highest sputtering power) and (ii) the growth mode of sputtered thin films (Volmer-Weber).

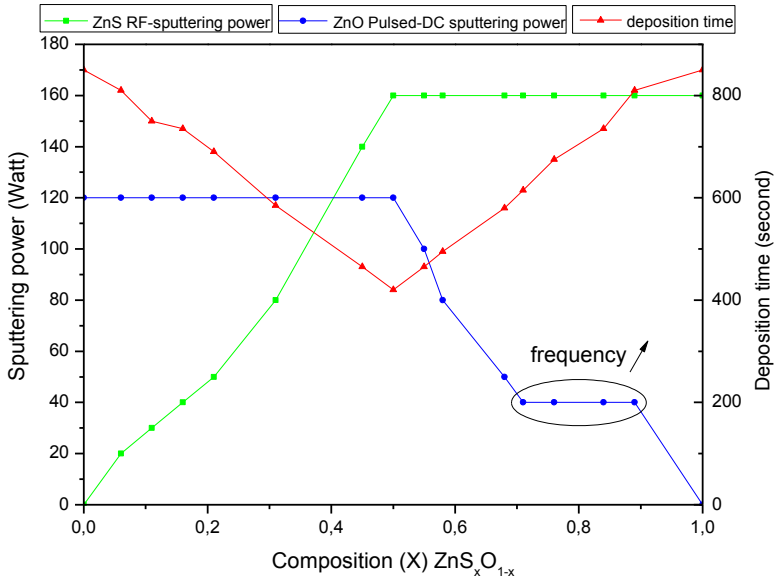

Figure 3.11: Sputtering deposition conditions for 100nm-thick ZnS_xO_{1-x} thin films.
(in order to tune the thickness of ZnO films, sputtering pulsed-DC power was decreased. Nevertheless, it cannot be decreased linearly down to zero without deactivating the plasma. In order to avoid this phenomenon, frequency parameter has been increased resulting in the decrease of the mean sputtering power)

3.8.2.2. Optical characterization

Optical transmittance measurements are presented in figure 3.12. Contrary to the case of using room temperature reactive sputtering, optical transmittance variations of the ALD-inspired deposited thin films are consistent with literature reports: a clear shift of the cut-off in transmittance toward higher wavelengths (red shift) as the sulfur to oxygen ratio decreases (1>x>0.5) down to roughly x = 0.5, then it shifts backwards (blue shift) as x decreases down to 0.

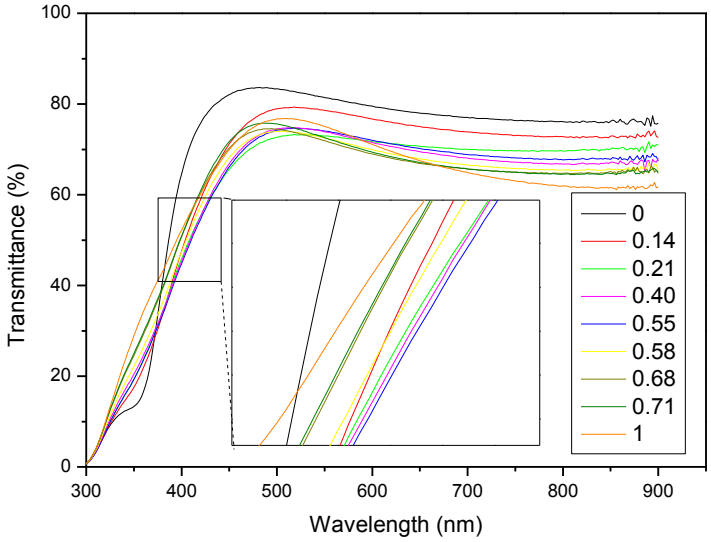

Figure 3.12: Optical transmittance spectra of 100nm-thick ZnS_xO_{1-x} thin films with various compositions (x). The inset shows a zoom on the cut-off in transmittance region.

The shift of the cut-off in transmittance reflects the band gap variation which origin is explained in detail in § 3.3.1.

Using Tauc's method, the band gap values were extracted and are displayed in figure 3.13. A clear valley-like curve representing the optical band gap variation as a function of the composition was obtained. Furthermore, by fitting the experimental curve, an optical bowing parameter (b) of 1.3eV was deduced ($Eg_{(ZnS)}$ = 3.5eV, $Eg_{(ZnO)}$=3.2eV).

Comparing to previously reported results, the deduced bowing parameter (1.3) and the valley minimum (~3eV) are found to be different: B.K. Meyer et al., A. Grimm et al. and others have reported on a bowing parameter and a valley depth of 3 and 2.6-2.8eV, respectively [B.K. Meyer. 2004] [A. Grimm. 2011].

On the other hand, theoretical calculations have shown that the bowing parameter is dependent on the crystalline structure with a higher value for the wurtzite structure compared to the zinc blende structure [X.F. Fan. 2009].

Comparing our results with those theoretical calculations, an initial conclusion was taken, attributing the low value of the bowing parameter to possible zinc blende crystalline structure; however, XRD analyses (see §3.8.2.3) have rapidly disproved/controverted this prediction and confirmed the wurtzite structure of our deposited thin films: so we cannot link this low value of bowing parameter to a matter of crystalline structure (at least in our case).

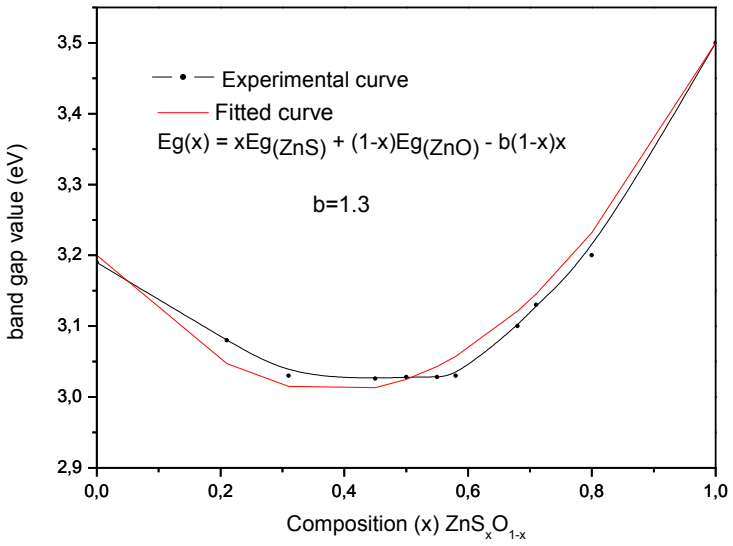

Figure 3.13: Optical band gap variation of 100nm-thick ZnS_xO_{1-x} thin film as a function of the composition x.

For a more accurate comparison to the other groups' results, optical transmittance of thicker (350nm) thin films was investigated and the obtained results are displayed in figure 3.14. On the other hand, since the band gap of pure ZnS thin films was found to be thickness dependent [H.R. Dizaji. 2011], it is more realistic to compare the shift of the cut-off wavelength of the optical transmittance between pure ZnS and ZnS_xO_{1-x} films that have the same thickness.

As can be seen in figure 3.14, thicker ZnS_xO_{1-x} films exhibit more important shift than thinner films. This result might explain the observed difference in bowing parameter, previously discussed.

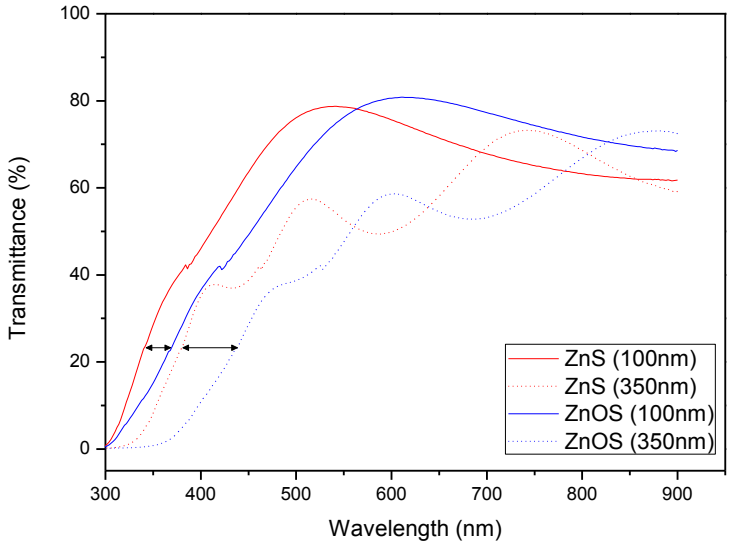

Figure 3.14: Optical transmittance spectra of ZnS and $ZnS_{0.34}O_{0.64}$ thin films with different thicknesses.

3.8.2.3. Structural and morphological characterization

In parallel to the optical transmittance, the structural properties and the surface morphology of the obtained thin films were investigated by means of XRD and SEM, respectively. For more clarity, results are divided in three parts: single phase oxygen rich ZnS_xO_{1-x} thin films, multiphase intermediate composition thin films and single phase sulfur rich ZnS_xO_{1-x} thin films.

** Oxygen rich ZnS_xO_{1-x} thin films ($0 \leq x \leq 0.21$)*

As can be seen in figure 3.15, XRD analyses have revealed the polycrystalline nature and the single hexagonal wurtzite structure of ZnS_xO_{1-x} thin films which composition x is in the range 0 to 0.21 (no secondary phases such as ZnO_2, $ZnSO_4$,… were observed), confirming the complete solubility of sulfur in ZnO matrix and the formation of a solid solution.

Furthermore, all thin films have shown a strong (002) preferred orientation along the c-axis. This preferred orientation might be attributed to both the surface energy of this (002) plan which is the lowest for ZnO [N. Fujimura. 1993] and the sputtering technique. Moreover, very weak (200), (103) and (004) diffraction planes were also detected, as can be seen in the inset of figure 3.15a.

On the other hand, as the composition in sulfur increases, the diffraction peak position shifts towards lower diffraction angles, evidencing the increase of the inter-planes distance. Furthermore, a degradation of the crystalline quality was observed as the composition in sulfur increases, as shown in figure 3.15b. This is most likely due to the induced distortion of the host matrix resulted from the incorporation of higher ionic radius element (1.40 Å for oxygen compared to 1.84 Å for sulfur).

Moreover, scanning electron microscopy images, as given in figure 3.16, reveal the coast pebbles shape-like surface morphology of the oxygen rich ZnS_xO_{1-x} thin films. However, the grain size was found to decrease as the composition in sulfur increases, which is in good consistency with the XRD results. Finally, the variation of the unit cell parameters of the wurtzite structure (a(=b) and c) deduced from the XRD measurements was found to verify Vegard's law (unit cell parameters vary almost linearly with composition as far as the formation of a solid solution is possible), as clearly shown in figure 3.17.

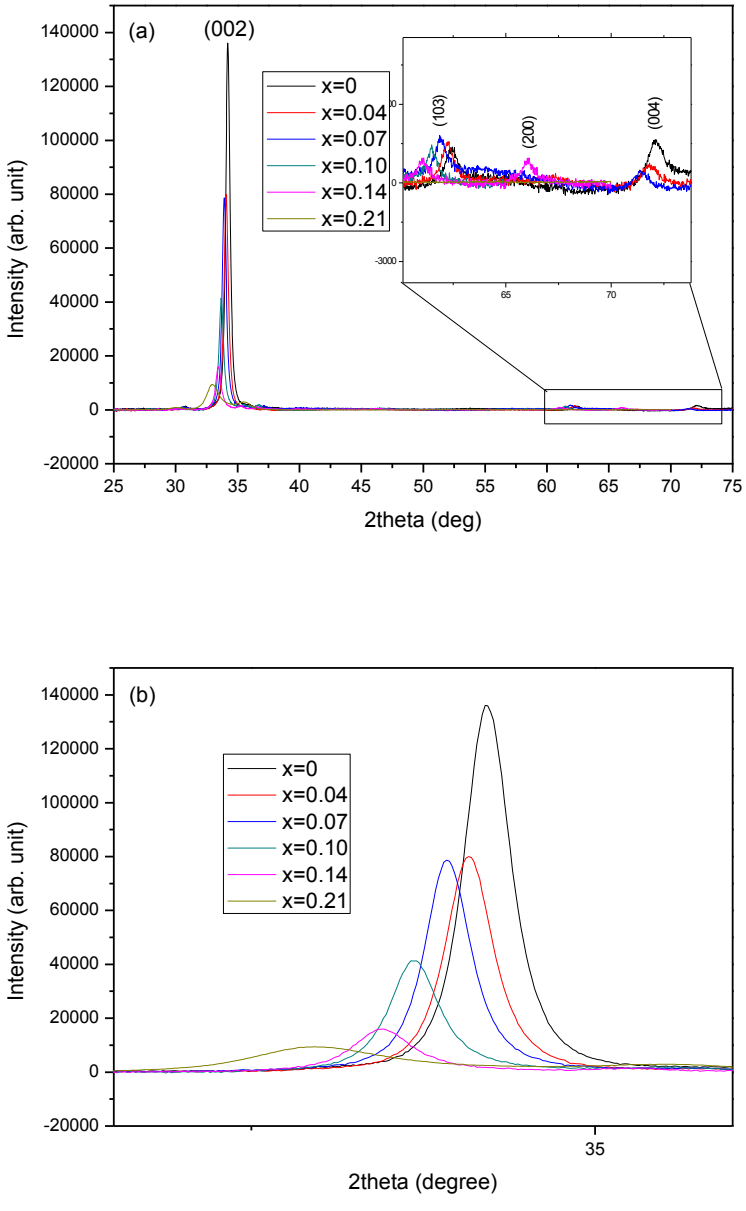

Figure 3.15: (a) XRD spectra of 100nm-thick ZnS_xO_{1-x} thin films: x ranges from 0 to 0.21. (b) Zoom in XRD spectra.

(x = 0) (x = 0.04)

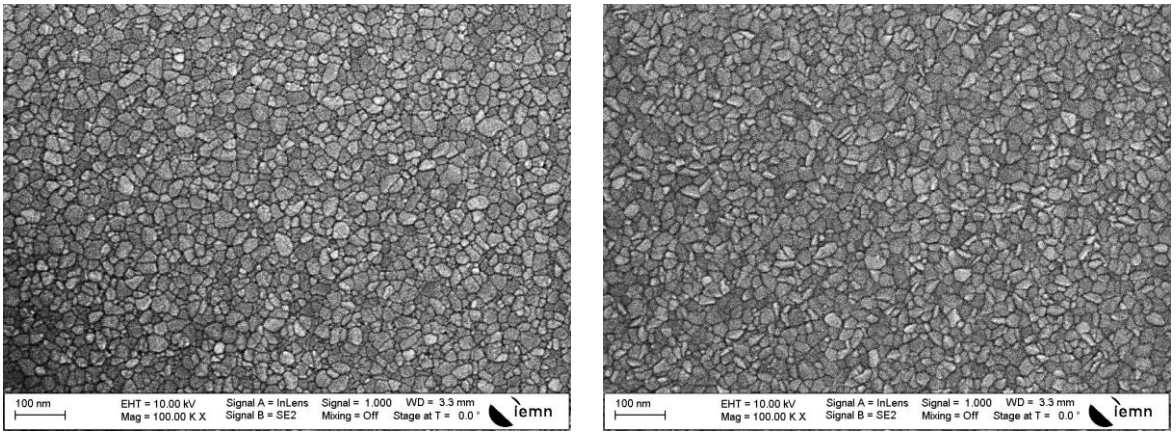

(x = 0.07) (x = 0.10)

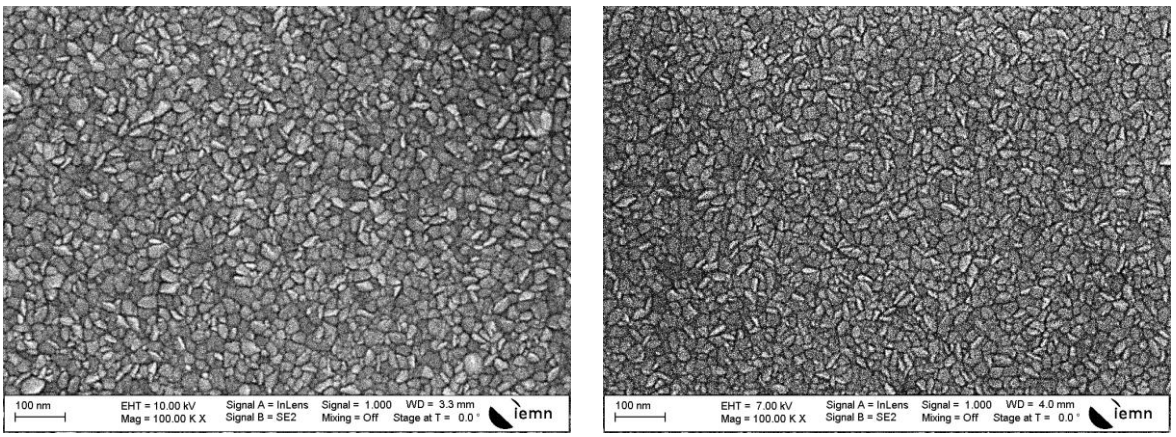

(x = 0.14) (x = 0.21)

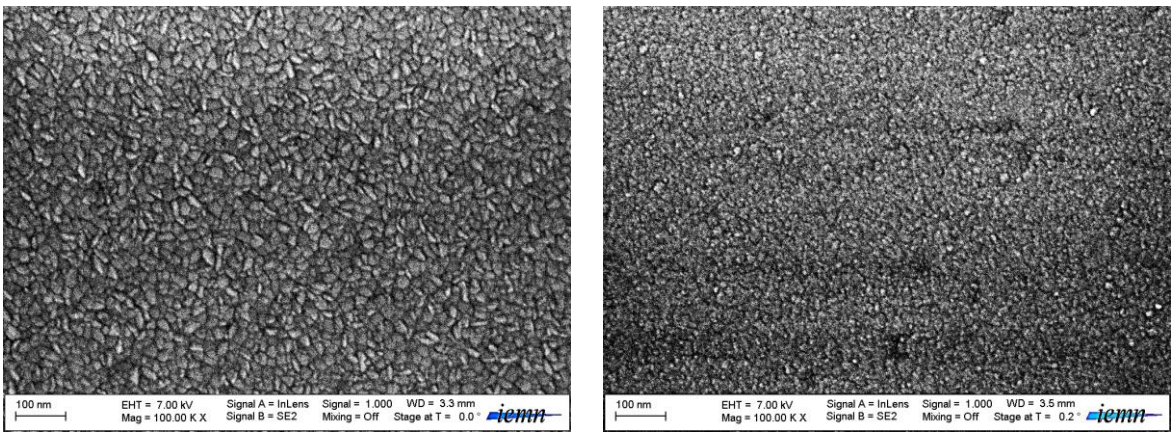

Figure 3.16: SEM images of 100nm-thick ZnS_xO_{1-x} thin films: x ranges from 0 to 0.21.

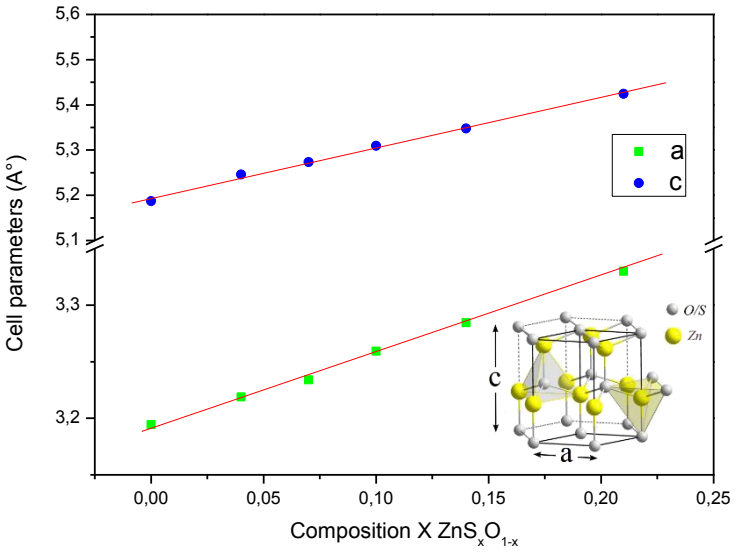

Figure 3.17: Unit cell parameters variation as a function of the composition.

**Intermediate composition ZnS_xO_{1-x} thin films ($0.31 \leq x \leq 0.66$)*

Even though sputtering is a non-equilibrium thermodynamic process, it was found that single phase ZnS_xO_{1-x} is difficult to achieve for intermediate compositions due to the limit of one element solubility in the other element rich matrix (S in oxygen rich ZnS_xO_{1-x} and O in S rich ZnS_xO_{1-x}), and instead, several phases were observed, as shown in figure 3.18. The nature of these phases is still a little bit confusing, and the only information we can confirm is that these phases are neither oxygen rich or sulfur rich ZnS_xO_{1-x}.

This remark is in good consistence with several previous reports, where similar results were obtained [A. Grimm. 2011] [H.L. Pan. 2010] [H. Xu. 2013] (despite that reported by Meyer et al. [B.K. Meyer. 2004] in which a single phase ZnS_xO_{1-x} thin film in the wurtzite structure was reported).

Furthermore, the weak and large diffraction peaks are a sign of the poor crystalline quality. This can also be clearly noticed on the SEM images in figure 3.19, where no granular surface morphology was observed.

**Sulfur rich ZnS_xO_{1-x} thin films ($0.76 \leq x \leq 1$)*

Further increase in composition x (from 0.76 up to 1) was found to lead to a single sulfur rich ZnS_xO_{1-x} phase, as can be seen in figure 3.20; nevertheless, relatively large and weak diffraction peaks, indicating a limited crystalline quality, were observed in case of deposited thin films with a composition x equal to 0.76 or 0.83, while highly oriented (002) wurtzite structure was again observed in case of pure ZnS thin films. On the other hand, the improved crystalline quality as approaching pure ZnS, was accompanied by the gradual reappearance of a clear granular surface morphology, as shown in figure 3.21.

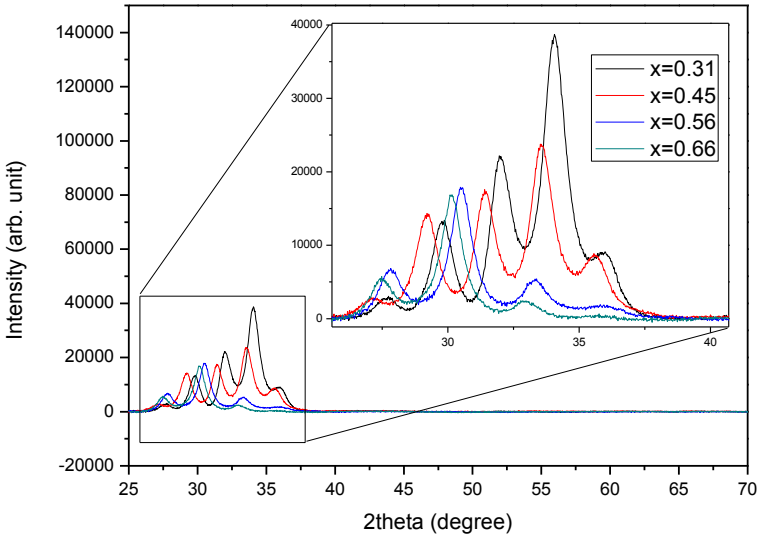

Figure 3.18: XRD spectra of 100nm-thick ZnS_xO_{1-x} thin films: x ranges from 0.31 to 0.66.

(x = 0.31) (x = 0.45)

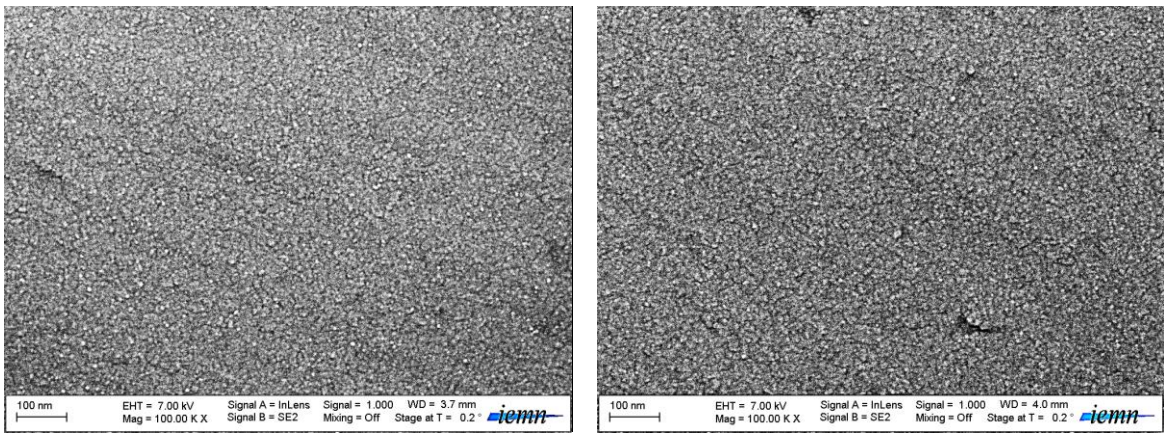

(x = 0.56) (x = 0.66)

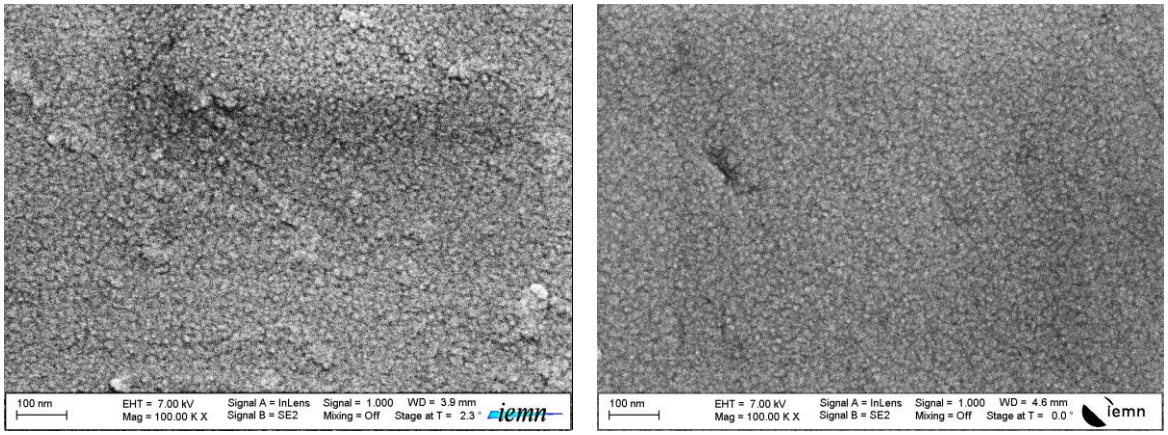

Figure 3.19: SEM images of 100nm-thick ZnS_xO_{1-x} thin films: x ranges from 0.31 to 0.66.

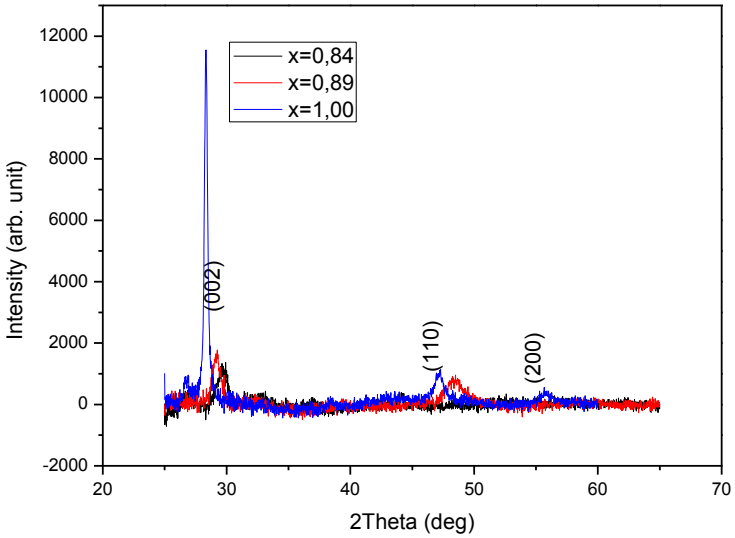

Figure 3.20: XRD spectra of 100nm-thick ZnS_xO_{1-x} thin films: x ranges from 0.76 to 1.

(x = 0.76)

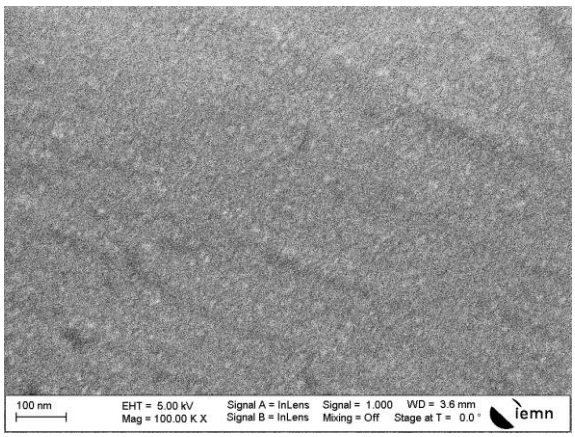

(x = 0.83)

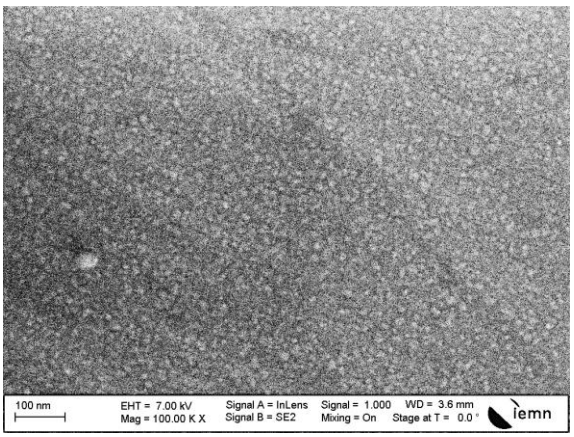

(x = 1)

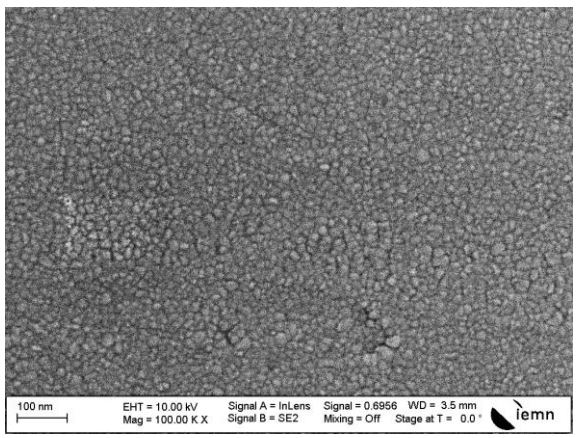

Figure 3.21: SEM images of 100nm-thick ZnS_xO_{1-x} thin films: x ranges from 0.76 to 1.

3.8.2.4. Effect of substrate continuous rotation

Finally, the use of substrate rotation (movement) for this ALD-inspired deposition scheme was investigated in order to check out if it has an effect on the structural properties of the deposited thin films. In figure 3.22, the XRD spectra of 100nm-thick pure ZnO thin films deposited either in static (standard) or dynamic (continuous rotation) mode are presented. Comparing these two spectra, mainly three important observations can be extracted:

(i) The first one is related to the difference in measured intensities. Taking into account that, on one hand, one of the parameters to which the intensity of the XRD peaks is proportional is the volume fraction of the phase in question and, on the other hand, both thin films have the same thickness, we can conclude that the crystalline fraction in the static deposited thin film is higher and therefore the crystalline quality is better than that of the thin film deposited with continuous rotation.

(ii) The second information we can extract is the similar crystallite size obtained in both cases since equal FWHMs were measured, as can be seen in the inset of figure 3.22.

(iii) The third information is that, using a continuous rotation, a lower stress state of the deposited thin film is obtained corresponding to the shift of the diffraction peak towards the free stress diffraction angle, as shown in the inset of figure 3.22.

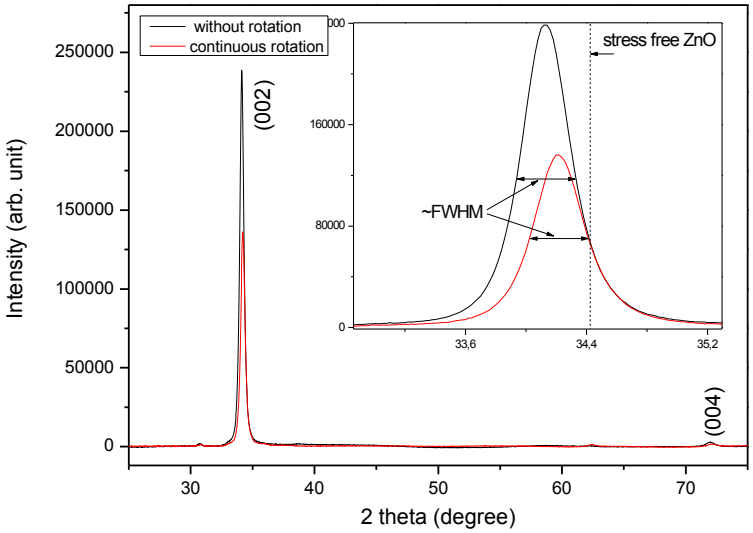

Figure 3.22: XRD spectra of 100nm-thick ZnO thin films deposited using different sputtering configurations (static and continuous rotation).

Furthermore, surface morphology of both thin films was also analysed and the obtained SEM images are given in figure 3.23. Despite the dispersed small particles on the surface of the deposited thin film without rotation, the observed background in both cases is almost the same.

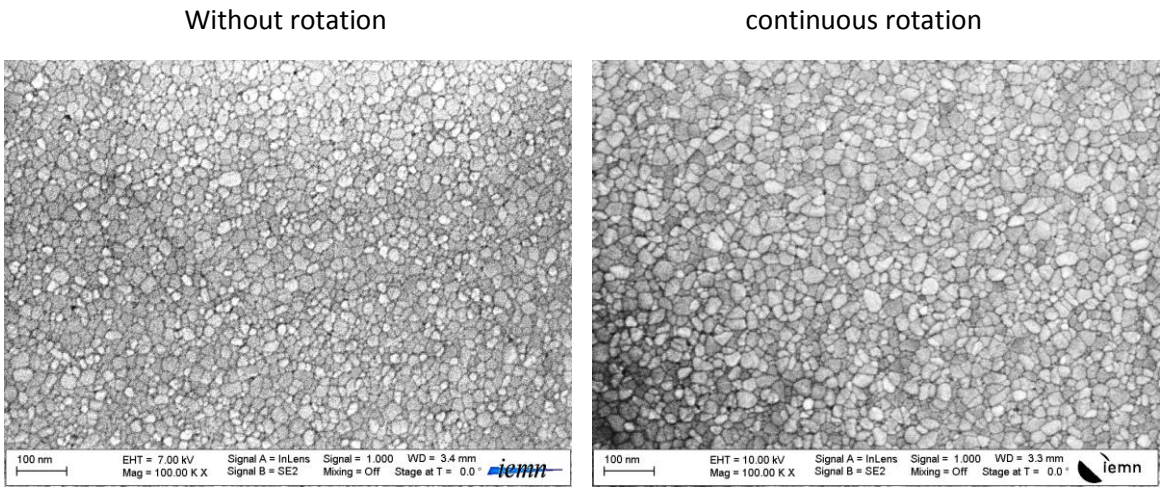

Figure 3.23: SEM images of 100nm-thick ZnO thin films deposited using different sputtering configuration.

3.8.3.Alternative process: Low sputtering power ZnS_xO_{1-x} thin films

In fact, two ways of using the ALD-inspired deposition mode can be considered: either by controlling the applied power to each target, previously detailed, and therefore a continuous rotation can be used, or by adjusting the deposition time under a fixed power and therefore sputtering can be regarded as in a static mode.

One very important advantage of this second process is the possibility of using low sputtering powers whatever the desired composition is. This point is very important when this layer is used as a buffer layer for CIGS solar cells where a low absorber surface degradation due to deposited particles bombardment is highly desired.

In the following, we give the properties of a thin film deposited using this process with a composition that is supposed to be $ZnS_{0.12}O_{0.88}$ (based on the above explained difference in results between thin films deposited with and without continuous rotation, no direct comparison to thin film with the same composition deposited with a power control will be given).

From the microstructural point of view, similarly to samples prepared using the power control mode, the recorded XRD spectrum reveals a (002) preferential orientation in the wurtzite structure with a shift towards lower diffraction angles from that of the pure ZnO, as can be seen in figure 3.24, which is, once again, related to the incorporation of higher ionic radius element (sulfur). On the other hand, the granular shape-like surface morphology was revealed, as shown in the SEM image in figure 3.25.

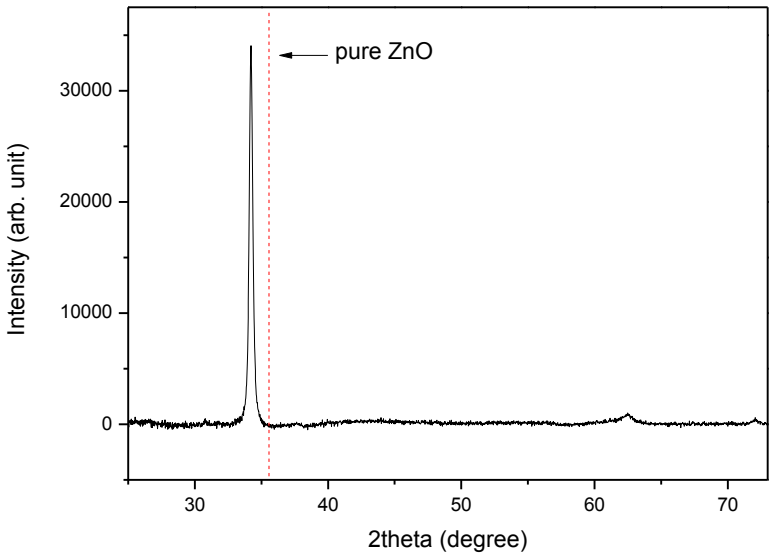

Figure 3.24: XRD spectrum of 100nm-thick $ZnS_{0.12}O_{0.88}$ thin film deposited at low RF-sputtering power (10w) in a static mode.

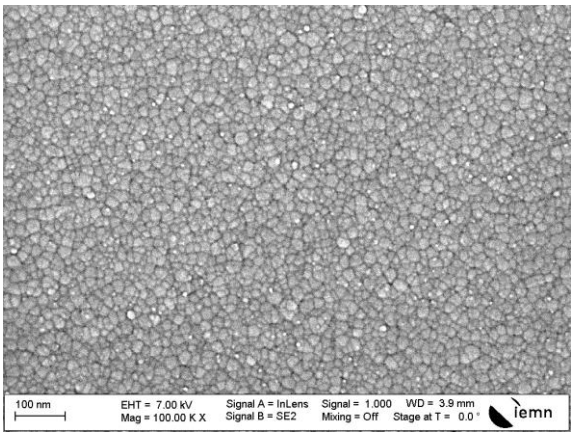

Figure 3.25: SEM image of 100nm-thick $ZnS_{0.12}O_{0.88}$ thin film deposited at low RF-sputtering power (10w) in a static mode.

3.9. Chapter conclusion

Cadmium sulfide (CdS) films, deposited using chemical bath technique, as reference buffer layer and room temperature sputtered zinc oxysulfide (ZnS_xO_{1-x}) films as an environmentally friendly alternative have been prepared.

Adjusting deposition conditions (ammonium hydroxide concentration and bath temperature) was found to lead to a good CdS coverage over a glass surface for a standard thickness (50nm). Furthermore, it was found that CdS thin films show a faster growth rate on CIGS covered substrate than on glass substrate and therefore shorter deposition time was used for the growth of standard thickness thin films. Structural and optical characterizations of 50nm-

thick CdS thin films have revealed a (002) hexagonal/ (111) cubic preferential orientation, and an optical band gap of 2.25eV.

On the other hand, reactive (O_2) sputtering of a ZnS target at room temperature was investigated as a first choice for ZnS_xO_{1-X} film fabrication. Unfortunately, the obtained results were disappointing; therefore, a so called ALD-inspired sputtering process was investigated as an alternative.

Optical analyses have shown a non-linear variation of the band gap value as a function of sulfur to oxygen ratio with a bowing parameter of 1.3. The observed difference compared to previously reported results was proved to be related to the film thicknesses, 100nm in our case and around 300nm for reported results.

Structural analyses have revealed the composition ranges in which a single phase ZnS_xO_{1-x} is achievable: $0 \leq x \leq 0.21$ and $0.76 \leq x \leq 1$. Almost the same ranges were reported by other groups using high temperature reactive sputtering process. Furthermore, the crystalline quality was found to degrade as more foreign atoms are incorporated into the host matrix (S in ZnO or O in ZnS), most likely due to the induced distortion in the lattice parameter.

Comparing the crystalline quality of ZnO thin films deposited in different sputtering configurations (dynamic or static), we have found out that the crystalline fraction and therefore the crystalline quality are higher in case of using the static mode; however, the reason behind such an observation is still not clear and further investigation seems to be necessary.

It is important to note that the previous study has been conducted in order to find the suitable buffer layer composition (the one that shows the optimum conduction band offset with the CIGS absorber layer), while a sputtering from a single ternary target (once the composition is fixed) is contemplated.

From the industrial point of view, sputtering from a single ternary target would be the optimum process; however, first results from other groups using a ternary target for the fabrication of laboratory cells have shown a Gaussian-like sulfur to oxygen ratio distribution [R. Klenk. 2014] [R. Klenk. 2013] [A. Grimm. 2012], which is most likely related to the distribution of sputtered elements within the plasma. Consequently, this would limit the large surface area operation of such a process, and therefore, the development of alternative processes will be highly appreciated.

Chapter 4: Window layer

Here we come to the last needed step for the fabrication of CIGS solar cells!!

In this chapter, we will first discuss the role of the window layer, the structural, electrical and optical properties of the composing layers and the limiting factor for each property; then, we will devote more attention to sputtered aluminum doped zinc oxide layer as a front contact: a detailed overview will be given.

In a second part, experimental results on the effect of all pulsed-DC sputtering parameters '' pressure, Ar flow, power ... etc '' as well as the post deposition annealing will be presented.

Also, experimental results on the use of RF-sputtering mode and a low temperature post deposition annealing for CdS based reference solar cells will be shown.

Finally, the origin of the limited optoelectronic properties of our sputtered AZO thin films will be discussed.

Part A. State of the art

4.1. The role of the window layer

Typically, the window layer consists of two layers: a highly resistive bottom layer (commonly i-ZnO) and a highly conductive top layer (commonly IIIA-doped ZnO). Despite the fact that each of those has its own specific role, the bilayer structure should ensure high transparency and therefore allows incident light to pass through and reach the absorber layer with minor losses.

Concerning the i-ZnO layer, even though no assertive conclusion about its exact role was published, some roles are commonly reported. One of them is the lowering in shunt paths. H. Anant et al. have reported on the need of i-ZnO layer especially in case of rough CIGS surface where a direct contact between the top conductive layer (e.g. AZO) and CIGS due to the low CdS layer recovering is possible, and therefore a loss in open circuit voltage due to the large band gap discontinuity [H. Anant. 2006].

According to the same authors, cell efficiency is i-ZnO thickness dependent where a too thin layer might be insufficient to prevent shunt paths while a very thick one might weaken the built-in field by spreading the space charge region over the thickness of i-ZnO layer. For that sake, it is worth to mention the commonly used thickness which is around 50 nm; however, it should not be taken as a holy value!!

In case of using zinc oxy-sulfide buffer layer, lowering cell metastability using i-ZnO layer was also observed [M. Buffiere. 2014] [N. Naghavi. 2015]. Despite the contradictory conclusions reported in these two papers, one thing that should be kept in mind is the dependence of ZnOS based solar cells stability on the i-ZnO properties.

Another reported role of the i-ZnO layer is related to the protection of the CdS buffer layer from high energy ions during AZO deposition [M. Buffiere. 2011]. However, knowing that i-ZnO layer itself is commonly deposited using sputtering technique adds some relativity in this speech!!

We might also find other confusing roles such as preventing aluminum diffusion from AZO layer into the buffer layer [R.S. Araoz. 2004]!! However, even if it is the case, which is a little bit hard to imagine, does aluminum has a negative effect on cell performance? D.J.L Bremaud even has observed an enhancement in cell performance due to presence of aluminum in the deposition bath during the buffer layer growth [D.J.L Bremaud.. 2009].

On the contrary to the i-ZnO bottom layer, the role of the highly doped top layer is quite clear: collecting and transporting the photo-generated electrons. Therefore, this layer should be as conductive as possible.

However, this high conductivity should be obtained for low free carrier concentration, otherwise, optical losses (absorption) at long wavelengths takes place (the reason behind that

will be discussed in the following). Taking these conditions in consideration, mainly IIIA doped ZnO TCOs were intensively studied: Al: ZnO, B: ZnO, Ga: ZnO, and In: ZnO.

Finally, it is interesting to note that the choice of ZnO material as a window layer for CIGS solar cells was not accidental: its physical, chemical and thermal properties, stability, ease in deposition, non-toxicity, availability and low cost might justify this choice. In the following we give a general review on ZnO properties.

4.2. intrinsic and doped ZnO properties

4.2.1.Structural

It is commonly reported that pure zinc oxide material, independently of its form: nanoparticle, thin film or bulk, crystallizes in the wurtzite structure. The reason behind that is believed to be related to the stability of the wurtzite structure, thermodynamically talking, compared to the other two possible crystalline structures: zinc blende and rocksalt [Ü. Özgür. 2005].

However, some exceptions might be found: A. Ashrafi et al. have shown that is possible to epitaxially grow zinc blende-zinc oxide thin films on GaAs substrate using an intermediate zinc blende ZnS layer [A. Ashrafi. 1999].

For further informations, we highly suggest to have a look on the very nice paper published by Ü. Özgür et al. (pages 3-7) [Ü. Özgür. 2005].

On the other hand, introducing impurities, such as Al, Ga, B, F…, was found to not influence the host matrix structure: the wurtzite structure is conserved while a tensile or a compressive stress, depending on the impurity size and the occupied site, might take place.

4.2.2.Electrical

In the following, we briefly summarize the main origins of the n-type conductivity in both intrinsic and doped zinc oxide material, and we present the mechanisms controlling/limiting carrier transport.

4.2.2.1. Origins of the n-type conductivity in i-ZnO

It is largely accepted that native defects resulting from the imperfection of the crystalline lattice are at the origin of both p and n type conductivity. The three possible types of defects leading to n-type ZnO are: oxygen vacancies (V_O), zinc in an octahedral interstitial site and zinc in an anti-site (zinc occupying an oxygen site) [S. Brochen. 2012].

As an exception, A. Janotti et al. have shown through theoretical calculations that all previously mentioned defects could not be at the origin of the n-type conductivity due to either their high formation energy or their deep position within the band gap [A. Janotti. 2007]. Their alternative explanation of the observed n-type conductivity in i-ZnO is based on the unintentional incorporation of donor impurities: mainly hydrogen in substitution of oxygen which needs a low formation energy and acts as a shallow donor [A. Janotti.2. 2007].

However, knowing that only traces of hydrogen (residual gas) could be present during ZnO deposition, a big question mark exists about the validity of A. Janotti's explanation and the real origin of n-type conductivity is most likely defect related as previously mentioned.

4.2.2.2. Origin of the n-type conductivity in intentionally doped ZnO

On the contrary of the previous case (i-ZnO), there is no confusion in explaining the n-type conductivity of intentionally doped ZnO. Independently of the impurity nature, higher atomic number impurity releases an electron once it substitutes a lower atomic number lattice atom: IIIA group elements are known to substitute zinc atoms, while fluorine substitutes oxygen atoms.

4.2.2.3. Mechanisms limiting electron transport

Scattering mechanisms are known to govern the electron transport in polycrystalline semiconductors. Besides the scattering at the grain boundaries, there exist also volume dependent scattering mechanisms: scattering due to the presence of impurities, structural defects, lattice vibrations, etc.

Grain boundary scattering: in an early time, T.I. Kamins has reviewed on the effect of grain boundaries on electron transport in silicon and has explained that the formation of a charged region surrounding the grain, which resulted from electron trapping, creates a potential energy barrier that impedes electrons transport from one grain to another [T.I. Kamins. 1971]. As a consequence, electron transport is insured either by thermionic emission (temperature dependent mechanism: α exp-1/T) and/or tunneling effect. Even though this explanation was generalized for oxide semiconductors, one should take care since it is only valid for non-degenerated semiconductors [M.A. Alim. 2006] [M.W.J Prins. 1998].

Ionized impurity scattering: this is known to be the result of electron deflection once approaching an ionized impurity due to the Coulomb potential. According to M.L. Addonizio et al. this mechanism can be valued in the Brooks-Herring approach, from which one can infer the temperature independence of this mechanism [M.L. Addonizio. 1999]. One other important point is the doping concentration dependence: the more heavily ZnO is doped (higher collision probability), the higher the importance of this mechanism is.

Lattice scattering (phonon scattering): There exist two type of phonon scattering. The first one is the optical phonon scattering (inelastic scattering) which results from the interaction (collision) of a moving electron with the electric field induced by electric polarization associated with lattice vibration. In other words, the vibration of the lattice perturbs the dipole moment between the atoms, which results in an electric field that scatters electrons. The second is the acoustic phonon scattering (elastic scattering) which is caused by the local energetic shift of the band edges induced by strain associated with acoustic phonons [Ü. Özgür. 2005]. This scattering mechanism is known to be a temperature dependent one (α $1/T^{3/2}$).

Structural defects scattering: Native defects such as dislocations are also considered as possible scattering centers. This is because of the acceptors centers trapping behavior of this defect, leading to similar scattering mechanism as in the case of grain boundaries scattering.

The other two possible volume scattering mechanisms are piezoelectric scattering and scattering from neutral impurities. Both of them have, in practical, negligible effects since the first might only contribute at low temperature while the low ionization energy makes the concentration of neutral impurities very low.

To sum up: (i) electrons transport in ZnO material with a given dopant concentration (from intrinsic to heavily doped) could be governed by one or more of those mechanisms simultaneously; (ii) the total effect is the sum of the individual contributions (known as Matthiessen's rule [Ü. Özgür. 2005]); (iii) Hall measurement as a function of temperature is a useful method to know whether one mechanism is responsible of transport limitation or not.

4.2.3. Optical

Both intrinsic and doped zinc oxide thin films are known to have a similar optical properties within the visible spectra: a very low absorption and a relatively low reflection (which is surface roughness dependent). Out of the visible spectrum range, some differences, mainly related to electrical properties, are commonly reported.

Within the UV spectrum: the short wavelength cut-off in transmittance shifts toward lower wavelengths (blue shift, band gap increases) as the doping level, and therefore the electrons concentration, increases [K.H. Kim. 1997]. This is mostly attributed to the shift of the Fermi level into the conduction band due to the increase in the carrier concentration, which is known as the Burstein–Moss effect [E. Burstein. 1953] [T.S. Moss. 1954].

Within the near-infrared and infrared spectra: intrinsic ZnO is known to keep its high transparency all along the near-infrared and even over the infrared spectra; nevertheless, with doping level increase, a dramatic decrease in transparency is commonly observed [J. N. Duenow. 2008]. This phenomenon is explained using Drude's model: free electrons in the conduction band oppose to all incident photons with frequency lower than that of the plasma frequency which is, itself, electron concentration dependent (the higher the electron concentration, the higher the plasma frequency is) [O. Tosoni. 2013].

As a consequence, using low electron concentration X-doped ZnO (to insure minor optical losses in the near-infrared region) while maintaining low resistivity (by increasing electron mobility) would be beneficial since the CIGS solar cell operational spectrum extends until about 1100 nm. To do so, one possible way is using an alternative dopant to aluminum such as boron [Y. Hagiwara. 2001].

Finally, it is worth to note that the red shift resulting from using lower electrons concentration X-doped ZnO would not affect cells performance since photon flux is low in the short wavelength range considered and, in any case, using i-ZnO under layer would prevent higher energy photons to pass through.

4.3. Detailed overview on AZO thin films

4.3.1. Deposition techniques: Why sputtering?

In parallel to the use of sputtering technique for AZO thin film development, several other deposition techniques, such as atomic layer deposition (ALD), pulsed laser deposition (PLD), pulsed electron deposition (PED), chemical vapor deposition (CVD), spray pyrolysis, sol-gel, etc, have been extensively studied in order to find the suitable one that achieves the ultimate trade-off between quality and cost.

Other than the superiority of sputtering technique from the environmental (clean technique) and the economical (high deposition rate over large surfaces) points of view, it has also, all along the years, shown its superiority in term of film quality compared to the other techniques (independently of the used deposition mode: RF, DC or pulsed DC).

In tables 4.1 and 4.2, we compare the quality of films obtained using different deposition techniques (non-exhaustive list) and we give a detailed overview on AZO thin film obtained using different sputtering modes, respectively.

Deposition technique	Mobility (μ) $cm^2\ V^{-1}\ s^{-1}$	Electron concentration (n) $10^{20} cm^{-3}$	Resistivity (ρ) 10^{-4} Ω.cm	Transmittance (%)	Reference
Sputtering	-	-	1.5	95	[W.J. Jeong. 2001]
ALD	60.4	2.4	4.3	-	[F.T. Tsai. 2015]
PLD	-	6.3	6.9	>90	[A. Mallick. 2014]
PED	-	-	3.5	>90	[F. Pattini. 2015]
LPCVD	-	-	36	>80	[W.H Kim. 2011]
Spray pyrolysis	5.6	0.14	760	>85	[N.J. Begum.2013]
Sol-gel	10.9	1.2	50	>90	[H. Hangendorfer. 2014]

Table 4.1: Optoelectronic properties of AZO thin films issued from different deposition techniques.

	Used sputt mode	Al_2O_3 wt %	Substrate	Deposition temperature (℃)	Ar flux (sccm)	Reactive gas flux (sccm)	Pressure (10^{-3} mbar)	Power (Wat/cm^2)	Frequency (KHz)	Distance targ-subst (mm)	Deposition duration (min)	Thickness (nm)	Annealing atmosphere	Annealing temperature (℃)	Annealing duration (min)	Transmittance (%)	Eg (eV)	μ (cm^2 V^{-1} s^{-1})	n (10^{20}cm^{-3})	ρ (10^{-4} Ω.cm)	Reference
High deposition temperture	RF	2	quartz	100	-	x	1.3	0.81	13560	50-70	-	-	x	x	x	90	-	-	-	2.5	[Y. Igasaki. 2001]
		2.5	Corning 1737	300	3	x	2.7	1	13560	50	120	1195	x	x	x	>85	-	-	-	1.9	[J. Yoo. 2005]
		-	quartz	450	-	x	2.5	2.6	13560	-	-	-	Ar/O_2	600	60	90	-	-	-	1.1	[X.R. Deng. 2012]
	DC	-	Glass	200	25	2 (O_2)	4	-	x	60	60	350	-	400	-	88	-	46	-	2.2	[B.R. Kumar. 2013]
		2	Glass	320	-	x	3	0.85	x	70	-	450	vacuum	400	120	90	-	33	12.6	1.5	[G. Fang. 2003]
		2	Glass	370	-	-	4	1.53	x	-	-	-	x	x	x	90	3.6	242	8.6	0.3	[A. Mosbah. 2012]
	Pulsed DC	-	Corning 2000	280	-	15% (O2)	6	0.98	30	45	30	1000	x	x	x	80	-	24	7.6	3.4	[X.L. Chen. 2012]
		2	Glass	230	-	x	4	!	70	95	-	-	x	x	x	90	3.6	-	58	2.2	[J.P. Kar. 2010]
Without intentional heating	RF	2	Quartz	RT	30	x	4	(300)	13560	70	-	250	x	x	x	93	-	15	8.6	4.6	[W. Yang. 2009]
		3 at	Si por	RT	-	x	!	2	13560	75	-	400	x	x	x	85	3.7	43	9.1	1.5	[Z.B. Ayadi. 2014]
		-	Corning 7059	RT	-	-	13	(180)	13560	50	-	500	x	x	x	95	3.2	-	-	1.4	[W.J. Jeong. 2001]
	DC	-	Glass	RT	20	-	-	-	-	-	-	-	x	x	x	-	-	-	-	6.6	[D. Horwat. 2007]
	Pulsed DC	-	Corning 1737	RT	-	x	27	!	30	80	-	200	x	x	x	84	-	-	-	12	[Y.M. Chung. 2005]
		//				!(H2)	//										-	-	-	8	[Y.M. Chung. 2006]
		2	Glass	RT	-	14 (H2)	-	4.5	20	70	-	350	x	x	x	85	-	-	-	4	[M.C. Li. 2010]
		2	Glass	RT	10	x	10	80	30	90	9	300	N_2H_2	400	1	85	3.6	22.1	6.1	4.5	[B. Ayachi. 2016]

Table 4.2: Worldwide status on sputtered aluminum doped zinc oxide (AZO) thin films.

4.3.2.Effect of different sputtering parameters

One important point to keep in mind while studying the already published works dealing with the influence of sputtering deposition parameters on AZO thin films properties is the uselessness trying to extract reference values since each of those was obtained using specific deposition conditions: target quality, sputtering machine type and configuration, etc. However, it is worth to note the global tendency of one film property as a function of one parameter since it has, in most cases, a high similarity from one laboratory to another:

4.3.2.1. Deposition temperature

Except the work published by K. Tominaga et al. [K. Tominaga. 1998], one might find, in literature, a sort of consensus about the effect of temperature on AZO thin film properties: a clear decrease in film resistivity as the substrate temperature increases up to a certain value, than the film resistivity re-increases for higher deposition temperatures. This is commonly attributed to the changes in electron mobility which are directly related to the changes (improvement or degradation) in crystalline quality.

Despite the complication of the fabrication process, the loss in time and the increase in cost resulting from the use of a high temperature deposition process (from the manufacturing point of view), one might basically wonder about the utility of improving AZO quality based on the use of high temperature process for CIGS solar cell application (reminding the harmful effect of high temperature on the pn junction).

4.3.2.2. Reactive gas: O_2

The effect of introducing oxygen as a reactive gas has also established a certain consensus within the AZO community: (i) an increase in film resistivity accompanied with a decrease in both electron concentration and mobility; (ii) a slight change in optical transmittance within the visible range accompanied by an improvement within the infrared region and a red shift of the short wavelength cut-off.

Optical transparency improvements are commonly related to the decrease in electron concentration (already discussed in the optical properties section); however, the interpretations of the observed electrical changes are, as far as we believe, not convincing.

Some authors have attributed electrical properties modification to the generated stress [S. Rahmane. 2014], oxygen vacancies compensation [H. Zhu. 2014], reduced interstitial zinc [L. N. Li. 2012] and others [H. Zhu. 2014]. Accepting the latter two explanations is so hard, especially when we know that the maximum electron concentration generated from these intrinsic defects is in the range of 10^{17}!!

May be the most acceptable explanations are those attributing those changes to the electron trapping due to the introduction of O_2 in excess [T. Tsuji. 2000] and/or the limitation of aluminum doping activation by forming aluminum oxide [D.S. Kim. 2013] [L. N. Li. 2012].

4.3.2.3. Doping concentration

AZO thin films resistivity as a function of aluminum doping concentration was a subject of several works. In almost all of them, authors have confirmed the possibility of reaching a minimum in resistivity for a given aluminum concentration. This is largely accepted to be originated from the increase in electrons concentration even though the mobility slightly decreases due to the effect of ionized impurity scattering (previously detailed). However, once reaching the aluminum miscibility limit, excess aluminum is not activated and is most likely segregated at the grain boundaries leading to a further decrease in mobility and therefore a re-increase in resistivity [K.H. Kim. 1997].

The optical transmittance changes as the aluminum concentration increases (an increase in absorption within the infrared region and a blue shift of the short wavelength cut-off in transmittance [J.N. Duenow. 2008]) were always explained based on Burstein–Moss effect and Drude's model (previously discussed).

4.3.2.4. Other sputtering parameters

The effect of other sputtering deposition parameters such as pressure, power, thickness, etc., will be discussed within the experimental results part.

4.3.3. AZO surface engineering/texturing for light trapping

One additional property of aluminum doped zinc oxide is its ability to be wet etched in HCl acid leading to a textured surface, commonly referred as crater like surface, without degrading its electrical properties [D.S. Kim. 2012].

Furthermore, this AZO surface texturation was found to be not only dependent on the HCl acid concentration and the etching time [J. Yoo. 2005], but also on the deposition conditions of the AZO layer and therefore on its properties [F. Ruske. 2007] [0. Kluth. 1997].

Surface texturation was first used in amorphous silicon based solar cells in order to improve light trapping through the enhancement of light scattering and the reduction of losses originated from reflection. Among the experimental works dealing with this subject, one can quote the one performed by O. Kluth at al. in which a gain in the short current density of about 3.3mA/cm was shown [O. Kluth.1999].

This very interesting property has attracted less attention in the CIGS community. In the best of our knowledge, A. Čampa et al. were the first group investigating, through numerical simulation, the effect of AZO front contact texturation on cell performance [A. Čampa. 2007]. They have concluded that such a process can also be gainful for CIGS solar cells: thanks to the improvement in quantum efficiency and therefore short current density originated from the decrease of the total reflectivity.

These theoretical predictions were then confirmed experimentally. Z. Jehl has shown through a very detailed study that adjusting AZO deposition and etching processes might lead to an equivalent antireflective effect to that of the standard MgF_2 antireflection layer [Z. Jehl.2012].

However, the expected increase in manufacturing cost resulted from the necessity for doubling AZO layer thickness (800nm) in order to ensure good texturation of the surface (get optimal surface texturation for better optical trapping) and maintain high electrical properties, and the need for an additional wet etching step which is also a costly one (waste recycling), make the utility of developing this process a subject of debate especially knowing that only one step is needed for the relatively thin (114nm) standard MgF_2 antireflection layer [G. Rajan. 2015].

4.4. Partial conclusion

In this first part, we have summarized and discussed the credibility of the commonly reported roles of the window layer. The different structural, optical and electrical properties as well as the possible routes for improving each property were also summarized. Then a special attention have been devoted to sputtered AZO thin films as a front contact. The choice of sputtering as an optimum deposition technique and the dependence of the deposited layers properties on some deposition conditions have been explained.

In the next part, we will show our contribution in the development of high quality pulsed-DC and RF-sputtered AZO thin films for ZnOS based and CdS based CIGS solar cells, respectively.

Part B. Experimental results

4.5. Effect of deposition pressure and argon flow

The effects of the sputtering pressure (for a constant sputtering gas (argon) flow) and argon flow (for a constant sputtering pressure) on AZO thin film optoelectronic properties were investigated by controlling the butterfly valve which equips our deposition chamber. The obtained results are presented in figures 4.1 to 4.4. Films are deposited in the pulsed-DC mode.

It was found that as the sputtering pressure increases the resistivity goes down to a certain value from which it re-increases for higher deposition pressure and then it goes down again for further increase of the sputtering pressure, as can be seen in figure 4.1. Similar dependence of AZO thin film resistivity on sputtering pressure was already observed by several groups [J.C. Lee. 2000] [W. Li. 2012] [J. Yoo. 2005]; however, no convenient explanations were published.

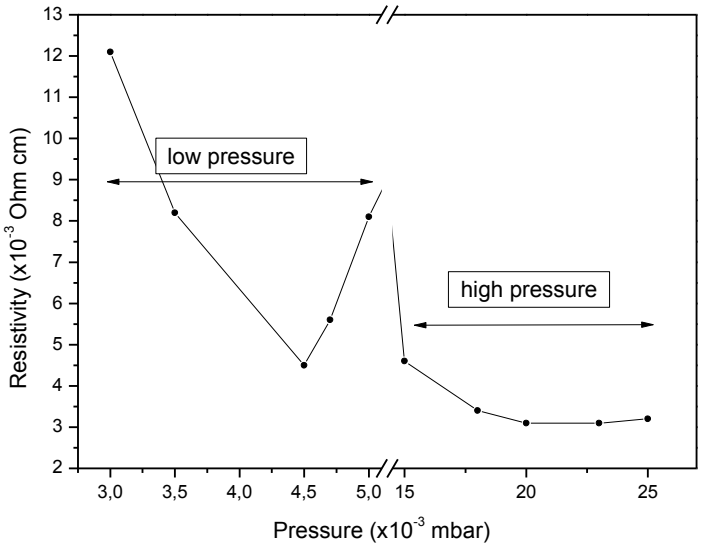

Figure 4.1: Variation of resistivity of 120 nm-thick AZO films measured at the centre of the samples (2" SLG substrates) as a function of sputtering pressure.

Several hypothetical explanations have been proposed:

At very low sputtering pressure, the limited conductivity of AZO thin films conductivity is commonly attributed to the high energy particles bombardment while the observed decrease is attributed to the enhancement in crystalline quality [J.P. Kar. 2010].

For higher sputtering pressure, K.H. Kim et al. and C. Charpentier have attributed the re-increase in resistivity to the decreases in both carrier concentration and mobility, resulting

from the chemisorbed oxygen on the rough surface and/or the increase of the grain boundary barrier height due to the degraded crystalline quality [K.H. Kim. 1997] [C. Charpentier. 2012].

A more convenient explanation has been proposed by J.P. Kar et al. [J.P. Kar. 2010]. They have attributed the increase in resistivity to the decrease in incorporated dopant concentration, most probably due to the dispersion of sputtered elements within the plasma, accompanied with a decrease in the activated aluminum dopant concentration. In the same context, even if Igasaki et al. have found that the concentration of incorporated aluminum is not affected by the sputtering pressure, they have confirmed that the carrier concentration is highly affected which means that lower aluminum concentration is activated [Y. Igasaki. 2001]. Moreover, both groups have shown a degradation of the crystalline quality as the sputtering pressure increases.

Based on the previous explanations ‘’the found relationship between the deposition pressure, the crystalline quality and the resistivity‘’, the observed re-decrease in resistivity for high deposition pressure should not take place. One possible explanation of this re-decrease is the presence of metallic like phases which leads the conductivity to be not anymore governed by aluminum doping; however, a deep investigation is needed before confirming whether this hypothesis is true or not.

Finally, it is interesting to note the found coherence between the changes in the stress state within the thin films and their conductivity. As it is well known, sputtered thin films stresses change from high compressive to high tensile passing by a free stress point and then again down to zero (or near to zero/ free stress state) as the sputtering pressure increases. That might lead to the conclusion that the observed changes in resistivity probably reflect the strain state of the sputtered thin films.

On the other hand, it was found that the optical transmittance is highly affected by the sputtering pressure. As can be seen in figure 4.2, a dramatic decrease in optical transmittance has taken place for high sputtering pressures, which is largely accepted as a result of the lack of oxygen, on one hand and on the other hand, of the presence of metallic Al interstitials which had not been incorporated into the ZnO lattice [C. Lennon. 2009].

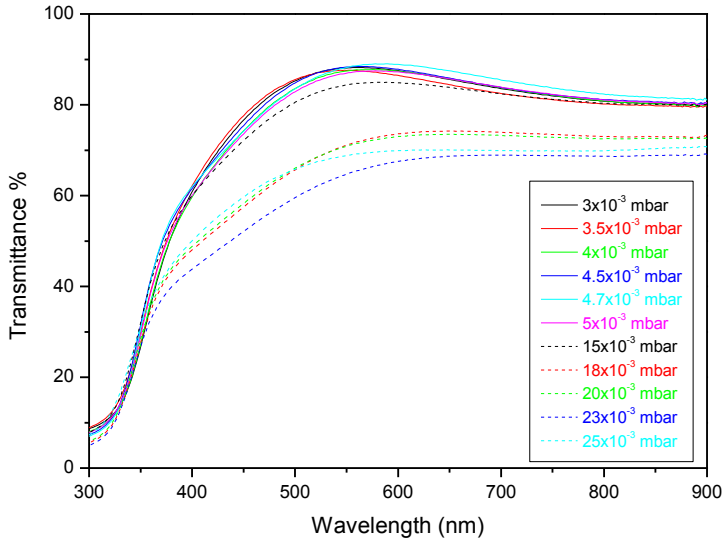

Figure 4.2: Optical transmittance spectra of 120 nm-thick AZO films deposited at different sputtering pressures.

For further optimization of AZO thin film quality, the sputtering pressure of 4.5 10^{-3} mbar corresponding to the lower resistivity obtained at low sputtering pressure will be used as a reference even if lower resistivity was obtained at higher sputtering pressure. This choice was made because of the poor optical transmittance, on one hand and on the other hand, the already proved low stability ‘’strong degradation during the damp heat test [T. Tohsophon. 2006]’’ of the high pressure deposited thin films.

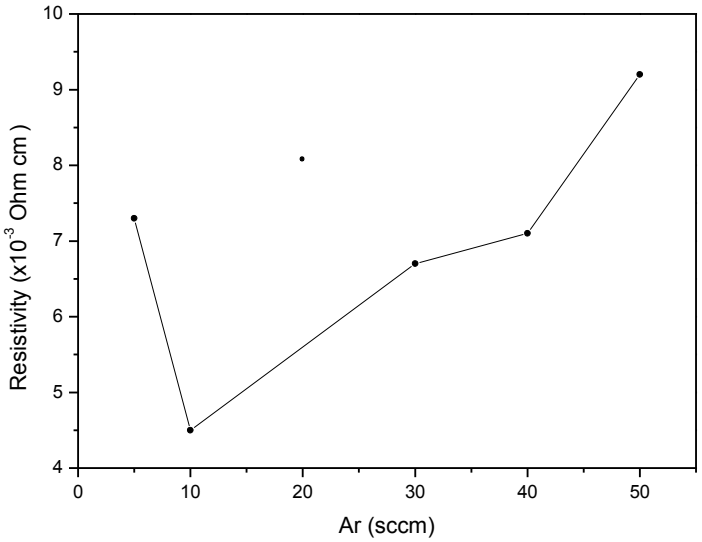

Figure 4.3: Variation of resistivity of 120 nm-thick AZO films measured at the centre of the samples (2" SLG substrates) as a function of argon flow.

Concerning the effect of argon flow, it was found that the lowest resistivity and the highest optical transmittance are achievable for low Ar gas flow, as can be seen in figure 4.3 and figure 4.4, respectively. This can be attributed to the generated stress and/or the degradation of the crystalline quality resulted from the incorporation of Ar atoms.

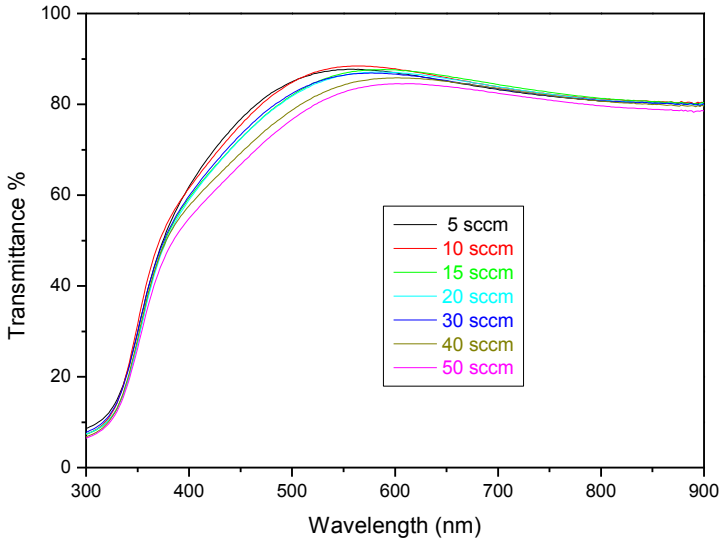

Figure 4.4: Optical transmittance spectra of 120 nm-thick AZO films as a function of argon flow.

4.6. Effect of sputtering power and thin films thickness

In order to investigate the effect of pulsed DC sputtering power on AZO thin film optoelectronic properties, several samples have been prepared by changing the sputtering power from 70W to 130W while all other parameters were kept constant; the measured thickness and resistivity values are displayed in figure 4.5.

The resistivity of the thin films was found to show a minim value at 80 Watts (close to a power density of 1W/cm²) while it increases for higher and lower sputtering powers. The observed re-decrease for higher sputtering power (from 90W to 130W, 1.1 to 1.6 W/cm²) is, without any doubt, related to the increase in thin films thickness, as illustrated in figure 4.6.

According to several authors, the resistivity dependence on the sputtering power is mainly governed by the changes of the crystalline quality [W. Yang. 2009] [C. Charpentier. 2012]. At low sputtering power, the kinetic energy of the sputtered particles arriving at the surface is relatively low therefore the crystalline quality is limited. As the sputtering power increases, the crystalline quality gets better until reaching the balance point between the enhancement due to the increase of the kinetic energy at the surface and the degradation resulted from the surface bombardment. For higher sputtering power the films will be damaged by too high energy ions, which leads to a poor crystal quality.

On the other hand, knowing that the optical transmittance is thickness dependent, as can be seen in figure 4.7, one should note that the optical transmittance dependence on the sputtering power obtained from our experiences does not have a high credibility since the samples thickness changes from one sample to another, that is why it is not presented.

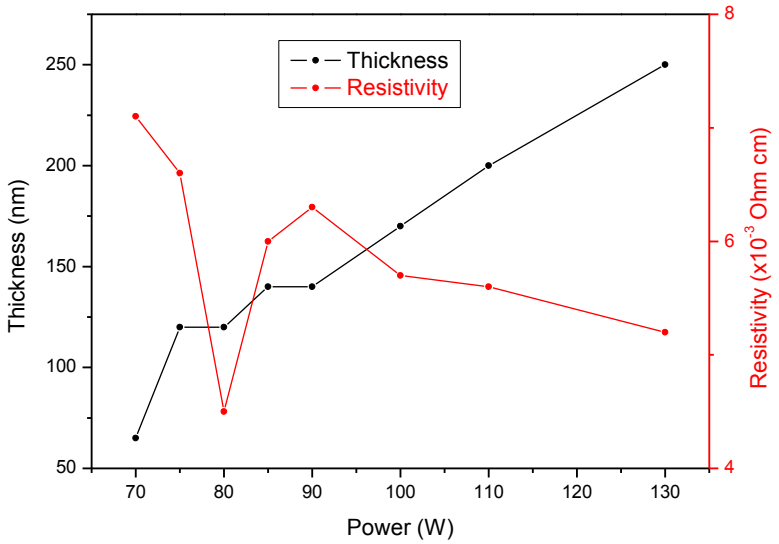

Figure 4.5: Variation of resistivity and thickness of AZO films obtained for a constant sputtering time, measured at the centre of the samples (2" SLG substrates) as a function of pulsed DC sputtering power.

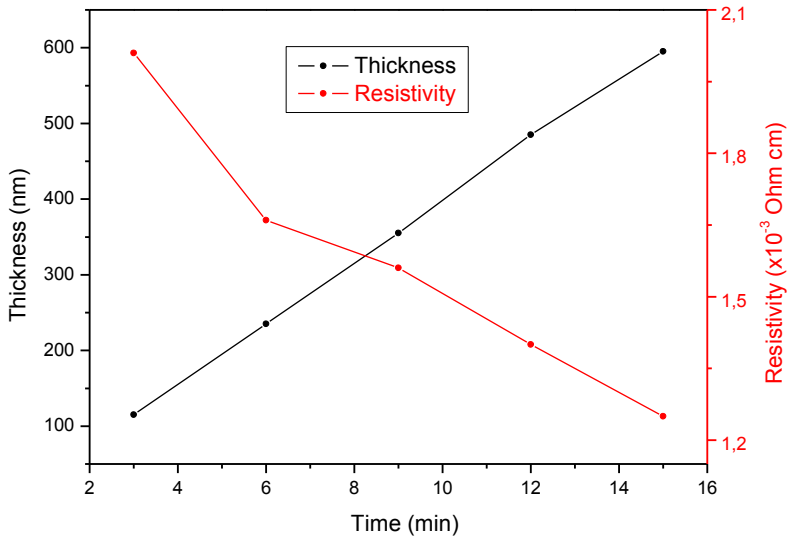

Figure 4.6: Variation of resistivity and thickness of AZO films obtained for a constant sputtering power, measured at the centre of the samples (2" SLG substrates) as a function of sputtering time.

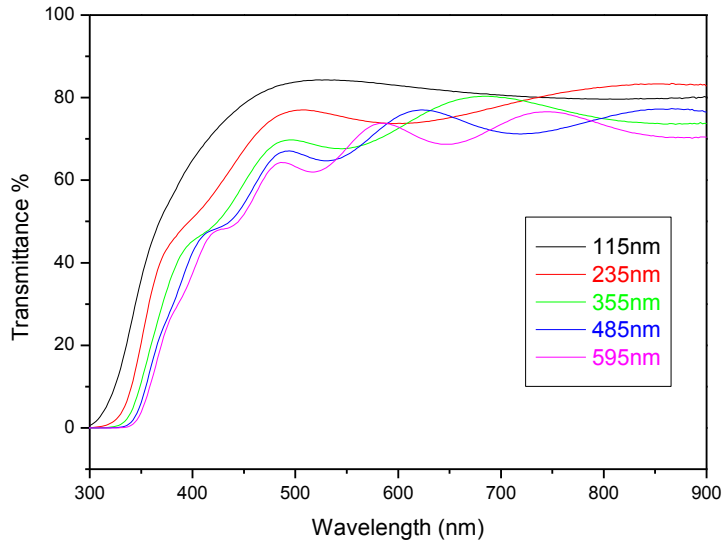

Figure 4.7: Optical transmittance spectra of AZO thin films as a function of thickness.

4.7. Effect of pulse parameters (duty cycle)

The last parameter we have tuned was the duty cycle, defined as the ratio between the pulse duration and the period ($t_{on}/(t_{on} + t_{off})$). To do so, the sputtering frequency and the pulse duration were changed, while all other sputtering parameters were kept constant. The sputtering time was fixed for each duty cycle in order to obtain films with almost the same thickness. The obtained resistivity, growth rate and optical transmittance variations as a function of the duty cycle are displayed in figure 4.8 and figure 4.9.

Apart from the outlier point at duty cycle of 0.7 ($11.8x10^{-3}$ Ohm.cm), a clear decrease in resistivity as the duty cycle increases was observed. This enhancement in conductivity is most likely related to the improvement of the crystalline quality, which is probably related, in somehow, to the increase of growth rate. Similar tendency was previously observed by H.Ko et al [H. Ko. 2005].

However, the degraded optical transmittance observed in figure 4.9 is still not clear, especially considering that higher duty cycle lead to better crystalline quality; therefore, a deeper investigation seems to be necessary to understand the origin of such a degradation in optical transmittance.

Finally, it is quite clear that for high duty cycle (higher than 0.92) the gain in conductivity becomes negligible compared to the loss in optical transmittance; as a consequence, duty cycle of 0.94 corresponding to a pulse frequency (υ) of 30 KHz and a pulse duration (t_{on}) of 31 µsec is used as a reference sputtering condition for further improvement of AZO thin films quality.

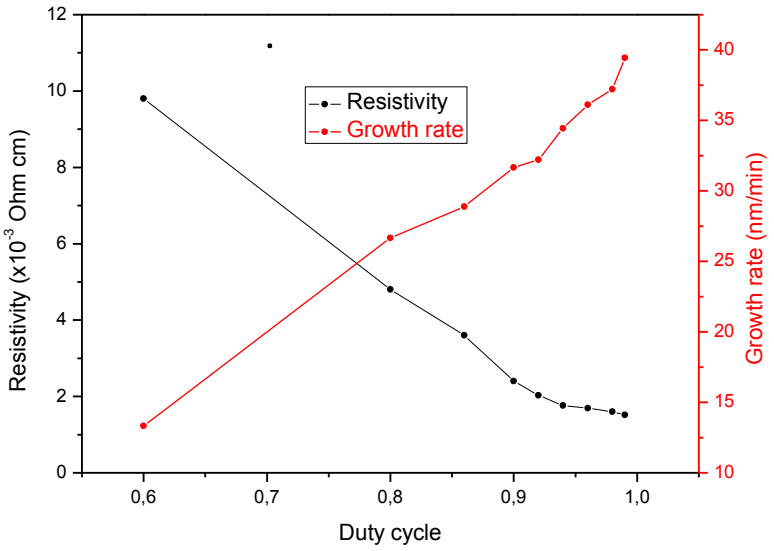

Figure 4.8: Variation of resistivity and growth rate of 300 nm-thick AZO films measured at the centre of the samples (2" SLG substrates) as a function of duty cycle.

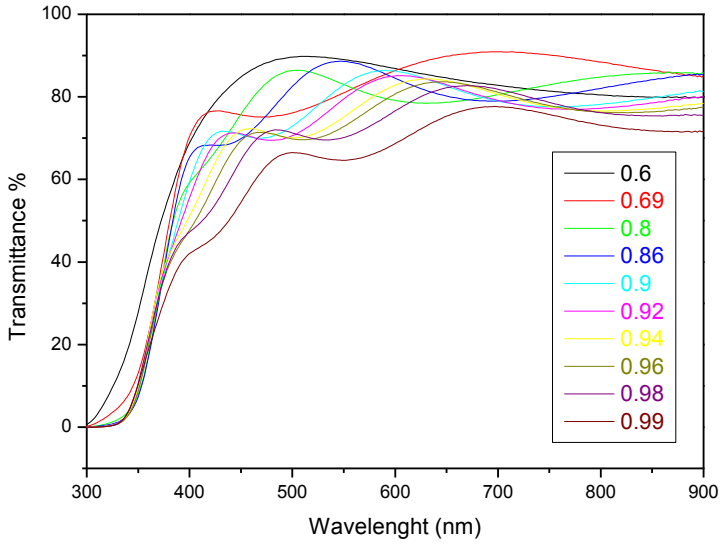

Figure 4.9: Optical transmittance spectra of 300 nm-thick AZO thin films as a function of duty cycle.

4.8. Thickness variation along a diameter of 2" SLG substrate

Distance from centre (cm)		-2	-1.5	-1	-0.5	0	0.5	1	1.5	2
Measured thickness (nm)	For target to substrate distance of 75mm	380	395	400	395	400	395	400	392	375
	For target to substrate distance of 88mm	285	285	305	305	305	300	320	300	300

Table 4.3: Evaluation of the AZO thin films thickness along the diameter of a 2'' SLG substrate.

The deduced thin films thickness from surface profilometry measurement along the diameter of a 2'' SLG substrate with a step of 0.5 cm reveals the quite good thickness uniformity with a maximum deviation of 6.5%, which excludes any relationship between the observed optoelectronic properties variation within the xy plane of the same sample and its thickness.

4.9. Effect of rapid thermal annealing

Unfortunately, the electrical measurements conducted on samples of room temperature pulsed-DC magnetron sputtered AZO thin films have revealed the non-uniform spatial distribution of resistivity, with extreme increases in resistivity at substrate locations corresponding to the erosion pattern of the target (see figure 4.12). Therefore, a post deposition treatment appeared to be compulsory to overpass this non-uniformity issue. To do

so, the rapid annealing was investigated; the used annealing protocol is presented in figure 4.10.

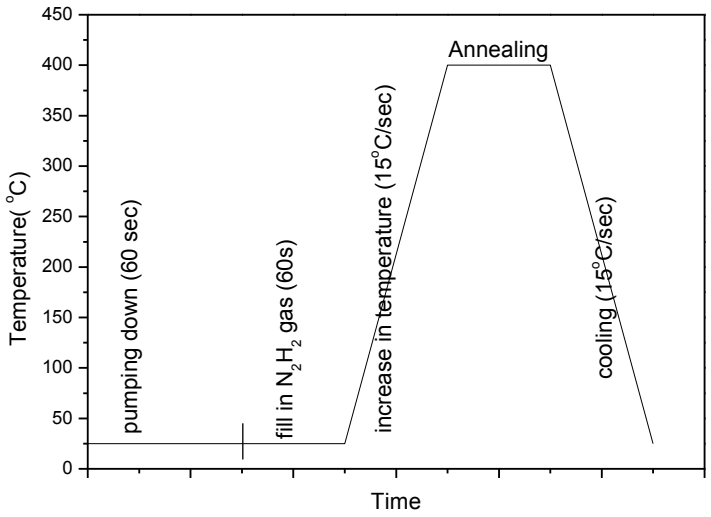

Figure 4.10: Schematic representation of the used annealing protocol.

Annealings have been performed at atmospheric pressure under N_2H_2 atmosphere at 400°C where the heating and cooling rates were 15°C/sec. the rapid thermal annealing (RTA) process was investigated for different plateau region durations.

Resistivity, mobility and carrier concentration of AZO thin films, obtained by 4-probe and Hall measurements at the centre of samples that got different annealing times are reported in figure 4.11(a). The resistivity of as-deposited AZO thin films is 1.7×10^{-3} Ω·cm and it decreases down to 5.1×10^{-4} Ω·cm after RTA for 30 sec. Correspondingly, the carrier concentration and the Hall mobility increased from 2.6×10^{20} cm^{-3} to 5.7×10^{20} cm^{-3} and from 13.6 cm^2 V^{-1} s^{-1} to 21.8 cm^2 V^{-1} s^{-1}, respectively. The sample annealed for 1 min showed a further slight decrease in resistivity value (4.6×10^{-4} Ω·cm) owing to a small increase in both mobility and carrier concentration of about 0.3 cm^2 V^{-1} s^{-1} and 0.4×10^{20} cm^{-3} respectively.

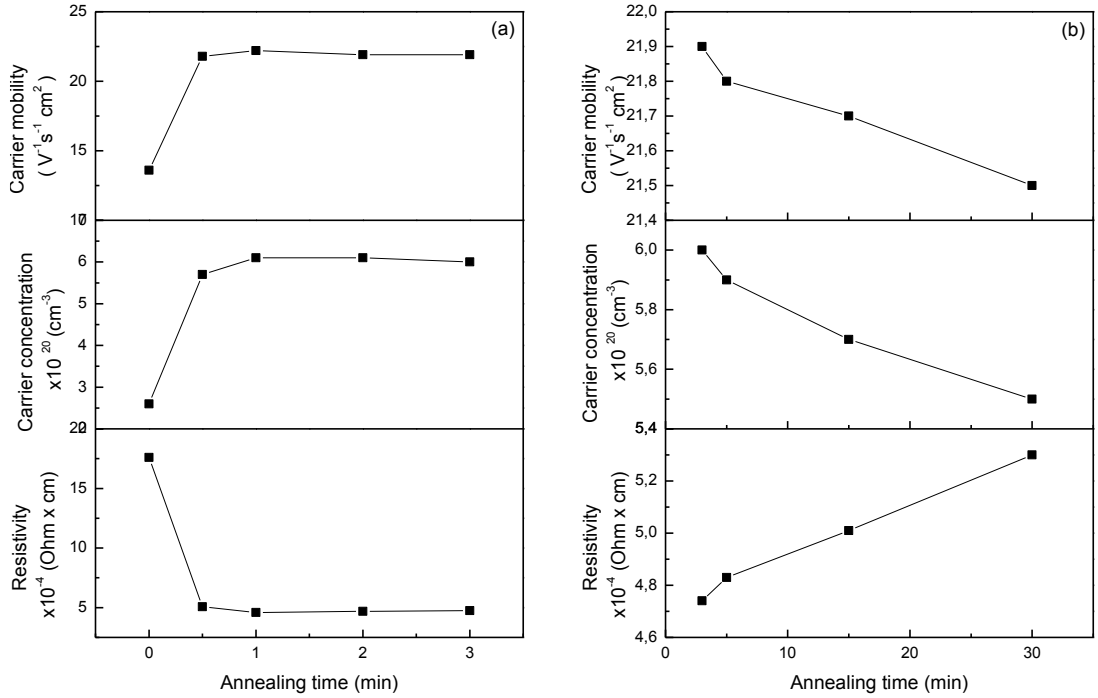

Figure 4.11: Variation of resistivity, mobility and carrier concentration of 300 nm-thick AZO films measured at the centre of the samples (2" SLG substrates) as a function of annealing time (400°C plateau duration).

However, further extending in the annealing time did not result in additional improvement of the conductivity. On the contrary, a slight increase in resistivity, from 4.6×10^{-4} Ω·cm to 4.7×10^{-4} Ω·cm, mainly related to a slight drop in the mobility, was observed.

One may wonder about the real relevance of such a slight modification which can be attributed to the standard deviation of uncertainty in measurement or to the non-reproducibility of the samples. In order to validate this increase in resistivity, a group of AZO thin films were annealed using the same conditions but for longer durations, 5 min, 7 min, 15 min and 30 min; the measured resistivity values are displayed in figure 4.11(b).

It was observed that the resistivity kept increasing and reached a maximum of 5.3×10^{-4} Ω·cm for an annealing time of 30 min. This confirms that the increase in resistivity observed when the samples were annealed for 2 or 3 min corresponds to a real resistivity increase with anneal time. The reason for this deterioration will be discussed later.

On the other hand, quantitative evaluation of the resistivity spatial distribution on the substrate surface, before and after annealing, is shown in figure 4.12. Considering the as-deposited sample, the resistivity mapping is a rather accurate replication of the target erosion phenomenon and the decrease in resistivity has been related to decreases in both the carrier concentration and the mobility, as shown in figure 4.13.

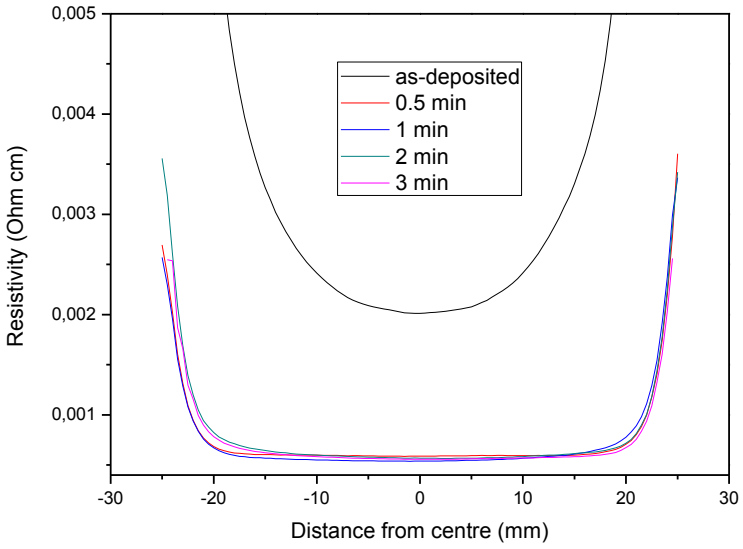

Figure 4.12: Spatial resistivity distribution of 300 nm-thick AZO films deposited on 2" SLG substrates and annealed at 400°C under N_2H_2 for different anneal times.

This increase in resistivity can be attributed to either the bombardment by energetic oxygen ions [H. Sato. 1992] [M. Chen. 2000], or the spatial distribution of both the amount and the position of oxygen reaching the substrate surface [T. Minami. 1992] [T. Minami. 2000] [K. Ichihara. 1994]. In both cases, negatively charged oxygen species are located at grain boundary surfaces, creating a potential barrier and acting as trapping sites for carriers.

Additionally to the well-known role of rapid annealing in the activation of Al doping, annealing under N_2H_2 atmosphere allows hydrogen atoms to reduce this potential barrier by oxygen desorption, known as passivation of grain boundary surfaces [B.Y. Oh. 2005], which improves both carrier concentration and mobility. Consequently, the resulting spatial distribution of resistivity on the substrate surface, after RTA under N_2H_2 atmosphere, exhibited high uniformity even for short annealing time, as shown in figure 4.12.

Also, it is interesting to note that the increase of the carrier concentration owing to the incorporation of hydrogen in the ZnO matrix, in which hydrogen acts as a shallow donor, was theoretically unpredictable since calculations showed that interstitial hydrogen atoms in ZnO matrix are unstable at high temperatures and tend to be desorbed [M.G. Wardle. 2006].

However, using N_2H_2 may also be one of the reasons of resistivity deterioration after annealing for long time, since previous researches have proven that trapped nitrogen atoms at grain boundary surfaces lead to considerable increase in resistivity [H. Tong. 2011].

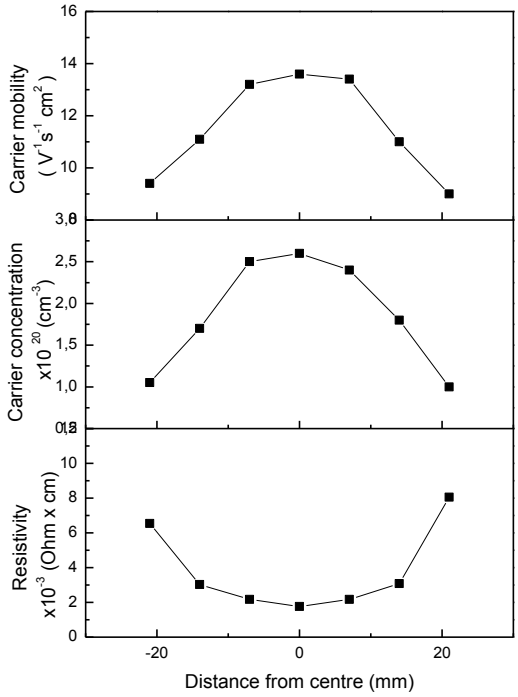

Figure 4.13: Profiles of resistivity, mobility and carrier concentration of the as-deposited AZO thin films along a diameter of 2" SLG substrate.

Concerning optical properties, transmittance measurements have been done and the results are displayed in figure 4.14. The improvement of transmittance from 73 % for the as-deposited thin film to 86 % after annealing for 30 sec, at wavelength of 550 nm, is obviously observed. Moreover, in the case the thin film was annealed for 1 min, better optical quality was obtained with 88 % of transmittance. However, further extending in the annealing time did not result in additional improvement of the transmittance.

This enhancement in the optical quality can be attributed to the improvement of the thin film stoichiometry by local rearrangement of the atoms [C. Lennon. 2009]. The short wavelength cut-off in transmittance presents also a clear blue shift after annealing. This is attributed to the movement of the Fermi level into the conduction band due to the increase in the carrier concentration (see §4.2.3). This result is consistent with the previous Hall measurements that showed such an increase of carrier concentration with annealing (see figure 4.11).

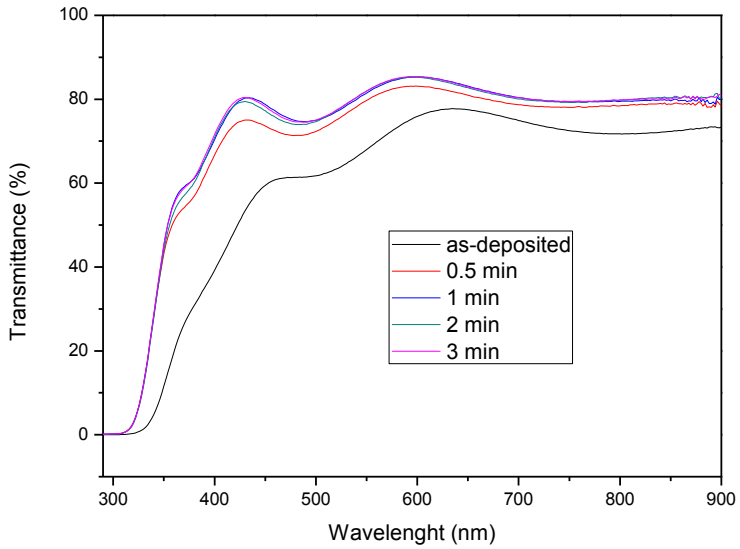

Figure 4.14: Optical transmittance spectra of 300 nm-thick AZO films before and after annealing at 400°C under N_2H_2 atmosphere.

The crystal structure of the AZO thin films before and after annealing was also analysed by XRD. As can be seen in figure 4.15(a), the XRD spectra revealed strong preferred orientation along c-axis with a single peak (002), indicating that the films are polycrystalline with hexagonal wurtzite structure. This preferred orientation can be attributed to the surface energy of the (002) plane which is the lowest for ZnO [N. Fujimura. 1993]. Also, it is interesting to note that no secondary phases, such as Zn, Al, Al_2O_3, $ZnAl_2O_4$, were detected.

The average crystallite size calculated using Scherrer's equation was about 30 nm, which confirms that the electrical properties of the films are limited due to the large surface area of the grain boundaries. No significant change in the crystallite dimension after annealing for 30 sec, 1 min, 2 min, and even for 3 min, was observed.

Moreover, a shift of the peak towards the shorter diffraction angles compared to the powder value was observed for the as-deposited thin films which can be explained by the native tensile stress.

Furthermore, the peaks corresponding to annealed thin films have shown a progressive shift towards higher diffraction angles, compared to the as-deposited thin films, as the annealing time increased (figure 4.15(b)). This clearly indicates strain relaxation, which is associated with the diffusion of interstitial Al atoms into Zn lattice sites [C. Lennon. 2009], known as doping activation phenomenon [S. Brochen. 2012].

However, it should be noted that after annealing for 1 min, the main factor responsible of this shift cannot be anymore the Al diffusion, since no increase in carrier concentration was observed. As a result, the shift observed for longer anneal times can be only attributed to

thermal relaxation of residual stress which showed no positive effect on the electrical properties of the AZO thin films (see figure 4.11(b)).

Also, one can confirm that no hydrogen was incorporated into the AZO matrix, since hydrogen incorporation in the AZO matrix induces further expansion of the crystal lattice that should result in lower diffraction angle shifts.

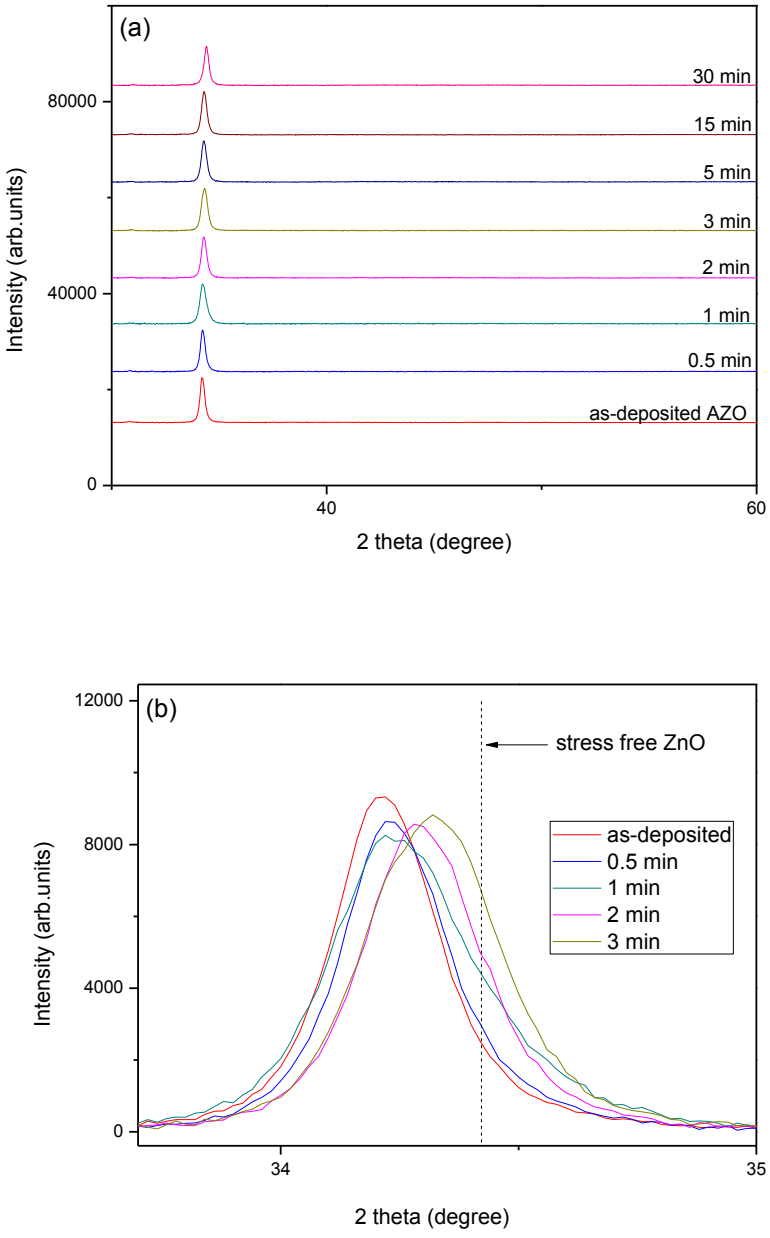

Figure 4.15. (a) XRD patterns of AZO thin films annealed at 400°C under N_2H_2 atmosphere for different anneal times. (b) Zoom in XRD profiles.

Scanning electron microscope pictures, as given in figure 4.16, show the surface morphologies of the AZO thin films before and after annealing. The morphology of the as-

deposited AZO thin films as well as of those annealed for 30 sec, 1 min, 2 min, and 3 min is found to be continuous and dense with an average grain size that varies from 10 to 50 nm.

However, further increase in the annealing time resulted in a progressive damage of the surface, with the appearance of some voids, in the case of the samples annealed for 5 and 15 min, and separate grains when the sample was annealed for 30 min.

Although the observed surface damage, it should be noted that the grain size of the thin films annealed for long time does not change compared with those annealed for shorter time, which agrees with the XRD results.

Consequently, the observed degradation of the samples compactness can be considered as the main factor causing the observed increase in resistivity of the AZO thin films annealed for long time (see figure 4.11(b)).

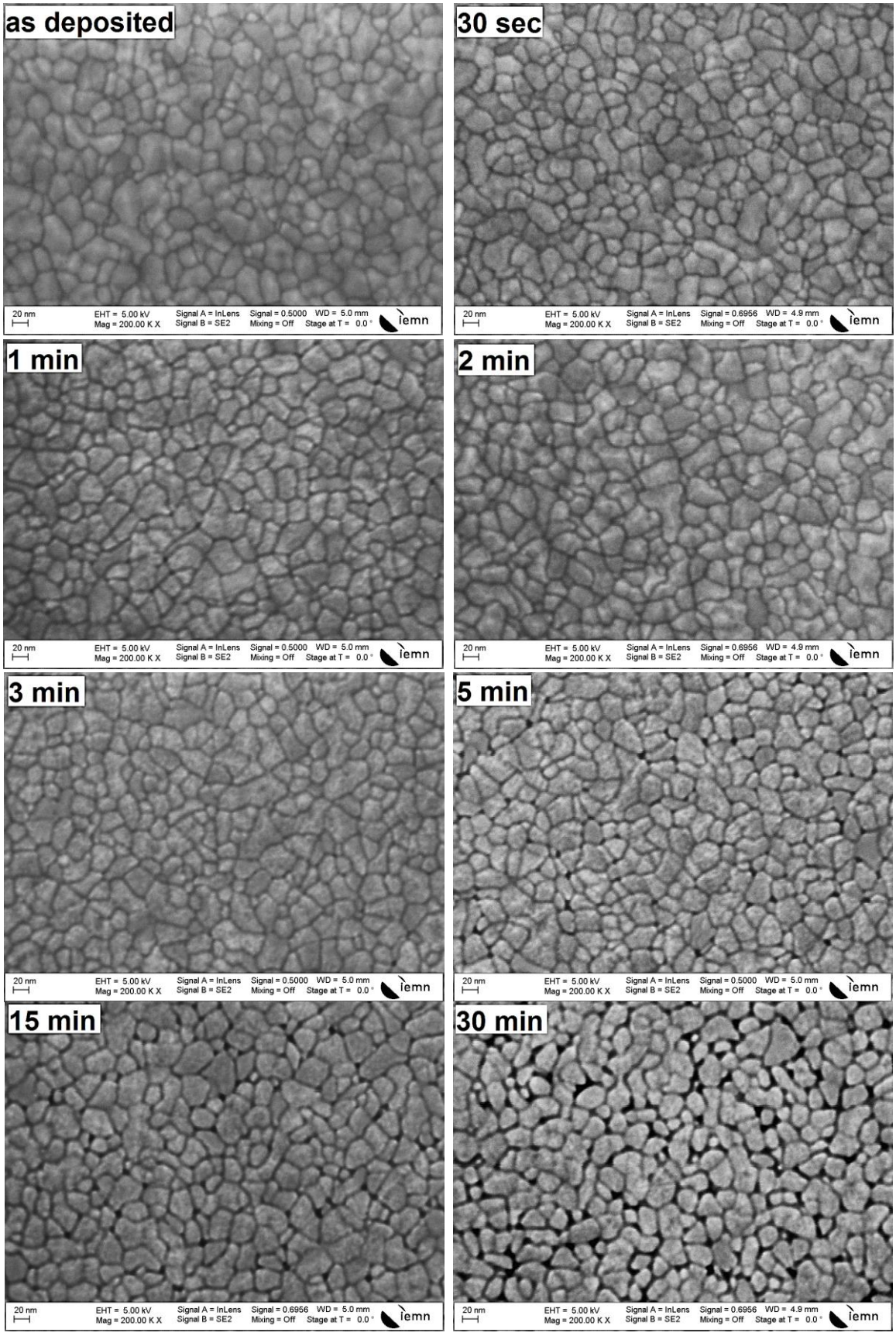

Figure 4.16: SEM images of AZO thin film surface before and after annealing at 400°C under N_2H_2 atmosphere.

4.10. RF deposited AZO thin films

It is very important to note that the integration of our developed pulsed-DC deposited AZO thin films in CIGS solar cells is only possible in case of using a low diffusivity buffer layer such as zinc oxysulfide (ZnOS) due to the needed post deposition annealing in order to improve the spatial resistivity distribution.

Furthermore, the use of such a process for the preparation of reference solar cells based on cadmium sulfide (CdS) buffer layer is expected to have a harmful effect on cell performance because of the pn junction deterioration due to the high diffusivity of Cd for higher temperature than 200°C.

For that sake, RF sputtering mode, commonly reported as the one that leads to better spatial resistivity distribution of AZO thin films [R. Cebulla. 1998] [T. Minami. 2010] [J.I Oda. 2010] [J.I. Nomoto. 2011], is investigated as an alternative process for the development of the front contact of reference cells. Furthermore, we have also checked if it is possible to further improve the optoelectronic properties using the RF sputtering mode.

Using the previously adjusted deposition conditions (deposition pressure an argon flow), the variation of resistivity as a function of RF-sputtering power was found to have a similar tendency as in case of using pulsed-DC mode, with an optimum sputtering power of 140W (around 1.7W/cm²) leading to a slightly lower resistivity in the RF mode (≈ 1.5 x 10^{-3} ohm.cm) compared to that obtained using pulsed-DC mode (≈ 1.7 x 10^{-3} ohm.cm), as can be seen in figure 4.17. However, the origin of the observed dependence is believed to be the same as in case of using the pulsed DC mode (change of the crystalline quality).

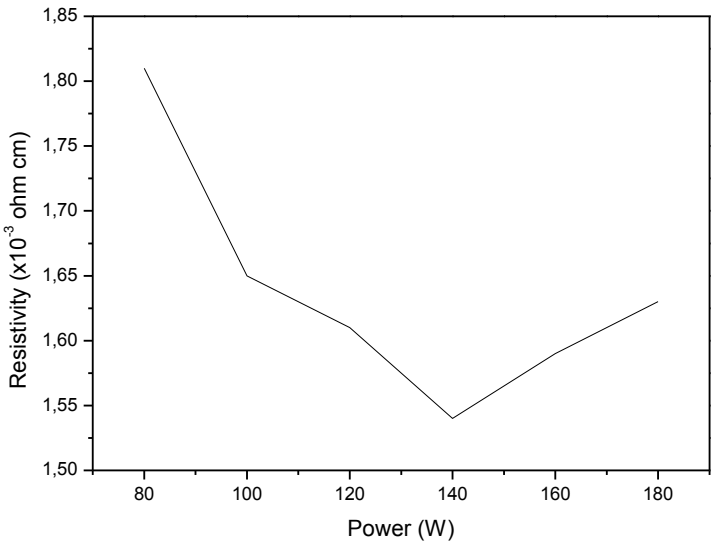

Figure 4.17: Variation of resistivity of 300 nm-thick AZO films, measured at the centre of the samples (2" SLG substrates) as a function of RF sputtering power.

The more important point is the clear enhancement in resistivity spatial distribution, without any need for post deposition annealing, resulted from the use of RF sputtering mode, as shown in figure 4.18. However, the origin of such an enhancement is still not clear neither for us nor for the authors who previously investigated this subject (we are still unable to give a clear explanation).

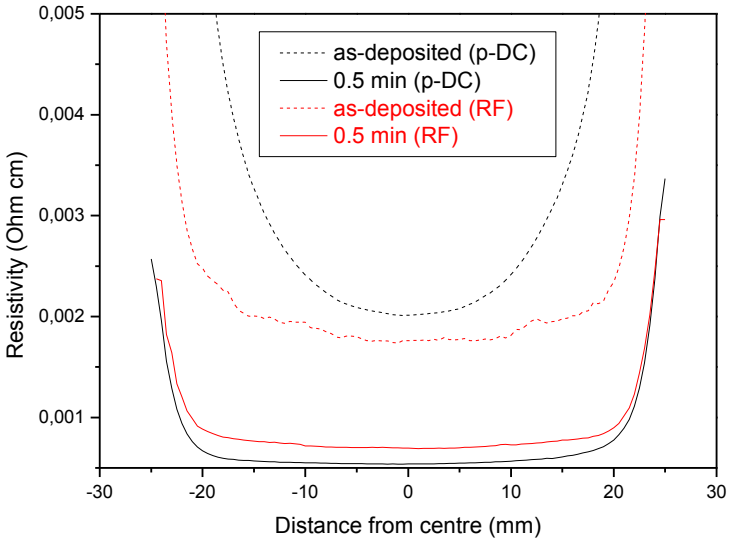

Figure 4.18. A comparison between spatial resistivity distributions of 300 nm-thick AZO films deposited on 2" SLG substrates using either pulsed-DC or RF sputtering mode; before and after annealing at 400°C for 0.5 min under N_2H_2.

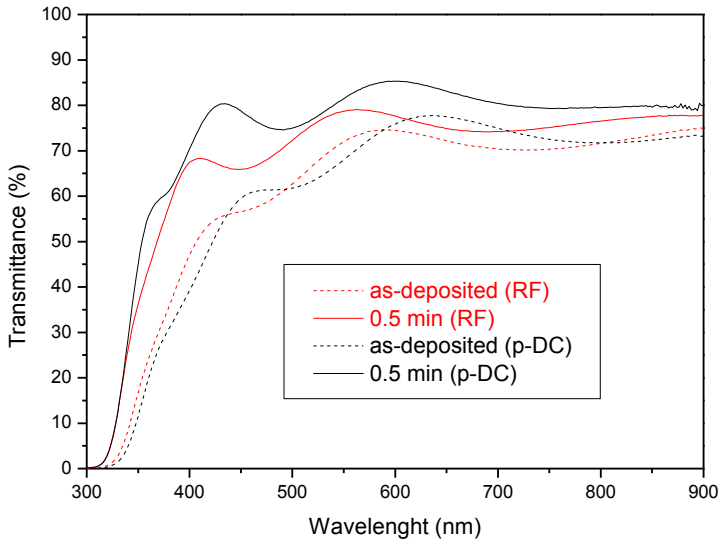

Figure 4.19: Optical transmittance spectra of 300 nm-thick AZO films obtained using either pulsed-DC or RF sputtering mode, before and after annealing at 400°C for 0.5 min under N_2H_2 atmosphere.

Furthermore, RF-sputtered thin films subjected to a rapid thermal annealing treatment have shown similar changes in electrical and optical properties to those deposited using the pulsed-DC mode. A comparison between the electrical and optical properties of thin films obtained using both sputtering modes before and after rapid thermal annealing of 0.5 min are shown in figure 4.18 and 4.19.

It is clear that pulsed-DC sputtered thin films subjected to a rapid thermal annealed have slightly better electrical and optical properties; as a consequence, pulsed-DC sputtering mode will be used for the preparation of ZnOS based solar cells.

4.11. Low temperature RTA

Finally, a low temperature rapid thermal annealing was investigated. The chosen temperature (200°C) and annealing time (2 min) correspond to the maximum that a CdS based solar cell can withstand before degrading. The obtained changes in electrical an optical properties after such an annealing process are displayed in figure 4.20 and 4.21, respectively. The measured resistivity at the centre of the 2'' substrate decreases from 15.5 $\times 10^{-4}$ Ω·cm to almost 10×10^{-4} Ω·cm while a slight increase in optical transmittance was observed.

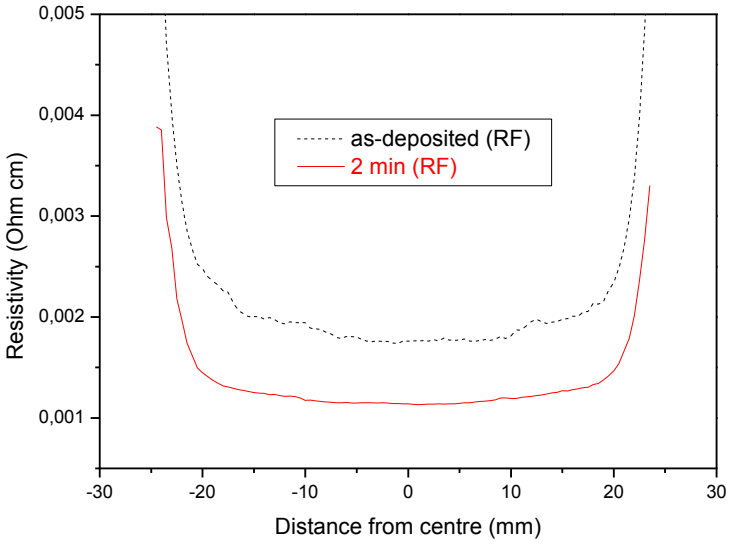

Figure 4.20: Spatial resistivity distribution of 300 nm-thick RF sputtered AZO films deposited on 2" SLG substrates before and after annealing at 200°C for 2 min under N_2H_2.

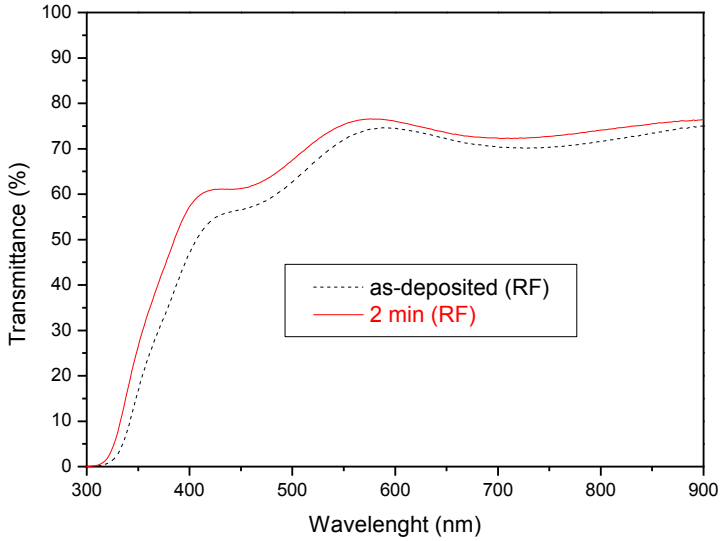

Figure 4.21. Optical transmittance spectra of 300 nm-thick RF sputtered AZO films deposited on 2" SLG substrates before and after annealing at 200°C for 2 min under N_2H_2.

4.12. Origins of limited optoelectronic properties of our samples

EDX analysis of 1 µm-thick AZO films have revealed the existence of additional elements with a total atomic concentration of 1.7 % (0.7 at % for iron and almost 0.5 at % for both nickel and chromium). It is worth to note that the used target is of high purity and the source of these impurities was found to be the fixing ring that covers the edge of the target (complementary mechanical element needed for the re-use of a ZnO target that was not previously designed to fit the equipment we used).

The induced effects from the incorporation of these elements and others into AZO thin films have already been investigated by several groups:

Chromium incorporation in AZO thin films was found to have a harmful effect on films conductivity resulted from the decrease in both carrier concentration and hall mobility. Furthermore, the amount of degradation was found to be dependent on the concentration of incorporated Cr (the higher the concentration of Cr, the sharper the increase in resistivity) [T. Minami. 2001] [K. Tominaga. 2002]. The observed increase in resistivity was attributed to the induced degradation in crystallinity from the incorporation of chromium.

Furthermore, T. Minami et al. have also observed a gradual decrease in optical transmittance as the Chromium concentration increases. According to them, this decrease in optical transmittance can be explained by the fact that chromium exhibits optical absorption in the visible range!!! [T. Minami. 2001].

On the other hand, even though not clear conclusion about the effect of nickel and iron on AZO thin film electrical properties was published, several groups have reported on the degradation of optical transmittance when iron or nickel is incorporated either in ZnO or AZO thin films [J.P. Mathew. 2014] [G. Shanmuganathan. 2014] [K.S. Hui. 2011].

4.13. Chapter conclusion

Looking for high optical transmittance and low resistivity aluminium doped zinc oxide thin films, almost all possible pulsed-DC sputtering parameters ‘’ pressure, power, Ar flow and duty cycle‘’ have been fixed and a trade-off was found.

It was found that the optimum sputtering pressure and power correspond to the balance point between the enhancement of crystallinity and the induced defects from atomic peening effect. Furthermore, sputtered thin films at low argon flow were found to have better optoelectronic properties due to the low concentration of implanted Ar atoms and therefore low generated stress.

Rapid thermal annealing of pulsed-DC sputtered thin films at 400°C under N_2H_2 atmosphere for only 30 sec was found to be beneficial. On one hand, the electrical properties were improved, evidenced by a clear decrease in resistivity value from 1.7×10^{-3} Ω.cm to 5.1×10^{-4} Ω.cm and showing uniform spatial resistivity distribution, due to both doping activation and grain boundary surface passivation. On the other hand, an increase in optical transmittance

from 73 % to 86 % owing to the enhancement of the thin films stoichiometry was also achieved.

Moreover, AZO thin films showed the lowest resistivity after 1 min of annealing; however, further extending in the annealing time caused a slight increase of the resistivity. A clear correlation between AZO thin films surface degradation and the increase of their resistivity has been pointed out.

Despite the slight difference in the resistivity value between AZO thin films annealed for 1 min and those annealed for 30 sec, both have shown uniform spatial distribution of resistivity. Therefore, and for CIGS based solar cell applications, annealing for 30 sec, or even less, would be advantageous, since the shorter the annealing time, the lower the risk of the p-n junction deterioration will be.

Furthermore, due to the poor resistivity spatial distribution of as deposited thin films and the known harmful effect of high temperature even for short time on CdS based solar cells, the use of the pulsed DC sputtering mode is excluded and an alternative deposition process was studied.

As deposited RF sputtered AZO thin films have shown a quite homogenous resistivity spatial distribution with slightly lower resistivity mean value compared to that obtained using the pulsed-DC mode, while no significant change in optical transmittance was observed.

Taking in consideration both the maximum annealing temperature and duration to which CdS based solar cells can withstand before degrading, a low temperature rapid thermal annealing process was investigated. The resistivity was decreased from 1.5×10^{-3} Ω.cm to 1×10^{-3} Ω.cm while a slight increase in optical transmittance of about 4% was observed.

Finally, elemental composition analysis have revealed the presence of several metallic impurities to which a harmful effect is already attributed in literature. Therefore, we are reasonably confident that using an adapted target will lead to a noticeable improvement in both electrical and optical properties.

Chapter 5: Solar cells characterization

In this last chapter, the four elementary processes reported before have been joined in order to fabricate solar cells. Electrical characterizations as well as microstructural analyses of some of the fabricated solar cells will be presented. For the sake of clarity, we only report the more significant results; they only represent less than 25% of the work dedicated to the fabrication of a complete solar cell.

On the contrary to the previous chapters, this one consists of only one part in which only experimental results will be presented. The state of the art has already been, implicitly, presented within the previous chapters.

5.1. Overall view of cell fabrication process

The different trials hereafter reported were done on an ongoing process. The various process improvements that have been presented before concerning each elementary layer fabrication are not fully implemented in all trials. Each trial will sum up the main fabrication processes that have been used.

As a general matter, all cells have been fabricated on 2" SLG substrates. After the whole set of layers have been deposited, a Ni/Au based trident-shaped grid contact has been deposited using lift-off technique. Elementary 0.5 cm² (7mm x 7mm) surface area cells have been delineated by scribing the CIGS and top layers. A typical view of a full wafer is shown in figure 5.1.

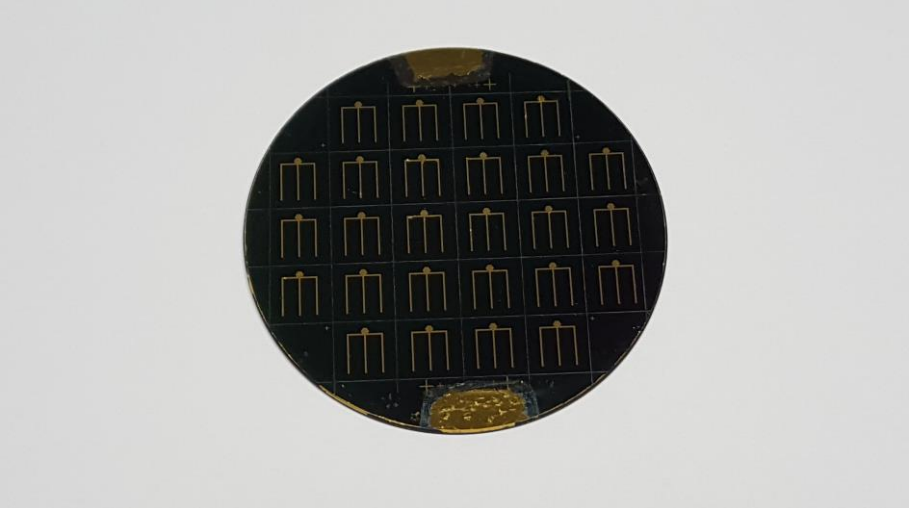

Figure 5.1: Final view of a 2" wafer on which 26 0.5cm² cells have been defined. The gilded zones that are visible at bottom and top correspond to back electrode contacting areas.

5.2. ZnOS based solar cells: first tests

A first set of full sputtering solar cells has been prepared using a ZnS_xO_{1-x} buffer layer of which the composition, x, was tuned between 0.04 and 1 (0.04, 0.07, 0.1, 0.14, 0.21, 0.6, 0.83, 1). The ZnS_xO_{1-x} buffer layer has been prepared using a continuous rotation configuration, previously detailed in §3.8.2. On the other hand, the used CIGS layer deposition process was presented in §2.9: a stack of multi-bilayer which overall thickness is 1 µm. A schematic of the fabricated cell structure is presented in figure 5.2 as well as the main steps of fabrication in figure 5.3.

Pulsed-DC: 1W/cm^2, P: 4.5x10^{-3}mbar	AZO: 300 nm
Pulsed-DC: 1W/cm^2, P: 4.5x10^{-3}mbar	i-ZnO: 50 nm
P: 4.5x10^{-3}mbar - ZnO pulsed DC: 0→1.5W/cm^2 - ZnS RF: 0→2W/cm^2	ZnOS: 50 nm
1 bilayer: - pulsed DC: 1W/cm^2 P: 4x10^{-3}mbar - pulsed DC: 1W/cm^2 P: 1.8x10^{-2}mbar	CIGS: 920 nm 5 bilayers: 45/140 nm
pulsed DC: 1W/cm^2 P: 1.8x10^{-2} mbar	CIGS adhesion layer: 100 nm
DC: 1 W/cm², P: 4.5x10^{-3}mbar	Mo trilayer: 50/100/350 nm
DC: 1 W/cm², P: 2x10^{-2}mbar	
DC: 0.5 W/cm², P: 2x10^{-2}mbar	
SLG substrate	

Figure 5.2: Structure and processing parameters of the CIGS cell.

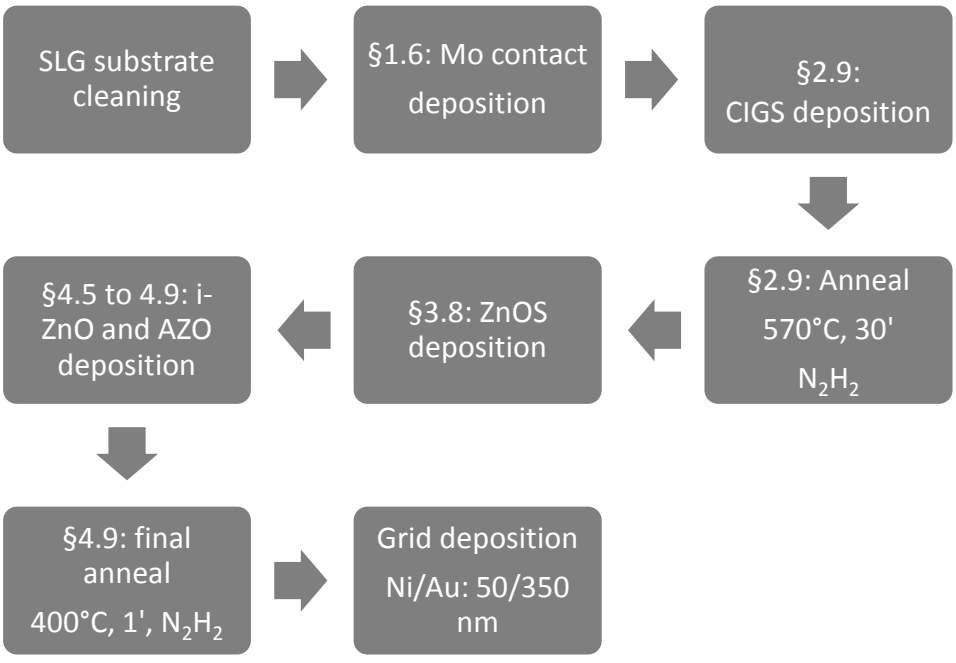

Figure 5.3: Overall view of fabrication process.

The electrical characterization of this first set of solar cells was disappointing. The J-V characteristic did not relate a diode function but was rather similar to a resistance behaviour: an example of the obtained J-V characteristic is given in figure 5.4.

Furthermore, the commonly reported treatments ‘’light soaking for 30min and annealing at 200^{o}C for 10min’’ did not lead to any improvement.

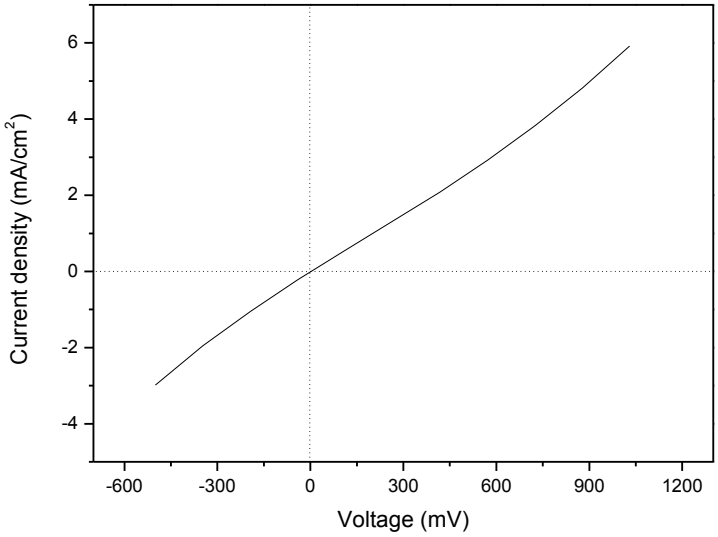

Figure 5.4: Dark Current-Voltage characteristic of 0.5 cm^2 CIGS solar cell. The composition x of the ZnS_xO_{1-x} buffer layer is 0.21.

Mainly two parameters were thought to be at the origin of such an electrical behaviour: the low crystalline quality of the CIGS layer and/or the induced CIGS surface deterioration during the deposition of the ZnS_xO_{1-x} buffer layer (due to the use of high sputtering power).

For that sake, and before preparing a second set of solar cells, the CIGS layer quality was improved and a low power sputtering process for the deposition of the ZnS_xO_{1-x} layer was developed, as previously presented in §2.10 and §3.8.3, respectively. Furthermore, in order to exclude any possible contribution of the high temperature annealing step, RF-sputtering mode was used for the deposition of the window layer (i-ZnO and AZO (§4.10). The deposition processes for the Mo layer was kept unchanged. The cell structure is so the one shown in figure 5.5.

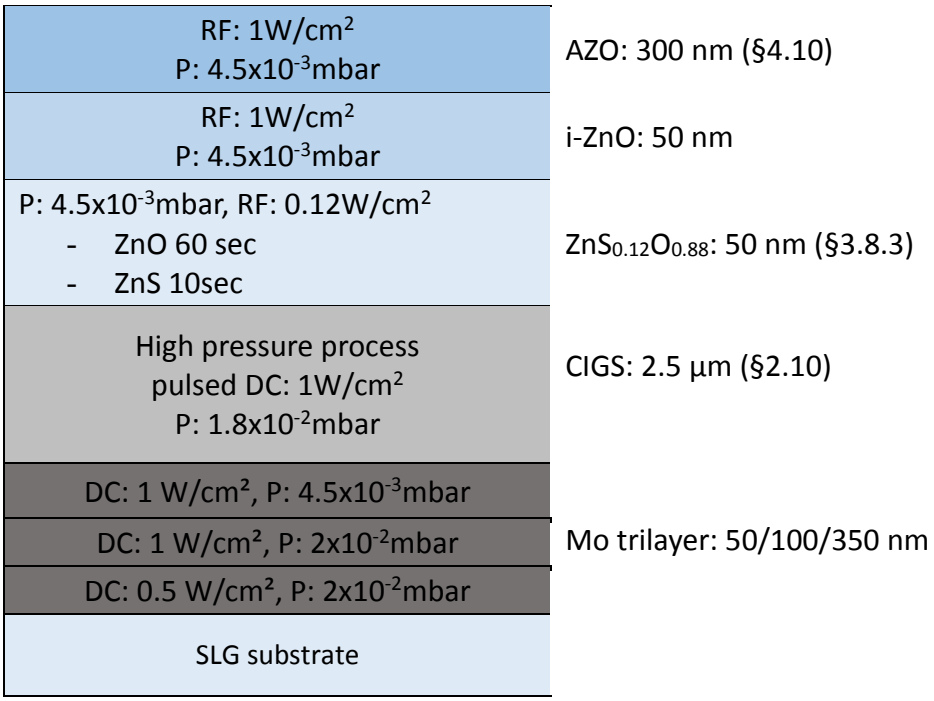

Figure 5.5: Structure and processing parameters of the CIGS cell.

Consequentially, a photovoltaic effect was observed, as shown in figure 5.6; however, the obtained electrical characteristic does not reflect the high microstructural quality shown in figure 5.7. Moreover, light soaking for 30min and annealing at 200°C for 10min were found to be useless (no further improvement was achieved).

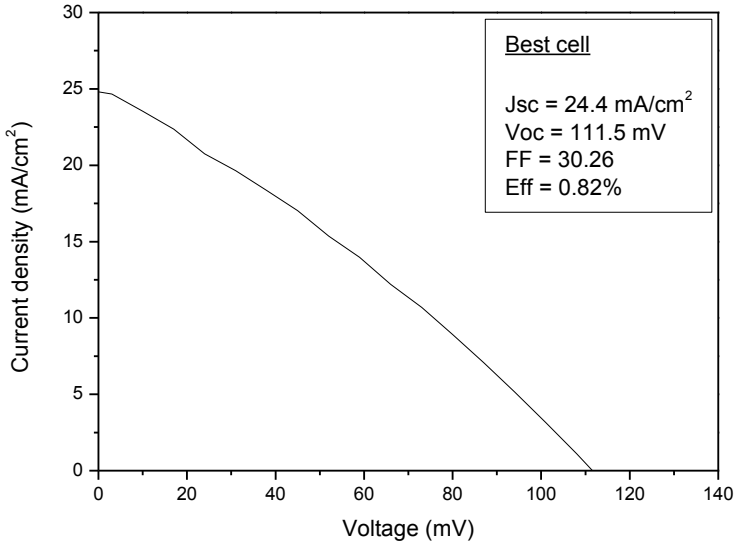

Figure 5.6: Best Current-Voltage characteristic of 0.5 cm^2 CIGS solar cell using an improved quality CIGS layer and a low power sputtered $ZnS_{0.12}O_{0.88}$ buffer layer.

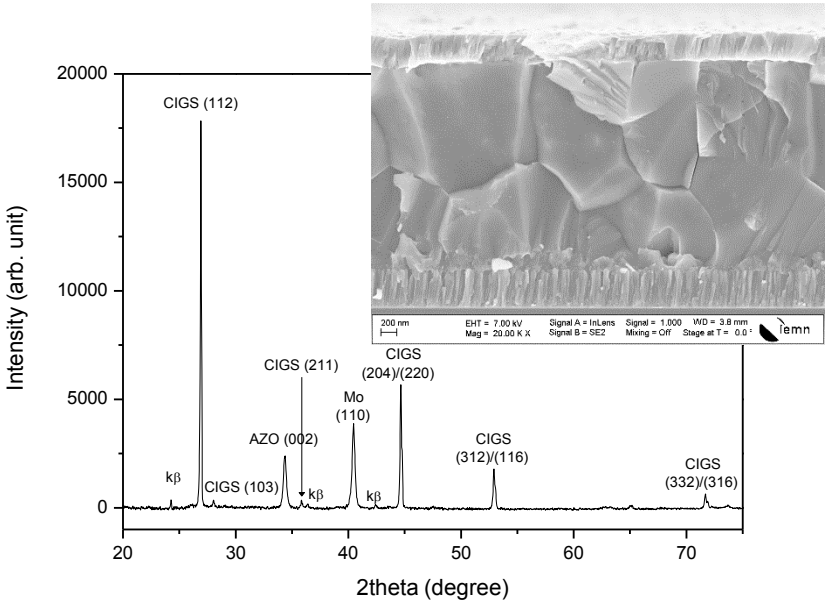

Figure 5.7: XRD pattern and SEM cross sectional image corresponding to the solar cell of which the J-V characteristic is shown in figure 5.6.

Because of the ambiguous situation and the unclear reason behind such limited electrical characteristics, we decided to first evaluate the quality of our CIGS absorber layer using a standard CBD-CdS buffer layer (see §3.7) instead of the sputtered ZnS_xO_{1-x}. The process flow is then identical to the one presented in figure 5.5 except for the ZnOS deposition hereby replaced by a CdS deposition. The cell structure is so the one shown in figure 5.8.

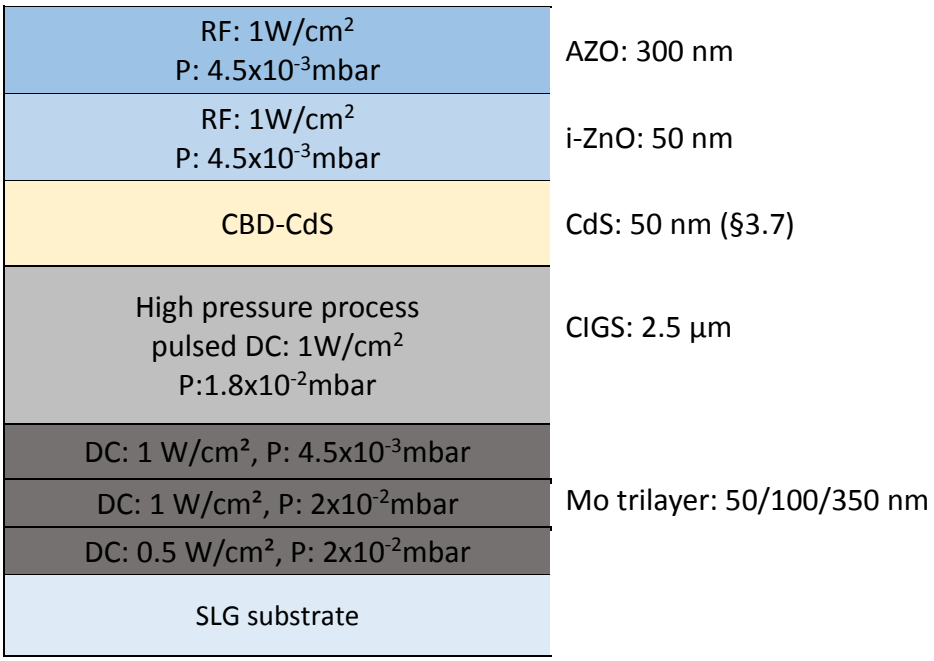

Figure 5.8: Structure and processing parameters of the CIGS cell.

The obtained results were not better, and even worst!! It was not good news; however, at least we have confirmed that the sputtered ZnS_xO_{1-x} layer was not the limiting factor.

Based on that, a deeper analysis of the final solar cell was then performed using GDOES (Glow discharge optical emission spectroscopy by courtesy of Horiba Jobin-Yvon dedicated team) depth profiling: *The obtained results were more than surprising*. We found out that non-negligible concentrations of iron, nickel and chromium were present within the CIGS layer, as can be clearly seen in figure 5.9.

Comparing the GDOES signals of these elements before and after annealing, we have concluded that the presence of these elements within the CIGS layer was originated from their out diffusion from the molybdenum layer. Furthermore, the EDX analysis of the molybdenum layer revealed the presence of these elements in the following concentrations: Fe 0.7at%, Ni and Cr 0.5at% each.

It is important to note that the GDOES signals, presented in figure 5.9, have already been normalized considering the GDOES signals within the as-deposited CIGS layer as a reference background (for normalization). Therefore, considering that the maximum signal within the molybdenum layer is equal to the measured concentration using EDX, one can give an estimation of the concentration of these elements within the annealed CIGS layer: Fe 0.126at%, Ni 0.026at % and Cr 0.044at%.

The effect of each of those elements on solar cells performance was previously reviewed in §2.5.1. In our case, we have the contribution of the three elements at the same time, which makes the impact more pronounced.

NB: it is worth to note that the used molybdenum target is of high purity; however, it was not initially dedicated to our sputtering equipment. Therefore, the detected metallic impurities within the molybdenum layer are believed to be originated from the complementary target locking ring that has been added to fix it at the right position within the equipment: it appears that this locking ring had a very little but dramatic exposure to deposition plasma and its constitutive elements have so been sputtered jointly with Mo.

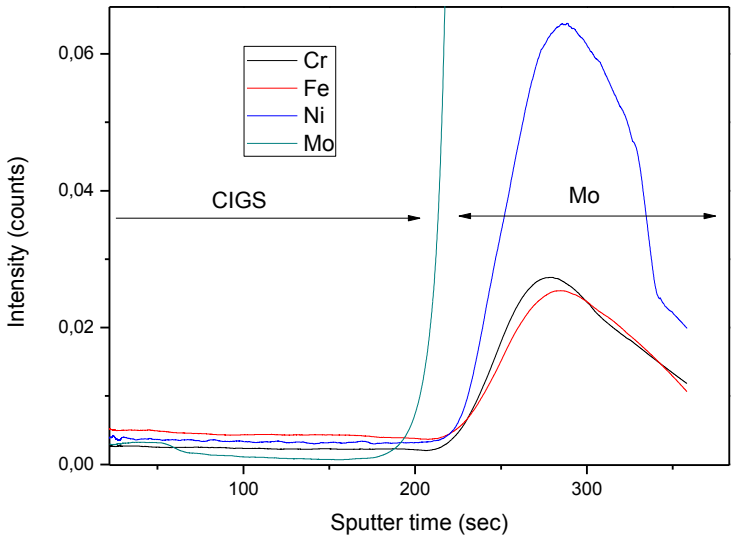

Figure 5.9: Normalized GDOES depth profiles of Mo, Cr, Fe and Ni within an annealed CIGS/Mo bilayer.

5.3. Solar cells fabrication using high purity molybdenum back contact

Based on the above shown GDOES results, we have decided to use another sputtering machine for the deposition of the molybdenum layers, in which target and backing plate were matched to the equipment.

It is worth to note that the new sputtering machine has a different configuration (no magnetron, different target to substrate distance…etc) and therefore the used deposition conditions of the molybdenum layer for the preparation of the first solar cell were "judiciously randomly" chosen *(no reinvestigation of the molybdenum layer properties was performed because the use of this machine was temporary –waiting for the arrival of a new molybdenum target matched to our "routine" equipment).* The deposition processes for all the other layers (CIGS, CdS, ZnO and AZO) were kept unchanged. The cell structure is so the one shown in figure 5.10.

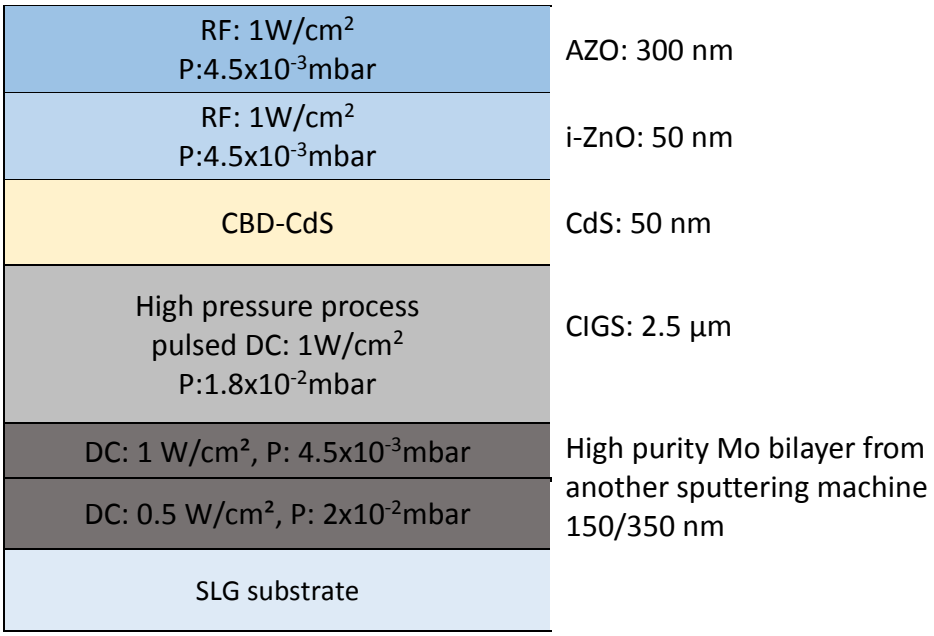

Figure 5.10: Structure and processing parameters of the CIGS cell.

The obtained J-V curves of the first set of cells are shown in figure 5.11, while the microstructural analyses (XRD and SEM) corresponding to the best cell are shown in figure 5.12.

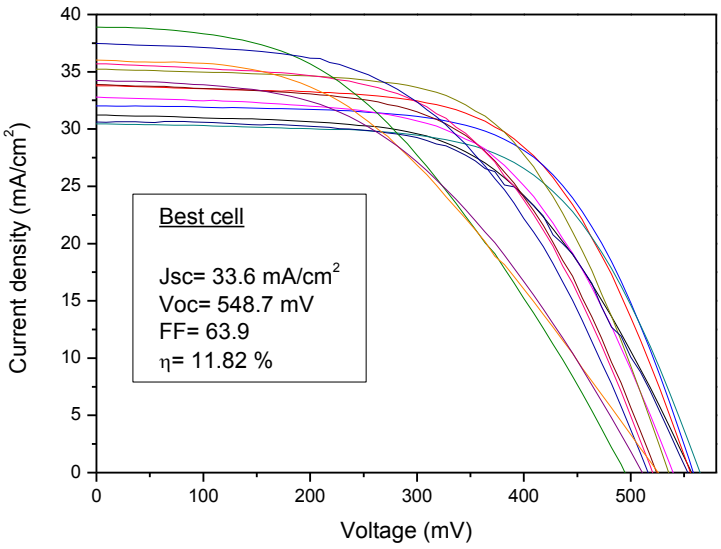

Figure 5.11: Current-Voltage characteristics of 0.5 cm^2 CIGS solar cells.

NB: It is worth to note that all these J-V curves were obtained from the same 2" SLG substrate (26 cells of 0.5 cm^2 each per 2'' sample).

Finally, operating solar cells were obtained, which confirms our conclusion based on the analysis of the GDOES results: metallic impurities were one of the limiting factors for cells operation, other factors might also have a contribution, but it should have been the killing one.

More surprisingly, it was found out that the CIGS layer was not completely recrystallized after the annealing process and not any more (112) preferentially oriented but rather slightly (220). This is believed to be related to the properties (mainly the density) of the used molybdenum layer, as previously discussed in §2.13.1.

Even though the relatively very poor microstructure, this first set of solar cells has shown acceptable efficiencies: relatively high current density (since no antireflection layer was used) and limited open circuit voltage on which the fill factor is directly dependent.

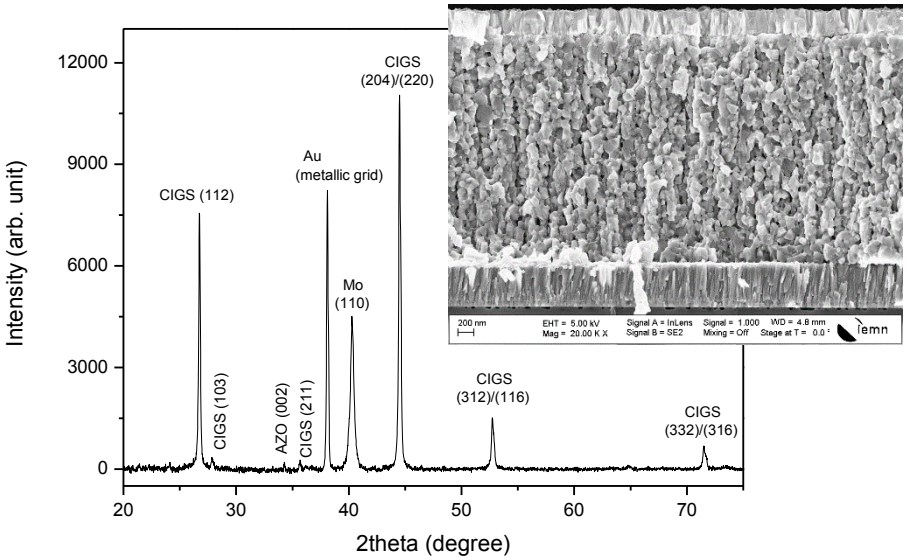

Figure 5.12: XRD pattern and SEM cross sectional image corresponding to the best solar cell of which the J-V characteristic is shown in figure 5.11.

5.4. Highly crystalline quality CIGS layer based solar cells

In the light of these results, we have intuitively sought to further improve the efficiency by further improving the crystalline quality of the CIGS layer.

To do so, and based on our experience in CIGS layer recrystallization, two ways have been followed: either by increasing the molybdenum density (lowering the sputtering pressure) or by increasing the annealing temperature.

5.4.1.High-density molybdenum layer based solar cells

On the contrary to our ambitions, increasing the compactness of the molybdenum layer did not lead to further improvement of the electrical characteristics but rather to a dramatic degradation, as can be seen in figure 5.13, even though a better microstructural quality has been achieved, as shown in figure 5.14.

NB: it is important to note that the deposition processes for all the other layers (CIGS, CdS, ZnO and AZO) were kept unchanged.

The so-called roll over effect (a strong current-blocking behavior at forward biases exceeding the open-circuit voltage) was clearly observed in figure 5.13. This roll over effect is commonly reported as a sign of lack of sodium [D. Rudmann. 2004] [D. Rudmann. 2005] [P.P. Choi. 2011].

The effect of molybdenum compactness on the concentration of the out-diffused sodium was previously summarised in §1.1.4.

From literature, the non-passivated defect states within the CIGS layer and therefore low carrier density, and/or the secondary diode at the Mo/CIGS interface, are considered as the possible origins of such a distortion of the J-V curve [D. Rudmann. 2004] [D. Rudmann. 2005] [P.P. Choi. 2011].

The effect of sodium on defect passivation and $MoSe_2$ interfacial layer formation was previously reviewed in detail in §2.5.2 and 2.7, respectively.

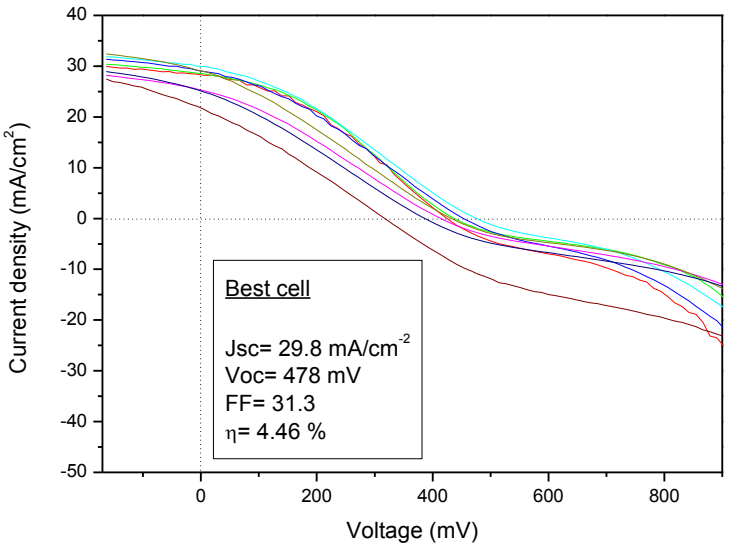

Figure 5.13: Current-Voltage characteristics of the fabricated solar cells using a dense molybdenum layer.

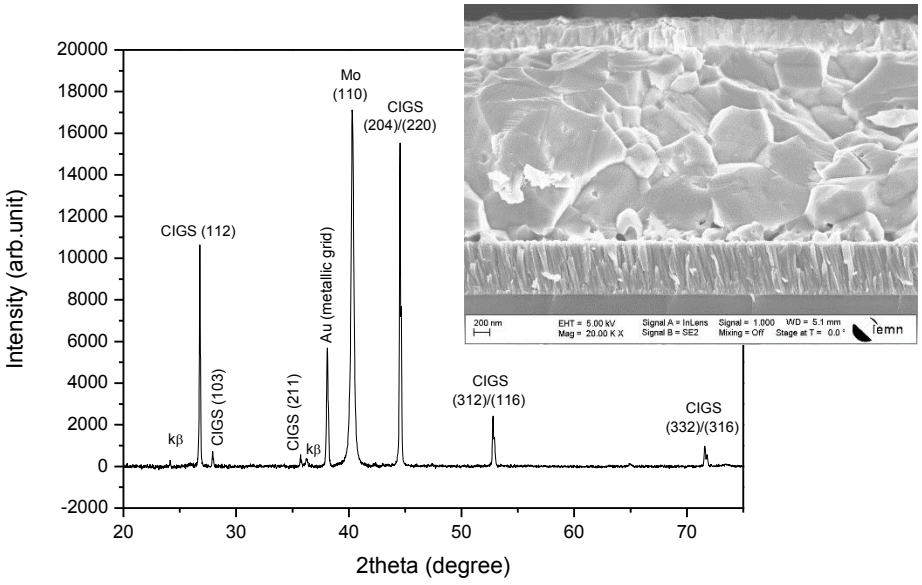

Figure 5.14: XRD pattern and SEM cross sectional image corresponding to the best solar of which the J-V characteristic is shown in figure 5.13.

Further lowering in the molybdenum sputtering pressure, so densifying more the Mo layer, and therefore further blocking sodium out diffusion was found to give completely ‘’dead’’ solar cells, as can be seen in figure 5.15. Corresponding to this, excellent CIGS microstructure was obtained, as shown in figure 5.16; *however, it did not save the day!!*

From literature, even sodium free CIGS solar cells have shown respectable efficiencies: around 11% from J Eid et al [J. Eid. 2015] and 8 to 10% from A. Rockett et al [A. Rockett. 2000].

So why it does not work in our case, even though the microstructure quality of the CIGS layer is far better than that reported in both works!!

The reason behind such an observation is still a subject of further investigation.

Based on this result, one can conclude that the use of high compactness molybdenum layer, and consequentially lack of sodium, had also a contribution in limiting the electrical properties of the first set of solar cells presented in §5.2.

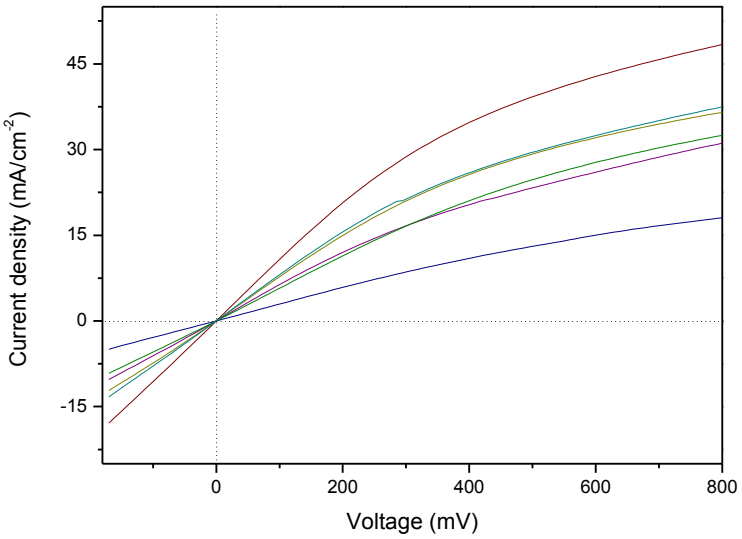

Figure 5.15: Dark J-V characteristics of the fabricated solar cells using a high density molybdenum layer.

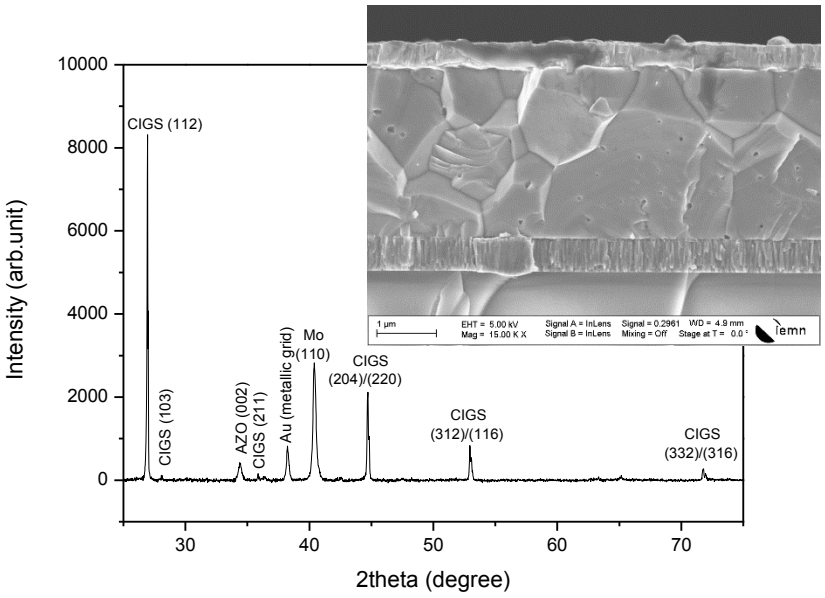

Figure 5.16: XRD pattern and SEM cross sectional image corresponding to the solar cells of which the J-V characteristics are shown in figure 5.15.

5.4.2.Higher temperature annealed CIGS layer based solar cells

Based on the commonly reported role of sodium (passivation of defects at the grain boundaries: §2.5.5), and for a given molybdenum density, one can logically expect better electrical characteristics in case of using high microstructural quality CIGS layer solar (less grain boundaries). Furthermore, one can expect that sodium concentration is higher in higher temperature annealed CIGS layer.

In figure 5.17, we show the J-V characteristics of two solar cells of which Mo/CIGS stacks were deposited in the same conditions but annealed at different temperatures. Furthermore, both cells have been completed using the same deposition processes for the upper layers (CdS, i-ZnO and AZO) as previously presented in figure 5.10.

Surprisingly, and on the contrary to our predictions, solar cell based on the use of low temperature annealed CIGS layer and therefore poor microstructure has shown better electrical properties!!

The question that comes intuitively to mind is the following: why does well-crystallized CIGS based solar cell shows lower electrical behaviour?

To answer this question, defects analyses using admittance spectroscopy (AS) and/or deep level transient spectroscopy (DLTS) would be very helpful!!

Meanwhile, one possible hypothesis is the following: defects are not only at the grain boundaries but also present (with high density) within the grains.

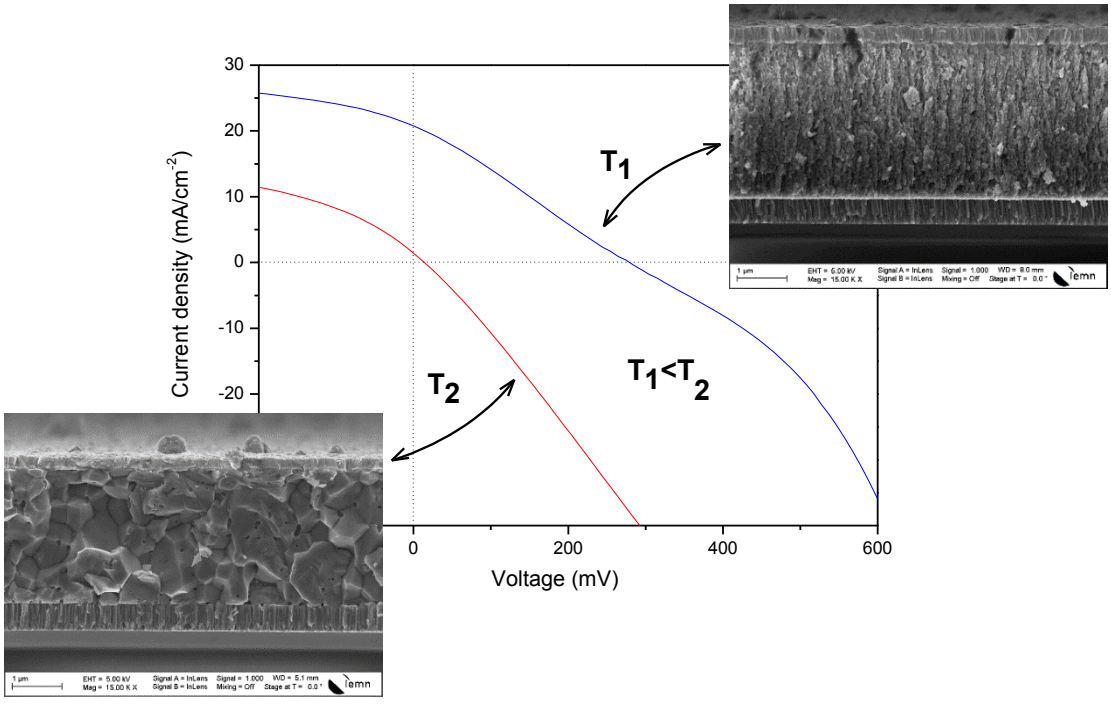

Figure 5.17: Current-voltage characteristics of CIGS solar cells as well as the corresponding SEM cross sectional images. Cells are prepared using a similar molybdenum back contact, but annealed at different temperatures.

5.5. Sodium post deposition process

Persuading that high crystalline quality CIGS thin films would lead to higher efficiency solar cells, and because of the faced challenge for achieving high crystalline quality CIGS layer and high sodium concentration at the same time *(due to the contradictory sputtering conditions of the molybdenum layer)*, we have decided to keep working on high quality CIGS layer based

solar cells and change the source of sodium using a post deposition treatment (in order to ensure whether it is a matter of sodium or not).

This kind of treatment is commonly performed using an evaporated NaF layer. Using this process, the precise control of the sodium concentration is possible by changing the thickness of the NaF layer.

Because of the unavailability of a dedicated system for such a process in our laboratory, an alternative process (less precise) was used, which is based on the spreading of NaCl solution on a preheated CIGS thin film (hot plate was used).

Please note that 300nm thick Al_2O_3 thin film was used as a barrier layer for sodium out-diffusion from the substrate. Please also note that Mo/Mo(O) back contact was used for the fabrication of this set of cells.

The deposition processes for all the other layers (CIGS, CdS, i-ZnO and AZO) were kept the same as shown in figure 5.10. The cell structure is so the one shown in figure 5.18.

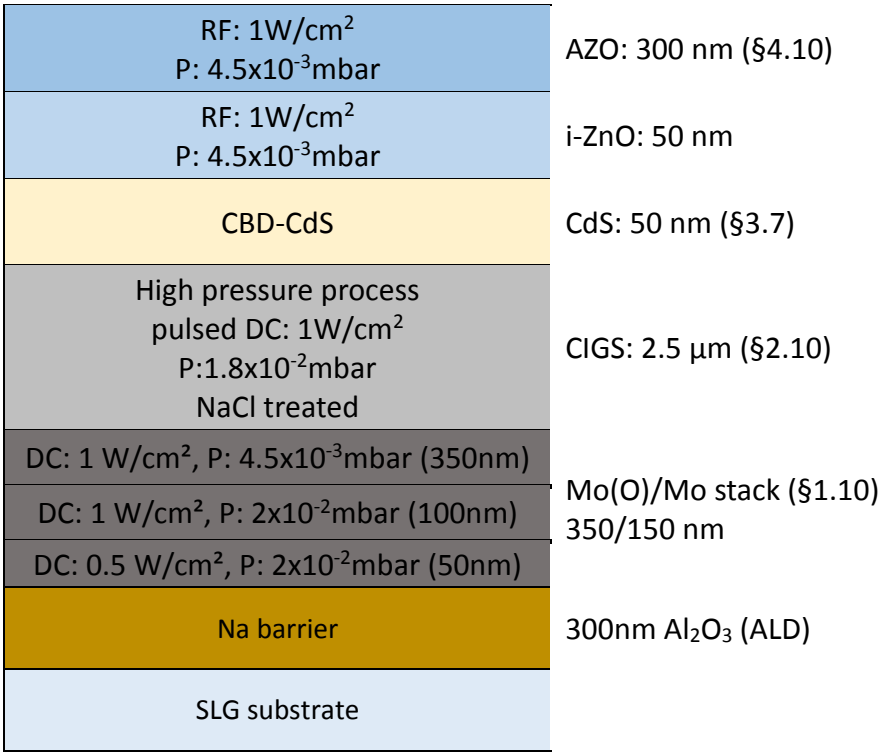

Figure 5.18: Structure and processing parameters of the CIGS cell.

Furthermore, to check out the effect of sodium concentration on high quality CIGS layer based solar cells, three different solutions with different NaCl concentrations have been used.

The obtained Current-Voltage characteristics and the corresponding SIMS profiles of sodium throughout the whole solar cell structures are presented in figures 5.19 and 5.20, respectively.

Once again, we were able to hit the 10% efficiency bar, but this time based on high quality CIGS layer, as can be clearly seen in figure 5.21(c).

In consequence of adding high concentration of sodium, all cells parameters have been improved. Such a dependence of solar cell efficiency on sodium concentration has been extensively studied in previous days by several groups.

As an example and not exclusively, one can cite the works performed by J. Eid et al [J. Eid. 2015] and that by Rockett et al [A. Rockett. 2000]. In both works, an optimum concentration was found, above which a harmful effect of sodium on solar cells performance was observed.

In our case we believe that we are still far from this optimum concentration, and any further increase in sodium concentration would lead to a further improvement of the cell efficiency.

On the other hand, and in order to check out whether sodium was the only parameter at the origin of such changes in the electrical behaviour or not, deeper investigation was carried out: the XRD, SIMS, SEM and Raman analyses of the three samples have been performed and compared to each other. The obtained results are presented in figures 5.21 to 5.24.

The SEM cross sectional images, given in figure 5.21, reveal the high microstructural quality of the CIGS layer used for the preparation of the three solar cells.

From the XRD analyses, despite the slightly higher (112) peak in case of cell A, almost no difference can be found, as can be seen in figure 5.22. Furthermore, the fact that all samples are (112) highly oriented confirms that such an orientation was not at the origin of the observed degradation in case of using high-density molybdenum layer without any additional sodium supply (§5.4.1).

Raman analyses have also been performed in order to mainly check out the existence of the Cu_2Se secondary phase. The obtained spectra, shown in figure 5.23, confirm the pure single chalcopyrite phase of the CIGS layer in both the 10% efficiency cell and the 0% efficiency cell. Furthermore, the observed peaks shift can be attributed to either a difference in the stress state or a slight difference in the composition between the two layers. Moreover, the observed difference in the peak full width at half maximum (FWHM) is in a good consistent with the XRD results: slightly higher CIGS crystallite size of the 0% efficiency solar cell.

NB: Please note that Raman analyses have been performed after a wet etching (in HCl) of the window and the buffer layers.

On the other hand, independently of the tested solar cell, the SIMS profiles of the constituent elements of the CIGS layer have shown a flat distribution throughout the whole CIGS layer thickness, no elemental accumulation and no strong diffusion into the molybdenum layer, as can be seen in figures 5.24(a, b and c).

Finally, comparing the SIMS profiles of cadmium, one can confirm that the CdS layer coverage was the same for the three solar cells, as can be seen in figure 5.24(d)

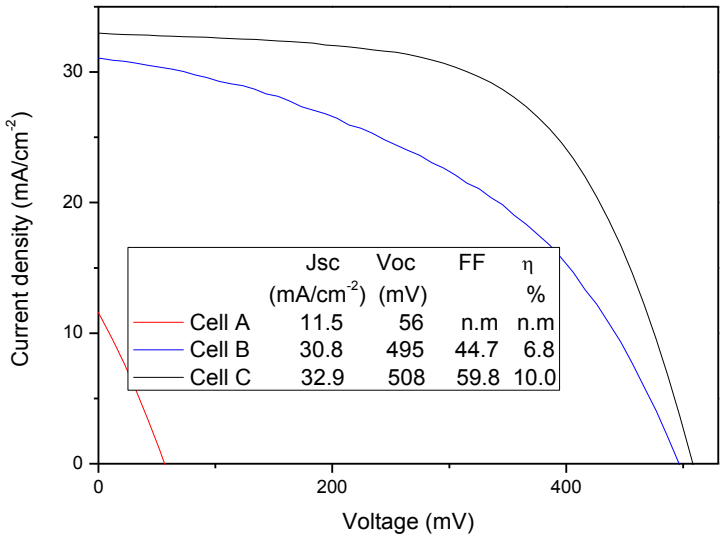

Figure 5.19: Current-Voltage characteristics of the obtained solar cells of which the CIGS layers have been subjected to NaCl post annealing treatment.

NaCl solutions of different concentrations $C_{(NaCl)}$ have been used:

$C_{(NaCl)}$ cell A< $C_{(NaCl)}$ cell B< $C_{(NaCl)}$ cell C

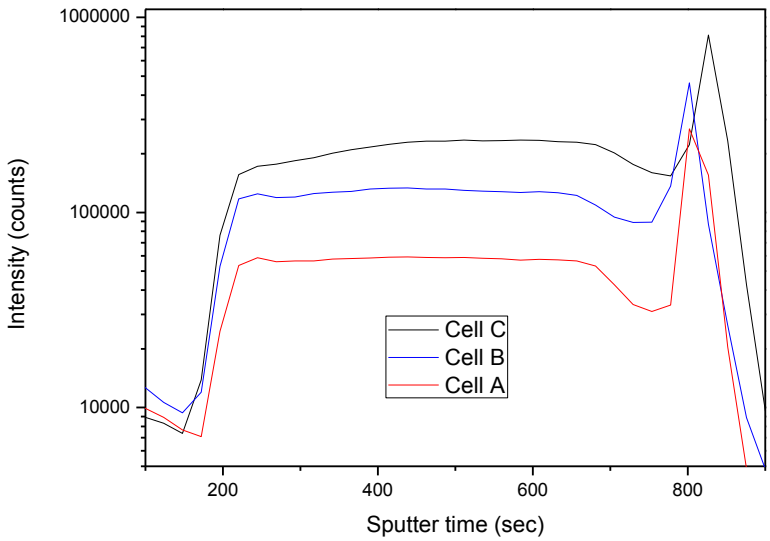

Figure 5.20: SIMS profiles of sodium throughout the final cells.

(Cell A) (Cell B)

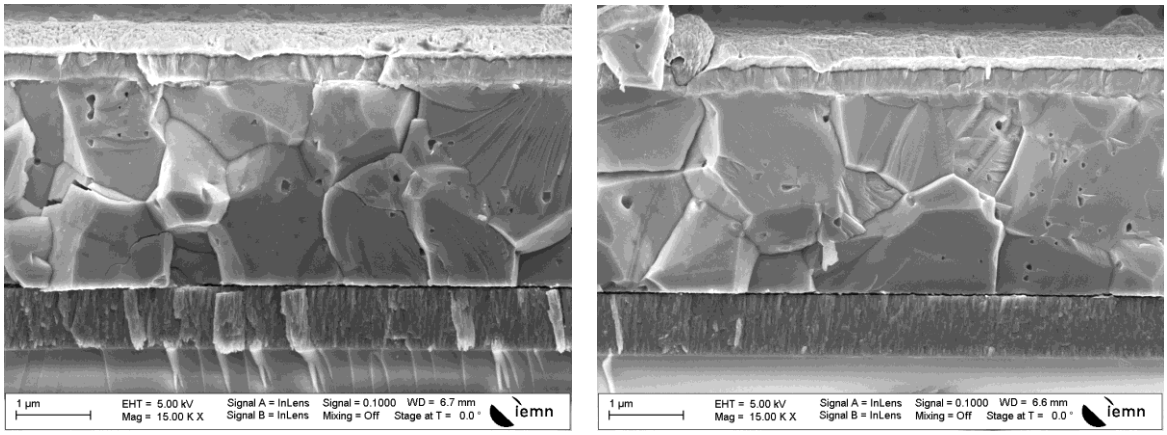

(Cell C)

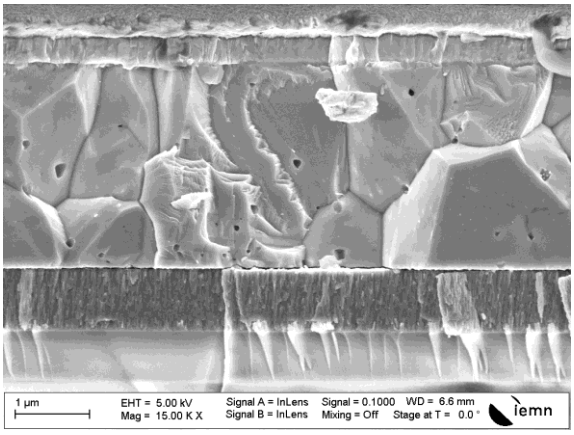

Figure 5.21: SEM cross sectional images corresponding to the final solar cells.

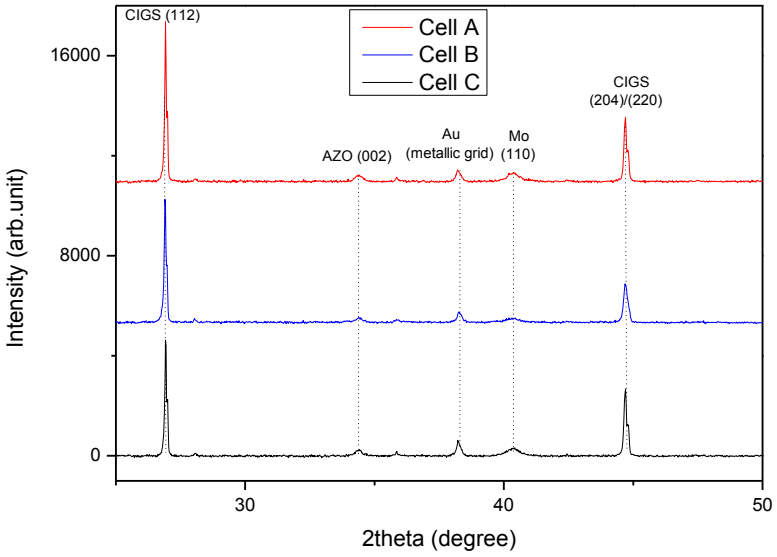

Figure 5.22: XRD patterns corresponding to the final solar cells

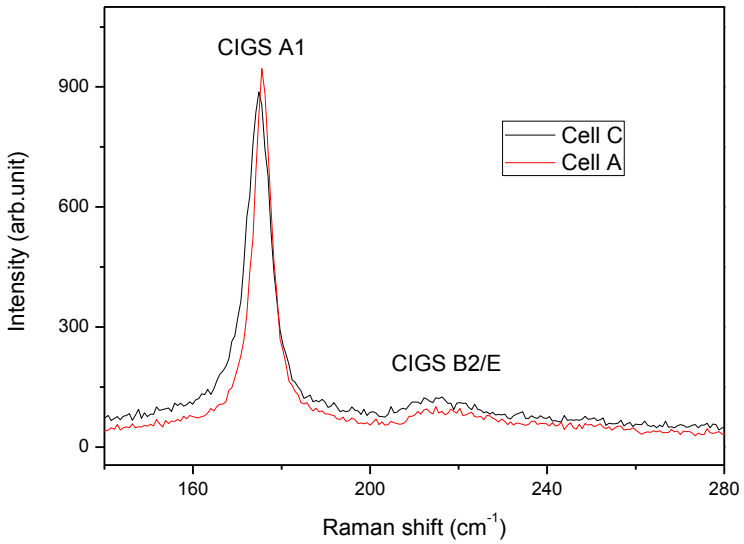

Figure 5.23: Raman spectra of the CIGS layers used for the preparation of the 10% and 0% efficiency solar cells.

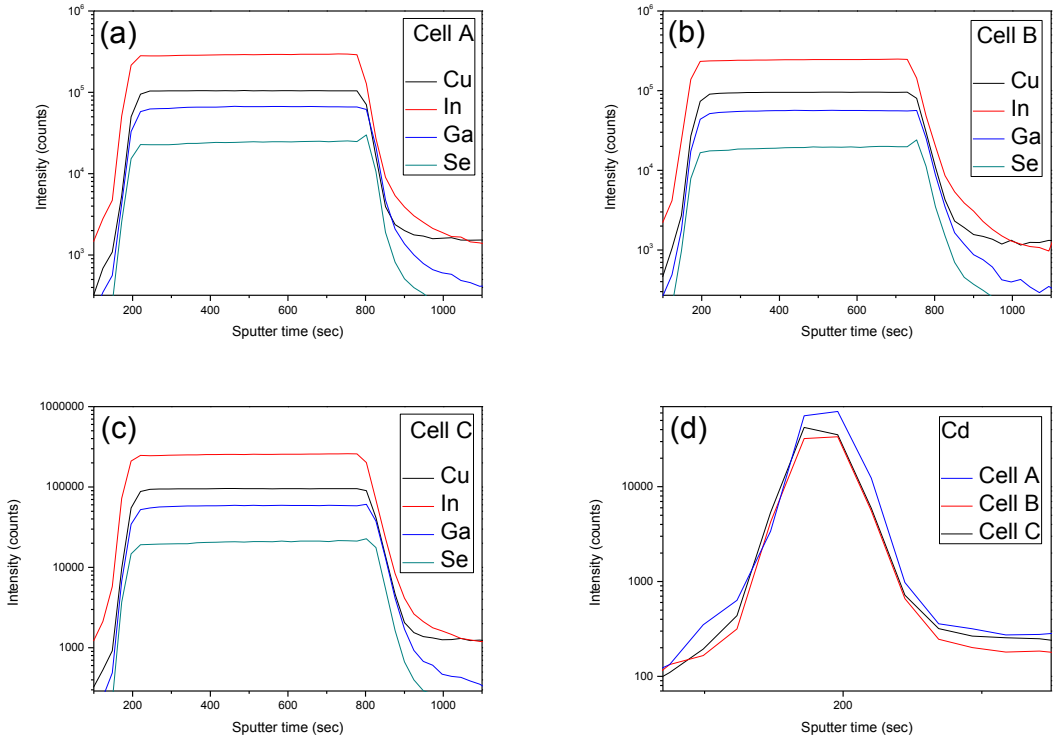

Figure 5.24: (a) (b) (c) SIMS depth profiles of the constituent elements of the CIGS layer throughout the entire solar cells A,B and C, respectively. (d) A comparison of the SIMS depth profiles of Cd from the three solar cells.

5.6. Chapter conclusion

Our first attempt for the fabrication of full sputtering CIGS solar cells has failed, even though the composition x of the zinc oxysulfide (ZnS_xO_{1-x}) buffer layer has been tuned from 0 to 1.

Our doubt about the possible negative effect of the used technique for the deposition of the buffer layer has conducted us to the use of an alternative process which is based on the use of a low sputtering power or even to completely replace this sputtered ZnS_xO_{1-x} layer by the standard CBD-CdS layer; nevertheless, the fabricated solar cells have shown no or negligible improvement of the electrical characteristics.

Based on that, we concluded that the origin of the limiting factor is neither related to the deposition technique nor to the buffer layer nature.

This conclusion has conducted us to deeply investigate the CIGS layer. From the microstructural point of view, no signs were obtained (large grains, single and pure chalcopyrite phase, and no secondary phases on the surface); however, the particularity of the GDOES technique in indicating the presence of any elements (even those with very small concentrations) without any preselection has allowed us to find out the presence of small quantities of undesirable metallic elements that are known, in literature, as a CIGS solar cells efficiency killer. A deep investigation has been made, and we have found out that those elements are out diffused from the used molybdenum layer (target issue).

Waiting for the arriving of the new target, an alternative molybdenum layer from another sputtering machine has been used for the preparation of solar cells. Based on that, slightly less than 12% of efficiency has been achieved, but more surprisingly, is the poor microstructure of the CIGS layer observed on this solar cell. On the contrary to our predictions, further improvement of the microstructure through the engineering of the molybdenum layer has led to a dramatic degradation of the cells performance.

In fact the use of an alternative sputtering machine for the deposition of the molybdenum layer has, with some chance, allowed us to conclude that metallic impurities were not the only limiting factor for cells operation but also the sodium blocking behaviour of the molybdenum layer due to its high compactness.

Based on those conclusions and believing that the better the microstructural quality of the CIGS layer the higher the solar cells efficiency, a sodium post annealing treatment of the CIGS layer was investigated. Consequently, solar cell efficiency as high as 10% has been achieved.

In the light of these recently obtained results (using a sodium treatment), we are reasonably confident of our capability to hit the 15% efficiency bar in the coming days!!

Finally, in parallel to our seeking for further improvement of cells efficiency, understanding the reason behind the need for higher sodium concentration in case of large grain CIGS absorber is our priority and therefore admittance spectroscopy (AS) and/or deep level transient spectroscopy (DLTS) analyses are contemplated.

Summary and outlook

Main results

Because of the extended spectrum of the performed experiences, several conclusions have been reached.

Starting by the molybdenum back contact layer, we have shown that the engineering of the initial stress within the molybdenum layer allowed keeping the substrate flatness after annealing. Furthermore, we have shown that the introduction of oxygen during the sputtering of the molybdenum layer is sufficient to change the stress state from tensile to compressive; however, the precise control of the oxygen flux for achieving the right initial stress, was found to be a little bit tough . For that reason, we have proposed an alternative solution which is based on the use of Mo/Mo(O) bilayer structure: it was found that it is easier to control the substrate flatness by tuning the top to the bottom layer thickness ratio than by tuning oxygen flux. Moreover, the use of such a process is expected to be very useful especially for the development of room temperature deposited CIGS thin films followed by an annealing step where the recrystallization of the CIGS thin films is found to contribute, in part, into the final substrate bending. Finally, we would like to highlight the fact that our proposed process for keeping substrate flatness is far simpler than that patented by Saint Gobain glass group.

In a second time, an original absorber deposition process which is based on magnetron pulsed-DC sputtering at room temperature from a single quaternary CIGS target using argon plasma without any additional selenium supply, followed by annealing under inert atmosphere, has been developed. As an instinctive reflection, low pressure process was used for the preparation of the first set of samples; however, this has mainly led to problems: substrate delamination and argon outgassing. To overcome these issues, several approaches have been followed: bilayer structure, stack of reduced thickness bilayer structure and finally, high pressure deposition process. The bilayer structure was found to enhance the adhesion; however, the induced crater-like defects were sill observed. Furthermore, the stack of the reduced thickness bilayer structure process was found to suffer from composition deviation from optimal and/or the presence of large holes at the interface Mo/CIGS. On the other hand, using high pressure deposition process, none of the previously mentioned issues was observed: high adhesion, no argon outgassing induced defects, optimum composition and excellent microstructure. Furthermore, the XRD, Raman and SIMS analyses have evidenced the presence of a single chalcopyrite phase, the absence of the $Cu_{2-x}Se$ secondary phase at the CIGS surface and the elemental distribution homogeneity throughout the whole thin film thickness. *In few words, we have shown that using such a very simple process might allow achieving CIGS thin films with similar quality to that obtained using the co-evaporation process.*

Concerning the buffer layer, both CBD-CdS and room temperature sputtered zinc oxysulfide (ZnS_xO_{1-x}) thin films have been studied. It was found that a good control of the CdS deposition conditions lead to an excellent coverage of the CIGS layer. It was also found that the growth rate of the CdS layer on CIGS covered substrate is faster compared to a direct growth on glass substrate. On the other hand, we have shown that the use of a room temperature reactive (O_2) sputtering (of a ZnS target) process for the deposition of ZnS_xO_{1-x} thin film does not provide the right material properties. So, an ALD-inspired sputtering

process was investigated as an alternative. The obtained results, both structural and optical, were found to have some consistency with previously published works using high temperature reactive sputtering process: the less intense change in the band gap was proved to be thickness related, while the composition ranges in which a single phase ZnS_xO_{1-x} is achievable ($0 \leq x \leq 0.21$ and $0.76 \leq x \leq 1$) was found to be almost the same.

In chapter 4, we focused on the development of high transparency and low resistivity aluminium-doped zinc oxide thin films. We found that low resistivity is achievable using pulsed DC mode; however, a post deposition rapid thermal annealing process was found to be necessary in order to improve the spatial resistivity distribution. This annealing process was also found to have a positive effect on the optical transparency. Unfortunately, integrating such a process for the fabrication of reference solar cells (CdS-based solar cells) is not possible due the expected high diffusivity of Cd into the CIGS layer and therefore p-n junction deterioration. Based on that, we have also investigated the optoelectronic properties of RF-sputtered thin films. The as deposited thin films have shown quite similar optical transparency and resistivity mean value; while, the spatial resistivity distribution was found to be far better. Finally, the adjustment of the annealing process for CdS-based solar cells was found to slightly improve both optical and electrical properties

In the last chapter, we have shown the main steps that led us to progressively improve the efficiency of complete solar cells. We have also shown that even the use of CIGS absorber layer with poor microstructural quality can lead to solar cells efficiency of 11%, while the high microstructural quality of the CIGS absorber layer does not necessary lead to operational solar cells. Finally, on the contrary to previous works, we have found out that no photovoltaic effect can be achieved in case of using sodium free process for the fabrication of CIGS solar cells. Highest value of efficiency we got is slightly under 12% on a cell using a single stage CIGS deposition and a CdS buffer which is rather in the state of art for CIGS cells using such a fabrication process (figure C.1).

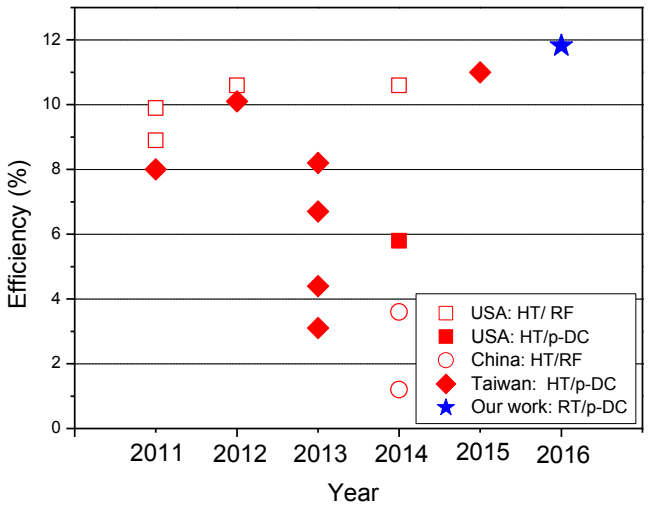

Figure C.1: State of the art of CIGS solar cells achieved by sputtering from single quaternary target, without additional Se supply.

Outlook

Concerning the used back contact bilayer structure (Mo/Mo(O)), a deep investigation of the Mo/CIGS interface seems to be necessary due to the observed oxygen accumulation at this interface.

For purely industrial reason, our first results, using a short annealing process (for CIGS recrystallization), have paved the way for further annealing time shortening (the shorter the annealing process, the higher the benefice).

Finally, our plan for further improving solar cells efficiency is the following (structured by priority):

- ✓ Further adjusting sodium concentration within the CIGS layer (by further adjusting the post deposition treatment);
- ✓ Understanding the reason behind the need for higher sodium concentration in case of large grains CIGS absorber: admittance spectroscopy (AS) and/or deep level transient spectroscopy (DLTS) analyses are contemplated;
- ✓ Using high microstructural quality and slightly (220) preferentially oriented CIGS absorber layer for the preparation of the next set of solar cells (§2.4.2);
- ✓ Improving the optoelectronic properties of the window layer through the use of a new AZO target matched to our equipment (removal of parasitic metallic elements from AZO thin films);
- ✓ Replacing the temporarily used CdS buffer layer by a sputtered ZnS_xO_{1-x} and finding the suitable composition for a full sputtering based process (the achieved result obtained hereby will give us the cell performance reference value);
- ✓ Finding an alternative process for the deposition of the ZnS_xO_{1-x} buffer layer (more suitable for an industrial up-scaling);
- ✓ Finally, using a stack of sputtered $CuIn_xGa_{1-x}Se$ thin films for band gap engineering, and why not, the investigation of potassium surface treatment.

Publications and communications

Publications in peer-reviewed journals

As a first author:

B. Ayachi, T. Aviles, J.P. Vilcot, C. Sion, Rapid thermal annealing effect on the spatial resistivity distribution of AZO thin films deposited by pulsed-direct-current sputtering for solar cells applications, *Appl. Surf. Sci.* 366 (2016) 53-58.

B. Ayachi , T. Aviles, J.P. Vilcot, C. Sion, P. Miska, Room temperature pulsed-DC sputtering deposition process for CIGS absorber layer: material and device characterizations, Submitted for publication to Solar Energy Materials & Solar Cells.

B. Ayachi , T. Aviles, J.P. Vilcot, C. Sion, Innovative solution to avoid substrate bending after thermal process, this article is being written for submission to Progress in Photovoltaics: Research and Applications.

As a co-author:

A. Bou, P. Torchio, D. Barakel, A. Guillou, B. Ayachi, P.Y Thoulon, M. Ricci, Optical and electrical properties of structured multilayer with tunable transparency rate, J. Phys. D: Appl. Phys. 48 (2015) 205102 (6pp).

H.Y. Abib, A. Iost, A. Montagne, K. Rahmoun, B. Ayachi, J.P. Vilcot, Investigations on the mechanical properties of the elementary thin films composing a $CuIn_{1-x}Ga_xSe_2$ solar cell using the nanoindentation technique, Submitted for publication to Thin Solid Films.

International conferences

As a first author:

B. Ayachi, T. Aviles, J.P. Vilcot, Room temperature deposition of ZnS_xO_{1-x} sputtered thin films, poster presentation in E-MRS Spring Meeting (May 2015, Lille).

B. Ayachi, T. Aviles, J.P. Vilcot, C. Sion,Towards a simple full sputtering processing of CIGS based solar cells, poster presentation in E-MRS Spring Meeting (May 2016, Lille).

B. Ayachi, T. Aviles, J.P. Vilcot, C. Sion, Single step and room temperature sputtering deposition process for the CIGS absorber layer of solar cells, poster presentation in EU-PVSEC (June 2016, Munich).

B. Ayachi, T. Aviles, C. Sion, J.P. Vilcot, Full sputtering deposition of thin film solar cells, poster presentation at Colloque UMI LN2 2016 (July 2016, Sherbrooke)

As a co-author:

T. Aviles, B. Ayachi, J.P. Vilcot, CIGS absorber by pulsed DC sputtering and N_2 annealing, poster presentation in E-MRS Spring Meeting (May 2015, Lille).

T. Aviles, B. Ayachi, C. Sion, J.P. Vilcot, Properties of Cu(In,Ga)Se_2 absorbers deposited by magnetron pulse DC sputtering at room temperature from a single target and annealed in an inert atmosphere poster presentation in PVTC (May 2015, Aix-en-Provence).

T. Aviles, B. Ayachi, J.P. Vilcot, Properties of CIGS material fabricated by pulsed DC sputtering from a quaternary target without selenization, poster presentation in E-MRS Spring Meeting (May 2016, Lille).

T. Aviles, B. Ayachi, J.P. Vilcot, CIGS solar cells fabricated by pulsed DC sputtering from a quaternary target without selenization, poster presentation in PVTC (May 2016, Marseille).

J-P. Vilcot, B. Ayachi, T. Aviles, P. Miska, Full sputtering deposition of thin film solar cells: a way achieving high efficiency sustainable tandem cells? oral presentation at International Workshop on Advanced Materials and Nanotechnology 2016 (November 2016, Hanoï)

National meetings

As a first author:

B. Ayachi, J.P. Vilcot, Déposition par pulvérisation cathodique à température ambiante des couches minces d'Oxysulfure de Zinc $ZnS_xO_{(1-x)}$, poster presentation in JNPV (December 2014, Dourdan).

B. Ayachi, J.P. Vilcot, Influence du recuit rapide sur les propriétés optoélectroniques et électroniques des couches minces d'Oxyde de Zinc dopé aluminium déposées par pulvérisation cathodique en mode DC-pulsé ou RF, poster presentation in GDR OXYFUN (December 2014, Paris).

B. Ayachi, T. Aviles, P. Miska, J-P Vilcot, Absorbeur CIGS déposé par pulvérisation cathodique à température ambiante et sans sélénisation, submitted to JNPV (December 2016, Dourdan)

As a co-author:

T. Aviles, B. Ayachi, J.P. Vilcot, Cu(In,Ga)Se_2 déposé par pulvérisation cathodique en mode DC pulsé sans chauffage intentionnel: étude de la composition et de la microstructure avant et après recuit. poster presentation in JNPV (December 2014, Dourdan).

T. Aviles, B. Ayachi, J.P. Vilcot, C. Sion, Cellules CIGS sans cadmium réalisées entièrement par pulvérisation cathodique sans sélénisation, poster presentation in JNPV (December 2015, Dourdan).

References

[A. Ashrafi. 1999] A.B.M.A. Ashrafi, A. Ueta, A. Avramescu, H. Kumano, I. Suemune, Growth and characterization of hypothetical zinc-blende ZnO films on GaAs (001) substrates with ZnS buffer layers, *Appl. Phys. Lett*. 76 (2000) 550-552.

[A. Čampa. 2007] A. Čampa, J. Krč, J. Malmström, M. Edoff, F. Smole, M. Topič, The potential of textured front ZnO and flat TCO/metal back contact to improve optical absorption in thin Cu(In,Ga)Se_2 solar cells, *Thin Solid Films* 515 (2007) 5968-5972.

[A. Chirila. 2013] A. Chirila, P. Reinhard, F. Pianezzi, P. Bloesch, A.R. Uhl, C. Fella, L. Kranz, D. Keller, C. Gretener, H. Hagendorfer, D. Jaeger, R. Erni, S. Nishiwaki, S. Buecheler, A.N. Tiwari, Potassium-induced surface modification of Cu(In,Ga)Se_2 thin films for high-efficiency solar cells, *Nature Mater.* 12 (2013) 1107-1111.

[A. Grimm. 2011] A. Grimm, D. Kieven, R. Klenk, I. Lauermann, A. Neisser, T. Niesen, J. Palm, Junction formation in chalcopyrite solar cells by sputtered wide gap compound semiconductors, *Thin Solid Films* 520 (2011) 1330-1333.

[A. Grimm. 2012] A. Grimm, D. Kieven, I. Lauermann, M.Ch. Lux-Steiner, F. Hergert, R. Schwieger, R. Klenk, Zn(O, S) layers for chalcoyprite solar cells sputtered from a single target, *EPJ Photovolt.* 3 (2012) 30302.

[A. Hultqvist. 2007] A. Hultqvist, C. Platzer-Bjorkman, T. Torndahl, M. Ruth, M. Edoff, Optimization of i-ZnO window layers for Cu(In,Ga)Se_2 solar cells with ALD buffers, in: *Proc. of the 22nd European Photovoltaic Solar Energy Conference* (2007) 2381-2384.

[A. Hultqvist. 2010] A. Hultqvist, Cadmium free buffer layers and the influence of their material properties on the performance of Cu(In,Ga)Se_2 solar cells, *PhD thesis, Uppsala University* (2010).

[A. Janotti. 2007] A. Janotti, C.G. Van de Walle, Native point defects in ZnO, *Phys. Rev. B* 76 (2007) 165202.

[A. Janotti2. 2007] A. Janotti, C.G. Van de Walle, Hydrogen multicentre bonds, *Nature Mater*. 6 (2007) 44-47.

[A. Laemmle. 2015] A. Laemmle, R. Wuerz, M. Powalla, Investigation of the effect of potassium on Cu(In,Ga)Se_2 layers and solar cells, *Thin Solid Films* 582 (2015) 27-30.

[A. Mallick. 2014] A. Mallick, A. Kole, T. Ghosh, P. Chaudhuri, D. Basak, Zinc aluminate spinel impurity phase in Al doped ZnO ceramic target and pulsed laser ablated films: Curse or blessing?, *Sol. Energy* 108 (2014) 80-87.

[A. Mosbah. 2012] A. Mosbah, M.S. Aida, Influence of deposition temperature on structural, optical and electrical properties of sputtered Al doped ZnO thin films, *J. Alloy. Compd*. 515 (2012) 149-153.

[A. Okamoto. 2011] A. Okamoto, T. Minemoto, H. Takakura, Application of sputtered $ZnO_{1-x}S_x$ buffer layers for Cu(In,Ga)Se_2 solar cells, *Jpn. J. Appl. Phys*. 50 (2011) 04DP10.

[A. Rockett. 1999] A. Rockett!, K. Granath, S. Asher, M.M. Al Jassim, F. Hasoon, R. Matson, B. Basol, V. Kapur, J.S. Britt, T. Gillespie, C. Marshall, Na incorporation in Mo and $CuInSe_2$ from production processes, *Sol. Energy Mater. Sol. Cells* 59 (1999) 255-264.

[A. Rockett. 2000] A. Rockett, J.S. Britt, T. Gillespie, C. Marshall, M.M. Al Jassim, F. Hasoon, R. Matson, B. Basol, Na in selenized Cu(In,Ga)Se_2 on Na-containing and Na-free glasses: distribution, grain structure, and device performances, *Thin Solid Films* 372 (2000) 212-217.

[A. Simchi. 2014] H. Simchi, Back surface studies of Cu(In,Ga)Se_2 thin film solar cells, *PhD thesis, University of Delaware* (2014).

[Avancis] Avancis, company, Vision and history. http://www.avancis.de/en/company/vision-and-history/, (accessed 26/08/16).

[B. Ayachi. 2016] B. Ayachi, T. Aviles, J.P. Vilcot, C. Sion, Rapid thermal annealing effect on the spatial resistivity distribution of AZO thin films deposited by pulsed-direct-current sputtering for solar cells applications, *Appl. Surf. Sci.* 366 (2016) 53-58.

[B.K. Meyer. 2004] B.K. Meyer, A. Polity, B. Farangis, Y. He, D. Hasselkamp, Th. Krämer, C. Wang, Structural properties and bandgap bowing of $ZnO_{1-x}S_x$ thin films deposited by reactive sputtering, *Appl. Phys. Lett*. 85 (2004) 4929-4931.

[B.R. Kumar. 2013] B.R. Kumar, T. S. Rao, Investigations on opto-electronical properties of DC reactive magnetron sputtered zinc aluminum oxide thin films annealed at different temperatures, *Appl. Surf. Sci.* 265 (2013) 169-175.

[B.Y. Oh. 2005] B.Y. Oh, M.C. Jeong, D.S. Kim, W. Lee, J.M. Myoung, Post-annealing of Al-doped ZnO films in hydrogen atmosphere, *J. Cryst. Growth* 281 (2005) 475-480.

[C. A. Davis. 1993] C. A. Davis, A simple model for the formation of compressive stress in thin films by ion bombardment, *Thin Solid Films*, 226 (1993) 30-34.

[C. Broussillou. 2011] C. Broussillou, Relations traitement thermique – phases – adhérence dans les couches minces constituant les cellules photovoltaïques $CuIn(S_x,Se_{1-x})_2$ electrodéposées (CISEL), *PhD thesis, ParisTech*, (2011).

[C. Charpentier. 2012] C. Charpentier, Investigation of deposition conditions and annealing treatments on sputtered ZnO:Al thin films: Material properties and application to c-Si:H solar cells, *PhD thesis, Ecole Polytechnique ParisTech* (2012).

[C.H. Chen. 2011] C.H. Chen, C.H. Hsu, C.Y. Chien, Y.H. Wu, C.H. Lai, A straight forward method to prepare chalcopyrite CIGS films by one-step sputtering process without extra Se supply, *in: Proc. of 37th IEEE Photovoltaic Specialists Conference* (2011) 2687-2690.

[C.H. Chen. 2012] C.H. Chen, W.C. Shih, C.Y. Chien, C.H. Hsu, Y.H. Wu, C.H. Lai, A promising sputtering route for one-step fabrication of chalcopyrite phase $Cu(In,Ga)Se_2$ absorbers without extra Se supply, *Sol. Energy Mater. Sol. Cells* 103 (2012) 25-29.

[C.H. Chen. 2013] C.H. Chen, T.Y. Lin, C.H. Hsu, S.Y. Wei, C.H. Lai, Comprehensive characterization of Cu-rich $Cu(In,Ga)Se_2$ absorbers prepared by one-step sputtering process, *Thin Solid Films* 535 (2013) 122-126.

[C. H. Henry. 1980] C. H. Henry, Limiting efficiencies of ideal single and multiple energy gap terrestrial solar cells, *J. Appl. Phys*. 51 (1980) 4494-4500.

[C.H. Hsu. 2015] C.H. Hsu, W.H. Ho, C.H. Lai, Effects of Se flux on the properties of the quaternary-sputtered CIGS thin film solar cells, *in: Proc. of 42th IEEE Photovoltaic Specialists Conference* (2015).

[C.H. Hsu2. 2015] C.H. Hsu, Y.S. Su, S.Y. Wei, C.H. Chen, W.H. Ho, C. Chang, Y.H. Wu, C.J. Lin, C.H. Lai, Na-induced efficiency boost for Se-deficient $Cu(In,Ga)Se_2$ solar cells, *Prog Photovolt.: Res. Appl.* 23 (2015) 1621-1629.

[C.L. Perkins. 2005] C.L. Perkins, F.S. Hasoon, H.A. Al-Thani, S.E. Asher, P. Sheldon, XPS and UPS investigation of NH_4OH-exposed $Cu(In,Ga)Se_2$ thin films, *NREL/CP-520-37419* (2005).

[C. Lennon. 2009] C. Lennon, R.B. Tapia, R. Kodama, Y. Chang, S. Sivananthan, M. Deshpande, Effects of annealing in a partially reducing atmosphere on sputtered Al-Doped ZnO thin films, *J. Electron. Mater.* 38 (2009) 1568-1573.

[C. Persson. 2006] C. Persson, C. Platzer-Bjorkman, J. Malmstrom, T. Torndahl, M. Edoff, Strong Valence-Band Offset Bowing of $ZnO_{1-x}S_x$ Enhances *p*-Type Nitrogen Doping of ZnO-like Alloys, *Phys. Rev. Lett*. 97 (2006) 146403.

[C. Platzer-Björkmana. 2006] C. Platzer-Björkman, T. Törndahl, D. Abou-Ras, J. Malmström, J. Kessler, L. Stolt, Zn(O,S) buffer layers by atomic layer deposition in Cu(In,Ga)Se_2 based thin film solar cells: Band alignment and sulfur gradient, *J. Appl. Phys.* 100 (2006) 044506.

[C. Roger. 2013] C. Roger, S. Noël, O. Sicardy, P. Faucherand, L. Grenet, N. Karst, H. Fournier, F. Roux, F. Ducroquet, A. Brioude, S. Perraud, Characteristics of molybdenum bilayer back contacts for Cu(In,Ga)Se_2 solar cells on Ti foils, *Thin Solid Films* 548 (2013) 608-616.

[CROSSLUX 2016] http://www.crosslux.eu/brevets-techno, (accessed 24/10/16).

[C.S. Jiang. 2003] C.S. Jiang, F.S. Hasoon, H.R. Moutinho, H.A. Al-Thani, M.J. Romero, M.M. Al-Jassim, Direct evidence of a buried homojunction in Cu(In,Ga)Se_2 solar cells, *Appl. Phys. Lett*. 82 (2003) 127-129.

[D. Abou-Ras. 2005] D. Abou-Ras, G. Kostorz, D. Bremaud, M. Kalin, F.V. Kurdesau, A.N. Tiwari, M. Dobeli, Formation and characterisation of $MoSe_2$ for Cu(In,Ga)Se_2 based solar cells, *Thin Solid Films* 480-481 (2005) 433-438.

[D. Abou-Ras2. 2005] D. Abou-Ras, G. Kostorz, A. Romeo, D. Rudmann, A.N. Tiwari, Structural and chemical investigations of CBD- and PVD-CdS buffer layers and interfaces in Cu(In,Ga)Se_2-based thin film solar cells, *Thin Solid Films* 480-481 (2005) 118-123.

[D. Cahen. 1988] D. Cahen, R. Noufi, Defect chemical explanation for the effect of air anneal on CdS/$CuInSe_2$ solar cell performance, *Appl. Phys. Lett*. 54 (1989) 558-560.

[D.H. Shin. 2012] D.H. Shin, Y.M. Shin, J.H. Kim, B.T. Ahn, K.H. Yoon, Control of the preferred orientation of Cu(In,Ga)Se_2 thin film by the surface modification of Mo film, *J. Electrochem. Soc*. 159(1) (2012) B1-B5.

[D. Hariskos. 2005] D. Hariskos, S. Spiering, M. Powalla, Buffer layers in Cu(In,Ga)Se_2 solar cells and modules, *Thin Solid Films* 480-481 (2005) 99-109.

[D. Hariskos. 2009] D. Hariskos, B. Fuchs, R. Menner, N. Naghavi, C. Hubert, D. Lincot, M. Powalla, The Zn(S,O,OH)/ZnMgO buffer in thin film Cu(In,Ga)$(Se,S)_2$-based solar cells part II: magnetron sputtering of the ZnMgO buffer layer for in-line co-evaporated Cu(In,Ga)Se_2 solar cells, *Prog. Photovolt: Res. Appl*. 17(2009) 479-488.

[D. Horwat. 2007] D. Horwat , A. Billard, Effects of substrate position and oxygen gas flow rate on the properties of ZnO: Al films prepared by reactive co-sputtering, *Thin Solid Films* 515 (2007) 5444-5448.

[D.J.L. Brémaud. 2009] D.J.L. Brémaud, Investigation and development of CIGS solar cells on flexible substrates and with alternative electrical back contacts, *PhD thesis, ETH Zurich* (2009).

[D. Kieven. 2012] D. Kieven, A. Grimm, I. Lauermann, M.Ch. Lux-Steiner, J. Palm, T. Niesen, R. Klenk, Band alignment at sputtered ZnS_xO_{1-x}/Cu(In,Ga)$(Se,S)_2$ heterojunctions, *Phys. Status Solidi RRL* 6 (2012) 294-296.

[D. Rudmann. 2003] D. Rudmann, G. Bilger, M. Kaelin, F.J. Haug, H. Zogg, A.N. Tiwari, Effects of NaF coevaporation on structural properties of Cu(In,Ga)Se_2 thin films, *Thin Solid Films* 431-432 (2003) 37-40.

[D. Rudmann. 2004] D. Rudmann, A.F. da Cunha, M. Kaelin, F. Kurdesau, H. Zogg, A.N. Tiwari, G. Bilger, Efficiency enhancement of Cu(In,Ga)Se_2 solar cells due to post-deposition Na incorporation, *Appl. Phys. Lett*. 84 (2004) 1129-1131.

[D. Rudmann. 2005] D. Rudmann, D. Brémaud, H. Zogg, A.N. Tiwari, Na incorporation into Cu (In , Ga) Se 2 for high-efficiency flexible solar cells on polymer foils, *J. Appl. Phys.* 97 (2005) 084903.

[D. Rudmann.t. 2004] D. Rudmann, Effects of sodium on growth and properties on Cu(In,Ga)Se_2 thin films and solar cells, *PhD thesis, ETH Zurich* (2004).

[D.S. Kim. 2012] D.S Kim, J.H. Park, B.K. Shin, K.J. Moon, M. Son, M.H Ham, W. Lee, J.M. Myoung, Effect of deposition temperature on the properties of Al-doped ZnO films prepared by pulsed DC magnetron sputtering for transparent electrodes in thin-film solar cells, *Appl. Surf. Sci*. 259 (2012) 596-599.

[D.S. Kim. 2013] D.S Kim, J.H. Park, S.J. Lee, K.J. Ahn, M.S. Lee, M.H. Ham, W. Lee, J.M. Myoung, Effects of oxygen concentration on the properties of Al-doped ZnO transparent conductive films deposited by pulsed DC magnetron sputtering, *Mater. Sci. Semicond. Proc.* 16 (2013) 997-1001.

[E. Burstein. 1954] E. Burstein, Anomalous optical absorption limit in InSb, *Phys. Rev*. 93 (1954) 632-633.

[E.H. Hirsch. 1980] E.H. Hirsch, *J. Phys. D: Appl. Phys*. 13 (1980) 2081-2094.

[E. H. Rhoderick. 1970] E.H. Rhoderick. *Rev. Phys. technol*. 1(2) (1970) 81.

[F.M. D'Heurle. 1970] F.M. D'heurle, *Metall. Trans*, 1 (1970) 725-732.

[F. Pattini. 2015] F. Pattini, F. Annoni, F. Bissoli, M. Bronzoni, J.P. Garcia, E. Gilioli, S. Rampino, Comparative study about Al-doped zinc oxide thin films deposited by pulsed electron deposition and radio frequency magnetron sputtering as transparent conductive oxide for Cu(In,Ga)Se_2-based solar cells, *Thin Solid Films* 582 (2015) 317-322.

[F. Pianezzi. 2012] F. Pianezzi, A. Chirilă, P. Blösch, S. Seyrling, S. Buecheler, L. Kranz, C. Fella, A.N. Tiwari, Electronic properties of Cu(In,Ga)Se_2 solar cells on stainless steel foils without diffusion barrier, *Prog. Photovolt: Res. Appl*. 20 (2012) 253-259.

[F. Pianezzi. 2013] F. Pianezzi, P. Reinhard, A. Chirilă, S. Nishiwaki, B. Bissig, S. Buecheler, A. N. Tiwari, Defect formation in Cu(In,Ga)Se_2 thin films due to the presence of potassium during growth by low temperature co-evaporation process, *J. Appl. Phys*. 114 (2013) 194508.

[F. Pianezzi. 2014] F. Pianezzi, P. Reinhard, A. Chirila, B. Bissig, S. Nishiwaki, S. Buecheler, A.N. Tiwari, Unveiling the effects of post-deposition treatment with different alkaline elements on the electronic properties of CIGS thin film solar cells, *Phys. Chem. Chem. Phys*. 16 (2014) 8843-8851.

[F. Pianezzi. 2015] F. Pianezzi, S. Nishiwaki, L. Kranz, C.M. Sutter-Fella, P. Reinhard, B. Bissig, H. Hagendorfer, S. Buecheler, A.N. Tiwari, Influence of Ni and Cr impurities on the electronic properties of Cu(In,Ga)Se_2 thin film solar cells, *Prog. Photovolt: Res. Appl*. 23 (2015) 892-900.

[F. Pianezzi.t. 2014] F. Pianezzi, Electronic transport and doping mechanisms in Cu(In,Ga)Se_2 thin film solar cells, *PhD thesis, ETH Zurich* (2004).

[F. Ruske. 2007] F. Ruske, C. Jacobs, V. Sittinger, B. Szyszka, W. Werner, Large area ZnO:Al films with tailored light scattering properties for photovoltaic applications, *Thin Solid Films* 515 (2007) 8695-8698.

[F.T. Tsai. 2015] F.T. Tsai, H.T. Hou, C.K. Chao, R.C. Chang, depositing high-performance conductive thin films by using atomic layer deposition, *Appl. Mech. Mater*. 764-765 (2015) 138-142.

[G. Fang. 2003] G. Fang, D. Li, B.L. Yao, Fabrication and vacuum annealing of transparent conductive AZO thin films prepared by DC magnetron sputtering, *Vac*. 68 (2003) 363-372.

[G. Hanna.2001] G. Hanna, A. Jasenek, U. Rau, H.W. Schock, Influence of the Ga-content on the bulk defect densities of Cu(In,Ga)Se_2, *Thin Solid Films* 387 (2001) 71-73.

[G. Rajan. 2015] G. Rajan, K. Aryal, T. Ashrafee, S. Karki, Abdel-Rahman Ibdah, V. Ranjan, R.W. Collins, S. Marsillac, Optimization of anti-reflective coatings for

CIGS solar cells via real time spectroscopic ellipsometry, *in: Proc. of 42nd IEEE Photovoltaic Specialist Conference (PVSC)* (2015).

[G. Shanmuganathan. 2014] G. Shanmuganathan, I.B.S. Banu, Influence of codoping on the optical opoperties of ZnO thin films synthesized on glass Substrate by chemical bath deposition method, *Adv. Condens. Matter Phys.* (2014) ID 761960.

[GVR 2016] http://www.grandviewresearch.com/industry-analysis/solar-cell-market, (accessed 24/10/16).

[G.X. Liang. 2014] G.X. Liang, P. Fan, C.M. Chen, Z.H. Zheng, D.P. Zhang, A promising sputtering for in situ fabrication of CIGS thin films without post-selenization, *J. Alloy. Compd*. 610 (2014) 337-340.

[H.A. Al-Than. 2001] H.A. Al-Thani, F.S. Hasoon, J.L. Alleman, M.M. Al-Jassim, The Deposition and Characterization of Mo/CuInGaSe$_2$/CdS/ZnO Solar Cells, *NREL/CP/520-29641* (2001).

[H. Anant. 2006] A.H. Jahagirdar, A.A. Kadam, N.G. Dhere, Role of i-ZnO in optimizing open circuit voltage of CIGS$_2$ and CIGS thin film solar cells, *in: Proc. of 4th IEEE World Conference on Photovoltaic Energy Conversion* (2006).

[H. Hagendorfer. 2014] *H. Hagendorfer, K. Lienau, S. Nishiwaki, C.M. Fella, L. Kranz, A.R. Uhl, D. Jaeger, L. Luo, C. Gretener, S. Buecheler, Y.E. Romanyuk, A.N. Tiwari,* Highly transparent and conductive ZnO: Al thin films from a low temperature aqueous solution approach, *Adv. Mater.* 26 (2014) 632-636.

[Himinsun 2016] http://www.himinsun.com/1-5-bipv-module.html, (accessed 24/10/16).

[H. Ko. 2005] H. Ko, W.P. Tai, K.C. Kim, S.H. Kim, SJ. Suh, Y.S. Kim, Growth of Al-doped ZnO thin films by pulsed DC magnetron sputtering, *J. Cryst. Growth* 277 (2005) 352-358.

[H. Kong. 2014] H. Kong, J. He, X. Meng, L. Zhu, J. Tao, L. Sun, P. Yang, J. Chu, Influence of Se supply for selenization of Cu(In,Ga)Se$_2$ precursors deposited by sputtering from a single quaternary target, *Mater. Lett*.118 (2014) 21-23.

[H.L. Pan. 2010] H.L Pan, T. Yang, B. Yao, R. Deng, R.Y. Sui, L.L. Gao, D.Z. Shen, Characterization and properties of ZnO$_{1-x}$S$_x$ alloy films fabricated by radio-frequency magnetron sputtering, *Appl. Surf. Sci*. 256 (2010) 4621-4625.

[H. Moualkia. 2009] H. Moualkia, S. Hariech, M.S. Aida, N Attaf , E.L Laifa, Growth and physical properties of CdS thin films prepared by chemical bath deposition, *J. Phys. D: Appl. Phys*. 42 (2009) 135404.

[H.R. Dizaji. 2011] H.R. Dizaji, A.J. Zavaraki, M.H. Ehsani, Effect of thickness on the structural and optical properties of ZnS thin films prepared by flash

evaporation technique equipped with modified feeder, *Chalcogenide Lett*. 8(4) (2011) 231-237.

[H.R. Hsu. 2012] H.R. Hsu, S.C. Hsu, Y.S. Liu, Improvement of Ga distribution and enhancement of grain growth of $CuInGaSe_2$ by incorporating a thin CuGa layer on the single CuInGa precursor, *Sol. Energy* 86 (2012) 48-52.

[H. Tong. 2011] H. Tong, Z. Deng, Z. Liu, C. Huang, J. Huang, H. Lan, C. Wang, Y. Cao, Effects of post-annealing on structural, optical and electrical properties of Al-doped ZnO thin films, *Appl. Surf. Sci*. 257 (2011) 4906-4911.

[H. Windischmann. 1987] H. Windischmann. An intrinsic stress scaling law for polycrystalline thin films prepared by ion beam sputtering, *J. Appl. Phys*. 62 (1987) 1800-1807.

[H. Xu. 2013] H. Xu, L. Zhu, J. Jiang, H. Cai, W. Chen, L. Hu, Y. Guo, Z. Ye, Wavelength tunable photoluminescence of ZnO1- x S x alloy thin films grown by reactive sputtering, *J. Appl. Phys.* 114 (2013) 083522.

[H. Zhu. 2014] H. Zhu, H. Wang, W. Wan, S. Yu, X.W. Feng, Influence of oxygen and argon flow on properties of aluminum-doped zinc oxide thin films prepared by magnetron sputtering, *Thin Solid Films* 566 (2014) 32-37.

[I.O. Oladeji. 1997] I.O. Oladeji, L. Chow, Optimization of chemical bath deposited cadmium sulfide thin films, *J. Electrochem. Soc.* 144 (7) (1997) 2342-2346.

[I.O. Oladeji. 2000] I.O. Oladeji, L. Chow, J.R. Liu, W.K. Chu, A.N.P. Bustamante, C. Fredricksen, A.F. Schulte, Comparative study of CdS thin films deposited by single, continuous, and multiple dip chemical processes, *Thin Solid Films* 359 (2000) 154-159.

[I. Repins. 2008] I. Repins, M.A. Contreras, B. Egaas, C. DeHart, J. Scharf, C.L. Perkins, B. To, R. Noufi, 19.9%-efficient ZnO/CdS/ $CuInGaSe_2$ Solar Cell with 81.2% Fill Factor, *Prog. Photovolt: Res. Appl*. 16 (2008) 235-239.

[J.A. Frantz. 2011] J.A. Frantz, R.Y. Bekele, V.Q. Nguyen, J.S. Sanghera, A. Bruce, S.V. Frolov, M. Cyrus, I.D. Aggarwal, Cu(In,Ga)Se_2 thin films and devices sputtered from a single target without additional selenization, *Thin Solid Films* 519 (2011) 7763-7765.

[J.A. Frantz2. 2011] J.A. Frantz, R.Y. Bekele, V.Q. Nguyen, J.S. Sanghera, I.D. Aggarwal, A. Bruce, S.V. Frolov, M. Cyrus. Characterization of Cu(In,Ga)Se_2 thin films and devices sputtered from a single target without additional selenization, *in: Proc. of 37th IEEE Photovoltaic Specialists Conference* (2011) 364-367.

[J.A. Frantz. 2012] J.A. Frantz, R.Y. Bekele, J.D. Myers, V.Q. Nguyen, J.S. Sanghera, S.I. Maximenko, M. Gonzalez, J.G. Tischler, R.J. Walters, M.S. Leite, A. Bruce, S.V. Frolov, M. Cyrus, Structural and electronic characteristics of

Cu(In,Ga)Se_2 thin films sputtered from quaternary targets, *in: Proc. of 38th IEEE Photovoltaic Specialists Conference* (2012) 3098-3101.

[J.A. Thornton. 1974] J.A. Thornton, Influence of apparatus geometry and deposition conditions on the structure and topography of thick sputtered coatings, *J. Vac. Sci. Technol*. 11 (1974) 666-670.

[J.A. Thornton. 1977] J.A. Thornton, D.W. Hoffman, Internal stresses in titanium, nickel, molybdenum, and tantalum films deposited by cylindrical magnetron sputtering, *J. Vac. Sci. Technol*. 14 (1977) 164-168.

[J.A. Thornton. 1989] J.A. Thornton, D.W. Hoffman, Stress-related effects in thin films, *Thin Solid Films* 171 (1989) 5-31.

[J.C. Lee. 2000] J.C. Lee, K.H. Kang, S.K. Kim, K.H. Yoon, I.J. Park, J. Song, RF sputter deposition of the high-quality intrinsic and n-type ZnO window layers for Cu(In,Ga)Se_2- based solar cell applications, Sol. Energy Mater. Sol. Cells 64 (2000) 185-195.

[J.D. Myers. 2014] J.D. Myers, J.A. Frantz, R.Y. Bekele, V.Q. Nguyen, J.S. Sanghera, Effects of sputtering technique on quaternary sputtered Cu(In,Ga)Se_2 films, *in: Proc. of SPIE* 9177 (2014) 917708.

[J.E. Jaffe. 2001] J.E. Jaffe, A. Zunger, Defect-induced nonpolar-to-polar transition at the surface of chalcopyrite semiconductors, *Phys. Rev. B* (2001) 241304-1-4.

[J. Eid. 2015] J. Eid, H. Liang, I. Gereige, S. Lee, J.V Duren, *Prog. Photovolt: Res. Appl*. 23 (2015) 269-280.

[J.H. Scofield. 1995] J.H. Scofield, A. Duda, D. Albin, B.L. Ballardb, P.K. Predecki, Sputtered molybdenum bilayer back contact for copper indium diselenide-based polycrystalline thin-film solar cells, *Thin Solid Films* 260 (1995) 26-31.

[J.H. Scofield2. 1995] J.H. Scofield, S. Asher, D. Albin, J. Tuttle, M. Contreras, D. Niles, R. Reedy, A. Tennant, R. Noufi, Sodium diffusion, selenization, and microstructural effects associated with various molybdenum back contact layers for CIS-based solar cells, *In: Proc. of the 24th IEEE Photovoltaic Specialists Conference* (1995) 164-167.

[J.H. Shi. 2011] J.H. Shi, Z.Q. Li, D.W. Zhang, Q.Q. Liu, Z. Sun, S.M. Huang, Fabrication of Cu(In, Ga)Se2 thin films by sputtering from a single quaternary chalcogenide target, *Prog. Photovolt: Res. Appl.* 19 (2011) 160-164.

[J. H. Yoon. 2012] J.H. Yoon, T.Y. Seong, J.h Jeong, Effect of a Mo back contact on Na diffusion in CIGS thin film solar cells, *Prog. Photovolt: Res. Appl*. 21(1) (2013) 58-63.

[J. H. Yoon. 2014] J.H. Yoon, W.M. Kim, J.K. Park, Y.J. Baik, T.Y. Seong, J.h Jeong, Control of the preferred orientations of Cu(In,Ga)Se2 films and the photovoltaic conversion efficiency using a surface-functionalized molybdenum back contact, *Prog. Photovolt: Res. Appl*. 22 (2014) 69-76.

[J. H. Yoon.2. 2014] J.H. Yoon, J.H. Kim, W.M. Kim, J.K. Park, Y.J. Baik, T.Y. Seong, J.h. Jeong, Electrical properties of CIGS/Mo junctions as a function of $MoSe_2$ orientation and Na doping, *Prog. Photovolt: Res. Appl*. 22 (2014) 90-96.

[J.H. Yun. 2007] J.H Yun, K.H. Kim, M.S. Kim, B.T Ahn, S.J. Ahn, J.C. Lee, K.H. Yoon, Fabrication of CIGS solar cells with a Na-doped Mo layer on a Na-free substrate, *Thin Solid Films* 515 (2007) 5876-5879.

[J. I Oda. 2010] J.i. Oda, J.i Nomoto, T. Miyata, T. Minami, Improvements of spatial resistivity distribution in transparent conducting Al-doped ZnO thin films deposited by DC magnetron sputtering, *Thin Solid Films* 518 (2010) 2984-2987.

[J. I. Nomoto. 2011] J.i. Nomoto, T. Hirano, T. Miyata, T. Minami, Preparation of Al-doped ZnO transparent electrodes suitable for thin-film solar cell applications by various types of magnetron sputtering depositions, *Thin Solid Films* 520 (2011) 1400-1406.

[J. Kessler. 1993] J. Kessler, M. Ruckh, D. Hariskos, U. Ruhle, **R.** Menner. and H.W. Schock, *in: Proc. of 23rd EEE Photovoltaic Specialists Conference* (1993).

[J. L. H. Rojas. 1992] J. L. Hernandez-Rojas, M. L. Lucia, I. Martil, J. Santamaria, G. Gonzalez-Diaz, F. Sanchez-Quesada, Chalcopyrite $CuGa_xIn_{1-x}Se_2$ semiconducting thin films produced by radio frequency sputtering, *Appl. Phys. Lett*. 60 (15) (1992) 1875-1877.

[J. L. H. Rojas. 1993] J. L. Hernandez-Rojas, M. L. Lucia, I. Martil, G. Gonzalez-Diaz, J. Santamaria, F. Sanchez-Quesada, Stoichlometry control over a wide composition range of sputtered $CuGa_xIn_{1-x}Se_2$, *Appl. Phys. Lett*. 64 (10) (1994) 1239-1241.

[J. Lindahl. 2013] J. Lindahl, U. Zimmermann, P. Szaniawski, T. Torndahl, A. Hultqvist, P. Salome, C. Platzer-Bjorkman, M. Edoff, Inline $Cu(In,Ga)Se_2$ Co-evaporation for high-efficiency solar cells and modules, *IEEE J. Photovoltaics* 3(3) (2013) 1100-1105.

[J. Liu. 2013] J. Liu, D. Zhuang, H. Luan, M. Cao, M. Xie, X. Li, Preparation of $Cu(In,Ga)Se_2$ thin film by sputtering from $Cu(In,Ga)Se_2$ quaternary target, *Prog. Nat. Sci.: Mater. Int.* 23(2) (2013) 133-138.

[J.N. Duenow. 2008] J.N. Duenow, T.A. Gessert, D.M. Wood, B. Egaas, R. Noufi, T.J. Coutts, ZnO:Al doping level and hydrogen growth ambient effects on CIGS solar cell performance, *NREL/CP-520-42537* (2008).

[J. P. Kar. 2010] J.P. Kar, S. Kim, B. Shin, K.I. Park, K.J. Ahn, W. Lee, J.H. Cho, J.M. Myoung, Influence of sputtering pressure on morphological, mechanical and electrical properties of Al-doped ZnO films, *Solid-State Electron*. 54 (2010) 1447-1450.

[J. P. Mathew. 2014] J.P. Mathew, G. Varghese, J. Mathew, Structural and Optical Properties of Ni:ZnO Thin Films-Effect of Annealing and Doping Concentration, *SOP Transactions Appl. Phys*. 1 (2014) 27-36.

[J. Schulte. 2015] J. Schulte, K. Harbauer. K. Ellmer, Toward efficient Cu(In,Ga)Se_2 solar cells prepared by reactive magnetron co-sputtering from metallic targets in an Ar:H_2Se atmosphere, *Prog. Photovolt: Res. Appl*. 23(12) (2015) 1793-1805.

[J. Tranchant. 2007] J. Tranchant, Etude de couches minces déposées par pulvérisation magnétron post ionisée pour l'ingénierie de contraintes -cas du MoCr et de nano-canaux de carbone, *PhD thesis, University of Nantes* (2007).

[J. Xiang. 2014] J. Xiang, X. Huang, G. Lin, J. Tang, C. Ju, X.S. Miao, CIGS Thin films for Cd-free solar cells by one-step sputtering process, *J. Electron. Mater*. 43(7) (2014) 2658-2666.

[J. Yoo. 2005] J. Yoo, J. Lee, S. Kim, K. Yoon, I.J Park, S.K. Dhungel, B. Karunagaran, D. Mangalaraj, J. Yi, High transmittance and low resistive ZnO:Al films for thin film solar cells, *Thin Solid Films* 480-481 (2005) 213-217.

[K. Granath. 2000] K. Granath, M. Bodegard, L. Stolt, The effect of NaF on Cu(In,Ga)Se_2 thin film solar cells, *Sol. Energy Mater. Sol. Cells* 60 (2000) 279-293.

[K. H Muller. 1986] K. H Muller , Monte Carlo calculation for structural modifications in ion-assisted thin film deposition due to thermal spikes, *J. Vac. Sci. Technol. A* 4 (1986) 184-188.

[K. H. Kim. 1997] K.H Kim, K.C. Park, D.Y. Ma, Structural, electrical and optical properties of aluminum doped zinc oxide films prepared by radio frequency magnetron sputtering, *J. Appl. Phys*. 81 (1997) 7764-7772.

[K. H. Liao. 2013] K.H. Liao, C.Y. Su, Y.T. Ding, Effects of Ga accumulation on the microstructure of Cu(In_{1-x},Ga_x)Se_2 thin films during selenization, *J. Alloy. Compd*. 581 (2013) 250-256.

[K. Ichihara. 1994] K. Ichihara, N. Inoue, M. Okubo, N. Yasuda, The origin of the inhomogeneity of electrical resistivity in magnetron-sputtered indium tin oxide thin films, *Thin Solid Films* 245 (1994) 152-156.

[K. Orgassa. 2003] K. Orgassa, H.W. Schock, J.H. Werner, Alternative back contact materials for thin film Cu(In,Ga)Se_2 solar cells, *Thin Solid Films* 431-432 (2003) 387-391.

[K. Ramanathan. 1998] K. Ramanathan, H. Wiesner, S. Asher, D. Niles, R.N. Bhattacharya, J. Keane, M.A. Contreras, R. Noufi, High efficiency Cu(In,Ga)Se_2 thin film solar cells without intermediate buffer layers, *NREL/CP-520-23898* (1998).

[K. Ramanathan. 2002] K. Ramanathan, F.S. Hasoon, S. Smith, A. Mascarenhas, H. Al-Thani, J. Alleman, H.S. Ullal, J. Keane, P.K. Johnson, J.R. Sites, Properties of Cd and Zn partial electrolyte treated CIGS solar cells, *in: Proc. of 29th IEEE Photovoltaic Specialists Conference* (2002) 523-526.

[K. Ramanathan. 2012] K. Ramanathan, J. Mann, S. Glynn, S. Christensen, J. Pankow, J. Li, J. Scharf, L. Mansfield, M. Contreras, R. Noufi, A Comparative study of Zn(O,S) buffer layers and CIGS solar cells fabricated by CBD, ALD, and sputtering, *in: Proc. of* 38^{th} *IEEE Photovoltaic Specialists Conference* (2012) 1-4.

[K. S. Hui. 2011] K.S. Hui, L. Li, J.Y. Lee, H.W. Park, P.K. Song, Y.R. Cho, H.S. Lee, K.N. Hui, Electrical and optical properties of composite transparent conductive oxide thin films, *in: Proc. of* 18^{th} *International conference of composite materials* (2011).

[K. Tominaga. 1998] K. Tominaga, N. Umezu, I. Mori, T. Ushiro, T. Moriga, I. Nakabayashi, Effects of UV light irradiation and excess Zn addition on ZnO:Al film properties in sputtering process, *Thin Solid Films* 316 (1998) 85-88.

[K. Tominaga. 2002] K. Tominaga, T. Takao, A. Fukushima, T. Morigab, I. Nakabayashi, Film properties of ZnO:Al films deposited by co-sputtering of ZnO:Al and contaminated Zn targets with Co, Mn and Cr, *Vac*. 66 (2002) 511-515.

[L.N. Li. 2012] L.N. Li, Y. Zhao, X.L. Chen, J. Sun, X.D. Zhang, Effects of oxygen flux on the aluminum doped zinc oxide thin films by direct current magnetron sputtering, *Phys. Procedia* 32 (2012) 687-695.

[L. Ouyang. 2014] L. Ouyang, M. Zhao, D. Zhuang, J. Han, L. Guo, X. Li, M. Cao, The relationships between electronic properties and microstructure of Cu(In,Ga)Se_2 films prepared by sputtering from a quaternary target, *Mater. Lett*. 137 (2014) 249-251.

[L. Ouyang. 2015] L. Ouyang, D. Zhuang, M. Zhao, N. Zhang, X. Li, L. Guo, R. Sun, M. Cao, *Phys. Status Solidi A* 212 (8) (2015) 1774-1778.

[L. Ribeaucourt.2011] L. Ribeaucourt, Electrodépôt et sélénisation d'alliages Cu-In-Ga en vue de la synthèse de couches minces de Cu(In,Ga)Se_2 pour cellules solaires, *PhD thesis, University of Pierre et Marie Curie* (2011).

[M. A. Alim.2006] M.A. Alim, S. Li, F. Liu, P. Cheng, Electrical barriers in the ZnO varistor grain boundaries, *Phys. Stat. Sol. (a)* 203 (2) (2006) 410-427.

[M.A. Contreras. 1997] M.A. Contreras, B. Egaas, P. Dippo, J. Webb, J. Granata, K. Ramanathan, S. Asher, A. Swartzlander, R. Noufi, On the role of Na and modifications to Cu(In,Ga)Se_2 absorber materials using thin-MF (M=Na, K, Cs) precursor layers, *in: Proc. of the 26th IEEE Photovoltaic Specialists Conference* (1997).

[M.A. Contreras. 1999] M.A. Contreras, B. Egaas, K. Ramanathan, J. Hiltner, A. Swartzlander, F. Hasoon, R. Noufi, Progress Toward 20% Efficiency in Cu(In,Ga)Se_2 Polycrystalline Thin-film Solar Cells, *Prog. Photovolt: Res. Appl*. 7 (1999) 311-316.

[M.A. Contreras. 2000] M.A. Contreras, K.M. Jones, L. Gedvilas, and R. Matson, *in: Proc. of the 16th European Photovoltaic Solar Energy Conference* (2000) 732-735.

[M.A. Contreras2. 2000] M.A. Contreras, B. Egaas, D. King, A. Swartzlander, T. Dullweber, Texture manipulation of $CuInSe_2$ thin films, *Thin Solid Films* 361-362 (2000) 167-171.

[M. Andritschky. 1993] O. Auciello, J. Engemann, Multicomponent and multilayered thin films for advanced microtechnologies: techniques, fundamentals and devices, *Kluwer Academic Publishers* (1993) 145.

[M. B. Ard. 2000] M. Bodeg Ard, K. Granath, L. Stolt, Growth of Cu(In,Ga)Se_2 thin films by coevaporation using alkaline precursors, *Thin Solid Films* 361-362 (2000) 9-16.

[M. Bodegard. 1999] M. Bodeg Ard, K. Granath, L. Stolt, A. Rockett, The behaviour of Na implanted into Mo thin films during annealing, *Sol. Energy Mater. Sol. Cells* 58 (1999) 199-208.

[M. Buffiere. 2011] M. Buffiere, Synthèse et caractérisation de couches minces de Zn(O,S) pour application au sein des cellules solaires à base de Cu(In,Ga)Se_2, *PhD thesis, University of Nantes* (2011).

[M. Buffiere. 2014] M. Buffière, N. Barreau, L. Arzel, P. Zabierowski. J. Kessler, Minimizing metastabilities in Cu(In,Ga)Se_2/(CBD)Zn(S,O,OH)/i-ZnO-based solar cells, *Prog. Photovolt: Res. Appl*. 23 (4) (2015) 462-469.

[M. C. Li. 2010] M.C. Li, C.C. Kuo, S.H. Peng, S.H. Chen, C.C. Lee, Influence of hydrogen on the properties of Al and Ga-doped ZnO films at room temperature, *Appl. Opt.* 50 (9) (2011) C197-200.

[M.G. Wardle. 2006] M.G. Wardle, J.P. Goss, P.R. Briddon, First-Principles Study of the Diffusion of Hydrogen in ZnO, *Phys. Rev. Lett*. 96 (2006) 205504.

[M. Izaki. 2015] M. Izaki, S. Sugiyama, T. Okamoto, Y. Kusano, T. Maki, H. Komaki, H. Shibata, S. Niki, Structure of chemically deposited Zn(S,O,OH) buffer layer

and the effects on the performance of Cu(In,Ga)Se_2 solar cell, *Prog. Photovolt: Res. Appl*. 24 (3) (2016) 397-404.

[M. J. Furlong. 1998] M.J. Furlong, M. Froment, M.C. Bernard, R. Cortes, A.N. Tiwari, M. Krejci, H. Zogg, D. Lincot, Aqueous solution epitaxy of CdS layers on $CuInSe_2$, *J. Cryst. Growth* 193 (1998) 114-122.

[M. Jubault. 2011] M. Jubault, L. Ribeaucourt, E. Chassaing, G. Renou, D. Lincot, F. Donsanti, Optimization of molybdenum thin films for electrodeposited CIGS solar cells, *Sol. Energy Mater. Sol. Cells* 95 (2011) S26-S31.

[M.L. Addonizio. 1999] M.L. Addonizio, A. Antonaia, G. Cantele, C. Privato, Transport mechanisms of RF sputtered Al-doped ZnO films by H_2 process gas dilution, *Thin Solid Films* 349 (1999) 93-99.

[M. Lee. 2015] M. Lee, S.M. Lee, S. Jung, S. Ahn, J.S. Cho, J. Park, Y. Eh, J. Gwak, K. Shin, K. Yoon, Y.S Cho, J.H Yun, Highly efficient flexible $CuIn_{0.7}Ga_{0.3}Se_2$ solar cells with a thick Na/Mo layer deposited directly on stainless steel, *Appl. Surf. Sci*. 346 (2015) 562-566.

[M. Terheggen. 2002] M. Terheggen, H. Heinrich, G. Kostorz, F.J. Haug, H. Zogg, A.N. Tiwari, Ga_2O_3 segregation in Cu(In,Ga)Se_2/ZnO superstrate solar cells and its impact on their photovoltaic properties, *Thin Solid Films* 403-404 (2002) 212-215.

[M. W. J. Prins. 1998] M.W.J. Prins, K.O. Grosse-Holz, J.F.M. Cillessen, L.F. Feiner, Grain-boundary-limited transport in semiconducting SnO_2 thin films: Model and experiments, *J. Appl. Phys*. 83 (1998) 888-893.

[Nexcis] Nexcis, from R&D to industrialization. http://www.nexcis.fr/en/societe/de-la-r-d-a-l-industrialisation, (accessed 26/08/16).

[N. Fujimura. 1993] N. Fujimura, T. Nishihara, S. Goto, J. Xu, T. lto, Control of preferred orientation for ZnO_x films: control of self-texture, *J. Cryst. Growth* 130 (1993) 269-279.

[N. H. Quang. 2004] N.H. Quang, The role of the heterointerfaces in the Cu(In,Ga)Se_2 thin film solar cell with chemical bath deposited buffer layers, *PhD thesis, University of Stuttgart* (2004).

[N. J. Begum. 2013] N.J. Begum, R. Mohan, K. Ravichandran, Effect of solvent volume on the physical properties of aluminium doped nanocrystalline zinc oxide thin films deposited using a simplified spray pyrolysis technique, *Superlattices Microstruct*. 53 (2013) 89-98.

[N. Naghavi. 2010] N. Naghavi, D. Abou-Ras, N. Allsop, N. Barreau, S. Bucheler, A. Ennaoui, C.H. Fischer, C. Guillen, D. Hariskos, J. Herrero, R. Klenk, K. Kushiya, D. Lincot, R. Menner, T. Nakada, C. Platzer-Bjorkman, S. Spiering, A.N.

Tiwari, T. Torndahl, Buffer layers and transparent conducting oxides for chalcopyrite Cu(In,Ga)(S,Se)$_2$ based thin film photovoltaics: present status and current developments, *Prog. Photovolt: Res. Appl*. 18 (2010) 411-433.

[N. Naghavi.2015] N. Naghavi, S. Temgoua, T. Hildebrandt, J.F. Guillemoles, D. Lincot, Impact of oxygen concentration during the deposition of window layers on lowering the metastability effects in Cu(In,Ga)Se$_2$/CBD Zn(S,O) based solar cell, *Prog. Photovolt: Res. Appl.* 23 (2015) 1820-1827.

[NREL 2016] http://www.nrel.gov/pv/assets/images/efficiency_chart.jpg, (accessed 24/10/16).

[O. Kluth. 1997] O. Kluth, A. Loffl, *S.* Wieder, C. Beneking, W. Appenzeller, L. Houben, B. Rech, H. Wagner, S. Hoffmann, R. Waser, J.A. Anna Selvan, H. Keppnet, Texture etched Al-doped ZnO: a new material for enhanced light trapping in thin film solar cells, *in: Proc. of 26th PVSC Photovoltaic Specialists Conference* (1997) 715-718.

[O. Kluth.1999] O. Kluth, B. Rech, L. Houben, S. Wieder, G. Schoepe, C. Beneking, H. Wagner, A. Loeffl, H.W. Schock, Texture etched ZnO:Al coated glass substrates for silicon based thin film solar cells, *Thin Solid Films* 351 (1999) 247-253.

[O. Tosoni. 2013] O. Tosoni, Conception, élaboration et intégration d'électrodes transparentes optimisées pour l'extraction des charges dans des dispositifs photovoltaïques, *PhD thesis, University of Grenoble* (2006).

[P. Blösch. 2014] P.Blösch, S. Nishiwaki, L. Kranz, C.M. Fella, F. Pianezzi, T. Jäger, C. Adelhelm, E. Franzke, S. Buecheler, A.N. Tiwari, Sodium-doped molybdenum back contact designs for Cu(In,Ga)Se$_2$ solar cells, *Sol. Energy Mater. Sol. Cells* 124 (2014) 10-16.

[P. Bommersbach. 2011] P. Bommersbach, L. Arzel, M. Tomassini, E. Gautron, C. Leyder, M. Urien, D. Dupuy, N. Barreau, Influence of Mo back contact porosity on co-evaporated Cu(In,Ga)Se$_2$ thin film properties and related solar cell, *Prog. Photovolt: Res. Appl*. 21 (3) (2013) 332-343.

[P. Chelvanathan. 2010] P. Chelvanathan, M.I. Hossain, N. Amin, Performance analysis of copper–indium–gallium–diselenide (CIGS) solar cells with various buffer layers by SCAPS, *Curr. Appl. Phys.* 10 (2010) S387-S391.

[P. Eraerds. 2016] P. Eraerds, C. Schubbert, T. Kwast, M. Grave, F. Braun, M. Algasinger, R. Lechner, T. Dalibor, J. Palm, Efficiency improvement of CIGSSe Cd-free solar module by optimized cell and interconnect design, *Oral presentation at the 32nd EUPVSE Conference 3BO.8.2* (2016).

[P. J. Rostan. 2005] P.J. Rostan, J. Mattheis, G. Bilger, U. Rau, J.H. Werner, Formation of transparent and ohmic ZnO:Al/$MoSe_2$ contacts for bifacial Cu(In,Ga)Se_2 solar cells and tandem structures, *Thin Solid Films* 480-481 (2005) 67-70.

[P. Jackson. 2015] P. Jackson, D. Hariskos, R. Wuerz, O. Kiowski, A. Bauer, T.M. Friedlmeier, M. Powalla, Properties of Cu(In,Ga)Se_2 solar cells with new record efficiencies up to 21.7%, *Phys. Status Solidi RRL* 9 (1) (2015) 28-31.

[P. M. P. Salomé. 2015] P.M.P. Salomé, V. Fjällström, P. Szaniawski, J.P. Leitão, A. Hultqvist, P.A. Fernandes, J.P. Teixeira, B.P. Falcão, U. Zimmermann, A.F. da Cunha, M. Edoff, A comparison between thin film solar cells made from co-evaporated $CuIn_{1-x}Ga_xSe_2$ using a one-stage process versus a three-stage process, *Prog. Photovolt: Res. Appl.* 23 (2015) 470-478.

[P. P. Choi. 2011] P.P. Choi, O. Cojocaru-Mirédin, R. Wuerz, D. Raabe, Comparative atom probe study of Cu(In,Ga)Se_2 thin-film solar cells deposited on soda lime glass and mild steel substrates, *J. Appl. Phys*. 110 (2011) 124513.

[P. Pistor. 2014] P. Pistor, D. Greiner, C.A. Kaufmann, S. Brunken, M. Gorgoi, A. Steigert, W. Calvet, I. Lauermann, R. Klenk, T. Unold, M.C. Lux-steiner, Experimental indication for band gap widening of chalcopyrite solar cell absorbers after potassium fluoride treatment, *Appl. Phys. Lett*. 105 (2014) 063901.

[P. W. Yu.1975] P.W. Yu, S.P. Faile, Y.S. Park, Cadmium−diffused $CuInSe_2$ junction diode and photovoltaic detection, *Appl. Phys. Lett*. 26 (1975) 384-385.

[Q. Guo. 2013] Q. Guo, G.M. Ford, R. Agrawal, H.W. Hillhouse, Ink formulation and low-temperature incorporation of sodium to yield 12% efficient Cu(In,Ga)$(S,Se)_2$ solar cells from sulfide nanocrystal inks, *Prog. Photovolt: Res. Appl*. 21 (2013) 64-71.

[R. Abermann. 1984] R. Abermann, H.P. Martinz, Gas adsorption on thin films of chromium studied by internal stress measurements, *Thin Solid Films* 111 (1984) 303-311.

[R. Abermann. 1985] R. Abermann, R. Koch, The internal stress in thin silver, copper and gold films, *Thin Solid Films* 129 (1985) 71-7.

[R. Cebulla. 1998] R. Cebulla, R. Wendt, K. Ellmer, Al-doped zinc oxide films deposited by simultaneous RF and DC excitation of a magnetron plasma: Relationships between plasma parameters and structural and electrical film properties, *J. Appl. Phys*. 83 (2) (1998) 1087-1095.

[R. Herberholz. 1997] R. Herberholz, M. Igalson, H.W. Schock, Distinction between bulk and interface states in $CuInSe_2$/CdS/ZnO by space charge spectroscopy, *J. Appl. Phys.* 83 (1998) 318-325.

[R. J. Matson. 1984] R.J. Matson, O. Jamjoum, A.D. Buonaquisti, P.E. Russell, L.L. Kazmerski, P. Sheldon, R. K. Ahrenkiel, Metal contacts to CuInSe, *Sol. Cells* 11 (1984) 301-305.

[R. Klenk. 2013] R. Klenk, P. Gerhardt, I. Lauermann, A. Steigert, F. Stober, F. Hergert, S. Zweigart, M.Ch. Lux-Steiner, Design, preparation and performance of Cu(In,Ga)(S,Se)$_2$ /Zn(O,S) /ZnO:Al solar cells, *in: Proc. of 39th PVSC Photovoltaic Specialists Conference* (2013) 853-856.

[R. Klenk. 2014] R, Klenk, A. Steigert, T. Rissom, D. Greiner, C.A. Kaufmann, T. Unold, M.Ch. Lux-Steiner, Junction formation by Zn(O,S) sputtering yields CIGSe based cells with efficiencies exceeding 18% *Prog. Photovolt: Res. Appl*. 22 (2014) 161-165.

[R.N. Bhattacharya. 2004] R.N. Bhattacharya, M.A. Contreras, G. Teeter, 18.5% Copper Indium Gallium Diselenide (CIGS) device using single-layer, chemical-bath-deposited ZnS(O,OH), *Jpn. J. Appl. Phys*. 43 (11B) (2004) L1475-L1476.

[R.S. Araoz. 2004] R.S. Araoz, Chemical bath deposition of Zn(S,O) buffer layers and application in Cd-free chalcopyrite-based thin-film solar cells and modules, *PhD thesis, University of Berlin* (2009).

[R. W. Hoffman. 1976] R. W. Hoffman, Stresses in thin films: the relevance of grain boundaries and impurities, *Thin Solid Films* 34 (1976) 185-190.

[R. Wuerz.2014] R. Wuerz, A. Eicke, F. Kessler, F. Pianezzi, Influence of iron on the performance of CIGS thin-film solar cells, *Sol. Energy Mater. Sol. Cells* 130 (2014) 107-117.

[S. Angle. 2014] S. Angle, L. Parissi, Interface between a I/III/VI$_2$ layer and a back contact layer in a photovoltaic cell, US 2014/0315346 A1.

[S. Ashour. 1993] S. Ashour, S. Alkuhaimi, H. Moutinho, R. Matson, F. Abou-Elfotouh, Junction formation and characteristics of CdS/CulnSe$_2$/metal interfaces, *Thin Solid Films* 226 (1993) 129-134.

[S. Brochen. 2012] S. Brochen, Propriétés électriques du ZnO Monocristallin, *PhD thesis, University of Grenoble* (2006).

[S. Chaisitsak. 2002] S. Chaisitsak, A. Yamada, M. Konagai, Preferred orientation control of Cu(In$_{1-x}$Ga$_x$)Se$_2$ (x≈0:28) thin films and its influence on solar cell characteristics, *Jpn. J. Appl. Phys*. 41 (2002) 507-513.

[S. Ishizuka. 2009] S. Ishizuka, A. Yamada, M.M. Islam, H. Shibata, P. Fons, T. Sakurai, K. Akimoto, S. Niki, Na-induced variations in the structural, optical, and electrical properties of Cu(In,Ga)Se$_2$ thin films, *J. Appl. Phys*. 106 (2009) 034908.

[S. Jost. 2015] S. Jost, J. Palm, Avoidance of glass bending in thermal processes, US 2015/0171235 A1.

[S. Karthikeyan.2014] S. Karthikeyanl, M. Sibakotil, R. Liptakl, S.H. Songl, J. Abrahamson, E.S. Aydi, S.A. Campbell, Challenges in deposition of wide band gap copper indium aluminum gallium selenide (CIAGS) thin films for tandem solar cells, *in: Proc. of 40th PVSC Photovoltaic Specialists Conference* (2014) 1632-1634.

[S. Marsillac. 2002] S. Marsillac, P.D. Paulson, M.W. Haimbodi, R.W. Birkmire, W.N. Shafarman, High-efficiency solar cells based on Cu(InAl) Se_2 thin films, *Appl. Phys. Lett.* 81 (2002) 1350-1352.

[S. Nishiwaki. 1998] S. Nishiwaki, N. Kohara, T. Negami, T. Wada, $MoSe_2$ layer formation at Cu(In,Ga)Se_2/Mo interfaces in high efficiency Cu($In_{1-x}Ga_x$)Se_2 solar cells, *Jpn. J. Appl. Phys.* 37 (1998) L71-L73.

[S. Nishiwaki. 2003] S. Nishiwaki, T. Satoh, Y. Hashimoto, S.I. Shimakawa, S. Hayashi, T. Negami, T. Wada, Preparation of Zn doped Cu(In,Ga)Se_2 thin films by physical vapor deposition for solar cells, *Sol. Energy Mater. Sol. Cells* 77 (2003) 359-368.

[S. Rahmane. 2014] S. Rahmane, M.A. Djouadi, M.S. Aida, N. Barreau, Oxygen effect in radio frequency magnetron sputtered aluminium doped zinc oxide films, *Thin Solid Films* 562 (2014) 70-74.

[S. S. Kulkarni. 2009] S.S. Kulkarni, G.T. Koishiyev, H. Moutinho, N.G. Dhere, Preparation and characterization of $CuIn_{1-x}GaxSe_{2-y}S_y$ thin film solar cells by rapid thermal processing, *Thin Solid Films* 517 (2009) 2121-2124.

[S. Sharbati. 2014] S. Sharbati, J.R. Sites, Impact of the Band Offset for n-Zn(O,S)/p-Cu(In,Ga)Se_2 Solar Cells, *IEEE J. Photovolt*. 4 (2) (2014) 697-702.

[S. Siebentritt. 2004] S. Siebentritt, Alternative buffers for chalcopyrite solar cells, Sol. Energy 77 (2004) 767-775.

[S. Y. Kuo. 2014] S.Y. Kuo, M.Y. Hsieh, D.H. Hsieh, H.C Kuo, C.H Chen, F.I Lai, Device modeling of the performance of Cu(In,Ga)Se_2 solar cells with V-shaped bandgap profiles, *Int. J. Photoenergy* (2014) ID 186579.

[Solar frontier] http://www.solar-frontier.com/eng/, (accessed 26/08/16).

[T. Dullweber. 2001] T. Dullweber, O. Lundberg, J. Malmstrom, M. Bodegard, L. Stolt, U. Rau, H.W. Schock, J.H. Werner, Back surface band gap gradings in Cu(In,Ga)Se_2 solar cells, *Thin Solid Films* 387 (2001) 11-13.

[T. Dullweber2. 2001] T. Dullweber, G. Hanna, U. Rau, H.W. Schock, A new approach to high-efficiency solar cells by band gap grading in Cu(In,Ga)Se_2 chalcopyrite semiconductors, *Sol. Energy Mater. Sol. Cells* 67 (2001) 145-150.

[T. Eisenbarth.2012] T. Eisenbarth, R. Caballero, C.A. Kaufmann, A. Eicke, T. Unold, Influence of iron on defect concentrations and device performance for Cu(In,Ga)Se_2 solar cells on stainless steel substrates, *Prog. Photovolt: Res. Appl*. 20 (2012) 568-574.

[T.I. Kamins. 1971] T.I. Kamins, Hall mobility in chemically deposited polycrystalline silicon, *J. Appl. Phys*. 42 (1971) 4357-4365.

[T. Kato. 2016] T. Kato, K. Kitani, K.F. Tai, R. Kamada, H. Hiroi & H. Sugimoto, Characterization of the back contact of CIGS solar cell as the origin of "rollover" effect, *Oral presentation at the 32nd EUPVSE Conference* 3AO.5.3 (2016).

[T. Kobayashi. 2014] T. Kobayashi, T. Kumazawa, Z.J.L. Kao, T. Nakada, Post-treatment effects on ZnS(O,OH)/Cu(In,Ga)Se_2 solar cells deposited using thioacetamide-ammonia based solution, *Sol. Energy Mater. Sol. Cells* 123 (2014) 197-202.

[T. Kobayashi. 2015] T. Kobayashi, H. Yamaguchi, Z.J.L. Kao, H. Sugimoto, T. Kato, H. Hakuma, T. Nakada, Impacts of surface sulfurization on Cu(In_{1-x},Ga_x)Se_2 thin-film solar cells, *Prog. Photovolt: Res. Appl*. 23 (2015) 1367-1374.

[T. Kobayashi. 2016] T. Kobayashi, Z.J.L. Kao, T. Kato, H. Sugimoto, T. Nakada, A comparative study of Cd- and Zn-compound buffer layers on Cu(In_{1-x},Ga_x)(Sy,Se_{1-y})$_2$ thin film solar cells, *Prog. Photovolt: Res. Appl.* 24 (2016) 389396.

[T. L. Chu.1992] T.L. Chu, S.S. Chu, N. Schultz, C. Wang, C. Q. Wu, Solution-grown cadmium sulfide films for photovoltaic devices, *J. Electrochem. Soc.* 139 (9) (1992) 2443-2446.

[T. Lepetit. 2015] T. Lepetit, Influence of KF post deposition treatment on the polycrystalline Cu(In,Ga)Se_2/CdS heterojunction formation for photovoltaic application, *PhD thesis, University of Nantes* (2015).

[T. Minami. 1992] T. Minami, H. Sato, H. Imamoto, S. Takata, Substrate temperature dependence of transparent conducting Al-doped ZnO thin films prepared by magnetron sputtering, *Jpn. J. Appl. Phys.* 31 (1992) L257-L260.

[T. Minami. 2001] T. Minami, S. Suzuki, T. Miyata, Transparent conducting impurity-co-doped ZnO:Al thin films prepared by magnetron sputtering, *Thin Solid Films* 398-399 (2001) 53-58.

[T. Minami. 2010] T. Minami, J.i. Oda, J.i. Nomoto, T. Miyata, Spatial resistivity distribution of transparent conducting impurity-doped ZnO thin films deposited on

substrates by dc magnetron sputtering, *J. Vac. Sci. Technol. A* 28 (2010) 842-845.

[T. Minemoto. 2001] T. Minemoto, T. Matsui, H. Takakura, Y. Hamakawa, T. Negami, Y. Hashimoto, T. Uenoyama, M. Kitagawa, Theoretical analysis of the effect of conduction band offset of window/CIS layers on performance of CIS solar cells using device simulation, *Sol. Energy Mater. Sol. Cells* 67 (2001) 83-88.

[T. Minemoto. 2011] T. Minemoto, A. Okamoto, H. Takakura, Sputtered ZnO-based buffer layer for band offset control in Cu(In,Ga)Se_2 solar cells, *Thin Solid Films* 519 (2011) 7568-7571.

[T. Nakada. 1999] T. Nakada, A. Kunioka, Direct evidence of Cd diffusion into Cu(In,Ga)Se_2 thin films during chemical-bath deposition process of CdS films, *Appl. Phys. Lett.* 74 (1999) 2444-2446.

[T. Nakada. 2000] T. Nakada, M. Mizutani, Improved efficiency of Cu(ln,Ga)Se_2 thin film solar cells with chemically deposited ZnS buffer layers by air-annealing-formation of homojunction by solid phase diffusion, *in: Proc. of 28th IEEE Photovoltaic Specialists Conference* (2000) 529-534.

[T. Nakada. 2002] T. Nakada, M. Mizutani, 18% efficiency Cd-Free Cu(In, Ga)Se_2 thin-film solar cells fabricated using chemical bath deposition (CBD)-ZnS buffer layers, *Jpn. J. Appl. Phys*. 41 (2002) L165-L167.

[T. Nakada. 2004] T. Nakada, Y. Hirabayashi, T. Tokado, D. Ohmori, T. Mise, Novel device structure for Cu(In,Ga)Se_2 thin film solar cells using transparent conducting oxide back and front contacts, *Sol. Energy* 77 (2004) 739-747.

[T. Nakada. 2005] T. Nakada, Microstructural and diffusion properties of CIGS thin film solar cells fabricated using transparent conducting oxide back contacts, *Thin Solid Films* 480-481 (2005) 419-425.

[T.S. Moss. 1954] T.S. Moss, The interpretation of the properties of indium antimonide, *Proc.Phys. Soc. Lond. Sect. B* 67 (1954) 775-782.

[T. Sugiyama. 2000] T. Sugiyama, S. Chaisitsak, A. Yamada, M. Konagai, Y. Kudriavtsev, A. Godines, A. Villegas, R. Asomoza, Formation of pn homojunction in Cu(InGa)Se_2 thin film solar cells by Zn doping, *Jpn. J. Appl. Phys*. 39 (2000) 4816-4819.

[T. Tohsophon. 2006] T. Tohsophon, J. Hupkes, S. Calnan, W. Reetz, B. Rech, W. Beyer, N. Sirikulrat, Damp heat stability and annealing behavior of aluminum doped zinc oxide films prepared by magnetron sputtering, *Thin Solid Films* 511-512 (2006) 673-677.

[T. Tsuji. 2000] T. Tsuji, M. Hirohashi, Influence of oxygen partial pressure on transparency and conductivity of RF sputtered Al-doped ZnO thin films, *Appl. Surf. Sci*.157 (2000) 47-51.

[T. Wada. 2001] T. Wadaa, N. Kohara, S. Nishiwaki, T. Negami, Characterization of the Cu(In,Ga)Se_2/ Mo interface in CIGS solar cells, *Thin Solid Films* 387 (2001) 118-122.

[T. Y. Lin. 2015] T.Y. Lin, C.H. Lai, Ga-grading CIGS solar cell by one-step sputtering from a quaternary target without post-selenization, *in: Proc. of the 42th IEEE Photovoltaic Specialists Conference* (2015).

[T. Yamaguchi. 1991] T. Yamaguchi, R. Miyagawa, Effect of oxygen on the properties of sputtered molybdenum thin films, *Jpn, J. Appl. Phys*. 30(9A) (1991) 2026-2073.

[T. Yamaguchi. 1992] T. Yamaguchi, J. Matsufusa, A. Yoshida, Structural properties of $CuIn_xGa_{1-x}Se_2$ thin films prepared by rf sputtering, J. Appl. Phys. 72 (1992) 5657-5662.

[Ü. Özgür. 2005] Ü. Özgür, Ya. I. Alivov, C. Liu, A. Teke, M.A. Reshchikov, S. Doğan, V. Avrutin, S.J. Cho, H. Morkoç, A comprehensive review of ZnO materials and devices, *J. Appl. Phys*. 98 (2005) 041301.

[V. Izquierdo-Roca. 2011] V. Izquierdo-Roca, R. Caballero, X. Fontané, C.A. Kaufmann, J. Álvarez-García, L. Calvo-Barrio, E. Saucedo, A. Pérez-Rodríguez, J.R. Morante, H.W. Schock, Raman scattering analysis of Cu-poor Cu(In,Ga)Se_2 cells fabricated on polyimide substrates: Effect of Na content on microstructure and phase structure, *Thin Solid Films* 519 (2011) 7300-7303.

[W.D. Nix. 1999] W.D. Nix, B.M. Clemens, Crystallite coalescence: A mechanism for intrinsic tensile stresses in thin films, *J. Mater. Res.* 14 (8) (1999) 3467-3473.

[W.H. Kim. 2011] W.H. Kim, W.J. Maeng, M.K. Kim, H. Kim, Low pressure chemical vapor deposition of aluminum-doped zinc oxide for transparent conducting electrodes, *J. Electrochem. Soc*. 158 (8) (2011) D495-D499.

[W.J. Jeong. 2001] W.J Jeong, G.C. Park, Electrical and optical properties of ZnO thin film as a function of deposition parameters, *Sol. Energy Mater. Sol. Cells* 65 (2001) 37-45.

[W. Li. 2012] W. Li • H. Hao, Effect of temperature on the properties of Al:ZnO films deposited by magnetron sputtering with inborn surface texture, *J. Mater. Sci*. 47 (2012) 3516-3521.

[W.T. Lin. 2014] W.T. Lin, S.H. Chen, S.H. Chan, S.C. Hu, W.X. Peng, Y.T. Lu, Crystallization phase transition in the precursors of CIGS films by Ar-ion plasma etching process, *Vac.* 99 (2014) 1-6.

[W. Witte. 2013] W. Witte, D. Abou-Ras, D. Hariskos, Chemical bath deposition of Zn(O,S) and CdS buffers: Influence of Cu(In,Ga)Se_2 grain orientation, *Appl. Phys. Lett*. 102 (2013) 051607.

[W. Witte.2. 2013] W. Witte, D. Hariskos, A. Eicke, R. Menner, O. Kiowski, M. Powalla, Impact of annealing on Cu(In,Ga)Se_2 solar cells with Zn(O,S)/(Zn,Mg)O buffers, *Thin Solid Films* 535 (2013) 180-183.

[W. Witte. 2014] W. Witte, S. Spiering, D. Hariskos, Substitution of the CdS buffer layer in CIGS thin-film solar cells: status of current research and record cell efficiencies, *Vakuum in Forschung und Praxis* 26(1) (2014) 23-27.

[W. Yang. 2009] W. Yang, Z. Liu, D.L. Peng, F. Zhang, H. Huang, Y. Xie, Z. Wu, Room-temperature deposition of transparent conducting Al-doped ZnO films by RF magnetron sputtering method, *Appl, Surf, Sci*, 255 (2009) 5669-5673.

[X.F. Fan. 2009] X.F. Fan, Z.X. Shen, Y.M. Lu, J.L. Kuo, A theoretical study of thermal stability and electronic properties of wurtzite and zincblende ZnO_xS_{1-x}, *New J. Phys.* 11 (2009) 093008.

[X.L. Chen. 2012] X.l. Chen, L.na Li, F. Wang, J. Ni, X.h. Geng, X.d. Zhang, Y. Zhao, Natively textured surface aluminum-doped zinc oxide transparent conductive layers for thin film solar cells via pulsed direct-current reactive magnetron sputtering, *Thin Solid Films* 520 (2012) 5392-5399.

[X.L. Zhu. 2013] X.L. Zhu, Y.M. Wang, Z. Zhou, A.M. Li, L. Zhang, F.Q. Huang, 13.6%-efficient Cu(In,Ga)Se_2 solar cell with absorber fabricated by RF sputtering of $(In,Ga)_2Se_3$ and CuSe targets, *Sol. Energy Mater. Sol. Cells* 113 (2013) 140-143.

[X.R. Deng. 2012] X.R. Deng, H. Deng, M. Wei, J.J Chen, Preparation of highly transparent conductive Al-doped ZnO thin films and annealing effects on properties, *J. Mater Sci. : Mater. Electron*. 23 (2012) 413-417.

[X. Zhu. 2012] X. Zhu, Z. Zhou, Y. Wang, L. Zhang, A. Li, F. Huang, Determining factor of $MoSe_2$ formation in Cu(In,Ga)Se_2 solar Cells, *Sol. Energy Mater. Sol. Cells* 101 (2012) 57-61.

[Y.C. Wang. 2013] Y.C. Wang, Y.T. Yen, C.H. Liu, C.H. Chen, W.C. Kuo, J.Y. Juang, C.H. Lai, Y.L. Chueh, Fabrication of large-scale single-crystal Cu(In,Ga)Se_2 nanotip arrays solar cell by one-step ion milling processes, *Thin Solid Films* 546 (2013) 347-352.

[Y.D. Chung. 2011] Y.D. Chung, D.H. Cho, N.M. Park, K.S. Lee, J. Kim, Effect of annealing on CdS/ Cu(In,Ga)Se_2 thin-film solar cells, *Curr. Appl. Phys*. 11 (2011) S65-S67.

[Y. Hagiwara. 2001] Y. Hagiwara, T. Nakada, A. Kunioka, Improved *J*sc in CIGS thin film solar cells using a transparent conducting ZnO:B window layer, *Sol. Energy Mater. Sol. Cells* 67 (2001) 267-271.

[Y. He. 2012] Y. He, L. Wang, L. Zhang, M. Li, X. Shang, Y. Fang, C. Chen, Solubility limits and phase structures in epitaxial ZnOS alloy films grown by pulsed laser deposition, *J. Alloy. Compd*. 534 (2012) 81-85.

[Y. Igasaki. 2001] Y. Igasaki, H. Kanma, Argon gas pressure dependence of the properties of transparent conducting ZnO:Al films deposited on glass substrates, *Appl. Surf. Sci*. 169-170 (2001) 508-511.

[Y.M. Chung. 2005] Y.M. Chung, C.S. Moon, M.J. Jung, J.G. Han, The low temperature synthesis of Al doped ZnO films on glass and polymer using magnetron co-sputtering: Working pressure effect, *Surf. Coatings Technol*. 200 (2005) 936-939.

[Y.M. Chung. 2006] Y.M. Chung, C.S. Moon, W.S. Jung, J.G. Han, The low temperature synthesis of Al doped ZnO films on glass and polymer using pulsed co-magnetron sputtering: H_2 effect, *Thin Solid Films* 515 (2006) 567-570.

[Y.S. Su. 2011] Y.S. Su, C.H. Hsu, C.H. Chen, Y.H. Wu, W.C. Shih, S.Y. Wei, W.T. Hsu, C.H. Lai, Investigation of sodium effects on CIGS thin films deposited by sputtering from a single quaternary, *in: Proc. of the 38th IEEE Photovoltaic Specialists Conference* (2012).

[Y.S. Su. 2013] Y.S. Su, C.H. Hsu, C. Chang, C.H. Lai, Investigation of the CIGS thin film solar cells with post-selenized absorbers deposited by sputtering from a single quaternary target using electrical characterization methods, *in: Proc. of 39th IEEE Photovoltaic Specialists Conference* (2013) 2039-2041.

[Z.B. Ayadi. 2014] Z.B. Ayadi, H. Mahdhi, K. Djessas, J.L. Gauffier, L. ElMir, S. Alaya, Sputtered Al-doped ZnO transparent conducting thin films suitable for silicon solar cells, *Thin Solid Films* 553 (2014) 123-126.

[Z.H. Li. 2011] Z.H. Li, E.S. Cho, S.J Kwon, Molybdenum thin film deposited by in-line DC magnetron sputtering as a back contact for Cu(In,Ga)Se_2 solar cells, *Appl. Surf. Sci*. 257 (2011) 9682-9688.

[Z.H. Li. 2013] Z.H. Li, E.S. Cho, S.J. Kwon, Selenization annealing effect of DC-sputtered metallic precursors using the rapid thermal process for Cu(In,Ga)Se_2 thin film solar cells, *Thin Solid Films* 547 (2013) 156-162.

[Z. J. L. Kao. 2012] Z.J.L. Kao, N. Naghavi1, F. Erfurth, J.F. Guillemoles, I. Gérard, A. Etcheberry, J.L. Pelouard, S. Collin, G. Voorwinden, D. Lincot, Towards ultrathin copper indium gallium diselenide solar cells: proof of concept study by chemical etching and gold back contact engineering, *Prog. Photovolt: Res. Appl*. 20 (2012) 582-587.

[Z. Jehl. 2012] Z. Jehl, Elaboration of ultrathin Copper Indium Gallium Di-Selenide based Solar Cells, *PhD thesis, University of Paris-sud-Orsay* (2012).

[ZSW] ZSW sets New World Record for Thin-film Solar Cells: https://www.zsw-bw.de/en/newsroom/news/news-detail/news/detail/News/zsw-sets-new-world-record-for-thin-film-solar-cells.html, (accessed 24/10/16).

Title: Towards full sputtering deposition process for CIGS solar cells fabrication: from single thin film deposition up to device characterization.

Abstract

Nowadays, and after more than four decades of research and development of the CIS based technology, a direct competition with silicon technology is still far from being won; however there exists some niche markets where the silicon technology cannot be used (flexible photovoltaic) or less favourable (BIPV). The current fabrication processes are still suffering from some drawbacks: (i) some of the used materials and/or techniques have a large environmental footprint (CBD-CdS/CBD-ZnS_xO_{1-x}), (ii) some developed alternatives are expensive (evaporated In_xS_y), (iii) the used techniques are not easily up scalable (evaporation) or based on the use of toxic atmospheres (Se based). This PhD work presents our strategy in moving towards a full sputtering process and in using only environmentally friendly materials. In this framework, we kept using standard material and process for the deposition of the back contact layer (sputtered molybdenum layer). We developed a new process for the deposition of the absorber layer which is based on pulsed DC-magnetron sputtering at room temperature from a single quaternary target using argon plasma without any additional selenium supply, followed by an annealing under inert atmosphere. We developed a room temperature sputtering process for the deposition of the ZnS_xO_{1-x} buffer layer. We also developed our appropriate pulsed DC and RF sputtering processes for the deposition of the window layer. Several characterisation techniques (XRD, SEM, FIB-SEM, EDX, Raman, SIMS, Hall Effect, GDOES, UV-Vis, and I-V) have been used to investigate the effect of deposition conditions on thin films properties as well as to characterize the final solar cells which best efficiency result is slightly under 12%.

Keywords: magnetron sputtering, thin film, thermal annealing, molybdenum back contact, CIGS absorber, buffer layer, CBD-CdS, sputtered ZnS_xO_{1-x}, ZnO window layer, solar cell.

Titre: Vers un processus de dépôt entièrement en pulvérisation cathodique pour la fabrication de cellules solaires à base de CIGS: du dépôt des couches minces élémentaires à la caractérisation du dispositif.

Résumé

De nos jours, et après plus de quatre décennies de recherche et développement de la technologie CIS, une concurrence directe avec la technologie silicium est toujours loin d'être gagnée; néanmoins, il existe certains marchés de niche où la technologie silicium ne peut pas être utilisée (photovoltaïque flexible) ou est moins appropriée (vitrages photovoltaïques à transparence contrôlée). Malheureusement, les procédés de fabrication actuels présentent certains inconvénients: (i) certain(e)s matériaux et/ou techniques utilisé(e)s ont une forte empreinte environnementale (CDB-CdS/CBD-ZnS_xO_{1-x}), (ii) certains matériaux alternatifs développés sont coûteux (In_xS_y par évaporation), (iii) certaines techniques utilisées ne sont pas facilement industrialisables (évaporation) ou basées sur l'utilisation d'atmosphères toxiques (Se). Ce travail de thèse présente une stratégie de transition vers un processus basé exclusivement sur l'utilisation à la fois de la pulvérisation cathodique et de matériaux respectueux de l'environnement. Dans ce cadre, nous avons utilisé la pulvérisation cathodique pour déposer le contact arrière en molybdène (plutôt un procédé standard). Nous avons développé un nouveau procédé de dépôt de la couche absorbante basé sur l'utilisation de la pulvérisation magnétron en mode DC-pulsé, à température ambiante et à partir d'une seule cible quaternaire en utilisant un plasma d'argon sans apport supplémentaire de sélénium, suivi d'un recuit sous atmosphère inerte. Nous avons développé un procédé de pulvérisation à température ambiante pour déposer la couche tampon ZnS_xO_{1-x}. Nous avons également développé un procédé de dépôt de la couche de fenêtre (toujours par pulvérisation cathodique soit en mode DC-pulsé soit en mode RF). Plusieurs techniques de caractérisation (XRD, SEM, FIB-SEM, EDX, Raman, SIMS, Effet Hall, GDOES, UV-Vis, et IV) ont été utilisées pour étudier l'effet des conditions de dépôt sur les propriétés des couches minces ainsi que pour caractériser les cellules solaires finales dont le meilleur résultat obtenu sur l'efficacité est proche de 12%.

Mots-clefs: cellule solaire de seconde génération, couche mince, pulvérisation magnétron, recuit thermique, atmosphère neutre, absorbeur en CIGS, couche tampon ZnS_xO_{1-x}, couche fenêtre en ZnO:Al.